STRUCTURE/PROPERTY RELATIONSHIPS

IN GEL-SPUN POLYETHYLENE FIBRES

A thesis submitted to the

UNIVERSITY OF MANCHESTER

for the degree of

DOCTOR OF PHILOSOPHY

in the

FACULTY OF TECHNOLOGY

by

WOEI FUH, WONG

MATERIALS SCIENCE CENTRE

OCTOBER, 1992

DECLARATION

No portion of the work referred to in this thesis has been submitted in support of an application for another degree or qualification of this or any other university or other institution of learning.

ABSTRACT

The structure and morphology of a series of gel-spun polyethylene (PE) fibres and one melt-spun PE fibre have been examined using scanning electron microscopy (SEM), transmission electron microscopy (TEM), wide-angle X-ray diffraction (WAXD) and differential scanning calorimetry (DSC). The mechanical properties of these PE fibres have been determined for different modes of deformation and attempt has been made to measure the dynamic mechanical properties of PE fibres in a monofilament form. Raman microscopy has been used to investigate the deformation of these high-performance PE fibres and well defined Raman spectra can be obtained for the symmetric C-C stretching mode (1128 cm^{-1}). During mechanical deformation, these Raman spectra show the existence of a bi-modal molecular stress distribution in the crystalline phase resulting in split bands. Such information is particularly useful in determining the molecular deformation behaviour of the fibres. The structure/property relationships in the PE fibres have been interpreted using a microfibrillar model and the low-strain mechanical properties have been analyzed using the Takayanagi models. It has been shown that the behaviour can be best interpreted using a parallel-series model.

ACKNOWLEDGEMENTS

I wish to thank Professor R.J. Young for his valuable guidance, support and encouragement given throughout the course of this work. Also, I like to thank Allied-Signal Inc. for providing all the polymer samples and financial support.

I also like to record my appreciation of the assistance given by all the colleagues, particularly Dr. R.J. Day and Dr. A.J. Ryan, and technicians of the Manchester Materials Science Centre. Finally, my gratitude must go to my parents and my wife, Siu Cheng, for their patience and understanding.

LIST OF SYMBOLS

a_T	horizontal shift factor
A	cross-sectional area, amorphous phase
A_1	area of broad peak in Raman spectrum
A_2	area of narrow peak in Raman spectrum
b_T	vertical shift factor
C_1	high-load bearing crystalline phase
C_2	low-load bearing crystalline phase
d	distance between crystal planes
e	strain, overall strain
e_0	initial strain
e_1	strain in the spring
e_2	strain in the dashpot
E	tensile modulus, electric field, energy level
E_0	amplitude of electric field
E_a	energy of molecules before Raman scattering
E_a	tensile modulus of amorphous phase
E_b	energy of molecules after Raman scattering
E_c	tensile modulus of crystalline phasae
E_{eff}	effective tensile modulus
E'	storage modulus
E''	loss modulus
E^*	dynamic modulus
f	applied force
$G(x)$	Gaussian function
h	Planck's constant

i	complex number, peak intensity
I	input
k	constant
k_l	extensional deformation force constant
k_θ	angular deformation force constant
l	chain repeat, gauge length
L	chain length
M_w	weight-average molecular weight
n	integer number
p	peak position
Q	coordinate
Q_0	coordinate of initial position
R	response
t	time
T_m	melting temperature
w	full width at half maximum of the peak
x	real number

α	angle, polarizability
α_0	polarizability at the equilibrium configuration
A_1	relative area of the fitted broad Raman peak
A_2	relative area of the fitted narrow Raman peak
δ	phase lag, small increment

λ	draw ratio, wavelength, volume fraction
η	viscosity
σ	stress, overall stress
σ_0	initial stress
σ_1	stress in the spring
σ_2	stress in the dashpot
τ	relaxation time
τ'	retardation time
θ	angle
ϕ	polymer concentration, volume fraction
ϕ_c	degree of crystallinity
ϕ^*	polymer overlap concentration
μ	dipole moment
ν_0	incident frequency of photons
ν'_0	scattered frequency of photons
ν_{vib}	vibrational frequency
ω	angular frequency
Δ	differencing symbol

ΔE	energy difference
ΔH_f	enthalpy of fusion
$\Delta H_{f,c}$	enthalpy of fusion of completely crystalline polymer
ΔP	power difference
ΔT	temperature difference

$\Delta\nu$	Raman shift
$d\Delta\nu/d\varepsilon$	rate of shifts of Raman bands in $cm^{-1}/\%$
$(d\Delta\nu/d\varepsilon)_1$	rate of shifts of high-load bearing Raman bands
$(d\Delta\nu/d\varepsilon)_2$	rate of shifts of low-load bearing Raman bands
$d\Delta\nu/d\sigma$	rate of shifts of Raman bands in cm^{-1}/GPa

LIST OF ABBREVIATIONS

ABPBO	Poly(2,5-benzoxazole)
CCD	Charge Coupled Device
DSC	Differential Scanning Calorimetry
DTA	Differential Thermal Analysis
EM	Electron Microscopy
FE-SEM	Field Emission Scanning Electron Microscope
PAN	Poly(acrylonitrile)
PBA	Poly(*p*-phenylene benzamide)
PBO	Poly(*p*-phenylene benzobisoxazole)
PBT	Poly(*p*-phenylene benzobisthiazole)
PE	Polyethylene
PP	Polypropylene
PPTA	Poly(*p*-phenylene terephthalamide)
PVA	Poly(vinyl alcohol)
SEM	Scanning Electron Microscopy
TEM	Transmission Electron Microscopy
TSHD	Bis(*p*-toluene sulphonate) of 2,4-hexadiyne-1,6-diol
UHMW-PE	Ultra-high Molecular Weight Polyethylene
WAXD	Wide-angle X-ray Diffraction

CONTENTS

1

INTRODUCTION

During the last two decades, techniques for effective control of the supermolecular structure of semicrystalline polymers have been developed, bringing about a dramatic change in their mechanical characteristics. High-performance polyethylene (PE) fibres, particularly gel-spun PE fibres, are the major result of such developments and already represent a new class of materials. High performance gel-spun PE fibres, with Young's moduli of 100-200 GPa and tensile strengths of 2-5 GPa [1-6], are superior to classical materials such as steel on a property-weight basis. It is of considerable interest to know what aspects of the structure give such good mechanical properties and to know what mechanisms or defects cause the properties to be below their theoretical limits. Theoretical calculations have shown that the theoretical modulus of linear PE could be about 300 GPa with a strength of 9-36 GPa [7-8]. If these values are realistic, further improvement in mechanical properties may still be possible. Experimental techniques that can yield information concerning the relation between microscopic morphology and mechanical properties are therefore valuable both for understanding the properties of the fibres as well as investigating ways of their improvement.

Raman microscopy has been proven a successful technique to study the deformation of high performance fibres, particularly in a monofilament form, at the molecular level [9-22]. It

provides an important insight into the response of the fibre molecules to various modes of deformation. When such polymers are deformed the bonds in the molecular backbone are strained and some of the frequencies of Raman active bands shift to lower wavenumbers. In PE, well-defined Raman spectra can be obtained and stress-induced frequency shifts are observed [18-22]. It is found that the most stress-sensitive bands are those due to C-C stretching i.e. the C-C asymmetric (1060 cm^{-1}) and C-C symmetric (1127 cm^{-1}) stretching bands. This allows the measurement of the local stress distribution within the monofilament and may help to relate mechanical properties to structure. Additionally, it may be possible to explore the complexity of the viscoelastic behaviour of the PE monofilaments at the molecular level.

Other structural characterization techniques such as electron microscopy (EM), wide-angle X-ray diffraction (WAXD) and thermal analysis provide complementary information on structure/property relationships in the gel-spun PE fibres. Transmission electron microscopy (TEM), in particular, provides details of morphology at levels down to molecular dimensions and WAXD primarily probes the degree of order in the regularity of interchain arrangements. In addition, thermal analysis provides information on the thermal properties of the fibres which is directly related to the structure and morphology.

The main purpose of this work is to investigate the structure/property relationships in gel-spun PE fibres. The initial part of the work has been concerned with an analysis of the structure and morphology of various gel-spun PE fibres together with melt-spun PE fibres for comparison purposes

(Chapter 3). Various techniques such as scanning electron microscopy (SEM), transmission electron microscopy (TEM), wide-angle X-ray diffraction (WAXD) and differential scanning calorimetry (DSC) have been used for the structural characterization of the fibres. This has been followed by an evaluation of the mechanical properties of the monofilaments including stress-strain and viscoelastic behaviour, stress relaxation and creep (Chapter 4). A study is then made of the deformation micromechanics in monofilaments using Raman microscopy (Chapter 5). Based on the microfibrillar model which consists of the structural units of microfibrils [23-24] and the Takayanagi model [25], an attempt has been made to correlate the observed mechanical behaviour to deformation processes occurring on a molecular scale (Chapter 6).

2

HIGH-PERFORMANCE GEL-SPUN POLYETHYLENE FIBRES

2.1 INTRODUCTION

The field of high-performance fibres has witnessed considerable growth in the last three decades. A large number of inorganic fibres and high-performance polymeric fibres are available in the market today. Significant research covering many diverse aspects of these fibres continues and, therefore, further improvements in properties and the development of new areas of applications can be expected in near future.

Inorganic fibres, notably carbon and glass fibres, have high melting points, high tensile moduli and physical properties that make them good reinforcement for polymer matrix composites, and they have been used widely for many years. Whereas polymeric fibres were, until recently, characterized by very low moduli, attempts to produce high-performance polymeric fibres have met with some success particularly from stiff-chain polymers such as *Kevlar* and flexible-chain polymers such as polyethylene (PE).

Today, high-performance PE fibres are potentially a material of choice in applications requiring good mechanical properties and light weight. They have relatively low density (<1 gcm^{-3}) and show a distinct advantage over metals and ceramics on a property-weight basis as illustrated in Fig.2.1. A wide range of applications have been explored and the fibres are gaining ground as reinforcement in advanced composites [26-28].

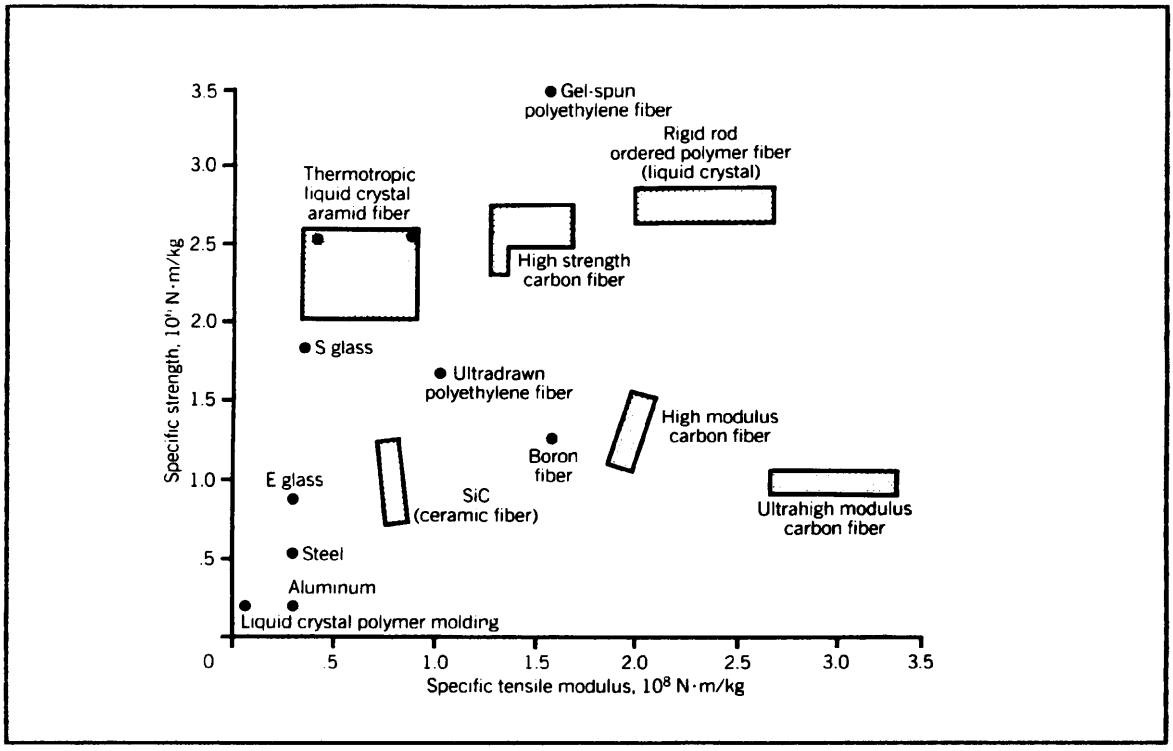

Fig.2.1 Comparison of specific strength vs specific modulus for a variety of high performance materials. Specific properties are normalized by material density [29].

2.2 HIGH-PERFORMANCE POLYMERIC FIBRES

There are two fundamentally different approaches to the making of high-performance polymeric fibres. One is the transformation of conventional, flexible chain, random coil polymers into an almost perfectly-oriented, extended-chain structures in the fibre. The most successful example of this approach is gel-spinning of ultra-high molecular weight polyethylene (UHMW-PE) [1-6] and poly(vinyl alcohol) (PVA) [1,30]. Other examples include tensile drawing [31-32], solid-state extrusion [32-33] and flow-controlled crystallization [34]. The second approach is the molecular design of stiff, planar molecules that exhibit liquid crystal behaviour in solution (lyotropic) or in melt (thermotropic) and by processing the polymers in ways that result in an extended rigid chain configuration. Two most important

lyotropic examples are aramid fibres such as poly(*p*-phenylene terephthalamide) [35-36], and rigid-rod polymeric fibres, a group of ultra-stiff lyotropic molecules that exhibit the highest modulus values yet observed in organic polymeric fibres [37-38]. Thermotropic liquid crystalline fibres such as aromatic copolyesters [39-40] are also slowly receiving attention as the polymers can be brought into the liquid crystalline state through temperature changes and hence, are melt-spinnable. The spinning of aromatic copolyesters is relatively simple, whereas aramid and rigid-rod polymeric fibres must undergo several complicated steps in going from the original polymers to the final fibre product. Consequently, thermotropic liquid crystalline polymers have attracted much interest, purely from an economic standpoint.

2.2.1 Aramid Fibres

The word *aramid* describes a class of fibre-forming polymers defined as *a long chain synthetic polyamide in which at least 85% of the amide linkages are attached directly to two aromatic rings* [41]. They include poly(*p*-phenylene terephthalamide), PPTA and poly(*p*-phenylene benzamide), PBA with the chemical structures shown in Fig.2.2. Both polymers exhibit anisotropic properties in solution due to the absence of flexible spacers and the extended chain conformation of their structures, which are inevitable in view of the 1,4-phenylene linkages and the planar amide groups (Fig.2.2). In addition, they form fibres with good thermal and chemical stability because of their substantial aromatic content.

The most common aramid fibre is PPTA fibre which was

Poly(*p*-phenylene terephthalamide), PPTA

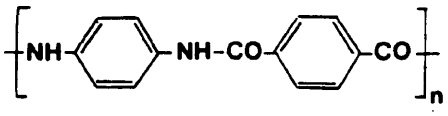

Poly(*p*-phenylene benzamide), PBA

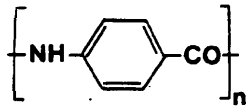

Fig.2.2 Chemical structures of aramids.

commercialized first by Du Pont as the *Kevlar* fibre. Another similar commercial aramid fibre is the *Twaron* fibre which was developed by Akzo. The fibres are spun from nematic liquid crystalline solutions using a dry-jet wet spinning technique, where aggressive solvents such as sulphuric acid are used. The mechanical properties can be enhanced by heat treatment under tension, which improves orientation and removes defects in the structure [35]. However, it is only the tensile modulus that is enhanced significantly by heat treatment and there is little effect on fibre strength [36].

There are three types of Kevlar fibres which are commercially available: Kevlar 29, Kevlar 49 and Kevlar 149. Kevlar 49 is produced through the heat treatment of Kevlar 29 which is an as-spun fibre. Kevlar 149 is the highest tensile modulus aramid fibre currently available with the modulus of 185 GPa and tensile strength 3.4 GPa [42]. Considering the density of PPTA which is only 1.45 gcm^{-3}, the specific properties are

even more impressive. However, Kevlar 149 is a relatively new fibre and most of the structural data are available on Kevlar 49. Based primarily on electron microscopy observations of the longitudinally-ultramicrotomed sections of Kevlar 49, Dobb *et al* [43] concluded that the supermolecular structure has radially oriented crystallites. It is also characterized by a pleated structure along the fibre axis with the angle between pleats reportedly being about 170° (Fig.2.3), and the overall fibre structure being fibrillar [35]. Obviously, such a structure will considerably influence the excellent mechanical properties of aramid fibres [44].

Aramid fibres have good thermal stability with a glass transition temperature >300°C [35]. The tensile strength is well preserved after high temperature exposure and the fibres can therefore be used in a relatively high temperature environment. Other properties of aramid fibres include low creep, good fatigue and good chemical resistance. However, low compressive strength,

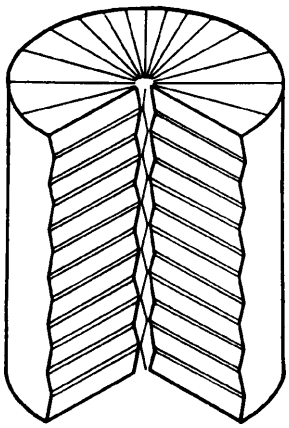

Fig.2.3 Schematic diagram of Kevlar 49 fibre showing the radially arranged pleated sheets [43].

poor transverse properties and a high sensitivity to ultraviolet light are among the disadvantages of aramid fibres.

Aramid fibres have become established in various applications in several areas. For example, the fibres are already used in body armour, helmets, cables and asbestos replacement friction materials [35]. However, the major application of aramid fibres involves the reinforcement of the polymer matrix composites which are used as structural engineering materials in the automotive and aerospace industries.

2.2.2 Ordered Polymeric Fibres

The term *ordered polymers* is generally used for aromatic heterocyclic rigid-rod and semi rigid-rod polymers because of their ability to form highly-ordered structures in the solid state. These polymers include the rigid-rods poly(*p*-phenylene benzobisthiazole), PBT and poly(*p*-phenylene benzobisoxazole), PBO, and semi rigid-rod poly(2,5-benzoxazole), ABPBO. Significant development work on these polymers has been done at the US Air Force Materials Laboratory since 1960. Of particular interest have been PBT and PBO (Fig.2.4) which enables the preparation of high-performance polymeric fibres having exceedingly attractive mechanical properties and good high temperature resistance.

Developments in the last decade in synthesis and processing of aromatic heterocyclic polymers have led to the consideration of commercialization of PBO fibres, while most early development work was done on PBT fibres. As with aramid fibres, both are produced by dry-jet wet spinning from concentrated acids such as polyphosphoric acid and their properties are improved by heat

Poly(*p*-phenylene benzobisthiazole), PBT

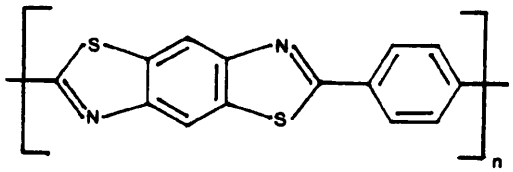

Poly(*p*-phenylene benzobizoxazole), PBO

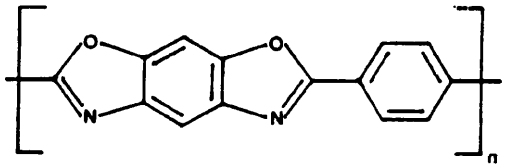

Fig.2.4 Chemical structures of rigid-rods ordered polymers.

treatment [37]. In fact, they have been found to achieve very high levels of modulus, in excess of 300 GPa and strengths of over 3 GPa [37,42].

PBT and PBO fibres are characterized by extremely high orientation and order. The concept of an amorphous phase as commonly understood in flexible chain polymers does not appear to exist in ordered polymeric fibres. Analysis of both wide- and small-angle X-ray diffraction patterns has indicated the presence of three-dimensional crystalline order in PBO fibres [42]. This is at variance with findings upon PBT fibres where the structure is axially disordered, being viewed as a frozen nematic or two-dimensional crystallite without registry of repeat units as illustrated in Fig.2.5 [38]. However, this highly oriented structure of PBT and PBO fibres is fibrillar in nature and there is a poor transverse coupling between the fibrils. This contributes to a microbuckling type of instability with compressive strains as low as 0.2% causing the propagation of

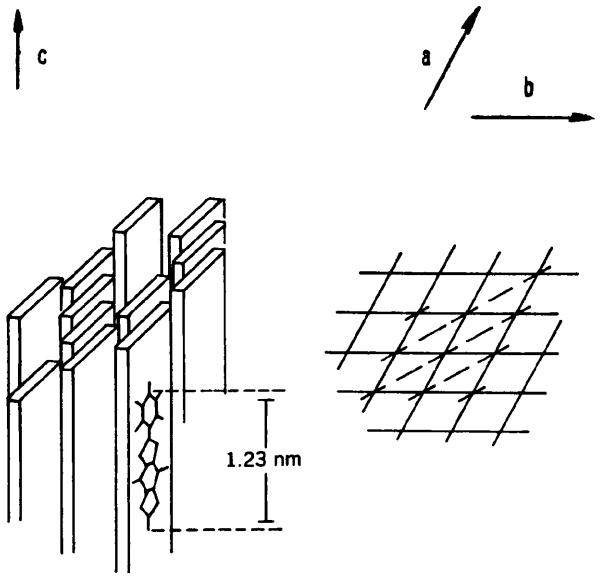

Fig.2.5 Suggested packing arrangement of PBT molecules [38].

kink banding [38].

PBT and PBO fibres have the highest thermal stability among the high performance polymeric fibres with long term retention of mechanical properties at elevated temperatures. Their environmental, chemical and radiation resistance are also excellent. However, the use of these fibres is limited to those applications where axial compressive loading is minimized, or hybrids of these fibres with good compressive strength fibres can be used [42]. Possible applications are: use as reinforcements in composites, marine applications, and ballistic and fire protection fabrics.

2.3 HIGH-PERFORMANCE POLYETHYLENE FIBRES

High performance polymeric fibres made from flexible chain polymers already represent a new class of materials. So far, this approach to the making of strong extended-chain structures has proved to be particularly successful in the case of PE which has

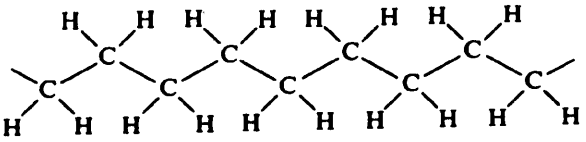

Fig.2.6 Chemical structure of polyethylene.

a simple chemical structure (Fig.2.6). In order to obtain a valuable insight into the failure processes that occur in such materials, it is of considerable interest to obtain an estimate of the theoretical stiffness for PE.

2.3.1 Theoretical Stiffness for Polyethylene

It is important to consider the tensile strength and modulus of a single chain because the ultimate stiffness and strength of a fibre depends on the load-bearing ability of aggregate of single chains. In fact, Treloar's estimation is based on a single chain in planar zig-zag conformation which is similar to the most stable molecular conformation of PE in crystal structure [45]. In this estimation, a relatively simple calculation is used which involves only the bending and stretching of the bonds along the molecular chain.

The model of the polymer chain used in calculation is shown schematically in Fig.2.7 [45-46]. It is treated as consisting n rods of length l which are capable of being stretched along their lengths but not of bending, and are joined together by torsional springs. The bond angles are taken initially to be θ and the angle between the applied force f and the individual bonds as initially α. The original length of the chain L is then (nl cos

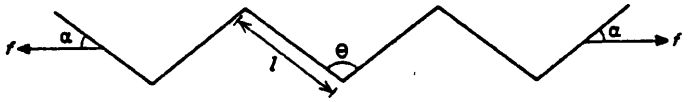

Fig.2.7 Model of a polymer chain undergoing deformation [45].

α) and so the change in length δL on deforming the chain is given by

$$\delta L = n.\delta(l\cos\alpha) = n(\cos\alpha.\delta l - l\sin\alpha.\delta\alpha) \qquad (2.1)$$

During bond stretching, the force acting along the bond direction is (f cos α). This can be related to the extension δl through the force constant for bond stretching k_l which can be determined experimentally from infra-red or Raman spectroscopy. k_l is the constant of proportionality relating the force along the bond to its extension i.e.

$$\delta l = \frac{f\cos\alpha}{k_l} \qquad (2.2)$$

The change in bond angle δθ is related to the angular deformation force constant k_θ which is equal to the torque acting around bond over the change in bond angle. The torque is the moment of the applied force about the angular vertices, i.e. (f.sin α).(l/2). Hence,

$$\delta\theta = \frac{fl\sin\alpha}{2k_\theta} \qquad (2.3)$$

But since it can be shown by a simple geometrical construction that α=90°-θ/2, then it follows that

$$\delta\alpha = -\frac{\delta\theta}{2} \tag{2.4}$$

Combining equations (2.3) and (2.4),

$$\delta\alpha = -(fl\sin\alpha)/4k_\theta \tag{2.5}$$

Putting equations (2.2) and (2.5) into (2.1) gives

$$\delta L = nf\left[\frac{\cos^2\alpha}{k_l} + \frac{l^2\sin^2\alpha}{4k_\theta}\right] \tag{2.6}$$

The Young's modulus of the polymer is given by

$$E = \left(\frac{f}{A}\right)\cdot\left(\frac{L}{\delta L}\right) \tag{2.7}$$

where A is the cross-sectional area supported by each chain and so,

$$E = \frac{l\cos\alpha}{A}\left[\frac{\cos^2\alpha}{k_l} + \frac{l^2\sin^2\alpha}{4k_\theta}\right]^{-1} \tag{2.8}$$

or in terms of the bond angle θ,

$$E = \frac{l\sin\left(\frac{\theta}{2}\right)}{A}\left[\frac{\sin^2\left(\frac{\theta}{2}\right)}{k_l} + \frac{l^2\cos^2\left(\frac{\theta}{2}\right)}{4k_\theta}\right]^{-1} \tag{2.9}$$

With the knowledge of the PE crystal structure which gives A, l and θ, and the spectroscopically-measured values of the force constants k_l and k_θ, the value E for PE is about 180 GPa. This value is generally rather lower than values obtained from more sophisticated calculations, which can be as high as 300 GPa [7-8]. This is because the above analysis does not allow for intramolecular interactions which tend to increase the modulus further.

2.3.2 Developments for High-Performance Polyethylene Fibres

In the chemical structure of PE (Fig.2.6), it has no side groups and so has a small cross-sectional area per chain. A tightly packed array of parallel PE chains has therefore a high density of load bearing elements and should produce a very strong material. Theoretical calculations have shown that the strength of linear PE could be as high as 19-36 GPa with a corresponding modulus of about 300 GPa [7-8]. However, these were calculated from loading individual, infinite chains to the rupture of C-C bond. In reality, they are finite chains and the oriented systems inevitably contain a number of flaws and molecular irregularities such as chain ends, molecular twists and entanglements. Hence, the theoretical values can never be attained in practice and the maximum values of modulus are determined by factors such as chain length, degree of chain orientation, crystallinity and, above all, chain extension. The effect of chain extension is shown schematically in Fig.2.8 for crystallites with the same

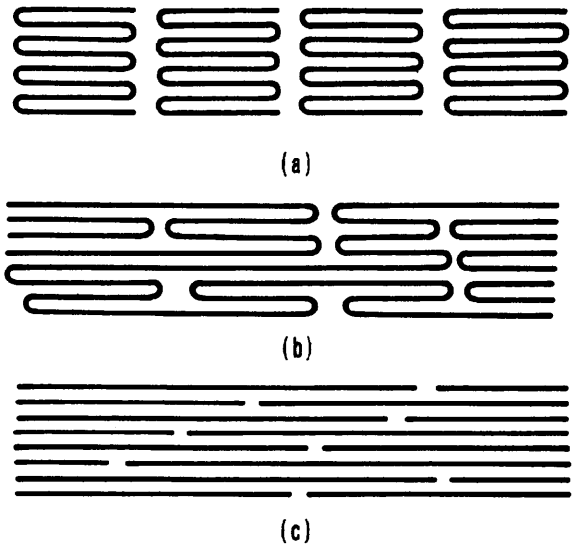

Fig.2.8 Molecules showing the same degree of orientation but differing in molecular extension [1].

orientation factor but differing in molecular extension. Clearly the level of modulus increases from a very low value for Fig.2.8a to its maximum value for Fig.2.8c. Hence, the development of techniques since 1970s to bring about a more complete orientation and extension of the macromolecules has resulted in fibres with surprisingly good mechanical characteristics.

2.3.2.1 Deformation in the Solid State

The early development of high-performance PE fibres was based on two general routes. The most straight forward way uses the deformation of PE in the solid state or in the melt.

In the early 1970s, Andrews and Ward [47] undertook a systematic investigation of the influence of natural draw ratio on the Young's modulus of melt-spun PE monofilaments. They reported that the axial Young's modulus increased up to about 20 GPa with increasing natural draw ratio. Later, Ward *et al* [32] studied the influence of spinning and cooling/quenching conditions of the as-spun PE filaments on the maximum drawability. By optimizing the conditions, fibres could be obtained possessing moduli of up to about 70 GPa. However, in the melt, the maximum molecular weight of the molecules that can be handled is limited due to a strong rise in melt viscosity [1]. In addition, with increasing molecular weight, the melt-spun PE monofilament increasingly resists deformation in the solid state as illustrated in Fig.2.9 [32,47]. Consequently, solid-state drawing leads to high modulus PE fibres, but with relatively low strength (about 1 GPa) and poor creep resistance.

Deformation in the solid state is not restricted to tensile

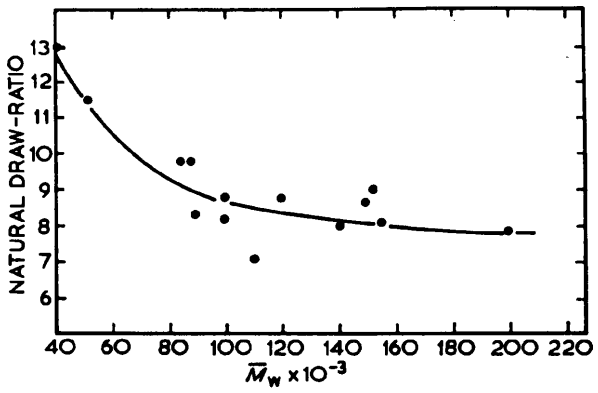

Fig.2.9 Maximum observed draw ratio of melt-spun PE fibres drawn at room temperature as a function of molecular weight [32].

drawing of spun filaments. In fact similar results can also be obtained by solid-state extrusion: hydrostatic extrusion [32] and ram extrusion [33] in which the achievable deformation ratio is largely determined by the die geometry. However, as with the tensile drawing technique, the same limitations are encountered with respect to higher molecular weight in extruding solid PE [32].

2.3.2.2 Solution Methods

In mid-70s, Pennings *et al* [48] developed a technique for continuous longitudinal growth of fibrillar crystals of linear PE subject to Couette flow. The fibres appeared to have a *shish-kebab* morphology, a central core consisting of more or less extended PE molecules and folded-chain type crystals (with lamellar overgrowths) deposited on the core as illustrated in Fig.2.10. This intriguing structure is far from the ideal arrangement of PE molecules with respect to stiffness and strength.

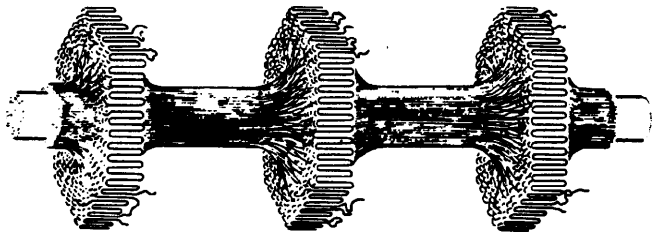

Fig.2.10 Schematic representation of the *shish-kebab* morphology [1].

The work on stirring-induced crystallization was followed by various techniques such as free growth, culminating in the so-called surface-growth technique [34]. Fig.2.11 shows a schematic diagram of the surface-growth technique [1]. A seed crystal is immersed into the gap between the cylinders and when its tip contacts the moving surface (rotor), it starts growing. A take-up roll is then switched on and a continuous fibre is slowly produced.

In the late 1970s, Pennings *et al* [34] reported that under optimized experimental conditions, a extended-chain PE fibres could be obtained possessing tensile moduli of over 100 GPa and strength values above 3 GPa. The significance of the work was that long molecules i.e. UHMW-PE were used. Although a technological process was not feasible in view of the limited

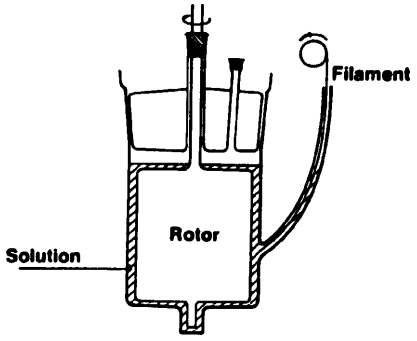

Fig.2.11 Schematic diagram of surface-growth technique [1].

take-up speeds (<1 m min^{-1}), it provided the experimental proof that high performance fibres based on UHMW-PE were possible.

2.4 GEL-SPINNING

In spite of its poor processability in fibre spinning, investigations were continued on producing fibres from UHMW-PE because of its superiority in mechanical properties such as toughness, strength, creep properties and chemical resistance. By the end of 1970s, Smith *et al* [49] developed an alternative route to high performance UHMW-PE fibres at a substantially higher production rate. This technique [49-50] is based on a simple solution-spinning followed by hot-drawing that can be performed continuously as shown in Fig.2.12. The as-spun filaments were quenched in cold water to form *gel filaments*. These *gel filaments* could be ultra-drawn to high-strength/high-modulus fibres with Young's modulus of about 100 GPa and strength of 3 GPa. Although at first glance this technique seems similar to conventional solution-spinning of fibres, it is now often referred to as gel-spinning.

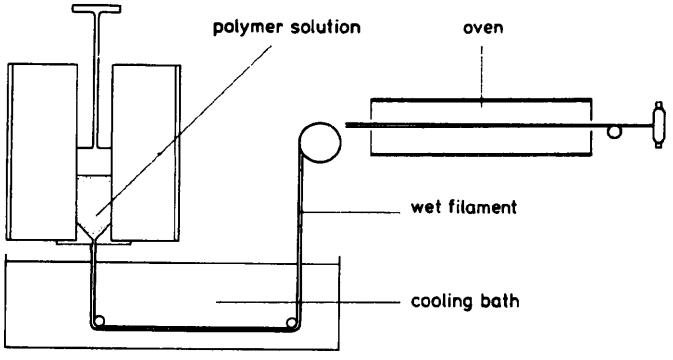

Fig.2.12 Schematic diagram of the solution spinning/drawing process [50].

2.4.1 Mechanisms for Gel-spinning and Ultra-drawing

The remarkable feature of gel-spinning is that after complete solvent removal from the as-spun filament, ultra-drawing is still possible. It is a sharp contrast with melt-spun filaments in which the drawability is limited by molecular weight.

The PE *gel filament* itself is a highly solvated network [51]. The term *highly solvated* signifies that most of the macroscopic volume consists of solvent and the network is a very loose one. Apparently within the network, the connected points or junctions are physical associations, i.e. they are not permanent chemical bonds. They result from crystallization, where the junctions are either the crystallites themselves [51], or entanglements stabilized (trapped) in the solid structure (gel) that is generated [1,51-52].

Based on systematic investigations of the effect of initial UHMW-PE concentration in solution and the subsequent ultra-drawing characteristics, Smith *et al* [53] concluded that the strongly enhanced drawability i.e. ultra-drawing is due to the reduction of the entanglement density in the *gel filaments*. Lemstra *et al* [1,52] further elaborated this model by suggesting the concept of crystallization from *semi-dilute solution* for the mechanism of gel-spinning as illustrated in Fig.2.13. If the polymer concentration, ϕ is too low, below the overlap concentration, ϕ^*, chains are separated and, upon cooling, individual folded-chain crystals will precipitate. If spinning is performed from semi-dilute solution ($\phi > \phi^*$) in which chains overlap and are entangled to a certain extent, a coherent filament will be obtained in which the coherence is provided

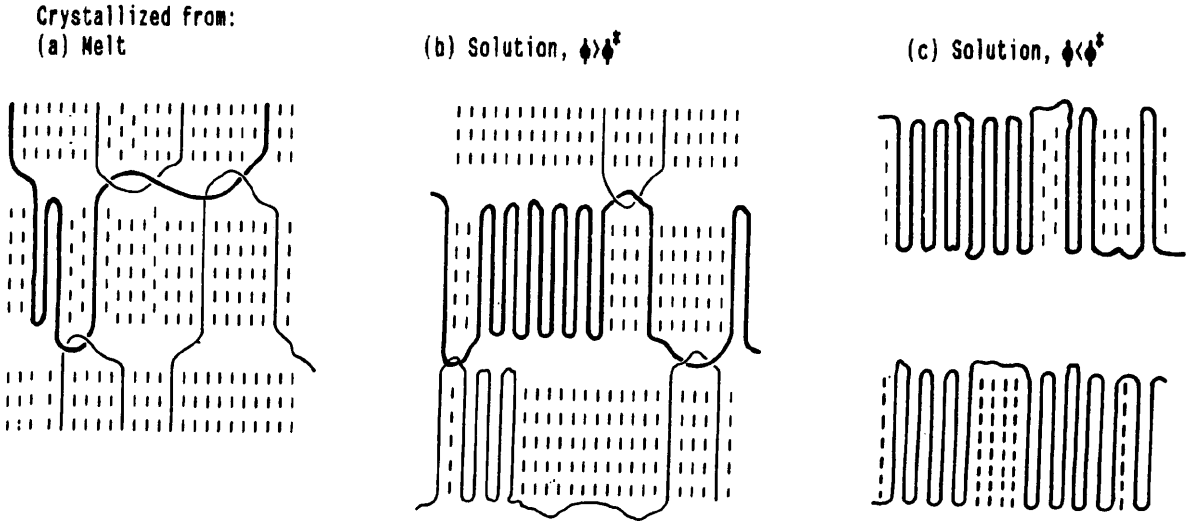

Fig.2.13 Chain topology in crystallized UHMW-PE showing polymer chain (bold line) with entangled neighbours (light line) and non-entangled neighbours (dashed line) [52].

through trapped entanglements. However in the case of melt-crystallized UHMW-PE, the high entanglement density per chain is prohibitive to ultra-drawing. This stops the UHMW-PE from being able to undergo melt-spinning as the high entanglement density is retained to a large extent in the solidified filaments.

Obviously the drawability implies molecular connectedness. An unconnected system of chains in the solution state will not draw, but flow. However, if there are too many junction points, the network is too tight and the extensibility is limited. Hence during drawing, the forces required will be too high for the molecules to sustain the system and consequently, the macroscopic sample will rupture before sufficient extension takes place. Although this model involves gross oversimplifications, it conveys the basic principles of the gel-spinning technique.

2.4.2 Processing

Figure 2.14 shows schematically a typical gel-spinning set-up

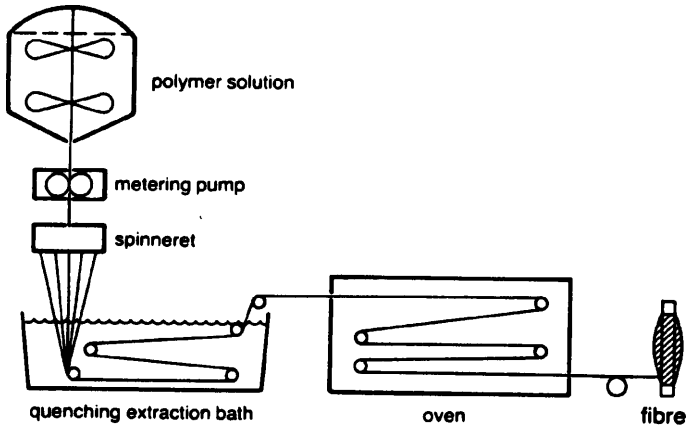

Fig.2.14 Schematic diagram of gel-spinning process [1].

[1]. The UHMW-PE is dissolved in decalin at ~150°C. The viscous solution is spun at ~130°C into a water bath, forming *gel filaments* due to immiscibility of the solvent with water. The filaments are then ultra-drawn at high temperature (~120°C) and the solvent is removed simultaneously and potentially recycled.

Several developments and refinements have appeared in recent years describing variations of this technique including the use of alternative solvents such as paraffin oil [54-55]. In this development, the UHMW-PE is dissolved in paraffin oil at ~150°C and to form a gel upon cooling. The gel is extruded and the solvent is extracted from the filaments with *n*-hexane before ultra-drawing (Fig.2.15). In fact under optimized conditions, these *dry gel filaments* can be ultra-drawn to Young's modulus of about 160 GPa and a strength exceeding 6 GPa [55].

Today, the gel-spinning technique has been commercialized by Dyneema VoF, a joint venture of Dutch State Mines (DSM) with Toyobo to produce *Dyneema* fibres and by Allied-Signal to make

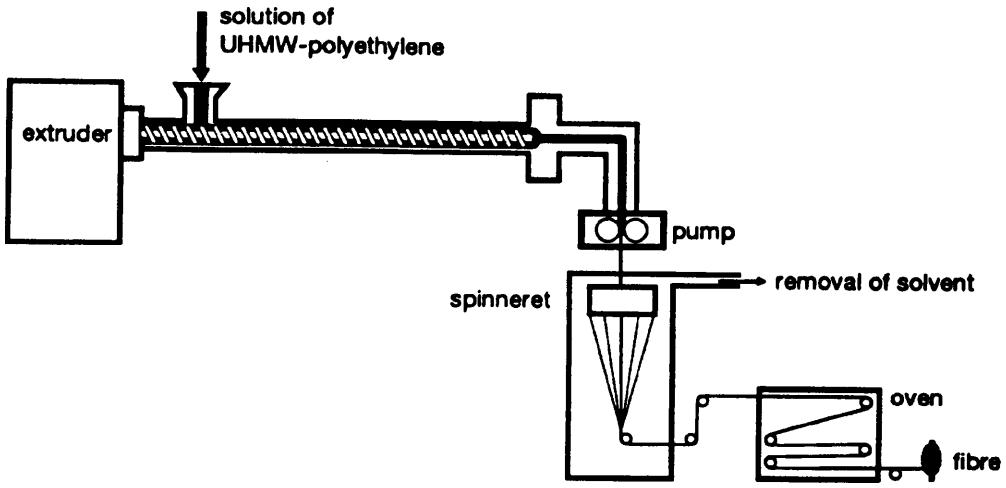

Fig.2.15 Schematic diagram of alternative method of gel-spinning process [56].

Spectra fibres. Significantly, this technique has enabled the industry to convert a relatively cheap high-volume polymer into a valuable high performance material.

2.5 PROPERTIES AND APPLICATIONS

The properties of gel-spun PE fibres in comparison to other high performance fibres have given rise to a real new class of materials. It has been the unique combination of physical properties which has led to the relatively rapid acceptance of this new material on a commercial scale with a wide range of applications.

2.5.1 Properties

The particularly favourable property of PE is its low density which causes gel-spun PE fibres to be the polymeric fibres with the highest specific strength (Table 2.1). This, combined with the high values of stiffness, makes gel-spun PE fibres a prime

Table 2.1

MECHANICAL PROPERTIES OF VARIOUS COMMERCIAL HIGH PERFORMANCE POLYMERIC FIBRES.

Fibre	Modulus (GPa)	Tensile Strength (GPa)	Density (kg/m^3)	Specific Modulus ($x10^8 N.m/kg$)	Specific Tensile Strength ($x10^6 N.m/kg$)	Reference
Spectra 1000	170	3.0	970	1.75	3.09	42
Dyneema SK60	87	2.7	970	0.90	2.78	4
Kevlar 29	58	2.7	1440	0.40	1.88	4
Kevlar 49	125	3.5	1440	0.87	2.43	42
Kevlar 149	185	3.4	1450	1.28	2.34	42

choice in engineering applications from the viewpoint of weight saving. Apart from that, the chemical structure of PE (Fig.2.6) contains no aromatic rings and no amide, hydroxylic or other groups that are sensitive to attack by external aggressive agents. Hence, on the basis of its chemical structure, this results in an excellent resistance to UV light.

However, as with other PE fibres, gel-spun PE fibres perform poorly in some respects such as thermal properties. They have a low melting point (~150°C) which eliminates many applications at elevated temperatures. Although the fibres are based on UHMW-PE, they still exhibit significant creep and a higher strain rate dependence of mechanical properties than other reinforcing fibres. Another drawback is their weak interfacial bonding to matrix resins which imposes some restrictions on the use of these fibres in composites.

2.5.2 Applications

Gel-spun PE fibres have significant potential in composite applications, even though they have poor bonding with resins.

This is because these fibres have the advantages of weight reduction, impact improvement and an increase in damage tolerance [3].

Recently Allied-Signal has developed a new fibre-reinforced composite called *Spectra Shield* based on their Spectra fibres which is claimed to be 30-50% lighter than comparable composites [26-28]. In fact, a ballistic system comprising both a ceramic composite and *Spectra Shield* has been developed to allow improved protection level, while reducing weight [27-28]. It is already finding application as a lightweight armour for use in military helicopters [27-28]. A further application of these fibres in composites includes its uses in certain strategic composite parts in Fairchild's aircraft fleet [27] and as a reinforcing component in an epoxy resin composite developed by the US Army Special Forces for the lightweight, portable antenna [28].

Gel-spun PE fibres can also be used as fabrics to make very strong, light tents, and filter cloths which are suitable for use in aggressive and corrosive environments. Other applications include strings, ropes, and knitted products. It is interesting to see that through new technical know-how, old fashioned PE can become a *high-tech* material with a wide range of unforseen applications.

3

STRUCTURE AND MORPHOLOGY OF THE FIBRES

3.1 INTRODUCTION

The attainment of high levels of mechanical properties close to the theoretical levels inevitably prompts the question as whether the structure of high-performance polyethylene (PE) fibres might be completely different from that of conventional fibres. In an attempt to answer this, a range of techniques which probe different levels of morphological and molecular organisation need to be used.

This chapter is concerned with the results obtained from various techniques of characterization to determine the microstructure and the morphology of the PE fibres. The range of techniques used in this work will be reviewed (Section 3.3) and followed by a discussion of the results of characterization (Section 3.5).

3.2 MICROSTRUCTURE OF HIGH-PERFORMANCE POLYETHYLENE FIBRES

Ultra-high molecular-weight PE (UHMW-PE) shows a number of different microstructures depending on the method of preparation of specimens and their treatment [57-64]. Generally, lamellar and fibrillar structures are the main morphological forms found in the PE fibres.

Lamellae are found to grow with dimension typically of the order of 100 A thick [46]. The chain axis of the molecule is

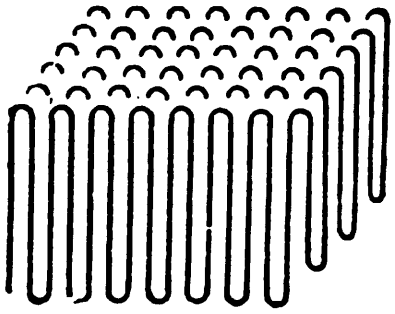

Fig.3.1 Lamellar structure formed by regular bends of a chain molecules [65].

close to perpendicular to the plane of the lamellae and the molecules are repeatedly bent back on themselves to form a *folded structure* as shown in Fig.3.1. According to Bashir *et al* [57-58], such lamellar structures can be found in the melt-processed high-modulus PE fibres in the form of an interlocking shish-kebab structure (Fig.3.2). It consists predominantly of stacked lamellae with the layer normals along the fibre axis. However, this is a composite morphology with the central core consisting of extended PE molecules which is, in fact, a fibrillar structure. Similarly, Schaper *et al* [59-60] have observed such a morphology in the surface-growth PE fibres and it was found

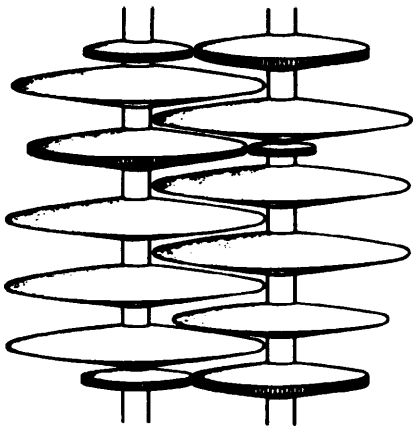

Fig.3.2 Schematic diagram of the interlocking shish-kebab structure in melt-processed PE fibres [57].

that upon drawing the fibres, the shish-kebabs were transformed into a well-aligned fibrillar structure. These shish-kebabs were also found as an intermediate morphology during the gel-spinning of UHMW-PE fibres as reported by Pennings *et al* [61].

The main feature of the fibrillar structure is its high degree of chain extension. This supermolecular structure was first proposed by Peterlin [23-24] with extended structural units are arranged more or less parallel to the fibre axis as shown in Fig.3.3. The individual fibril can be composed of smaller units called microfibrils. The microfibrils consist of crystalline and non-crystalline regions which are arranged in regular succession, leading to a substructure oriented predominantly in the fibre direction. Using both techniques of permanganic etching and chlorosulphonic acid staining of the samples, Hoffmann *et al* [62-63] have actually observed long and smooth microfibrillar crystals in the gel-spun PE fibres on transmission electron microscopy.

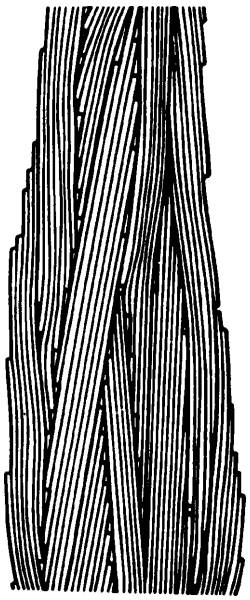

Fig.3.3 Fibrillar model of fibrous structure [23].

Microfibrillar and lamellar structures are the two extreme cases of microstructure in PE fibres. However, it is the chain extension rather than the orientation which has a dominant effect on the mechanical properties of fibres. Therefore, the principle underlying the attainment of high-performance PE fibres is to stretch out instead of merely orienting the chains in the microstructure.

3.3 TECHNIQUES OF STRUCTURAL CHARACTERIZATION

Several techniques are usually required in order to provide complementary information for a full characterization to be undertaken. Polymeric fibres, in particular, require techniques such as electron microscopy, X-ray diffraction and thermal analysis to reveal the complexity in the multi-phase structure of the crystalline and amorphous regions. X-ray diffraction is useful in determining the crystalline structure and the level of molecular orientation. However, details of morphology can best be inferred from continuum analytical measurement such as electron microscopy. Electron microscopy can provide detailed and unambiguous morphological information, although great care must be taken to avoid artifacts that might lead to serious errors. In addition, methods of thermal analysis such as differential scanning calorimetry (DSC) provide average information on the thermal properties which are closely related to structure and morphology of the fibres.

3.3.1 Scanning Electron Microscopy (SEM)

The essential feature of a scanning electron microscope is that

the image is formed point by point, by scanning a probe across the specimen [66]. The probe of an SEM is a focused electron beam and the detected signal is displayed as a TV type image.

Polymeric fibres, particularly PE, have low conductivity which is not conducive to satisfactory image formation in the high vacuum of the SEM where electrostatic charging is a major hindrance. This can be overcome by operating the microscope at a low accelerating voltage (i.e. about 10 keV) which also increases the surface detail and minimizes bright edge effects due to charging on the fibres. However, this is at the expense of lower spatial resolution due to insufficient electrons being collected to form an image within a reasonable time. Using the field emission guns, which necessitate an ultra-high vacuum, enables big improvements to be made in the resolving powers of the instrument [67]. The advent of field emission sources means that brighter electron beams with higher beam current than those from conventional tungsten filaments can be obtained using a small spot. This results in an improved signal-to-noise ratio and better resolution even under the reduced operating conditions necessary to avoid the electrostatic charging.

3.3.2 Transmission Electron Microscopy (TEM)

A transmission electron microscope is an electron optical instrument analogous to light microscope, where the specimen is illuminated by an electron beam. This requires operation in a vacuum since air scatters electrons. The TEM provides detailed structural information at levels down to atomic dimensions, but such high resolution is seldom achievable with polymers.

Nevertheless, it is possible to obtain information within the range of 1-100 nm with varying degrees of difficulty [68].

The most difficult aspect of this technique is specimen preparation. Usually there are two different specimen preparation methods for PE fibres. They are (i) the permanganic acid etching technique, which was developed by Bassett *et al* [69-70], followed by replication, and (ii) chlorosulphonic acid staining followed by ultramicrotoming [66]. In method (i), permanganic acid preferentially diffuses into and attacks the amorphous regions whereas the crystalline lamellae remain on the surface [69]. Method (ii) is a staining technique which chlorosulphonic acid introduces heavier atoms, principally chlorine and sulphur, into interlamellar regions and produces enhanced contrast in the PE [69].

Unfortunately, using method (i) it is not be possible to quantify molecular orientation of fibres by electron diffraction. However, it is still an important technique because the etching reveals significant detailed microstructural information. Also, the replica is much more stable in the electron beam than the ultramicrotomed sections and thus can be examined in the TEM for long periods at convenient levels of magnification and brightness [68].

3.3.3 Wide-angle X-ray Diffraction (WAXD)

Wide-angle X-ray Diffraction (WAXD) is a powerful tool for investigating spatially-ordered arrangements of atoms or molecules in crystals through the interaction of electromagnetic radiation to give interference effects with structures comparable

in size to the wavelength of the radiation employed [71]. The crystallites present in the polymer structure diffract X-ray beams from crystal planes for incident angles θ which are determined by the Bragg equation [46,71],

$$n\lambda = 2d\sin\theta \qquad (3.1)$$

where λ is the wavelength of the radiation, d is the distance between the parallel planes in the crystallite, and n is an integer.

In highly-oriented structures such as high-performance polymeric fibres, the crystallites tend to become aligned in the direction of the fibre axis. With such alignment in the structure, the X-ray diffraction pattern is modified such that the diffraction maxima occur in rows perpendicular to the fibre axis, known as *layer lines* [72]. In a symmetrical polymers like PE, the degree of three-dimensional ordering of the chains is sufficiently high in the crystalline regions to allow a full structural analysis of the polymers to be accomplished by WAXD.

3.3.4 Differential Scanning Calorimetry (DSC)

When a substance undergoes a physical or chemical change, a corresponding change in enthalpy is observed. This forms the basis of the technique Differential Scanning Calorimetry (DSC) [71].

The expression *Differential Scanning Calorimetry* was originally applied to an instrument in which the signal was a differential power (ΔP), i.e. that required to keep both sample and reference at the same programmed temperature. If a transition takes place in the sample, a characteristic excursion in the DSC

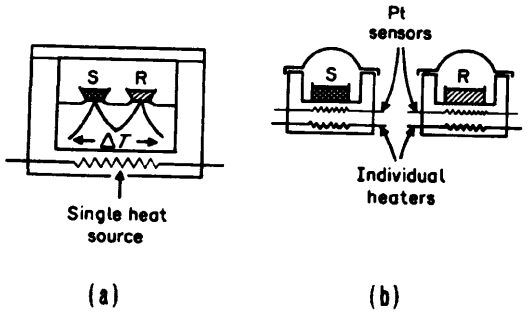

Fig.3.4 Schematic diagram shows the distinction between (a) heat flux and (b) power compensation DSC [73].

curve can then be related to the transitional properties of the sample. The thermogram obtained represents the actual amount of electrical energy supplied to the system and so the area under the resulting curve is a direct measure of the heat of transition.

In terms of instrumentation there is confusion in the definition due to great similarity between DSC and Differential Thermal Analysis (DTA) in which the change in enthalpy is detected by measuring temperature difference (ΔT) with constant heat input. In fact, it is already customary to refer to all potentially quantitative instruments as DSC's although the distinction is made between *heat flux* (ΔT) and *power compensation* (ΔP) DSC [67] as illustrated in Fig.3.4. Indeed, they are often associated with the names of specific manufacturers. For instance, the Du Pont instruments produce heat flux DSC while Perkin Elmer ones are based on power compensation DSC.

3.4 EXPERIMENTAL

3.4.1 Materials

The fibres used in this work included both commercial (Fibres A

Table 3.1

COMMERCIAL AND EXPERIMENTAL SAMPLES OF UHMW-PE FIBRES USED IN THE PRESENT STUDY.

Fibre	Sample/Code	Diameter (μm)
A	Spectra 1000	26.0 ± 4.5
B	Snia*	15.3 ± 2.5
C	10131A18	14.3 ± 1.2
D	10131B2	27.4 ± 1.2
E	10131C1	29.8 ± 2.7
F	10131C21	23.8 ± 1.8
G	10220E41	15.1 ± 2.5
H	10225C15	21.6 ± 2.5
I	00713A-3	27.8 ± 6.4

* Conventional molecular-weight melt-spun PE fibres obtained from DRA Farnborough.

and B) and experimental (Fibres C to I) PE fibres as shown in Table 3.1. The diameters of the fibres were measured using an Olympus BH-2 optical microscope which is interfaced with the image analyzer for precise measurement. The commercial Spectra 1000 and all the experimental PE fibres were provided by Allied-Signal Inc. with the reported properties of the experimental fibres shown in Table 3.2 [74]. They were gel-spun using different conditions with most of them being produced from UHMW-PE (except Fibres G and H which have different values of intrinsic viscosity as shown in Table 3.2). This work has concentrated principally upon the gel-spun fibre Spectra 1000 (Fibre A), the melt-spun fibre Snia (Fibre B) and the experimental gel-spun fibre of code 10131A18 (Fibre C). Spectra 1000 is a commercial gel-spun UHMW-PE fibre and Snia is a commercial melt-spun conventional PE fibre which was used for comparison purposes. The experimental gel-

Table 3.2

THE REPORTED PROPERTIES OF THE EXPERIMENTAL GEL-SPUN PE FIBRES [74].

Fibre	Code	Intrinsic Viscosity (dl/g)	Modulus		Ultimate Strength	
			(g/den)*	(GPa)	(g/den)*	(GPa)
C	10131A18	18	2060	178	45	3.9
D	10131B2	18	1110	96	35	3.0
E	10131C1	18	560	48	21	1.8
F	10131C21	18	980	85	36	3.1
G	10220E41	7	1831	158	42	3.6
H	10225C15	11	1615	140	34	2.9
I	00713A-3	18	1243	108	33	2.9

* Assuming all the samples have the same density of 0.98 gcm^{-3}, 1.0 GPa is equivalent to 11.56 g/den [1].

spun Fibre C has been investigated because it was reported to have the highest value of modulus among the samples (Table 3.2). However, some of the investigations were undertaken on all of the samples. All these fibres were in the form of multi-filament yarns with an opaque/white appearance. Most of the experiments including mechanical testing (Chapter 4), dynamic-mechanical measurement (Chapter 4) and the Raman microscopy (Chapter 5) were based on the samples of monofilaments (i.e. single fibres).

3.4.2 Scanning Electron Microscopy (SEM)

The monofilaments were viewed in different directions to examine their perfection both externally and internally. A JOEL field-emission scanning electron microscope (FE-SEM) of model JSM6300F was used operated at 2-3 keV. This was found to produce significantly better resolution micrographs than a conventional

SEM (Philips SEM models 505 and 525) as discussed in Section 3.5.1.

The specimens were prepared by attaching the monofilaments onto a stub by means of double-sided tape. To reveal the internal texture of the monofilaments, it was necessary to prepare the specimens using the peel-back method to produce longitudinal splitting of monofilaments. This involved the cutting of a monofilament with a sharp razor blade at an oblique angle, half-way into the filament and followed by peeling it back longitudinally with a pair of tweezers. All specimens were rendered conductive by sputter coating with a thin layer of gold before being placed into the stage inside the microscope by means of a spigot.

3.4.3 Transmission Electron Microscopy (TEM)

In this work, the specimens were prepared by the permanganic acid etching technique [69-70] followed by two-stage replication. The permanganic etching involved the following steps :

(1) A mixture of 1 volume of concentrated sulphuric acid (H_2SO_4) to 1 volume of concentrated orthophosphoric acid (H_3PO_4) was prepared.

(2) 1% by weight of potassium permanganate ($KMnO_4$) was added to the acids mixture with continuous magnetic stirring and occasional shaking. The resulting dark green solution is conventionally called *permanganic acid* [66].

(3) The monofilaments were peeled-back longitudinally and treated in the permanganic acid for 15 min at room temperature.

(4) The treated monofilaments were soaked in dilute H_2SO_4 followed by dilute hydrogen peroxide (H_2O_2) solution.

(5) The specimens were then washed with several changes of water and dried with acetone before replication.

For two-stage replication, the procedure involved as follows:

(1) Treated monofilaments were attached onto the glass slide by double-sided tapes with peeled surfaces facing up.

(2) Replicas were made by laying a cellulose acetate sheet onto the monofilaments for about 15 min before being stripped from the samples.

(3) The replica was carbon coated and shadowed at an angle of about 45° perpendicular to the fibre axis with Ag/Pd in a vacuum evaporator.

(4) The replica was cut into pieces of smaller sizes (about 2x2 mm^2) and soaked in acetone for at least 30 min to remove the cellulose acetate. The replicas were then collected on copper grids for observation in TEM.

The transmission electron microscope used was a Philips EM301 operated at 100 keV.

3.4.4 Wide-angle X-ray Diffraction (WAXD)

WAXD patterns of the fibres were obtained using a flat-plate transmission geometry and Ni-filtered CuKα radiation (wavelength = 1.542 Å). This enabled the level of molecular orientation of the fibres to be compared. The WAXD data for the equatorial reflection of the fibres were obtained using a Philips horizontal X-ray diffractometer to enable accurate lattice spacings to be measured. The diffractometer was controlled by a computer (PC)

using the Philips Software PW1877 (Version 2.1a). Again, Ni-filtered CuKα radiation was used and the diffracted beam was detected by Xe-filled proportional counter.

3.4.5 Differential Scanning Calorimetry (DSC)

A Du Pont 2000 heat flux DSC was used with a scan speed of 5°C/min under nitrogen to prevent degradation of the specimens. The mass of specimens employed were between 6.0-10.0 mg using standard aluminum sample pans that were sealed. The instrument was calibrated for temperature using both tin and indium while indium was also used as a standard for the calibration of the enthalpy of fusion. The results of melting points and enthalpies were analyzed using the Du Pont General Software (Version 4.1c). The melting points (T_m) were simply determined from the position of the maximum in the endothermic peaks, whereas the enthalpy of fusion (ΔH_f) were measured by integrating the area of the endothermic peaks over a constant melting range as illustrated

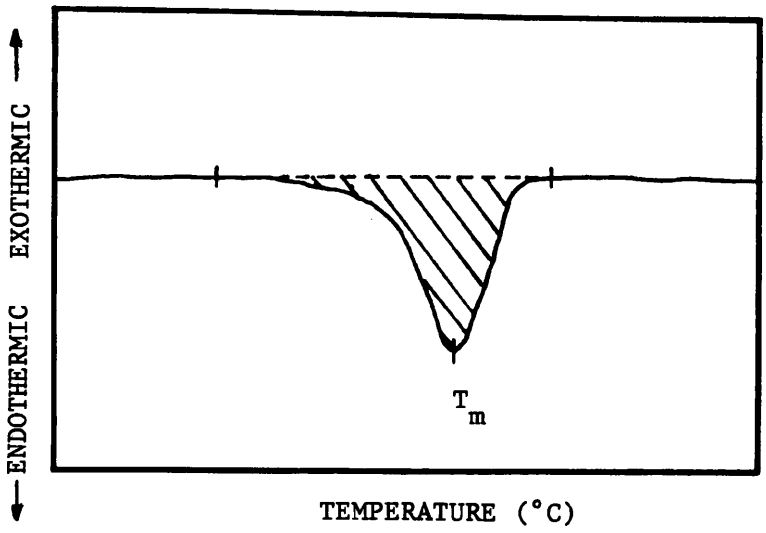

Fig.3.5 Schematic diagram of the measurement of enthalpy of fusion (ΔH_f) from the DSC curve.

Table 3.3
THE ENTHALPY OF FUSION FOR PE CRYSTALS ($\Delta H_{f,c}$) [75].

Crystal System	Enthalpy of Fusion, $\Delta H_{f,c}$ (J/g)	Reference
Orthorhombic	286.8	76
Orthorhombic	290.0	77
Orthorhombic	309.6	78
-	298.9	79

in Fig.3.5. This requires good matching of isothermal baselines which, in this case, could be fitted with linear straight lines. In order to reveal the high level of crystallinity in the fibres, the results were compared with the quenched specimens and the degree of crystallinity was determined by knowing the enthalpy of fusion of a completely crystalline specimen (Table 3.3).

3.5 MOLECULAR STRUCTURE AND MORPHOLOGY

3.5.1 Scanning Electron Microscopy (SEM)

High performance PE fibres, particularly gel-spun PE fibres, may exhibit supermolecular structure at different levels leading to a range of mechanical properties. Fig.3.6 shows conventional SEM micrographs of the PE monofilaments. Operating the microscope at 20 keV, the surface structure was affected by the strong electron beam radiation and electrostatic charging was found at the edge of the monofilament (Fig.3.6a). Although charging could be minimized by reducing the accelerating voltage, it was at the expense of lower spatial resolution as shown in Fig.3.6b. In contrast, the FE-SEM micrographs of Fig.3.7 show high resolution micrographs with the microscope operated at 2-3 keV.

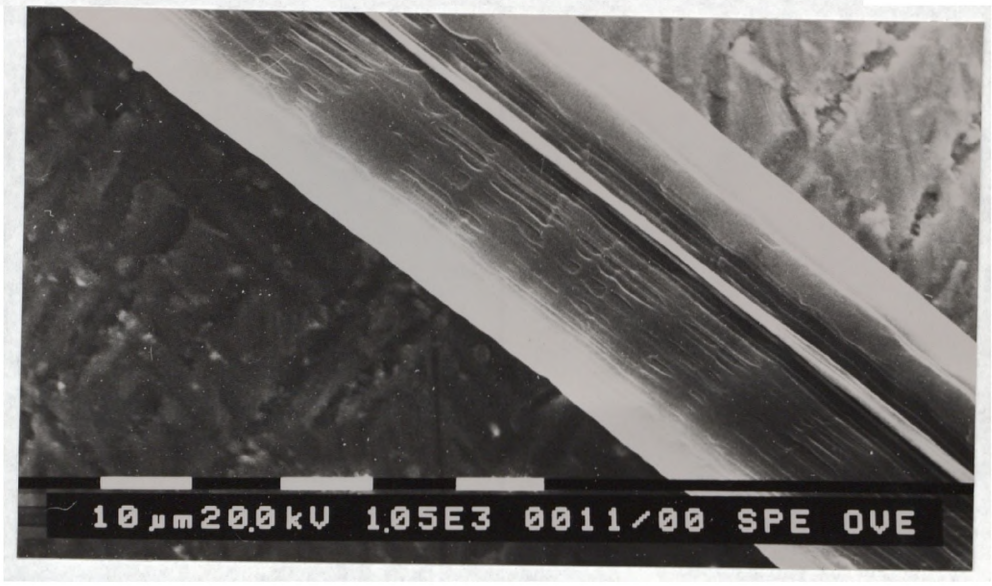

(a)

(b)

Fig.3.6 Conventional SEM micrographs of the (a) surface structure (20 keV), and (b) internal structure for the monofilaments of Fibre A (10 keV).

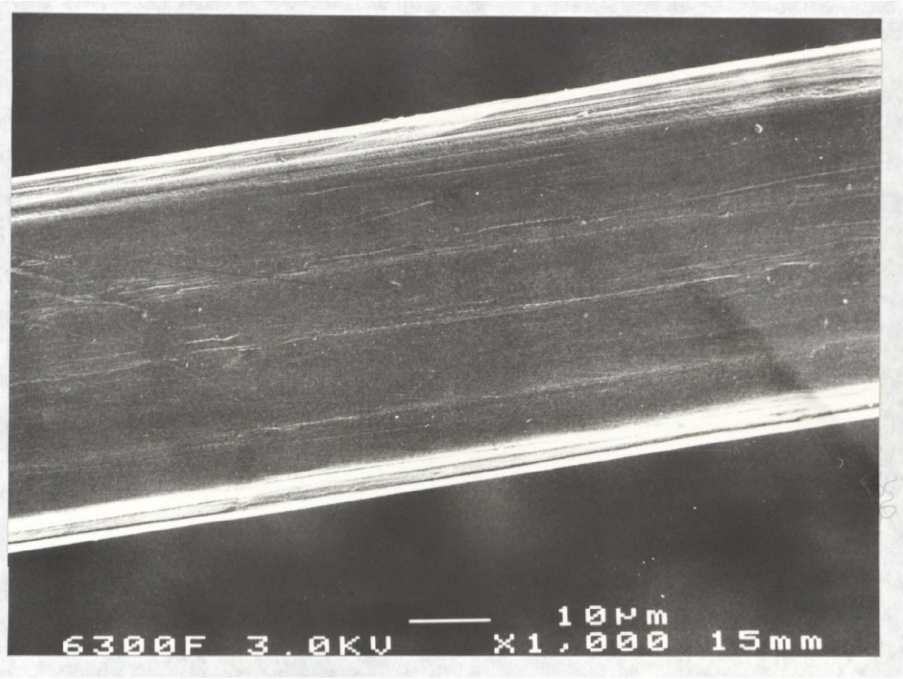

(a)

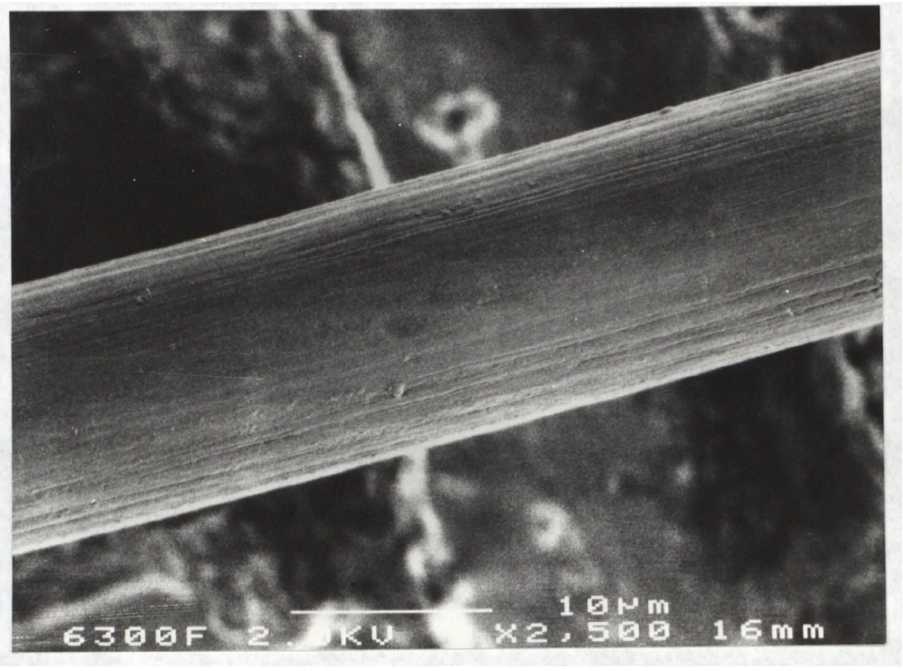

(b)

Fig.3.7 FE-SEM micrographs of the surface for the monofilaments of (a) Fibre A, and (b) Fibre B.

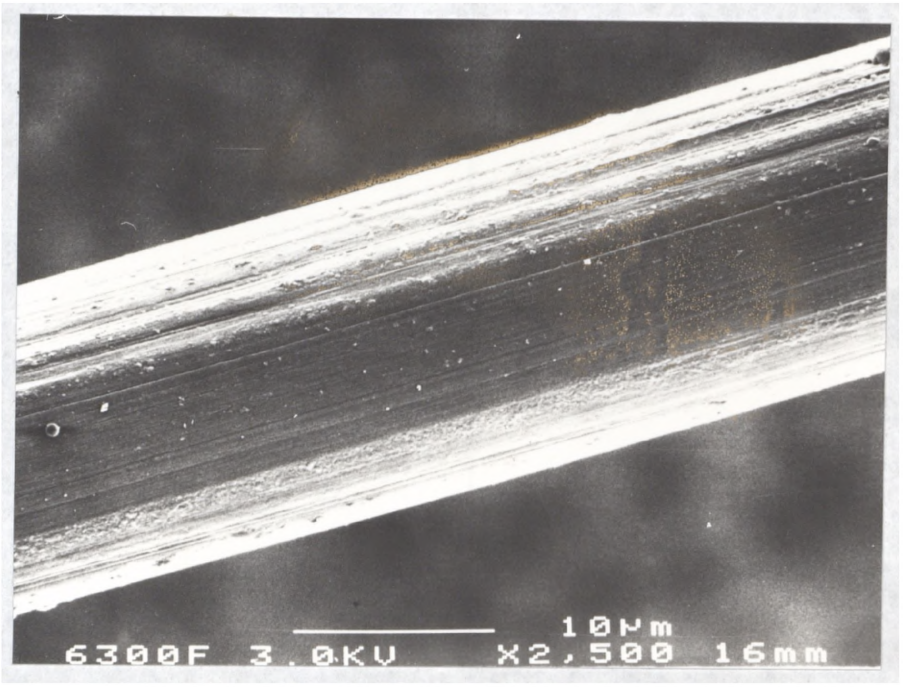

(c)

Fig.3.7c FE-SEM micrograph of the surface for the monofilament of Fibre C.

3.5.1.1 Surface Morphology

At a fairly gross morphological level, the surface topography may be resolved using the FE-SEM. Fig.3.7 shows the surface textures of the monofilaments of Fibres A, B and C which are differently-spun PE fibres. Both Fibres A (Fig.3.7a) and C (Fig.3.7b) are gel-spun whereas Fibre B (Fig.3.7b) is melt-spun. Fibre C is the highest modulus experimental gel-spun PE fibre (Table 3.2). However from the surface appearance, there is no significant difference in surface morphology between the three PE fibres with an uniform longitudinal continuity of the striations parallel to

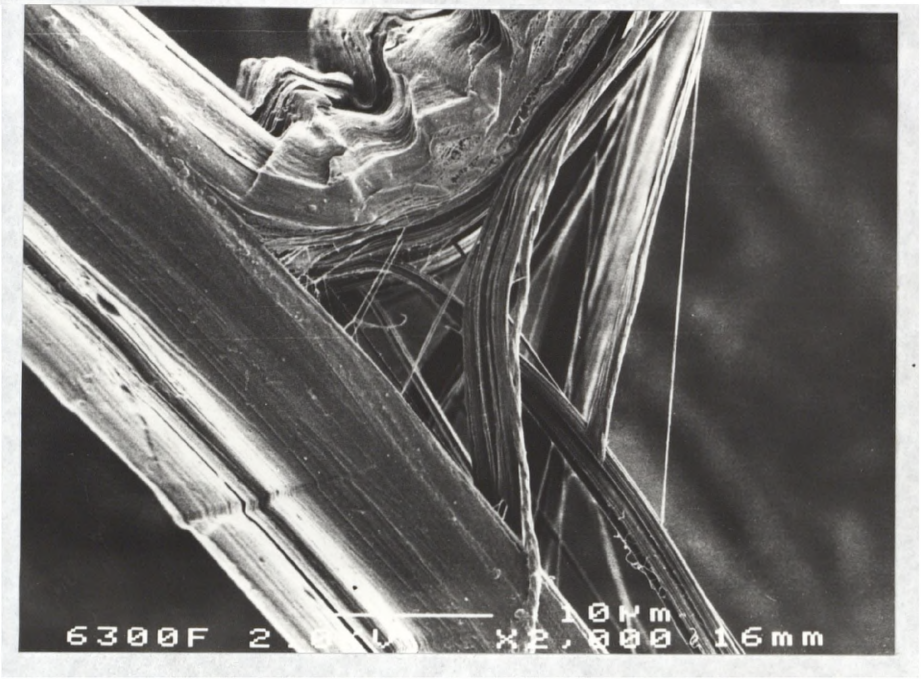

(a)

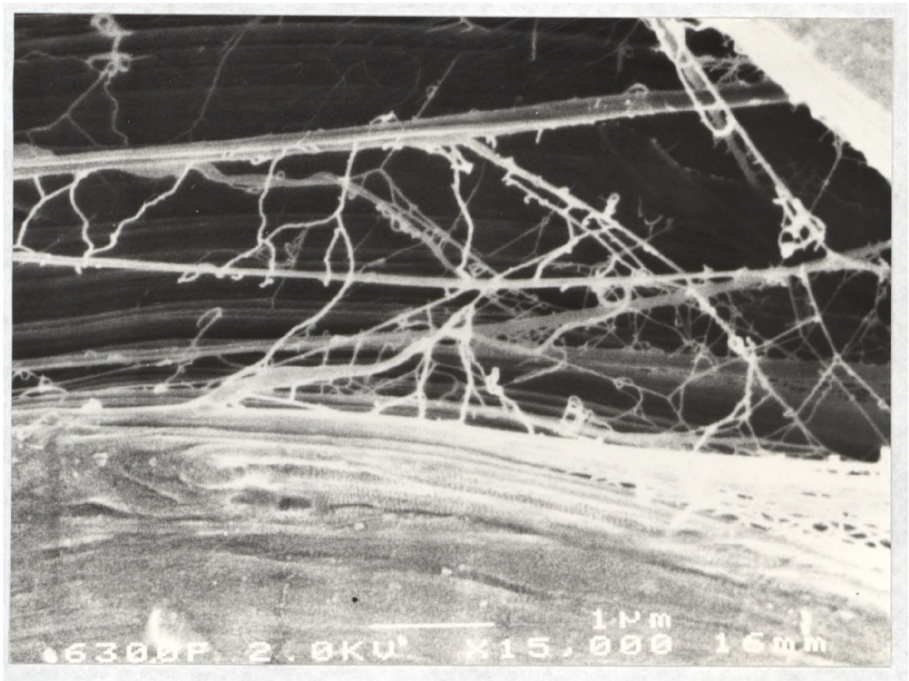

(b)

Fig.3.8 FE-SEM micrographs of the monofilament of Fibre A upon longitudinal splitting to reveal the internal microstructure at magnifications of (a) 2K, and (b) 15K.

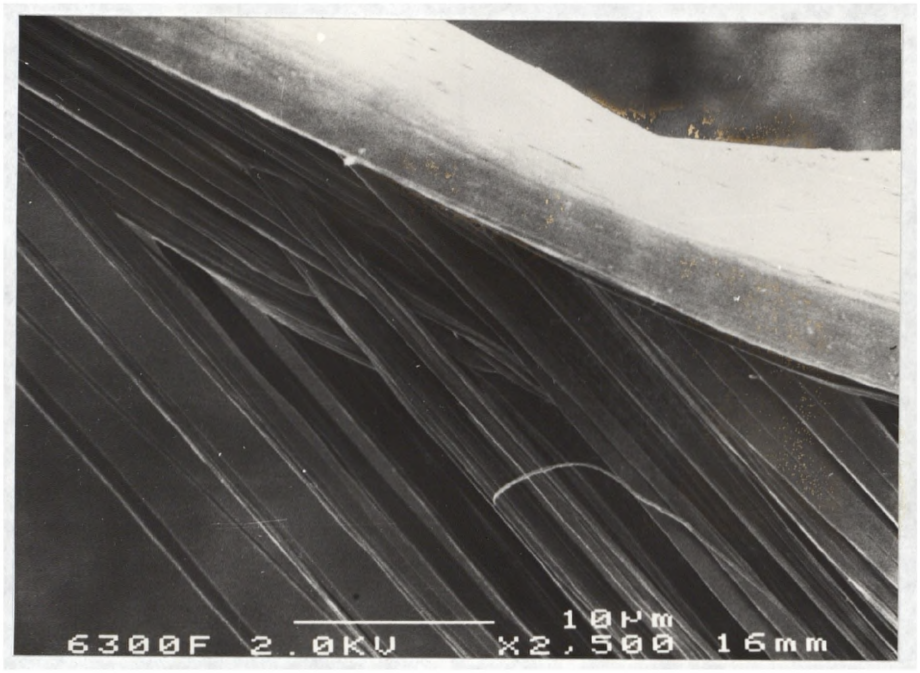

(a)

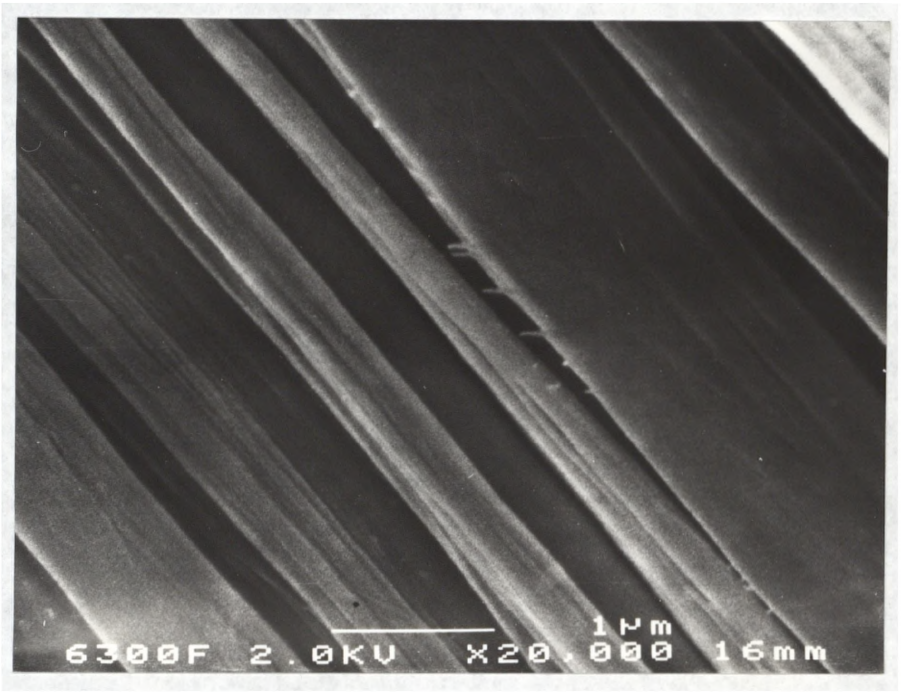

(b)

Fig.3.9 FE-SEM micrographs of the monofilament of Fibre B upon longitudinal splitting to reveal the internal microstructure at magnifications of (a) 2.5K, and (b) 20K.

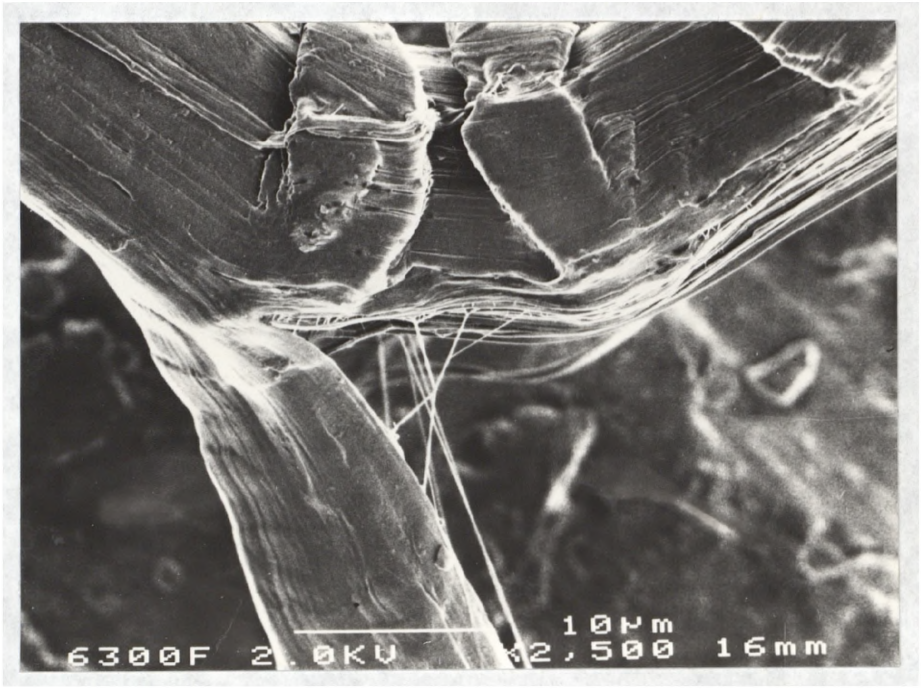

(a)

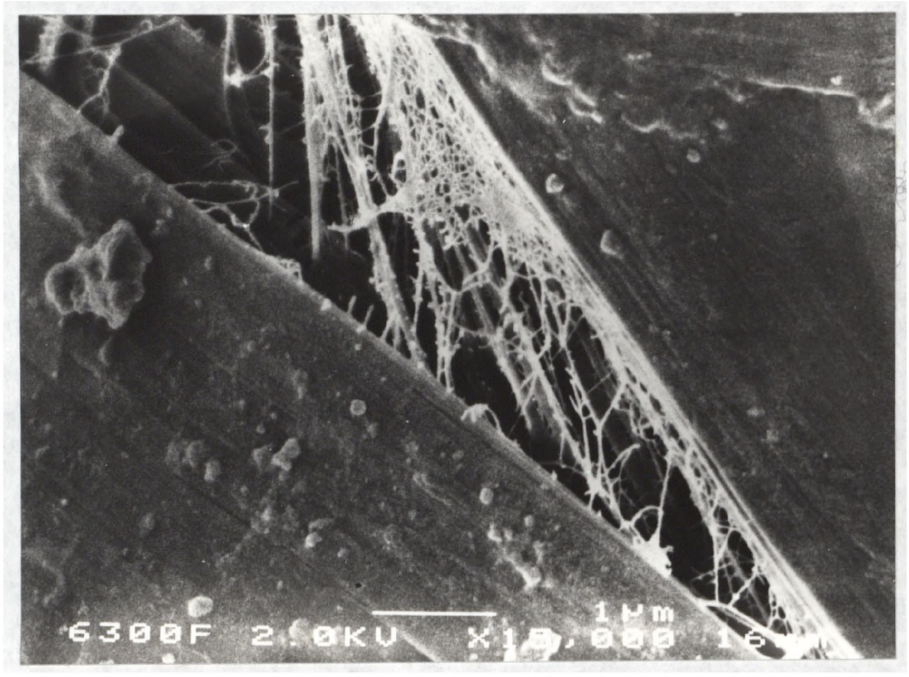

(b)

Fig.3.10 FE-SEM micrographs of the monofilament of Fibre C upon longitudinal splitting to reveal the internal microstructure at magnifications of (a) 2.5K, and (b) 15K.

the fibre axis. Similar observations were obtained from other experimental gel-spun PE fibres and these results suggest significant similarities between the surfaces of the gel-spun and melt-spun PE fibres.

3.5.1.2 Internal Structure

Using the peel-back method for longitudinal splitting of the monofilaments, the internal fibrillar texture can be clearly seen at different magnification using FE-SEM as shown in Fig.3.8-3.10. It should be noted that such detail cannot be obtained using conventional SEM (Fig.3.6b). Again, monofilaments of Fibres A, B and C were used and were seen to be composed mainly of fibrils which appear to be bundles of microfibrils. This is particularly obvious for the monofilaments of the gel-spun Fibres A and C where the microfibrils (30-60 nm in diameter) appear to be loosely entangled during the splitting (Fig.3.8 and Fig.3.10). The diameters of the fibrils are significantly different between the samples. The melt-spun Fibre B (Fig.3.9) shows the highest diameter of 0.2-0.3 μm for the fibrils which is twice the sizes of the fibrils of the gel-spun Fibres A and C. This indicates that the two processes produce different fibrillar structure in the PE fibres.

3.5.2 Transmission Electron Microscopy (TEM)

Fig.3.11 shows the TEM micrograph of the replica of an unetched longitudinally split monofilament of Fibre A. This, again reveals the internal microstructure of the monofilament which was nearly completely composed of smooth microfibrils. Within the

Fig.3.11 TEM micrograph of the replica for the unetched monofilament of Fibre A.

microfibrils, any crystalline and non-crystalline regions and the details of such morphology can not be seen without permanganic etching. This technique has already widely been used in the morphological studies of the PE monofilaments [57-60,62-63]. Fig.3.12 and Fig.3.13 illustrate the difference between the unetched and etched monofilaments of Fibre A at different magnifications, respectively. These TEM micrographs of the etched Fibre A (Fig.3.13) reveals the microfibrils which are well oriented along the fibre axis with a length of 2-3 μm and the diameter of ~30 nm. This observation is in accordance with those made for Spectra 900 (commercial gel-spun PE fibre with lower modulus than Spectra 1000) by Hoffmann *et al* [62-63].

Fig.3.14-3.17 show the TEM micrographs for the replicas of etched monofilaments of Fibres B, C, E and I, respectively. Fibre E is the experimental fibre with the lowest value of modulus (Table 3.2) and Fibre I has the lowest melting point (T_m) among

(a)

(b)

Fig.3.12 TEM micrographs of the unetched monofilaments of Fibre A at magnifications of (a) 9.8K, and (b) 13K.

(a)

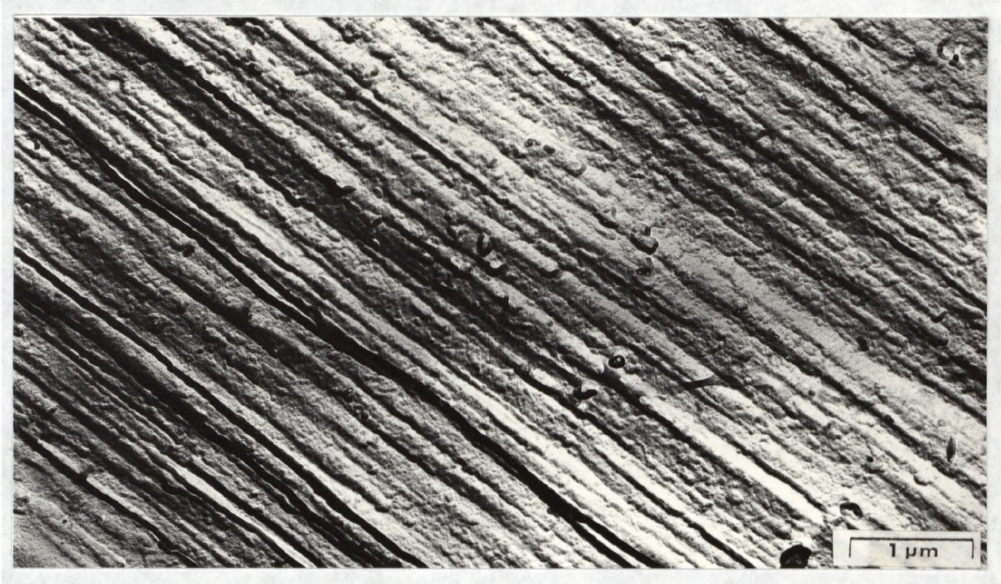

(b)

Fig.3.13 TEM micrographs of the etched monofilaments of Fibre A at magnifications of (a) 9.8K, and (b) 13K.

(a)

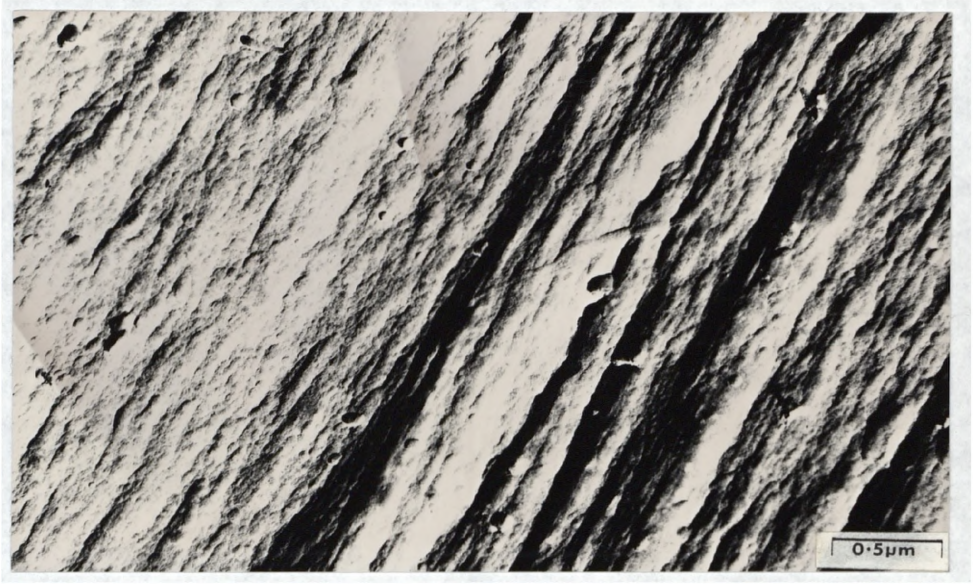

(b)

Fig.3.14 TEM micrographs of the etched monofilaments of Fibre B at magnifications of (a) 18K, and (b) 22K.

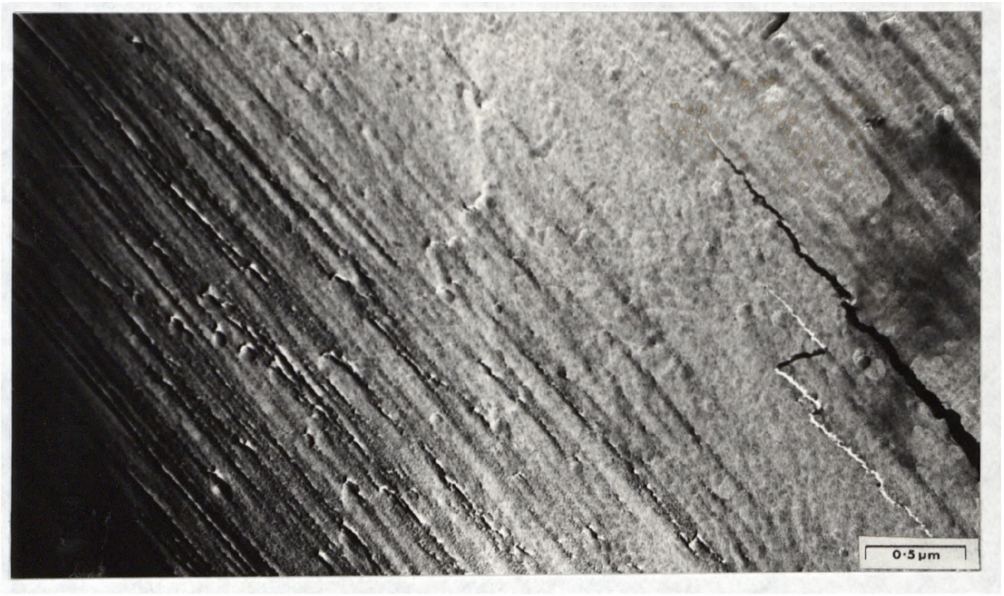

(a)

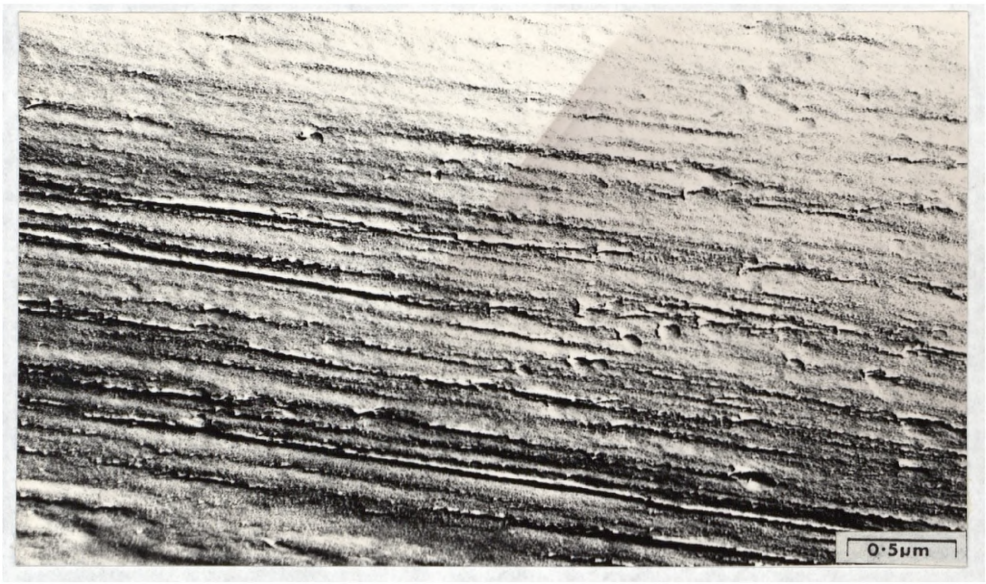

(b)

Fig.3.15 TEM micrographs of the etched monofilaments of Fibre C at magnifications of (a) 18K, and (b) 22K.

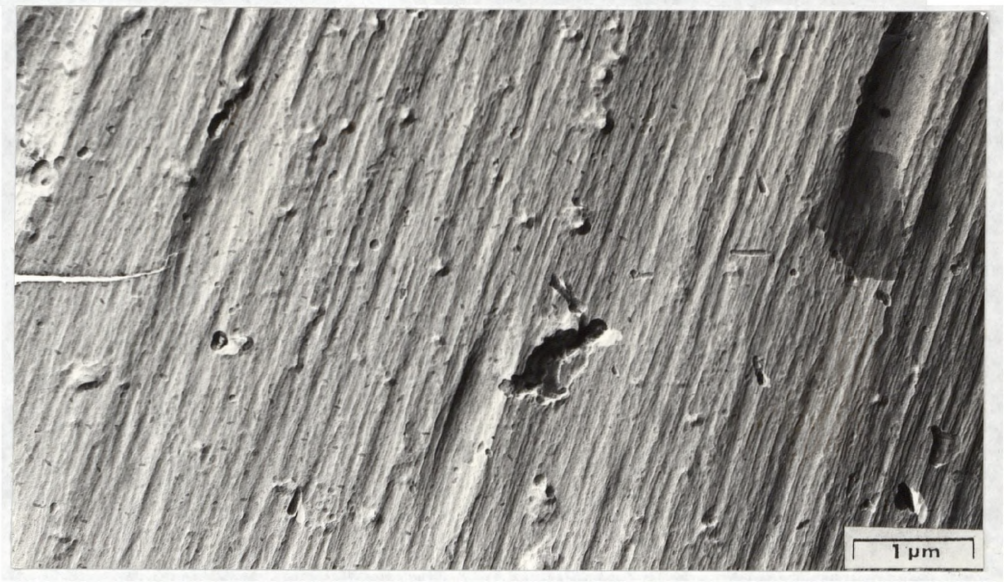

(a)

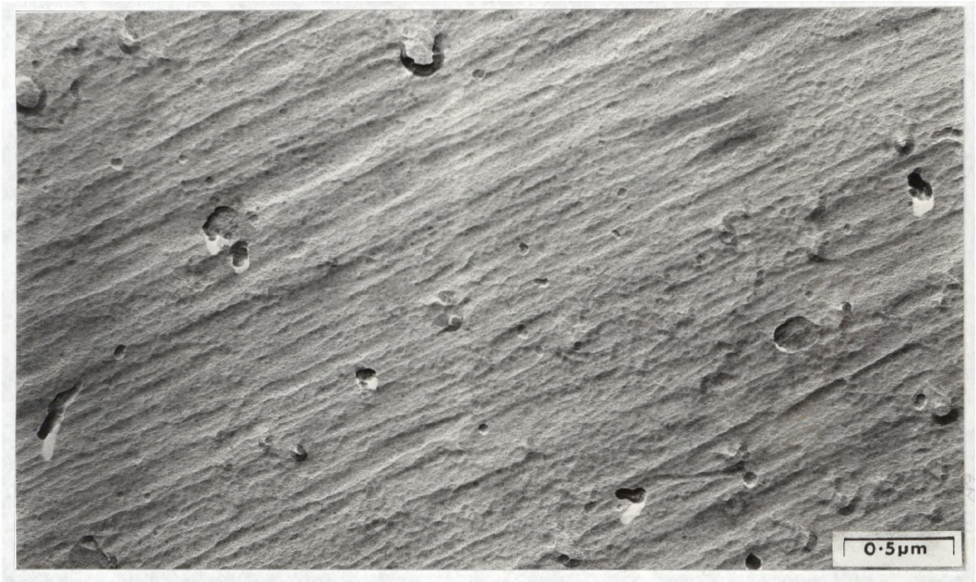

(b)

Fig.3.16 TEM micrographs of the etched monofilaments of Fibre E at magnifications of (a) 13K, and (b) 22K.

(a)

(b)

Fig.3.17 TEM micrographs of the etched monofilaments of Fibre I at magnifications of (a) 9.8K, and (b) 13K.

all the samples which will be discussed later (Table 3.6). The morphology of the melt-spun Fibre B (Fig.3.14) appears to be far from highly chain-extended, although there are striations parallel to the fibre axis which are in line with the observation by FE-SEM (Section *3.5.1.2*). Within the fibrillar structure, there appears to be also a block-like lamellar structure not found in the gel-spun fibres. In contrast, the internal structure of Fibre C (Fig.3.15) is composed of well-oriented smooth microfibrils which are similar to those of Fibre A (Fig.3.13). Again, both Fibre E (Fig.3.16) and I (Fig.3.17) also exhibit a longitudinal striated texture with an obvious highly chain-extended fibrillar structure. It appears that the gel-spun PE fibres (Fibres A, C, E and I) are more highly chain-extended than the melt-spun PE fibres (Fibres B).

3.5.3 Wide-angle X-ray Diffraction (WAXD)

Fig.3.18 shows the flat-plate WAXD patterns obtained from bundles of PE monofilaments of Fibres A, B and C. The sharp equatorial reflections and the presence of meridional layer lines indicate the crystallites and molecules are well oriented along the fibre axis. These are typical diffraction patterns for the other experimental PE fibres investigated and apparently they have similar high levels of molecular orientation. It is not possible to determine if the exact level of orientation is different in the fibres studied using the flat-plate method, but it has been reported by Allied-Signal to be similar in all the gel-spun fibres investigated [74].

Fig.3.19 is a X-ray diffractogram of Fibre A and shows the

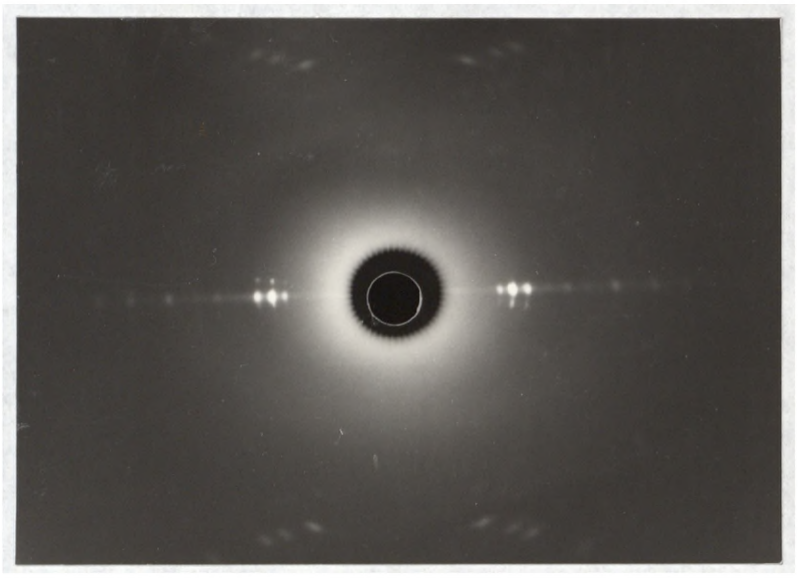

(a)

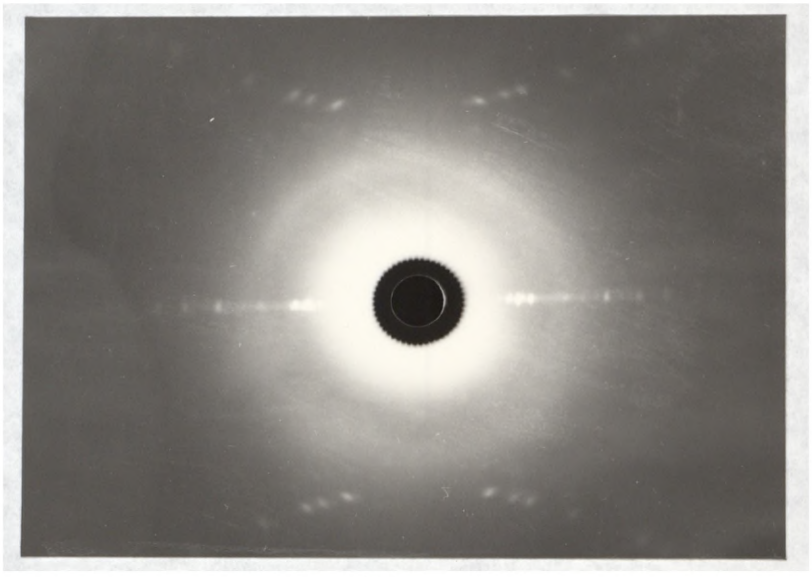

(b)

Fig.3.18 Flat-plate WAXD pattern of (a) Fibre A, and (b) Fibre B.

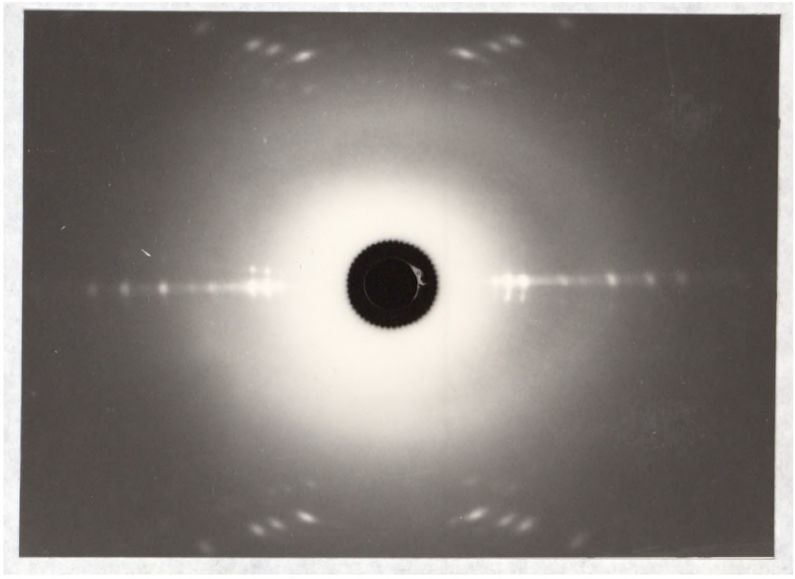

Fig.3.18c Flat-plate WAXD pattern of Fibre C.

intense reflections have sharp maxima indicative of a high degree of crystallinity within the PE fibre. In fact, similar diffractograms were obtained for all PE fibres investigated including the melt-spun Fibre B. The *d*-spacings of the observed reflections across the equator of the WAXD pattern for Fibre A are tabulated in Table 3.4. The Bragg reflection for 2θ of about 18.3° corresponds to the (001) reflection of the monoclinic phase [80]. This indicates that the WAXD pattern cannot solely be indexed on the usual orthorhombic unit-cell first reported by Bunn [81] as shown in Fig.3.20. The diffraction spots may be indexed consistent with a partial transformation from the orthorhombic to monoclinic phase which is characteristic of mechanically deformed PE [80]. The transformation takes place by means of a simple two-dimensional shear of the orthorhombic

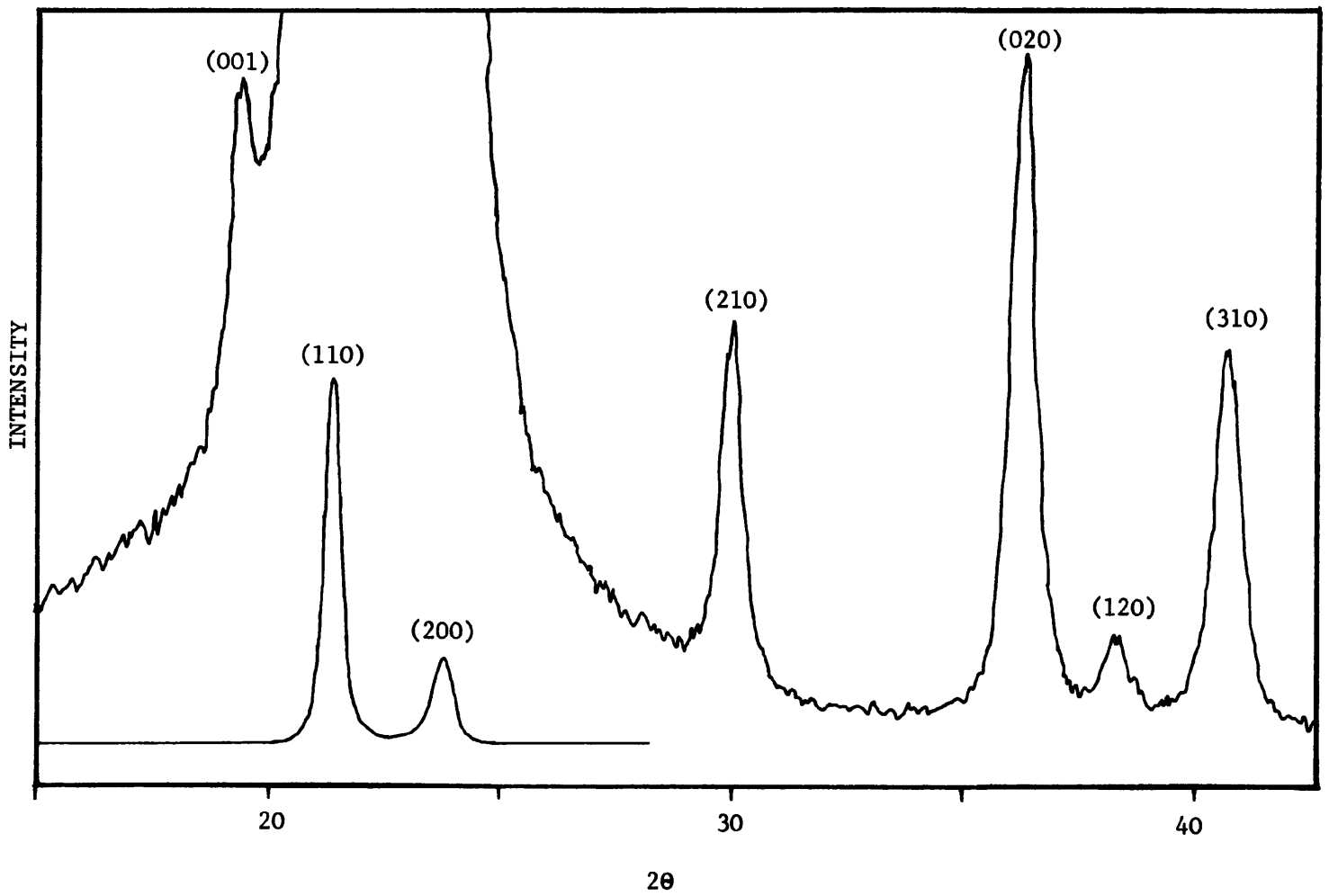

Fig.3.19 X-ray diffractogram of Fibre A across the equator of the diffraction pattern (at two different intensity levels).

Table 3.4

OBSERVED EQUATORIAL WAXD REFLECTIONS OF GEL-SPUN PE FIBRE A.

Plane	2θ	Bragg *d*-spacing (Å)	Crystal System
(001)	18.3°	4.84	Monoclinic
(110)	21.5°	4.13	Orthorhombic
(200)	23.9°	3.69	Orthorhombic
(210)	30.0°	2.92	Orthorhombic
(020)	36.3°	2.46	Orthorhombic
(120)	38.4°	2.34	Orthorhombic
(310)	40.7°	2.21	Orthorhombic

crystal structure in a direction perpendicular to *c* [80]. This is probably due to the deformation in crystalline region during the ultra-drawing process of gel-spinning. Table 3.5 shows the *d*-spacings of (200) and (020) reflections of all the samples. These measurements indicate the lateral spacings in the PE crystal lattice and it appears that Fibre I shows the highest lateral *d*-spacings which will be discussed later (Section 6.3).

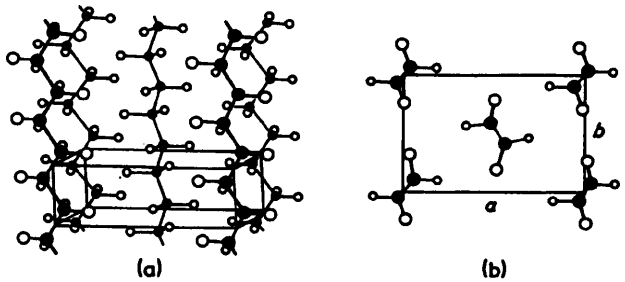

Fig.3.20 Crystal structure of orthorhombic PE with (a) general view of unit cell, and (b) projection of unit cell parallel to the chain direction *c* [46].

Table 3.5

THE *d*-SPACINGS OF (200) AND (020) EQUATORIAL WAXD REFLECTIONS OF ALL THE SAMPLES.

Fibre	*d*-spacing	
	(200)	(020)
A	3.69	2.46
B	3.70	2.46
C	3.70	2.46
D	3.69	2.47
E	3.70	2.46
F	3.70	2.46
G	3.70	2.46
H	3.69	2.46
I	3.74	2.47

3.5.4 Differential Scanning Calorimetry (DSC)

The melting temperature T_m is an important characteristic of a polymer and it generally increases with increasing molecular weight and crystallinity [68]. The melting temperature, however, may not be discrete if a range of crystal sizes is present, and the breadth of the endothermic peak may indicate the extent of size variation. Fig.3.21 shows the DSC curves for heating the Fibres A, B, C and I from 80°C to 180°C at the rate of 5°C/min. Both gel-spun Fibres A and C have similar melting behaviour which is the same for the other experimental gel-spun fibres except Fibre I which is also shown in Fig.3.21 and will be discussed later. At first sight, the melting behaviour of the gel-spun fibres seems rather complex with multiple distinct endothermic peaks. In contrast, the melt-spun Fibre B shows a rather simple

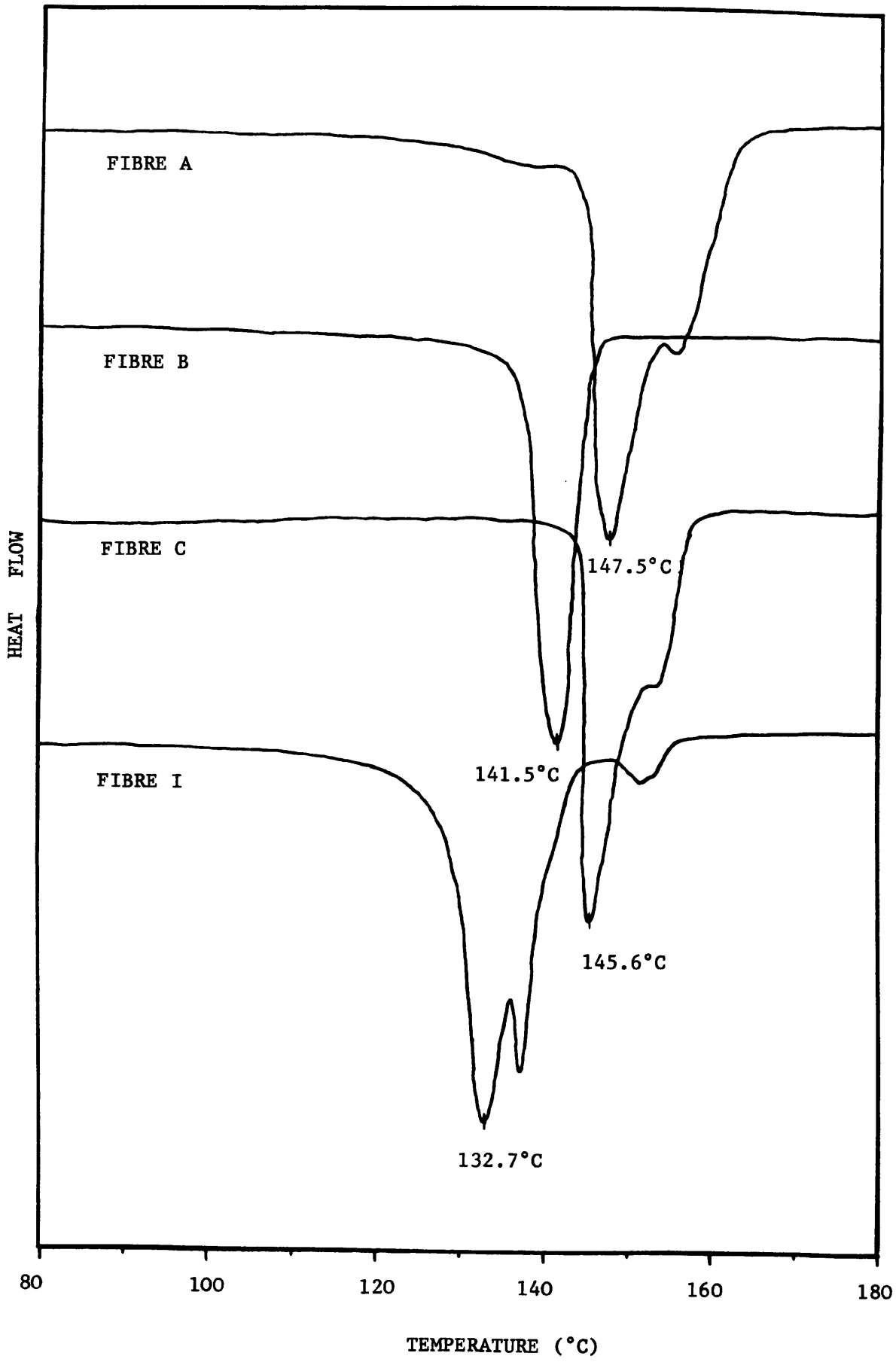

Fig.3.21 DSC curves of heating Fibres A, B, C and I at the rate of 5°C/min.

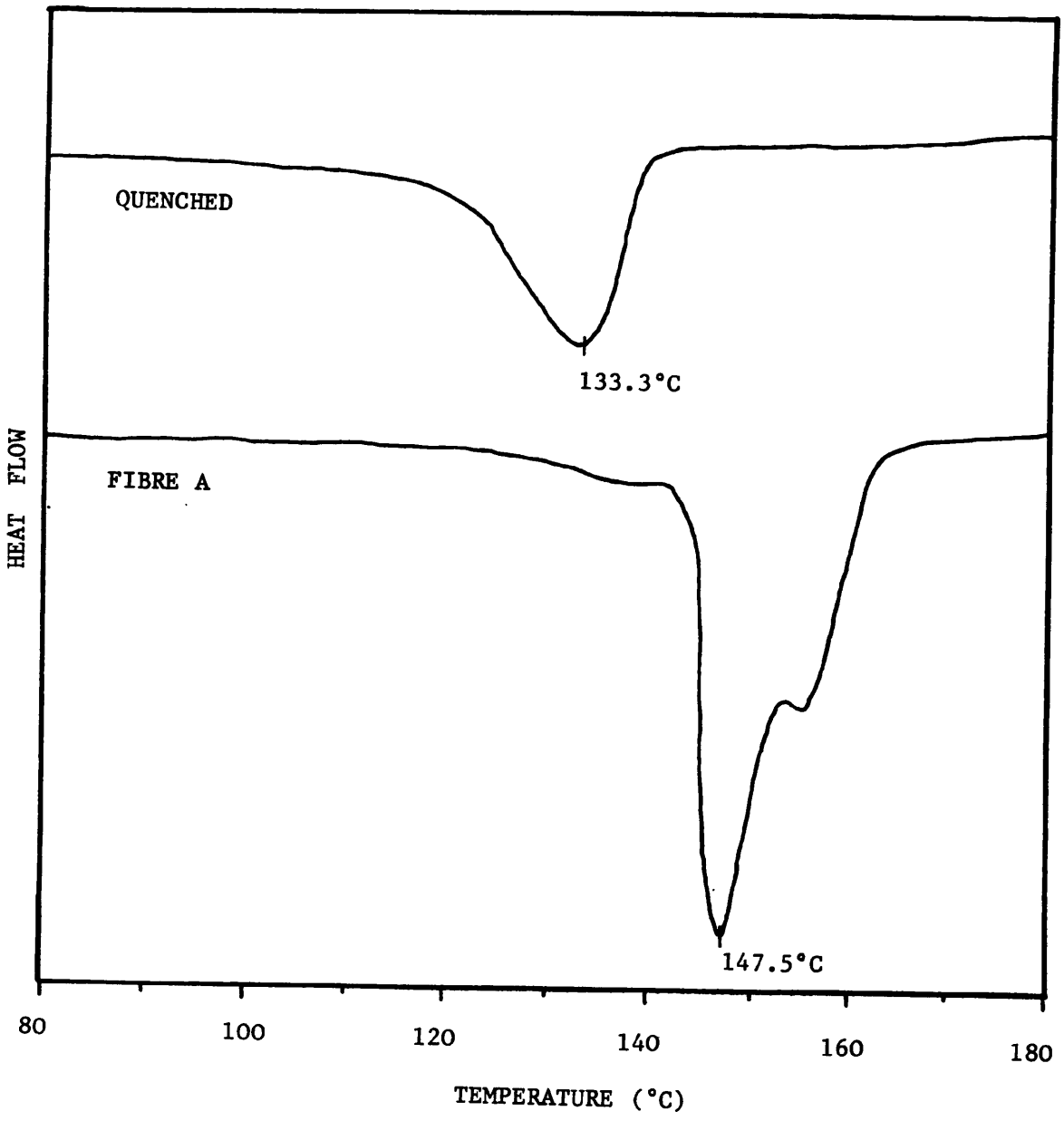

Fig.3.22 DSC curves of both the Fibre A and the quenched sample at the heating rate of 5°C/min.

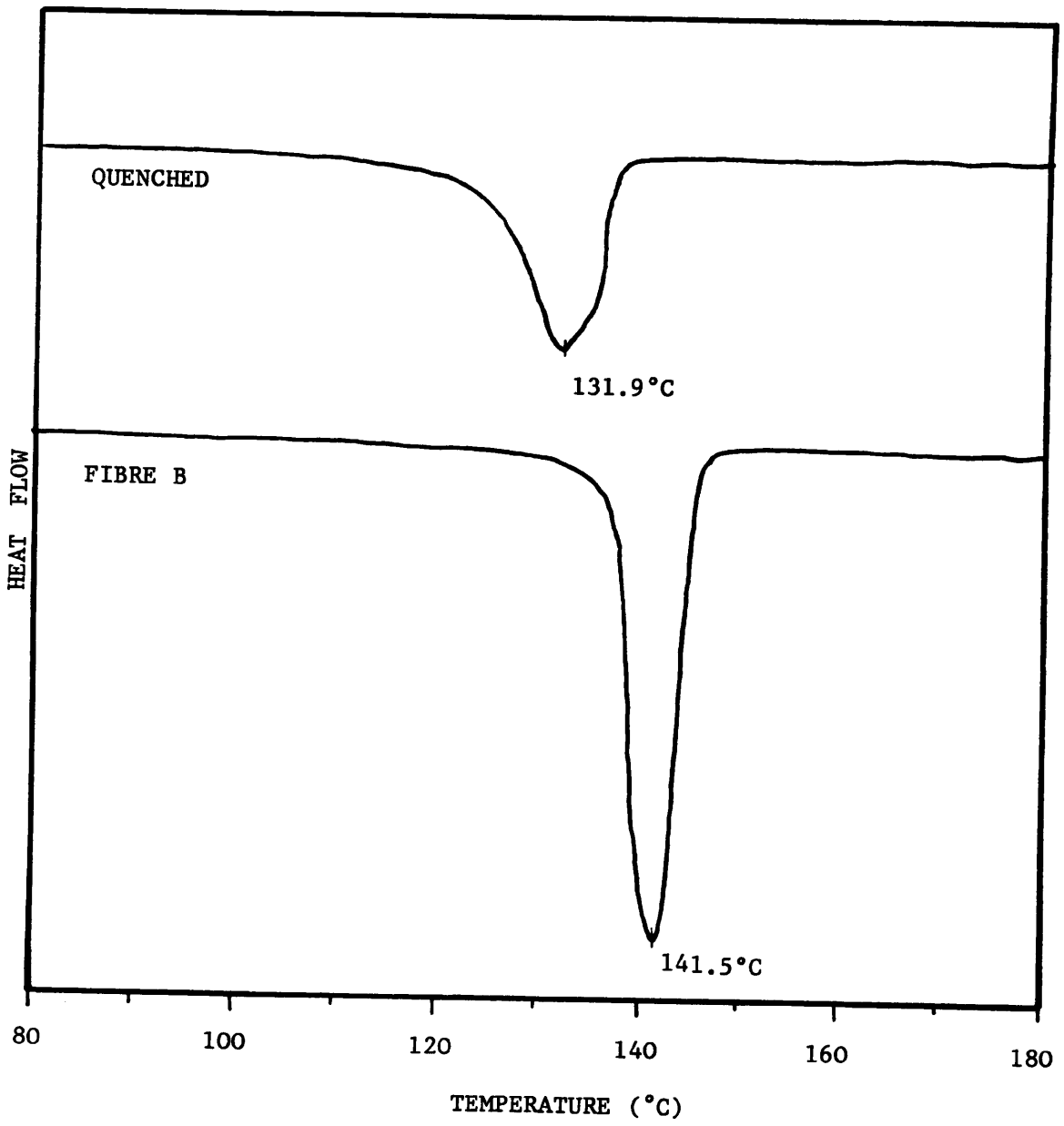

Fig.3.23 DSC curves of both the Fibre B and the quenched sample at the heating rate of 5°C/min.

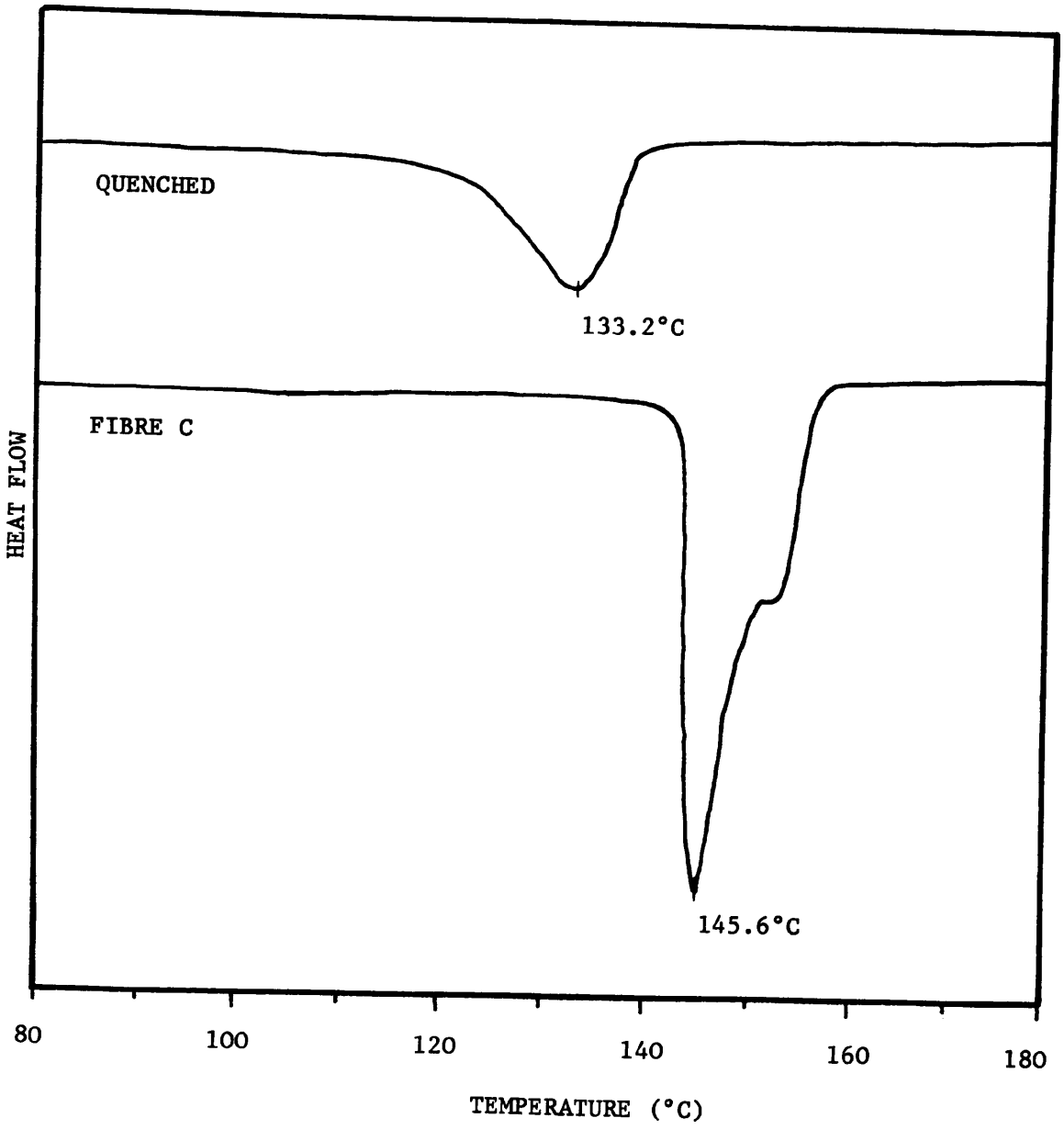

Fig.3.24 DSC curves of both the melt-spun Fibre C and the quenched sample at the heating rate of 5°C/min.

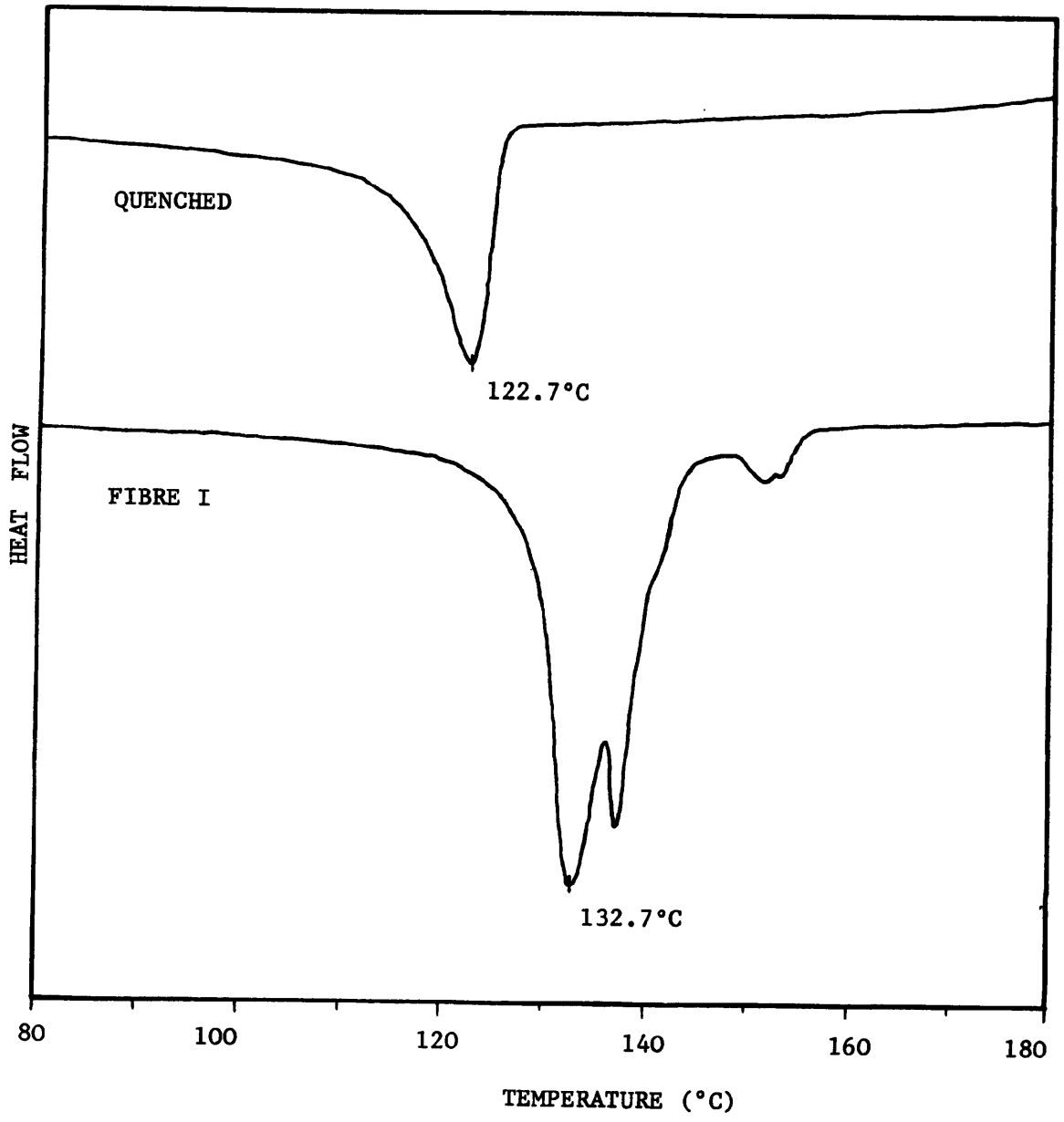

Fig.3.25 DSC curves of both the melt-spun Fibre I and the quenched sample at the heating rate of 5°C/min.

melting behaviour with a narrow endothermic peak at 141.5°C. By quenching the samples with liquid nitrogen after heating to 200°C (exceeding the melting point T_m) and then reheating, both the gel-spun and melt-spun fibres exhibit a simpler melting behaviour with only a single broad endothermic peak as illustrated in Fig.3.22-3.25. The melting temperature, enthalpy of fusion of the fibres have decreased indicating that the original morphology of the fibres is completely lost after the first heating in the DSC experiment.

This melting behaviour of gel-spun fibres has been observed by Bastiaansen *et al* [82] and they showed that the multiple endothermic peaks for the gel-spun PE fibres could be attributed to the coexistence of different morphological components. According to Pennings *et al* [83], the initial melting peak is due to the melting of the unconstrained crystallites (orthorhombic) while the second higher melting peak is due to orthorhombic-to-hexagonal transformation. There is sometimes a third peak which can split into several smaller peaks due to the melting of the hexagonal phase. This phenomenon has been confirmed by van Aerle *et al* [84] and Murthy *et al* [85] by a real-time wide-angle X-ray melting study of the gel-spun PE fibres. Therefore, the observed melting behaviour of the gel-spun PE fibres (Fig.3.22 and Fig.3.24-3.25) is contributed to by both unconstrained and constrained crystallites. The melt-spun Fibre B shows no melting of any constrained crystallites as illustrated in Fig.3.23. However, only Fibre I shows three distinct melting peaks (Fig.3.25) with a maximum at 132.7°C which is the lowest value among the all the samples (Table 3.6). The third peak is

Table 3.6

THE VALUES OF PEAK MELTING TEMPERATURE (T_m), ENTHALPY OF FUSION (ΔH_f) AND FRACTIONAL CRYSTALLINITY (ϕ_c) OF ALL THE PE FIBRES.

Fibre	T_m (°C)	ΔH_f (J/g)	ϕ_c (%)
A	147.5	273.3	92.5
B	141.5	267.3	90.5
C	145.6	284.5	96.3
D	145.0	266.5	90.2
E	142.4	264.9	89.6
F	144.5	262.7	88.9
G	144.7	262.2	88.7
H	144.2	268.3	90.8
I	132.7	259.0	87.6

apparently associated to the melting of hexagonal phase in the fibre structure as proposed by Pennings *et al* [83] and it is likely that the low T_m of Fibre I could be due to the fibres being spun from a different precursor polymer (Section 6.3).

In Table 3.6 the degree of crystallinity (ϕ_c) of the fibres was determined by knowing the enthalpy of fusion of a completely crystalline sample [68] i.e.

$$\phi_c = \frac{\Delta H_f}{\Delta H_{f,c}} \qquad (3.2)$$

where ΔH_f is the enthalpy of fusion of the sample and $\Delta H_{f,c}$ is the enthalpy of fusion of a completely crystalline sample. The value of $\Delta H_{f,c}$ can rarely be determined directly because of the difficulty of obtaining a totally crystalline sample. Table 3.3 shows several values of $\Delta H_{f,c}$ determined by various workers [75].

However in this calculation, it was assumed that for any other phases present (such as constrained crystallites) the enthalpy of fusion is equal to that of the orthorhombic crystal. Therefore, an average value of $\Delta H_{f,c}$ of the ones quoted [76-78] for orthorhombic PE crystals was used which is 295.5 J/g. It appears that all the fibres are highly crystalline with the Fibres A and C showing the highest values of ϕ_c.

3.6 CONCLUDING REMARKS

There are a great number of similarities in structure and morphology between the gel-spun and melt-spun PE fibres. These fibres show similar surface morphology using FE-SEM even though they were spun differently. However using permanganic etching, the details of the microstructure for the fibres could be seen on TEM and apparently the gel-spun fibres show a higher degree of chain extension than the melt-spun fibres. Again, the results of WAXD and DSC for both the gel-spun and melt-spun samples show the fibres are highly crystalline with considerable similarities, but the melting behaviours of the two is apparently different. From the observations by DSC, the melting behaviour of the gel-spun fibres is more complex with multiple endothermic peaks, whereas of the melt-spun fibre exhibits a simpler melting behaviour with a single narrow endothermic peak. Generally speaking, the melting points T_m of all the samples are very close except for Fibre I (Table 3.6) which has the lowest melting temperature before and after quenching which is indicative of the use of different precursor for the fibre spinning.

4

MECHANICAL PROPERTIES OF THE MONOFILAMENTS

4.1 INTRODUCTION

The mechanical properties of polymers are entirely dependent on polymer microstructure and molecular weight. In the study of mechanical properties, a polymeric specimen with simple molecular structure such as polyethylene (PE) may change in a complicated way during the course of the testing. Mechanical testing of polymeric fibres, particularly in tension, provides useful information and permits measurement of factors such as strength, toughness, recoverable and non-recoverable deformations, and failure criteria.

In this chapter, the mechanical properties of PE monofilaments were determined using various mechanical testing techniques (Sections 4.3). The deformation behaviour of the monofilaments will be described in Section 4.4. This is followed by the observation on dynamic mechanical analysis of PE monofilaments with a correlation with relaxation in crystalline regions (Section 4.5).

4.2 MECHANICAL TESTING OF POLYMERIC FIBRES

There are a bewildering number of mechanical tests available and most of these are very specialized in order to deal with the viscoelasticity of polymeric materials. However, mechanical testing involves deformation of the materials under the influence

of applied external force and it is generally tensile deformation that is applied to the polymeric fibres.

4.2.1 Stress-strain Measurements

The stress-strain test is probably the most widely used mechanical test, but its practical significance is frequently overrated. This is chiefly due to the fact that the data are generally supplied for one temperature, one speed of testing, one gauge length and one specimen history. The stress-strain performance of polymers, however, varies widely with changes in temperature, rate of deformation and also the test geometry (e.g. gauge length due to significant end effects [86]), particularly in highly-oriented structures such as PE fibres. End effects are due to the nonuniformity of the stress distribution which decays away exponentially near the sample ends. Therefore data supplied for one set of testing conditions are usually not applicable to those of another set of conditions.

Stress-strain measurements of polymers are performed by elongating (straining) the sample at a uniform rate and simultaneously measuring the force applied to the specimen so that a curve of the type shown in Fig.4.1 can be plotted [71]. The initial portion of the curve is linear and the tensile modulus *E* is obtained from its slope. The point L represents the stress beyond which a brittle material will fracture, and the area under the curve to this point is proportional to the energy required for brittle fracture. If the material is tough, no fracture occurs and the curve then passes through a maximum or inflection point Y, known as the *yield point*. Beyond this, the

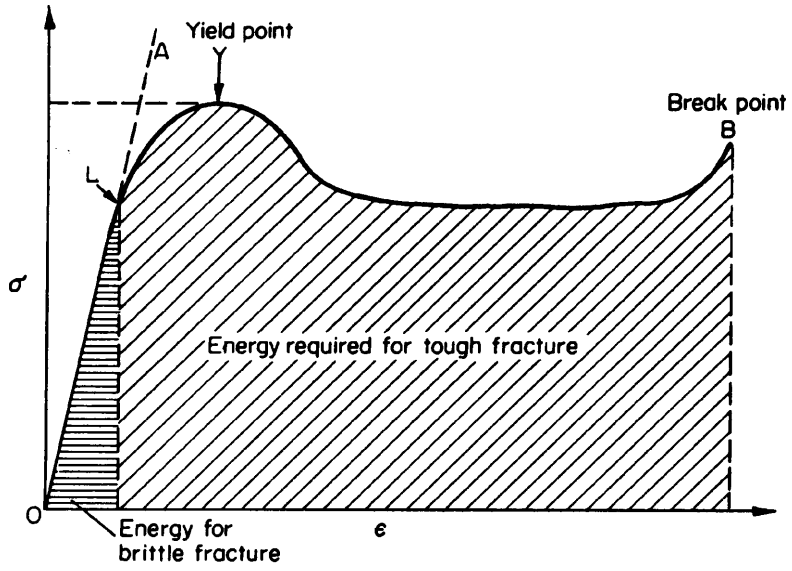

Fig.4.1 An idealized stress-strain curve with the modulus being measured from the slope of the line OA [71].

ultimate elongation is eventually reached and the polymer breaks at B. The area under this part of the curve is the energy required for tough fracture to take place.

For the testing of polymeric fibres, the geometry of the specimen prevents the use of normal strain-sensing devices, such as strain gauges, extensometers, etc. However, an optical method may be used to follow the gauge section elongation directly, or alternatively, the values of modulus and ultimate stress/strain may be corrected by extrapolating the values at different gauge lengths to infinite and zero gauge lengths respectively (as described in Section 4.4.1).

4.2.2 Transient Experiments

Consideration of the effect of time dependence adds additional

complications in the determination of mechanical properties of polymeric fibres. This is due to the distinctive feature of the mechanical behaviour of polymers which have an unique response to an applied stress or strain with time.

4.2.2.1 Linear Viscoelasticity

Hooke's law describes the mechanical behaviour of an ideal solid, relating the applied stress σ to the resultant strain e through a proportionality factor called the modulus E.

$$\sigma = Ee \tag{4.1}$$

The linear region in which the modulus does not change when the strain is changed is called the *Hookean region* of the material. In Newton's law of viscosity, the viscosity η is defined by stating that stress σ is proportional to the rate of strain.

$$\sigma = \eta\left(\frac{de}{dt}\right) \tag{4.2}$$

Both equations bring out the analogy between Hooke's law for elastic solids and Newton's law for viscous liquids. In the former the stress is linearly related to the strain and in the latter the stress is linearly related to the rate of strain.

Polymeric materials such as PE are examples of viscoelastic materials, which have some of the characteristics of both elastic solid and viscous liquid. An elastic solid has a definite shape and an ability to store mechanical energy with no dissipation of energy upon deformation. That implies it can regain its original shape after being deformed. On the other hand, a viscous fluid has no definite shape and flows irreversibly under the action of external forces with dissipation of energy.

In practice, the polymers generally do not show linear relationships between stress and strain as an elastic solid and such relationships are more complex. However, the situation is often simplified by assuming that the [illegible] strains are small and the polymers behave as a *linear viscoelastic* materials. A material is considered to be linearly viscoelastic if, when it is deformed under small strain, stress is linearly proportional to strain with the linearity depending on time (or frequency) and temperature only. As a result, the mechanical properties also show a marked time and temperature dependence.

4.2.2.2 Stress Relaxation and Creep

Transient experiments such as stress relaxation and creep measure the dimensional stability of a material over a long period of time. In creep test (Fig.4.2a), a constant tensile load is applied to the sample and the change of strain is measured. While in stress relaxation (Fig.4.2b), the sample is subjected to constant strain and the decay of tensile stress is observed. Both experiments are important for the theoretical understanding of the viscoelastic behaviour of polymers. By assuming the polymer

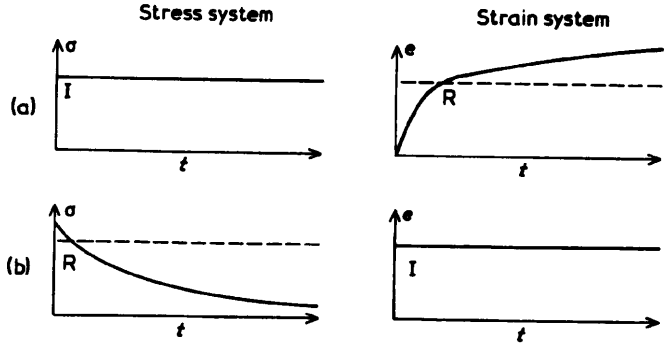

Fig.4.2 Schematic representation of the variation of stress and strain with time indicating the input (I) and response (R) for (a) creep and (b) stress relaxation [46].

behaves as a linear viscoelastic material, it is possible to divide the deformation of the polymer into an elastic component and a viscous component. In fact, a particularly useful method of formulating the combination of elastic and viscous behaviour is through the use of mechanical models.

4.2.2.3 Viscoelastic Mechanical Models

The two basic components used in the models are an elastic spring of modulus E which obeys Hooke's law (Equation 4.1) and a viscous dashpot of viscosity η, which obeys Newton's law (Equation 4.2). The simplest models consist of a single spring and a single dashpot either in series or in parallel and these are known as the Maxwell model and the Voigt (or Kelvin) model [46,71-72,87].

The Maxwell model consists of a spring and dashpot in series as shown in Fig.4.3a. This model is of particular value in considering a stress relaxation experiment which can be represented by

$$\sigma = \sigma_o \exp\left(-\frac{t}{\tau}\right) \qquad (4.3)$$

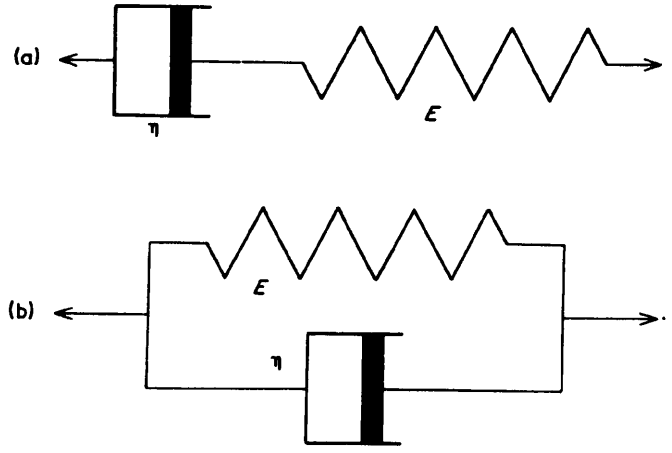

Fig.4.3 Mechanical model used to represent the viscoelastic behaviour of polymers: (a) Maxwell model, and (b) Voigt model [46].

where σ_0 is the initial stress and τ is the *relaxation time* which is a characteristic time constant η/E. Equation (4.3) predicts the stress relaxes completely over a long period of time which is not normally the case for a real polymer. However, the Voigt model consists of a spring and dashpot in parallel as shown in Fig.4.3b. Conversely, the Voigt model is particularly useful in describing the behaviour during creep where the stress is held constant at $\sigma=\sigma_0$. The variation of strain with time for a Voigt model undergoing creep loading is then given by

$$e = \frac{\sigma_o}{E}\left[1 - \exp\left(-\frac{t}{\tau'}\right)\right] \qquad (4.4)$$

where τ' is the *retardation time* which again equals the constant ratio η/E. This behaviour clearly represents the correct form of behaviour for a polymer undergoing creep and the relationships are analogous to the stress relaxation behaviour and the relaxation time of Maxwell model.

4.2.3 Dynamic Mechanical Analysis

The viscoelasticity of polymers may not be fully understood without the investigation of dynamic mechanical properties over a wide range of temperatures and frequencies. Dynamic mechanical analysis involves the determination of the dynamic mechanical properties of polymeric materials in order to explain the relationships between these properties and external variables i.e. temperature and frequency, and the structural parameters e.g. crystallinity and molecular orientation. The dynamic mechanical analysis of crystalline polymers such as PE, so far, has been characterized by identification of various relaxation

mechanisms and attempts to identify these with various types of molecular motion [88].

4.2.3.1 Principles of Dynamic Mechanical Testing

Dynamic mechanical properties are the mechanical properties of materials deformed under periodic forces. They can be expressed in terms of the dynamic or storage modulus, loss modulus and mechanical damping (or internal friction). The dynamic modulus is an indication of the inherent stiffness of material under dynamic loading conditions, whereas the internal friction is an indication of the amount of energy dissipated as heat during the deformation of the material and is sensitive to many kinds of molecular motion, transitions and relaxation processes [89].

In dynamic mechanical testing, an oscillatory strain is applied to the specimen and both the viscous and elastic properties of the specimen are determined simultaneously. For linear viscoelastic behaviour, when equilibrium is reached, the stress and strain will both vary sinusoidally but the strain lags behind the stress (Fig.4.4). Therefore,

$$e = e_o \sin\omega t \tag{4.5}$$

$$\sigma = \sigma_o \sin(\omega t+\delta) \tag{4.6}$$

where ω is the angular frequency, t is the time and δ is the phase lag. Then,

$$\sigma = \sigma_o \sin\omega t \cos\delta + \sigma_o \cos\omega t \sin\delta \tag{4.7}$$

The stress can be considered to consist of two components: one of magnitude ($\sigma_0\cos\delta$) in phase with the strain and the other of magnitude ($\sigma_0\sin\delta$) 90° out of phase with the strain. When

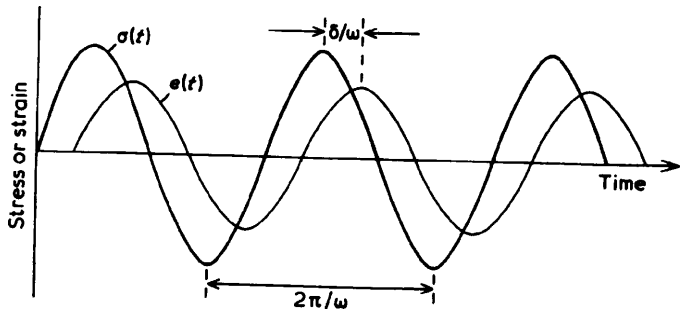

Fig.4.4 The variation of stress and strain with time for a linear viscoelastic material [46].

these are divided by the strain, the modulus can be separated into an in-phase (real) and out-of-phase (imaginary) components. These relationships are

$$\sigma = e_o E' \sin\omega t + e_o E'' \cos\omega t \tag{4.8}$$

where

$$E' = \frac{\sigma_o}{e_o}\cos\delta \qquad\qquad E'' = \frac{\sigma_o}{e_o}\sin\delta \tag{4.9}$$

This suggests a complex representation with E' as the real part of the modulus, and E'' the imaginary part. To describe this relation in a complex notation, a complex time-dependent strain and stress are defined as [88-89]

$$e = e_o \exp i\omega t \tag{4.10}$$

$$\sigma = \sigma_o \exp i(\omega t+\delta) \tag{4.11}$$

Then it follows that

$$\begin{aligned}\frac{\sigma}{e} = E^* &= \frac{\sigma_o}{e_o} e^{i\delta} = \frac{\sigma_o}{e_o}(\cos\delta + i\sin\delta) \\ &= E' + iE''\end{aligned} \tag{4.12}$$

where E^* is the dynamic modulus.

The real part of the modulus E', is called the *storage modulus* because it defines the energy stored in the specimen due to the [illegible] strain. The imaginary part of the modulus E'', defines the dissipation of energy and is called the *loss modulus*. The *loss tangent* tan δ, is also called internal friction and is the ratio of energy dissipated per cycle to the maximum potential energy stored during a cycle i.e. tan $\delta = E''/E'$.

4.2.3.3 Relation of Dynamic Mechanical Properties of Polyethylene to Molecular Motions

Dynamic mechanical properties, particularly loss modulus E'' and tan δ, are sensitive to many kinds of molecular motions or relaxation transitions. For a semi-crystalline polymer such as PE with a complex morphology, there may be some transitions with the crystalline regions and others within the amorphous regions.

It is well established that the dynamic mechanical analysis of PE prior to melting reveals three peaks termed the α, β and γ transitions (Fig.4.5) [88]. Early work on interpreting these three relaxations involved comparing the intensities and positions of the loss peaks in different types of PE. In high

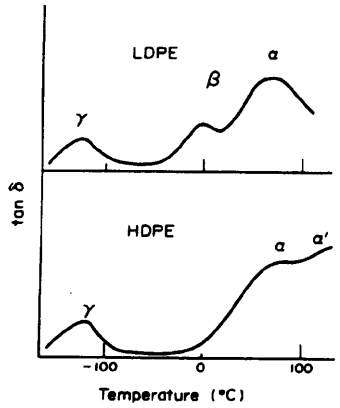

Fig.4.5 Schematic diagram showing α-, α'-, β- and γ-relaxation processes in low density PE and high density PE [88].

density PE, the γ-relaxation is very similar to that in the low density PE while the β-relaxation is almost absent and the α-relaxation is considerably modified. The α-relaxation appears to be a composite process of two transitions, known as α and α' or α_1 and α_2, with different apparent activation energies.

At present there is no generally accepted interpretation of the mechanical relaxations in PE. The difficulty in arriving at an unequivocal interpretation of the relaxations is probably due to the morphological complexity of PE and hence a largely empirical knowledge of the relaxations in PE has been derived. It is thought that the α- and α'- relaxations are associated with the crystalline regions (which have a lamellar texture); the β-relaxation is associated with side groups or short branches in the amorphous regions; the γ-relaxation is associated with the non-crystalline regions and defects in the crystalline regions (i.e. the lamellae) [88]. An additional partially-resolved relaxation in the α region shows the complexity of this mechanical process in crystalline regions. The interpretation of α- and α'-relaxations remains controversial and there is confusion in the literature over symbols and the exact identification of these relaxations at different frequencies between workers.

Based on the viscoelastic behaviour of a single crystal mat of PE, Takayanagi *et al* [90] observed an interesting aspect of the α process. They found no evidence for complex structure (i.e. α and α') in a morphology of greater degree of perfection and for this material the α process apparently appears to be a single relaxation. In fact, similar observation was found in highly-

oriented ultra-high molecular-weight PE (UHMW-PE) gel films by Matsuo *et al* [91] and by Roy *et al* [92]. Generally, highly-oriented PE behaves in a thermorheologically simpler manner than isotropic PE, although the interpretation of such relaxation phenomenon is still highly debatable.

4.3 EXPERIMENTAL

All the PE fibres in this work (Table 3.1) were tested by stress-strain analysis to determine the values of Young's modulus and ultimate stress/strain. Selected fibres were tested using cyclic loading (Section 4.3.1), constant displacement/creep deformation (Section 4.3.2) and dynamic mechanical testing (Section 4.3.3). All the samples were tested in the form of monofilaments (or single-fibres) including the dynamic mechanical testing. However for all the tests, Fibre A was mainly investigated as it is a commercial gel-spun PE fibre.

4.3.1 Stress-strain Measurement and Cyclic Loading

The stress-strain measurement were carried out for all the fibres. Individual monofilaments of PE fibres were mounted across a hole in a paper card using Ciba-Geigy HY/LY 1927 two-part solvent-free cold-setting epoxy resin. The card was then mounted between fibre testing grips in a model 1211 Instron tensile tester and the card edges were cut. A 5N capacity load was used with the scale calibrated at its maximum load. Gauge lengths of 10.0, 20.0, 50.0 and 100.0 mm with a constant initial strain rate of 1.67×10^{-3} s^{-1} (obtained by adjusting the cross-head speed for different gauge lengths) were used. At least 20 samples of each

gauge length were tested to obtain the average values.

For the effect of strain rates and cyclic loading, only the monofilaments of Fibre A were tested. Firstly, the monofilaments were tested at different strain rates i.e. 0.67×10^{-3}, 1.67×10^{-3}, and 3.33×10^{-3} s^{-1} using a constant gauge length of 50.0 mm. Then, cyclic loading was carried out at 1.67×10^{-3} s^{-1} using different loading conditions. All the mechanical tests were carried out at 23 ± 1°C and a relative humidity of 50 ± 2%.

4.3.2 Stress Relaxation and Creep Tests

Stress relaxation experiments were carried out for Fibres A, B, C and E with a gauge length of 50.0 mm at a constant displacement of 2.0% strain. The specimens (of the monofilaments) were prepared in a similar way to those of tensile testing (Section 4.3.1) and the constant displacement was applied to the monofilament using a model 1211 Instron tester. The decrease in load was then plotted against time on the chart paper. Additionally, the stress relaxation of Fibre A at different constant displacements was investigated.

Creep tests were carried out on similar specimens for Fibres A, B, C and E with a gauge length of 50.0 mm at a constant stress (i.e. 1.2 GPa). These particular fibres were investigated because both Fibres A and E were found to be the experimental gel-spun PE fibres of highest and lowest values of modulus respectively (Section 4.4.1); while the melt-spun Fibre B was used for comparison. The extension of the monofilament was determined by means of a linear displacement transducer attached at the lower end of the specimen. Both stress relaxation and creep experiments

were carried out over a period of time at 23 ± 1°C and a relative humidity of 50 ± 2%.

4.3.3 Dynamic Mechanical Testing

Previous dynamic mechanical testing on gel-spun ultra-high molecular-weight PE (UHMW-PE) has only been reported for either film [91-92] or multifilament yarn [93]. The aim of this present investigation was to see it was possible to obtain accurate and reliable data on monofilaments as small as 10-20 μm in diameter. Dynamic mechanical properties of PE monofilaments were measured using a Rheometrics RMS800 mechanical spectrometer. Again, only Fibres A, B, C and E were tested and the specimen were prepared similarly as for tensile testing (Section 4.3.1). However, the gauge length was fixed at 5.5 mm due to the geometry of the Rheometrics fibre fixture [94]. The specimen was then mounted

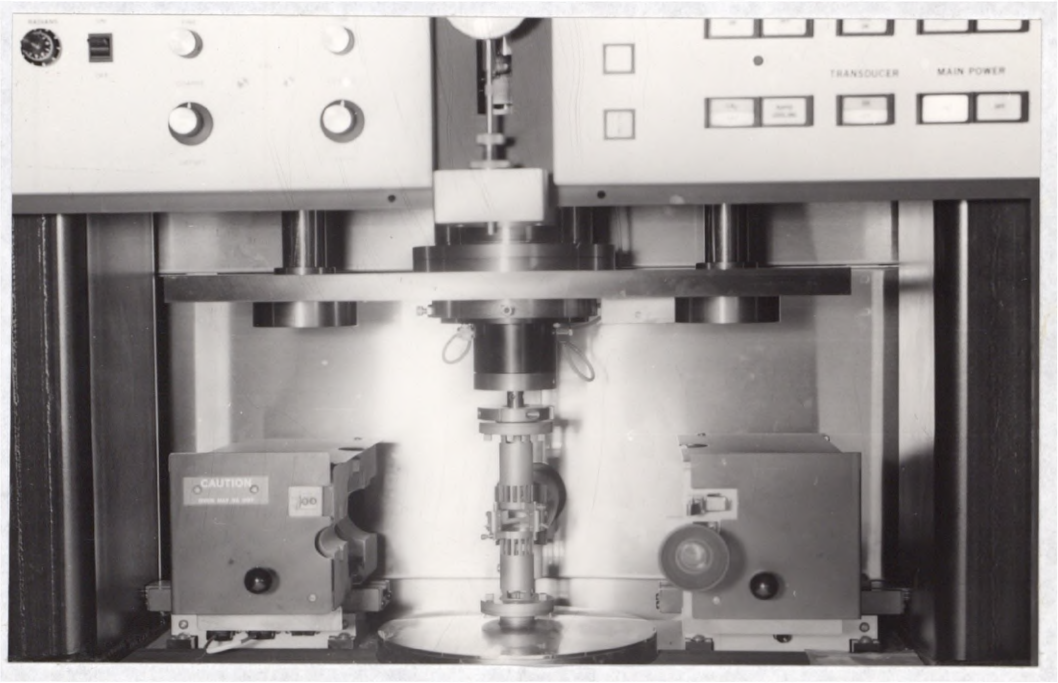

Fig.4.6 The arrangement of the PE monofilament specimen attached to the fibre fixture in Rheometrics Instrument RMS800 mechanical spectrometer.

onto the fixture (shown in Fig.4.6) by clamping.

The measurements were carried out from 30 to 150°C at constant frequency of 1 rad/s. Additionally, measurements from frequencies of 0.1 to 100 rad/s over the temperature range from 30 to 130°C were carried out in order to observe the temperature-frequency dependence of the materials. During the measurement, the monofilament was subjected to a static tensile stress of about 300 MPa in order to place the sample in slight tension with the axial sinusoidal oscillation produced a maximum strain of 0.03%. This is well within the linear viscoelastic region obtained from the stress-strain curves on the monofilaments.

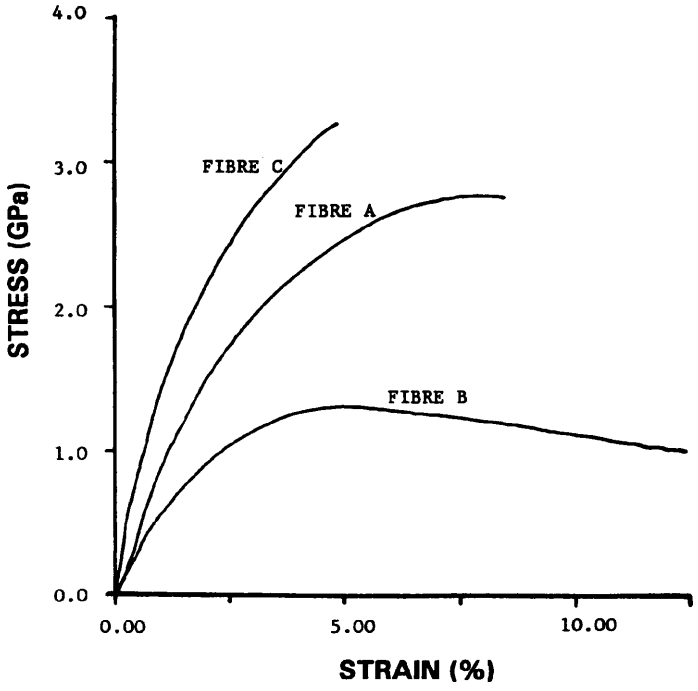

Fig.4.7 The stress-strain curves of Fibres A, B and C for a gauge length of 50.0 mm and a strain rate of $1.67 \times 10^{-3} s^{-1}$ at temperature 23 ± 1°C.

4.4 MECHANICAL DEFORMATION BEHAVIOUR OF MONOFILAMENTS

Fig.4.7 shows the stress-strain curves of Fibres A, B and C for the gauge length of 50 mm and at the strain rate of 1.67×10^{-3} s^{-1}. The stress-strain curves of the these monofilaments are essentially non-linear with significant differences in mechanical properties between the monofilaments. In fact, both gel-spun Fibres A and C show higher values of initial modulus and ultimate strength than the melt-spun Fibre B. In the practical determination of the mechanical properties of materials, it is usually assumed that stress concentrations imposed at the ends of the sample as a result of the particular clamping arrangement

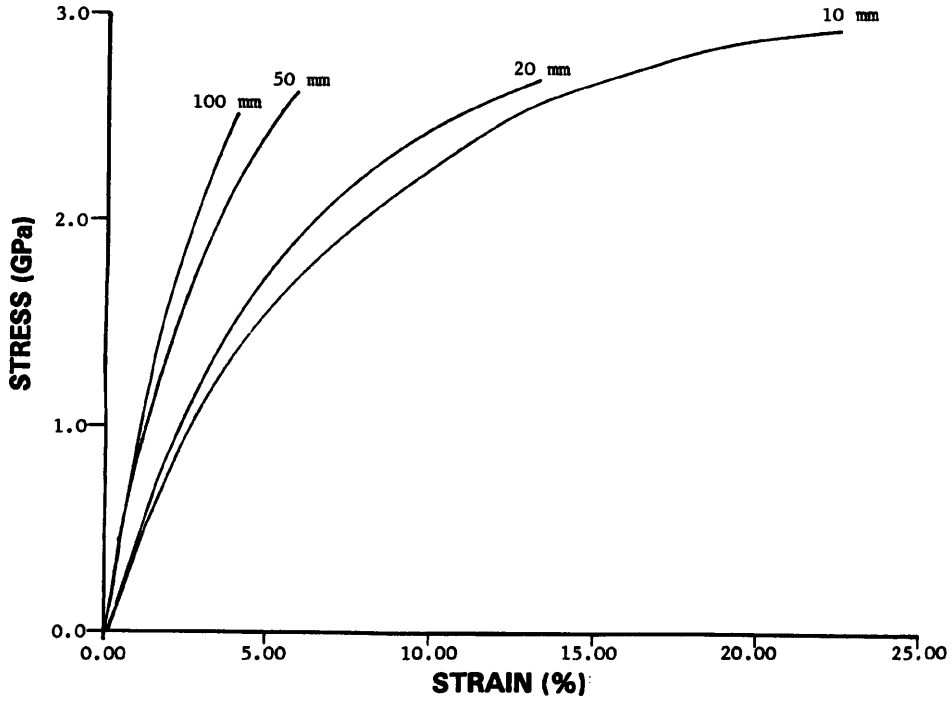

Fig.4.8 The stress-strain curves of Fibre A for different gauge lengths at a strain rate of 1.67×10^{-3} s^{-1} and a temperature 23 ± 1°C.

can be neglected. Recent work [86,95-96] has underlined the significance of these ends constraints in polymers especially for highly-anisotropic materials. Furthermore, there are other limitations to be considered particularly for the mechanical behaviour of polymeric materials, such as PE, which is time and temperature dependent. Therefore, a knowledge of this dependence is necessary for both the determination of mechanical properties of PE monofilaments and the sample assessment by a technique such as Raman microscopy (Chapter 5).

4.4.1 Effect of Gauge Lengths

Four set of specimens with different gauge length of PE monofilaments of all the samples (Table 3.1) were tested in the Instron 1211 at constant strain rate of 1.67×10^{-3} s^{-1} (Section 4.3.1). The stress-strain curves of Fibre A are shown in Fig.4.8 for different gauge lengths. Clearly, the increase of gauge lengths has increased the apparent modulus of the monofilaments.

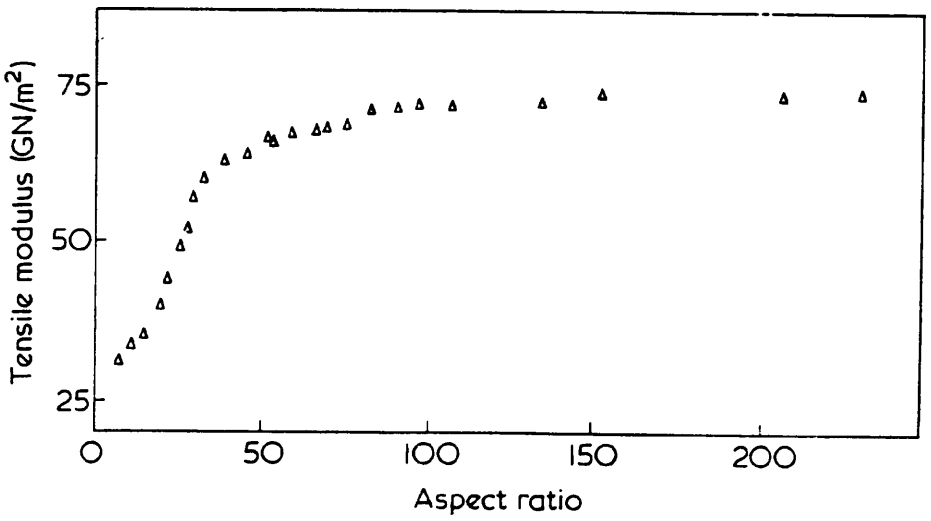

Fig.4.9 Apparent tensile modulus as a function of aspect ratio by Arridge *et al* [95].

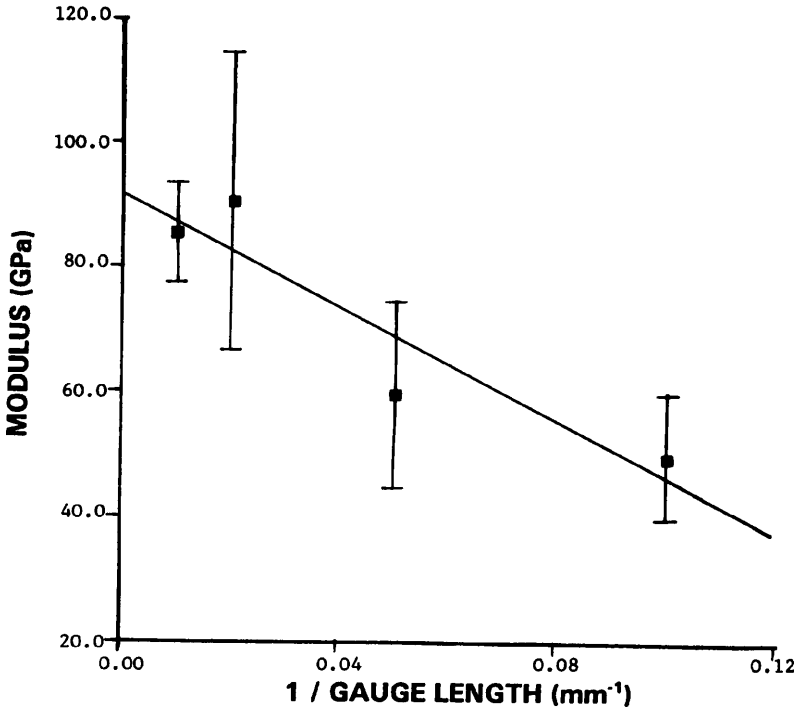

(a)

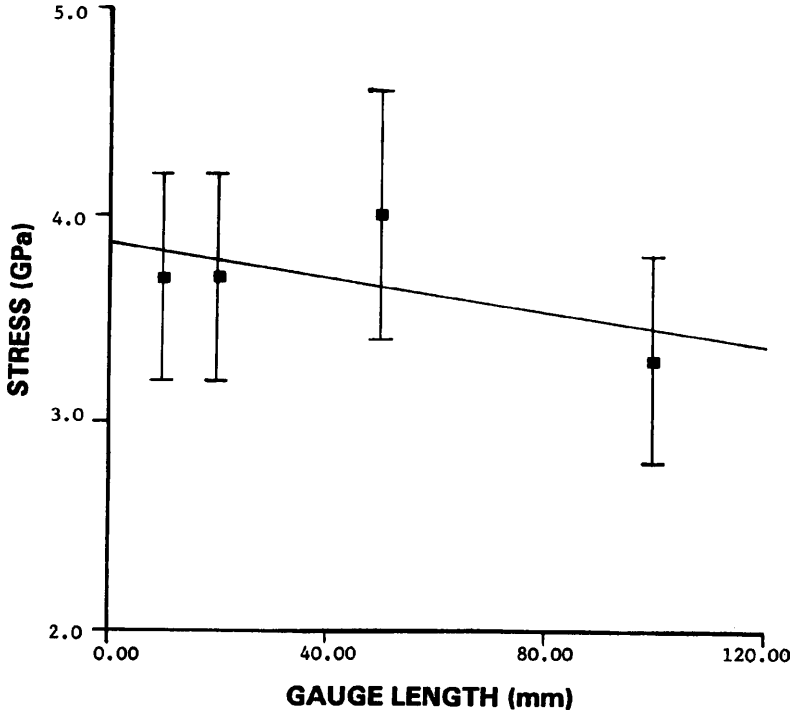

(b)

Fig.4.10 Dependence of (a) modulus, and (b) ultimate stress of the monofilaments of Fibre A on reciprocal of gauge length and gauge length respectively.

This is in line with the observation on the high-modulus PE films by Arridge *et al* [86,95] with different aspect ratio (i.e. length/width) as illustrated in Fig.4.9. It is apparent that the sample aspect ratio or gauge length must be sufficiently large for end effects to be ignorable particularly for highly oriented materials. By assuming a linear relationship between the modulus and the reciprocal of gauge length, the corrected modulus could be obtained by extrapolating the values to infinite gauge length as shown in Fig.4.10a.

Both the ultimate tensile stress and tensile strain are also significantly affected by gauge lengths. The decrease in ultimate stress of PE monofilaments with increasing gauge length may be due to the presence of defects. Monofilaments often contain defects randomly distributed along the length and the longer the gauge length, the greater the chance of encountering a defect. Therefore by extrapolating the values of ultimate stress to zero gauge length, an estimation could be made for the corrected ultimate stress of a defect-free monofilament (Fig.4.10b). It can be seen that there is a much stronger dependence of the modulus upon gauge length than for the fibre strength. This is

Table 4.1

EFFECT OF GAUGE LENGTH ON THE ULTIMATE STRESS OF A HIGH-STRENGTH PE FIBRE BY SCHWARTZ *ET AL* [90].

Gauge Length (mm)	Ultimate Stress (GPa)
10	2.992
50	2.982
100	3.025
200	3.053

Table 4.2

CORRECTED VALUES OF MODULUS AND ULTIMATE STRESS OF ALL THE PE SAMPLES (STRAIN RATE = 1.67×10^{-3} s^{-1}).

Fibre	Corrected Modulus (GPa)	Reported Modulus [74] (GPa)	Corrected Ultimate Stress (GPa)	Reported Ultimate Stress [74] (GPa)
A	91.7	-	3.9	-
B	50.7	-	0.9	-
C	163.6	178	5.4	3.9
D	61.7	96	2.3	3.0
E	37.8	48	1.9	1.8
F	51.5	85	2.7	3.1
G	88.5	158	3.1	3.6
H	60.7	140	1.5	2.9
I	61.2	108	1.9	2.9

consistent with the observation of Schwartz *et al* [97-98] who found no significant gauge length effects for the strength of the PE monofilaments as illustrated in Table 4.1. For Fibre A, the corrected modulus is 91.7 GPa and the corrected ultimate stress is 3.9 GPa at the strain rate of 1.67×10^{-3} s^{-1}. The corrected values of modulus and tensile stress of all the samples are tabulated in Table 4.2 together with the reported values. The reported moduli are higher because the fibres were tested by Allied-Signal in different conditions such as at higher strain rate.

4.4.2 Effect of Strain Rates

The monofilaments of Fibre A were deformed in the Instron 1211 at different strain rates using a constant gauge length of 50.0 mm. The deformation response of PE monofilaments appears to go

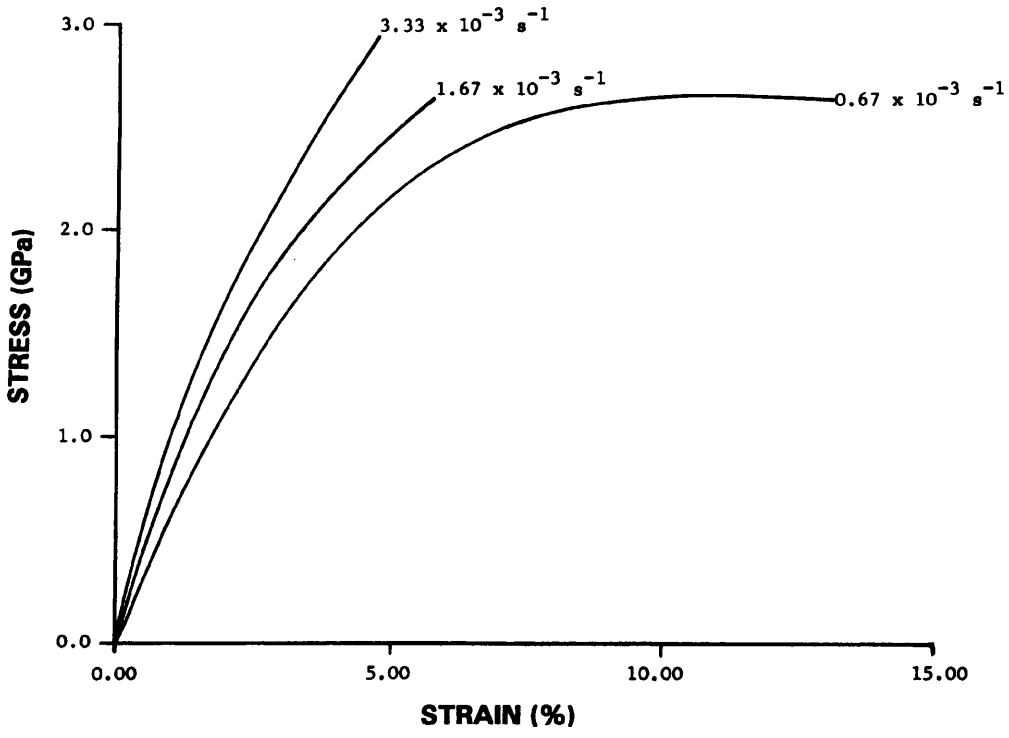

(a)

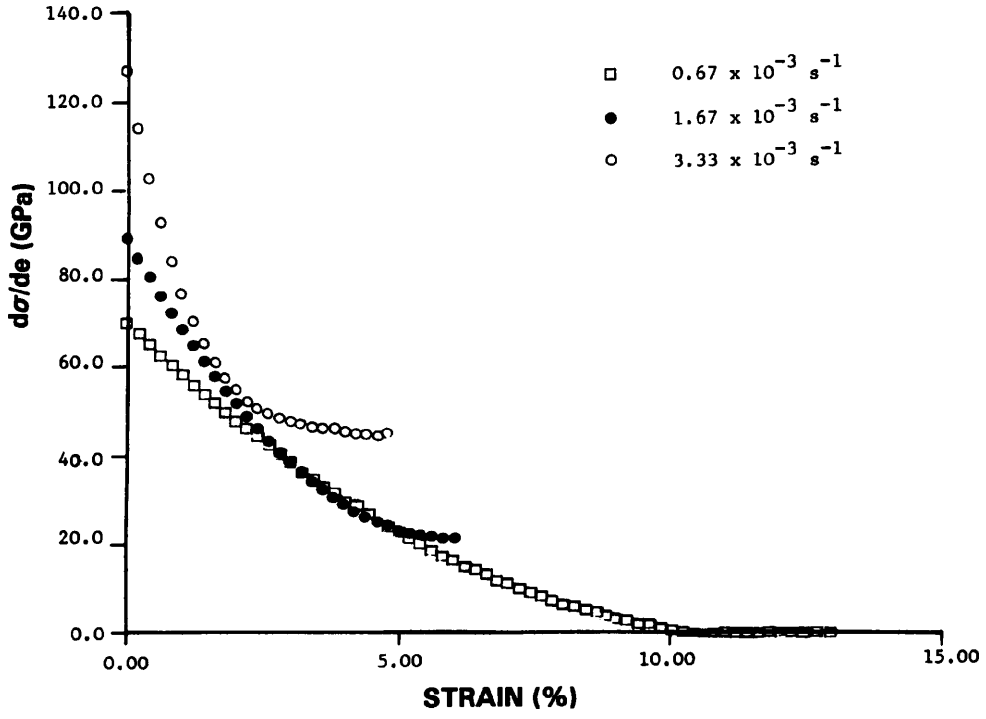

(b)

Fig.4.11 (a) The stress-strain curves, and (b) the differentiation of (a) vs strain of Fibre A at different strain rates with constant gauge length of 50.0 mm at temperature of 23 ± 1°C

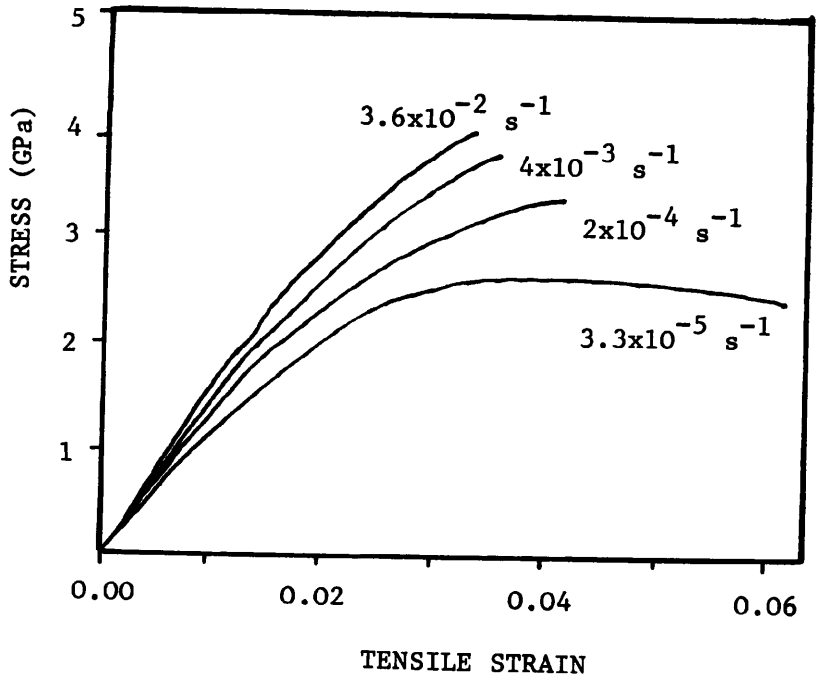

Fig.4.12 Stress-strain curves of gel-spun PE fibres at room temperature with various strain rates obtained by Dijkstra *et al* [99].

through two stages and it is highly sensitive to the effect of strain rate (Fig.4.11a) which is very similar to the observation on the gel-spun PE fibres by Dijkstra *et al* [99] as illustrated in Fig.4.12. At a low strain rate of 0.67×10^{-3} s^{-1}, the monofilament extends to a maximum load at yield of about 10% strain and the stress remains almost constant until fracture at a considerably higher strain. In contrast, at a higher strain rate of 3.33×10^{-3} s^{-1}, the curve is more linear and the monofilament fractures in a brittle manner at a comparatively low strain.

The non-linear character of the stress-strain curves is more easily observed from the corresponding modulus-strain plot as shown in Fig.4.11b. The plot shows a non-linear decrease of the modulus at different strain rates and obviously each curve can be divided into two distinct regions: a higher decrease rate of

modulus at low strains and almost no change of modulus at high strains. At the highest strain rate, the initial decrease of the modulus is most pronounced and the modulus levels out at an almost constant value before fracture. At the lowest strain rate, the modulus decreases to a zero value which is an indication of yielding of the monofilaments. Obviously, the PE monofilaments exhibit marked strain rate effects and this behaviour can be observed for all the values of mechanical properties such as modulus, ultimate stress and ultimate strain for all fibres.

4.4.3 Cyclic Loading

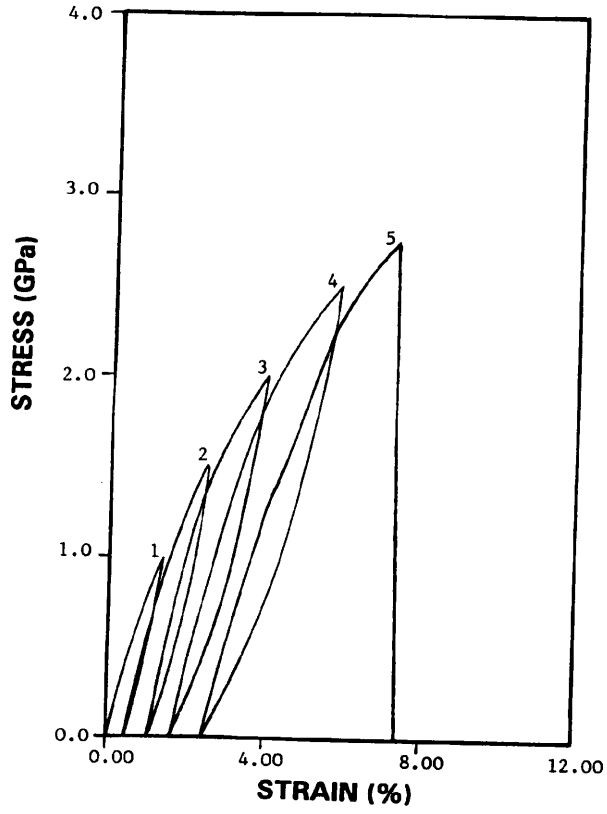

Fig.4.13 Effect of cyclic loadings of the monofilament of Fibre A to a series of five successively increasing loads.

Fig.4.13 illustrates the response of the PE monofilaments of Fibre A to a series of five successively increasing loads and shows hysteresis during cyclic deformations. The stress-strain curve follows different loading paths and becomes offset by different amounts due to the onset of structural deformation within the monofilament with increased loading. The hysteresis is clearly non-elastic in the two deformation cycles, i.e. the strain at which the stress becomes zero in the unloading curve is larger than the strain at which the loading cycle started. However by having a long delay time (about 2 days) between the two cycles, the stress-strain characteristics of the second cycle

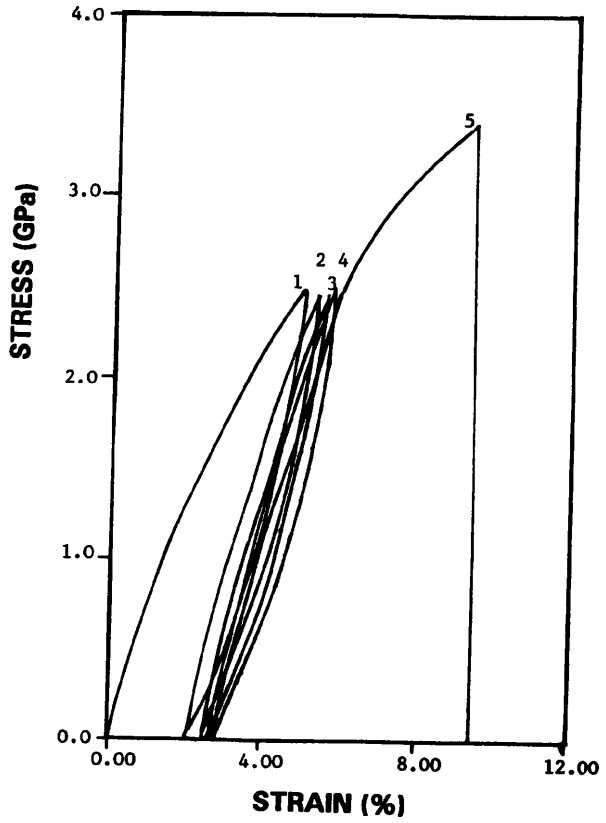

Fig.4.14 Effect of cyclic loadings of the monofilaments of Fibre A to a series of constant loads.

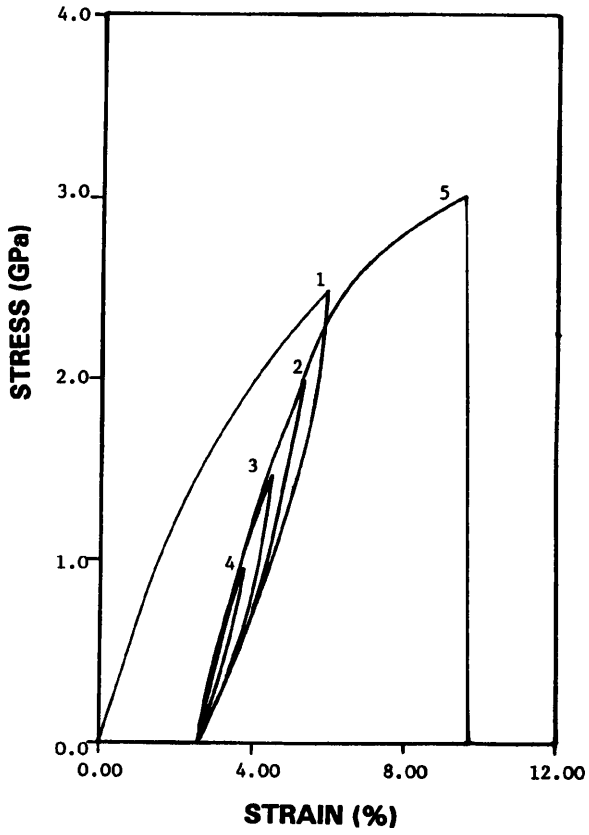

Fig.4.15 Effect of cyclic loadings of the monofilament of Fibre A to a series of decreasing loads.

becomes completely identical to the first due to recovery. This observation is consistent with the cyclic deformation to constant stress (i.e. 3.5 GPa) for the gel-spun PE fibres obtained by van der Werff *et al* [100]. This means that the structural deformation that causes the non-elastic hysteresis during the cyclic loading is reversible and that no permanent plastic deformation occurs. Further straining induces such structural deformation, the magnitude of which increases with strain. Likewise, the amount of this deformation increases for repeated loadings to constant stress (Fig.4.14) but no further increase is found after the first cycle for loadings of successively-decreasing magnitude

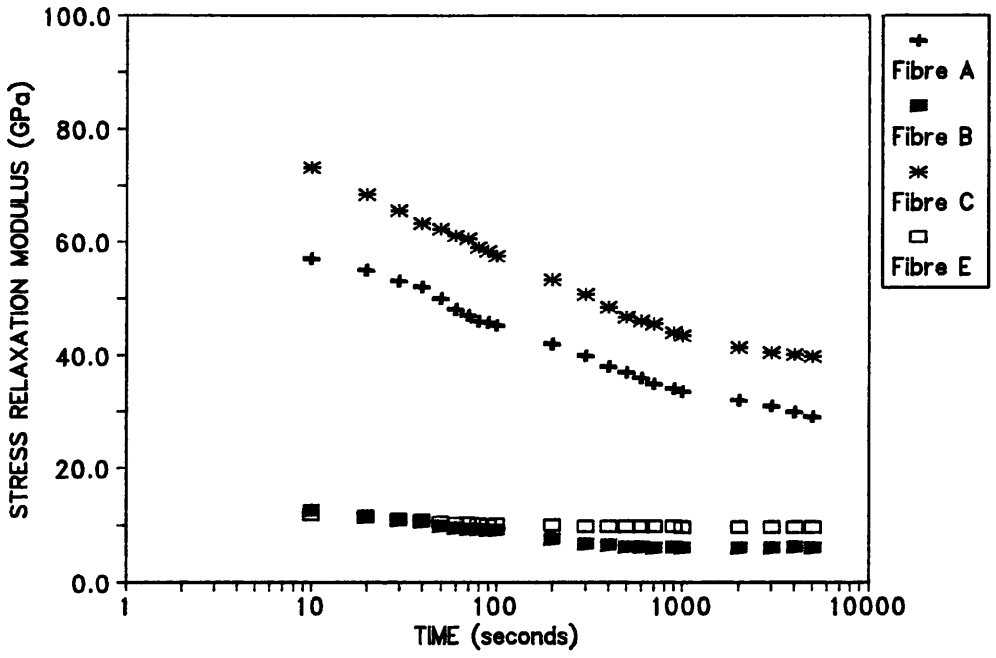

Fig.4.16 Stress relaxation curves of various monofilaments subjected to a constant displacement of 2.0% at 23°C.

(Fig.4.15). The reloading response curves are generally not parallel to one another which shows that there is strain hardening of the monofilaments for repeated loadings.

4.4.4 Stress Relaxation and Creep

Fig.4.16 shows the stress relaxation response for the monofilaments of Fibres A, B, C and E at 23°C using a logarithmic time-scale. Fibre E is the experimental gel-spun PE fibre of lowest modulus and it is of great interest to reveal the time-dependent behaviour of such monofilaments. Measurements were not made until after the first 5 seconds of the experiment. The monofilament was stretched to a fixed strain (i.e. 2.0% strain) and it was found that stress in the fibre decays with time. It can be seen that there is an approximately linear decrease in modulus with time over the logarithmic timescale. This is similar

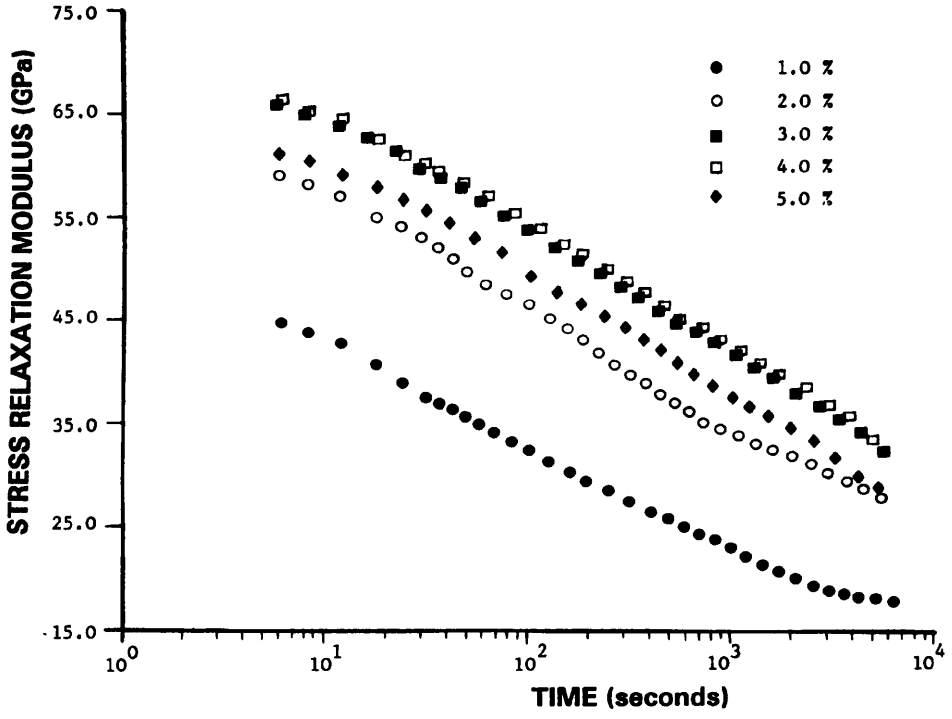

Fig.4.17 Stress relaxation of the monofilament of Fibre A at different constant displacements (temperature = 23°C).

to the stress relaxation response of another commercial gel-spun fibre (i.e. Dyneema SK66 with reported modulus of ~80 GPa) found by Govaert [93]. In Section *4.2.2.3* it was demonstrated that the Maxwell model can be used to describe the stress relaxation of a polymer to a first approximation. One measure of this stress relaxation is the relaxation time, τ, which is defined as the time taken for the material to relax to 1/e of its initial stress, σ_0 as derived from Equation (4.3). However it is not possible to determine the different values of τ in this case as the stress in none of the fibres has decayed to 1/e of the initial applied stress.

Simple stress relaxation tests were also performed at different constant displacements, namely, 1.0%, 2.0%, 3.0%, 4.0% and 5.0% strains for the monofilaments of Fibre A. Fig.4.17

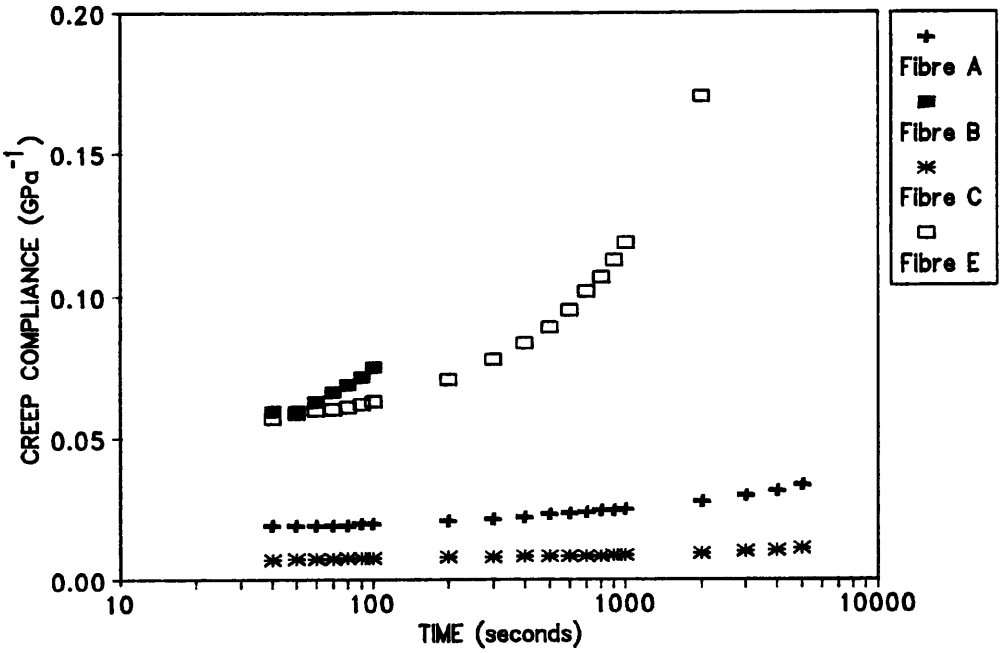

Fig.4.18 The creep curves of various monofilaments subjected to a constant stress of 1.2GPa at 23°C.

illustrates the various stress relaxation responses for the Fibre A at different displacements. Apparently, the stress relaxation modulus is dependent on the [illegible] strain due to the non-linear stress-strain relationship for the monofilaments as discussed in Section 4.4.2. In fact, there is an indication of yielding at a strain of >3.0% with no significant change in the stress relaxation response.

In the creep tests, a constant stress of 1.2 GPa was applied to the monofilaments of Fibres A, B, C and E at 23°C in order to reveal the creep properties of different fibres shown in Fig.4.18. The melt-spun Fibre B fractures after a short time at 1.2 GPa which is about the same as the ultimate strength of the fibre. Obviously, a considerable degree of permanent strain is developed in Fibre E as evidenced by a greater divergence of its creep curve over a long time. Due to insufficient knowledge provided on the processing of these fibres, it is difficult to

Table 4.3

RETARDATION TIME, τ', OF VARIOUS MONOFILAMENTS BASED ON VOIGT MODEL.

Fibre	Corrected Modulus (GPa)	Retardation Time, τ' (seconds)
A	91.7	~3000
B	50.7	~60
C	163.6	>5000
E	37.8	~400

correlate the observed properties with their structures. However, the magnitude of the creep apparently decreases markedly with the increasing values of modulus for the monofilaments. By assuming the PE monofilaments can be treated as a Voigt model (Section *4.2.2.3*), Equation (4.4) will represent the behaviour of the monofilaments undergoing creep and therefore it is possible to measure the retardation time, τ' based on the Voigt model as tabulated in Table 4.3. The melt-spun Fibre B has the lowest retardation time which is an indication of poor creep behaviour. In fact, it appears that the retardation time of creep increases with increasing modulus of the monofilaments. However, it is necessary to highlight that both Maxwell and Voigt models are too simple to describe the true viscoelastic behaviour of these highly-oriented PE fibres which has been shown earlier by Ward *et al* [101-103]. But, in this instance, both models are useful in assisting the basic understanding of the viscoelastic process in the PE monofilaments.

4.5 VISCOELASTIC BEHAVIOUR OF MONOFILAMENTS

In dynamic mechanical testing, it is necessary to impose a chosen

stress and to measure stress and deformation continuously (Section 4.3.3). However, the absolute values of measurement of the monofilament are very sensitive to the initial stress which is not possible to be accurately applied in the Rheometrics equipment. Therefore, the nature of the deformation not only depends on the specimen properties, but also on the magnitude of the applied stress. Thus, the absolute values will be of doubtful meaning, and it is not expected that absolute values can be obtained routinely. However, the values can be used for comparison purpose within a set of tests conducted under strictly controlled conditions and to identify important relaxations (particularly in crystalline region) without any attempt to acquire accurate modulus data.

4.5.1 Dynamic Mechanical Properties

PE monofilaments of both the gel-spun (Fibres A, C and E) and the melt-spun (Fibre B) fibres were used for the dynamic mechanical testing. Fig.4.19 show the temperature dependence of the dynamic mechanical properties i.e. dynamic modulus E^*, storage modulus E', loss modulus E'' and tan δ of the monofilaments at the constant frequency of 1 rad/s. The curves alter very little in shape between different monofilaments although they have quite different mechanical properties. It can be seen that both E^* (Fig.4.19a) and E' (Fig.4.19b) decrease with increasing temperature and the rate of fall increases in the high temperature region. The decrease, however, is less significant in the monofilaments of Fibres A and C which are the higher modulus fibres among the samples. The variation of the

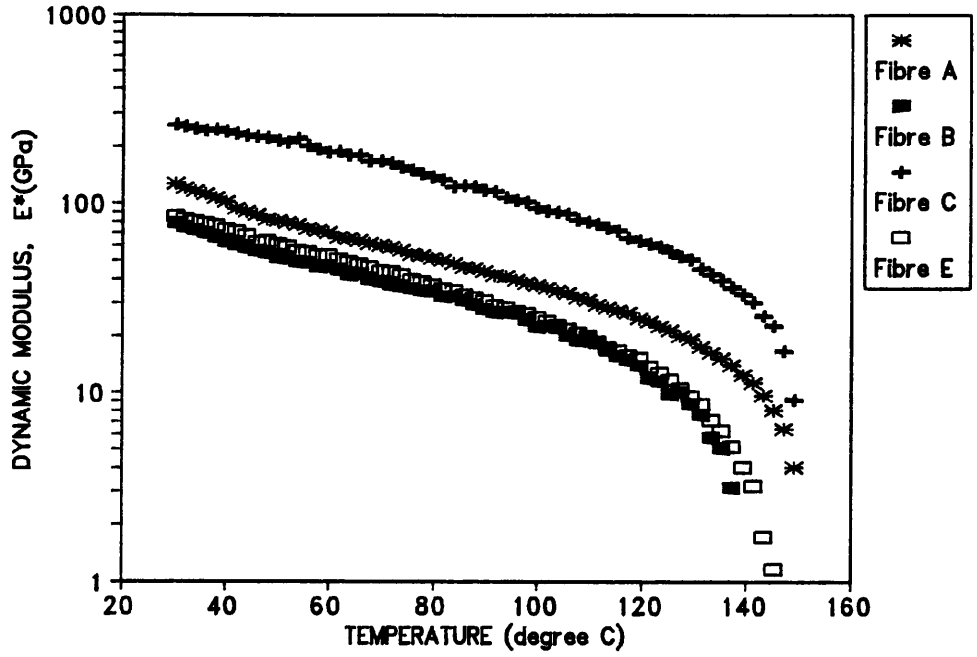

(a)

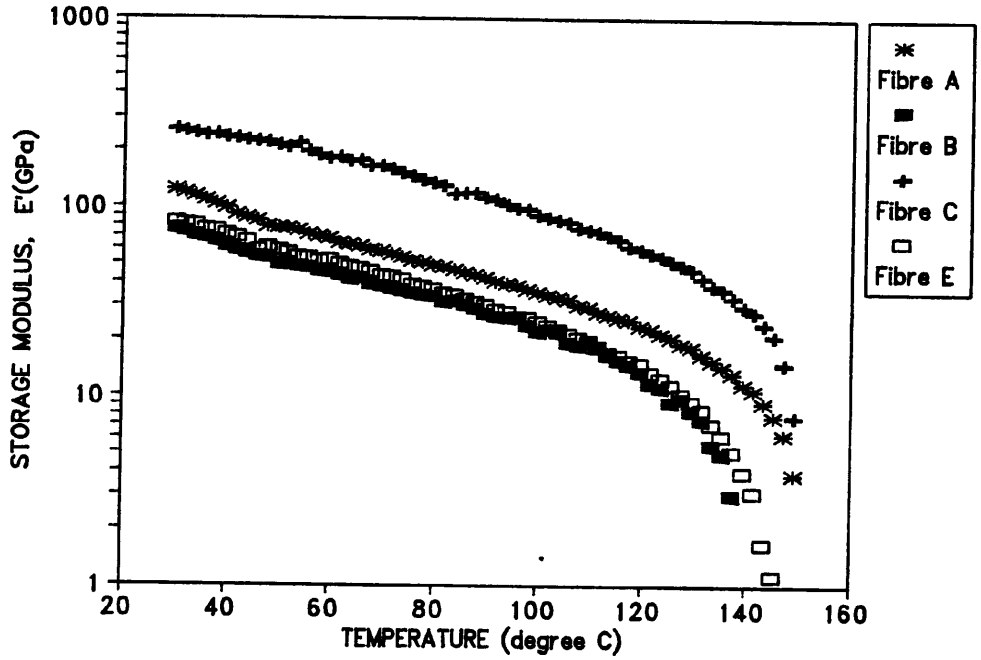

(b)

Fig.4.19 Temperature dependence of (a) E^* and (b) E'at constant frequency of 1 rad/s for the monofilaments of Fibres A, B, C and E.

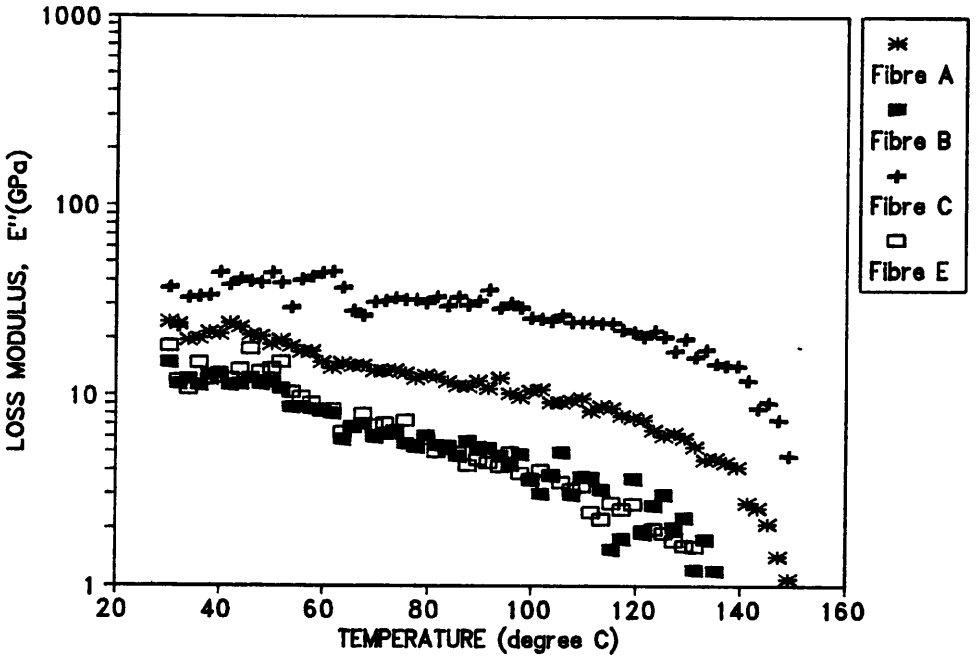

(c)

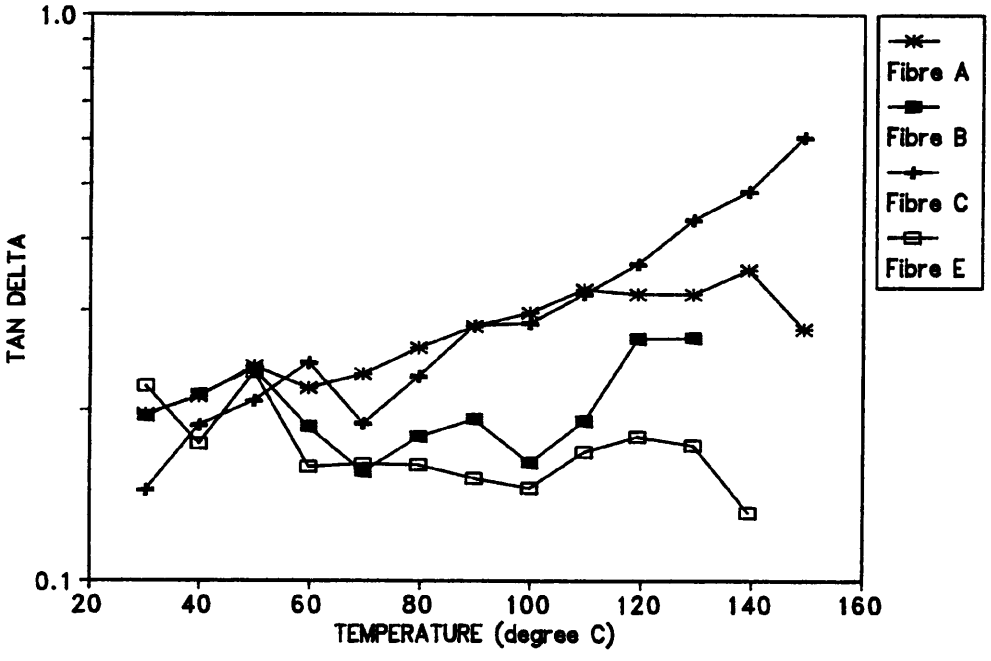

(d)

Fig.4.19 Temperature dependence of (c) E^* and (d) tan δ at constant frequency of 1 rad/s for the monofilaments of Fibres A, B, C and E.

corresponding E'' (Fig.4.19c) is apparently similar to E^* and E' although the data are rather scattered. However, the loss factor tan δ shows a different variation with temperature for different monofilaments. Fig.4.19d shows that the tan δ of Fibres A and C increases with temperature while Fibres B and E show decreasing tan δ with increasing temperature. It appears that both Fibres B and E, which are lower modulus fibres, show no distinct difference in dynamic mechanical behaviour even though they are spun differently from different precursors. In fact, Fibre B was melt-spun from conventional PE while the others were gel-spun from ultra-high molecular-weight PE (UHMW-PE). However, due to the limitation of the equipment, the temperature dependence of the dynamic mechanical properties over a wide range of temperature particularly below room temperature could not be obtained. Also since only monofilaments were used the tan δ values are very scattered. Therefore, it is not possible to determine all the loss peaks and to identify the temperatures of the relaxations (i.e. α-, α'-, β- and γ-) as illustrated in Fig.4.5. However, it is possible to carry out a detailed analysis of the α-relaxation by time-temperature superposition [91-92].

4.5.2 Time-temperature Superposition

Time-temperature superposition in its simplest form implies that the viscoelastic behaviour at one temperature can be related to that at another temperature by a change in the time/frequency scale only [88]. This principle holds when the shapes of the adjacent curves measured at different temperatures can match and the viscoelastic functions can be superimposed exactly by a

horizontal displacement a_T. This defines a horizontal shift factor a_T. However, in a more sophisticated analysis, it is possible to allow for changes in the magnitude of the response scale (y-axis) with temperature using a vertical shift factor b_T for the viscoelastic functions [88].

Fig.4.20 shows the temperature dependence of E' and E'' of the monofilaments of Fibre A measured as a function of frequency at temperatures from 30 to 130°C. It can be seen that all the values of E' decrease with increasing temperature at a given frequency, as well as with decreasing frequency at a fixed temperature (Fig.4.20a). On the other hand, E'' increases with decreasing frequency up to 100°C and reach a nearly constant value. From the observations of Matsuo *et al* [91], this can be considered as a maxima of the E'', which is generally ascribed to the α-relaxation process. The α-relaxation process is thought to be associated with the crystalline region as discussed in Section *4.2.3.3.*

Fig.4.21 and Fig.4.22 show the master curves of E' and E'', respectively, for the monofilaments of Fibres A, B, C and E at the reference temperature of 30°C. Each master curve was obtained by shifting horizontally and then vertically of adjacent curves until good superposition was achieved. In fact, an early attempt to obtain the master curves without vertical shift was not successful as no exact match could be obtained between the adjacent curves. The master curves obtained are however similar to the one for Dyneema SK66 by Govaert [93] as shown in Fig.4.23. The value of E' decreases with decreasing frequency and that of Fibre C shows a higher fall rate than the others. Comparing both

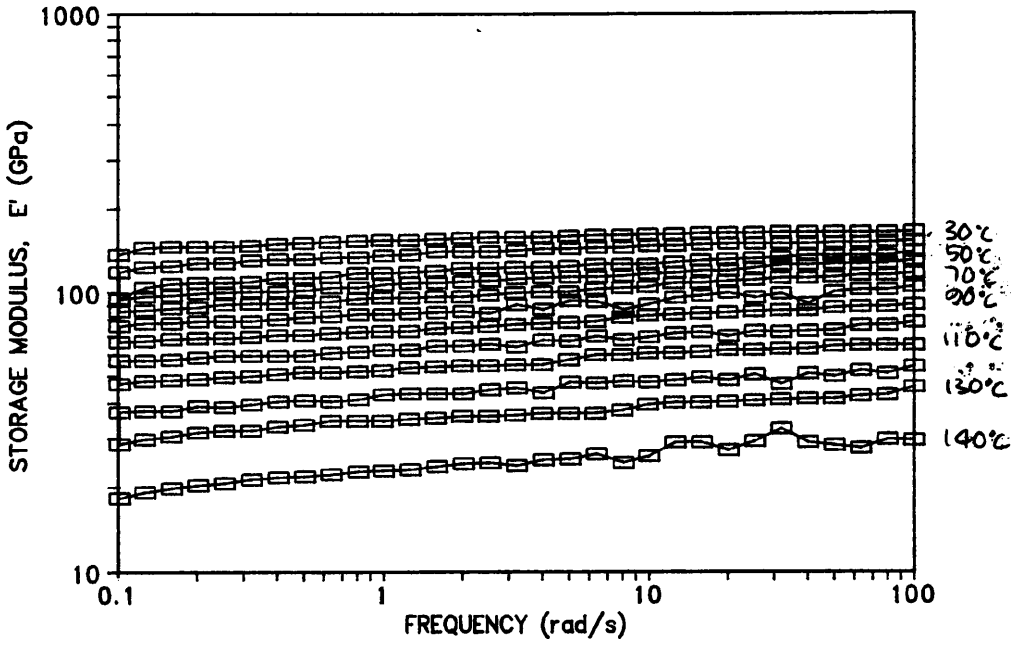

(a)

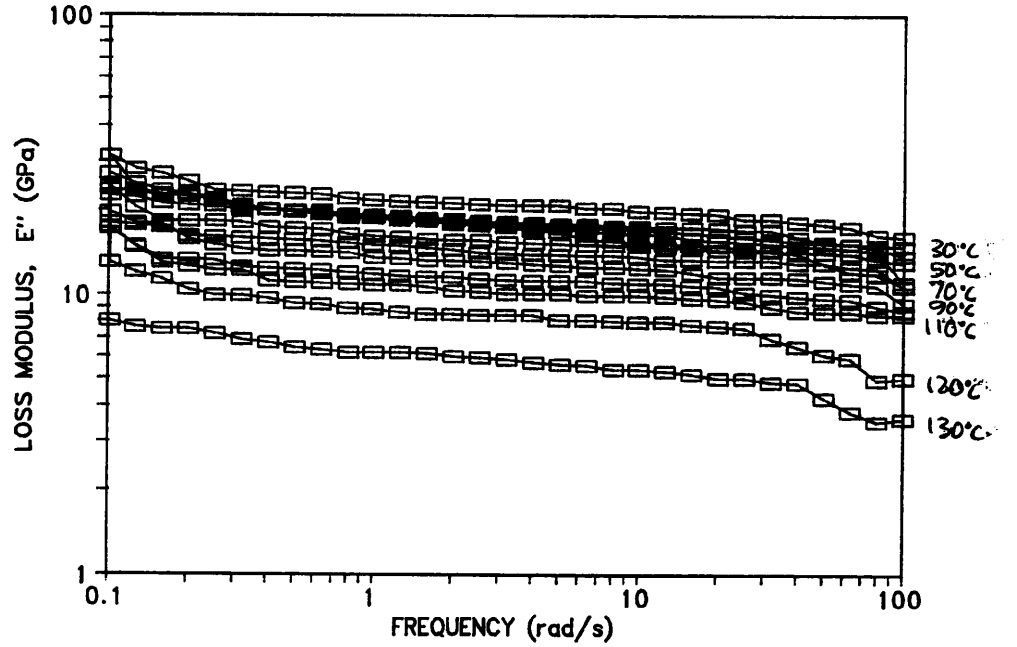

(b)

Fig.4.20 The values of (a) storage modulus, and (b) loss modulus vs angular frequency at temperatures of 30 to 130°C for the monofilaments of Fibre A.

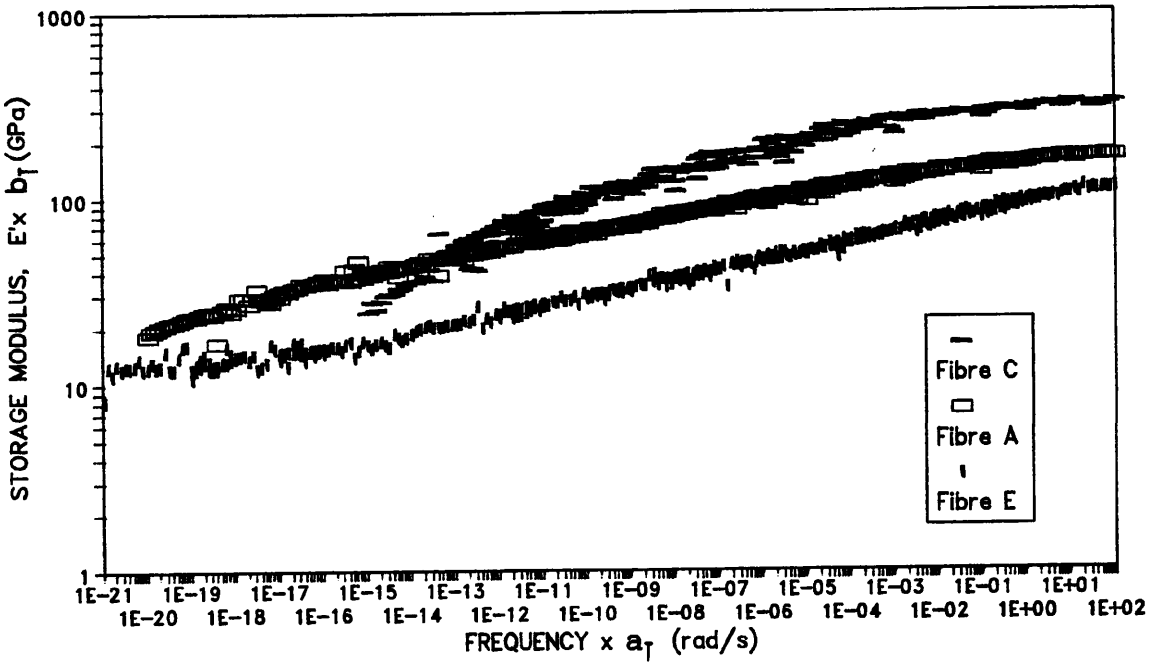

(a)

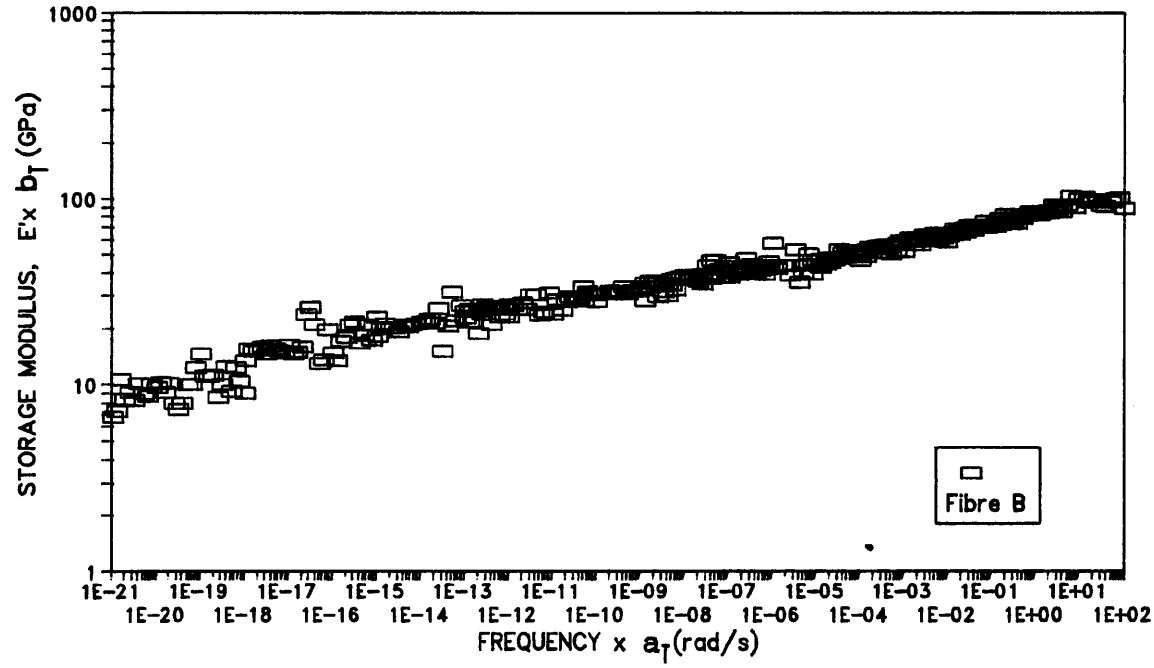

(b)

Fig.4.21 Master curves of E' for the (a) gel-spun (Fibres A, C and E), and (b) melt-spun PE monofilaments (Fibre B), at reference temperature of 30°C.

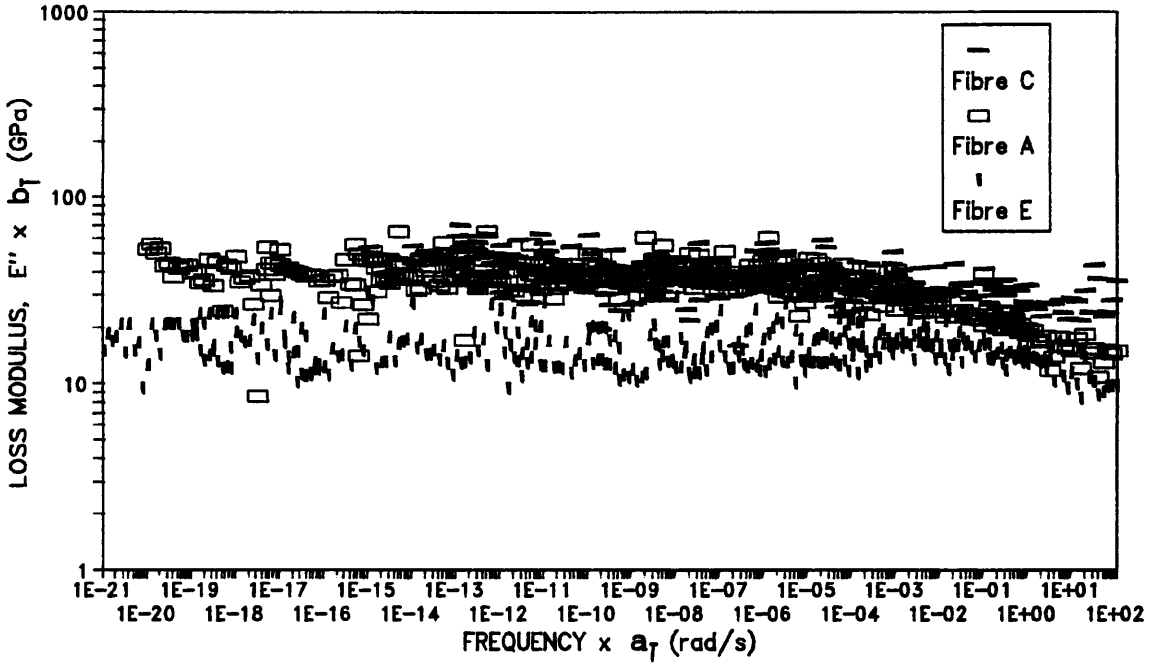

(a)

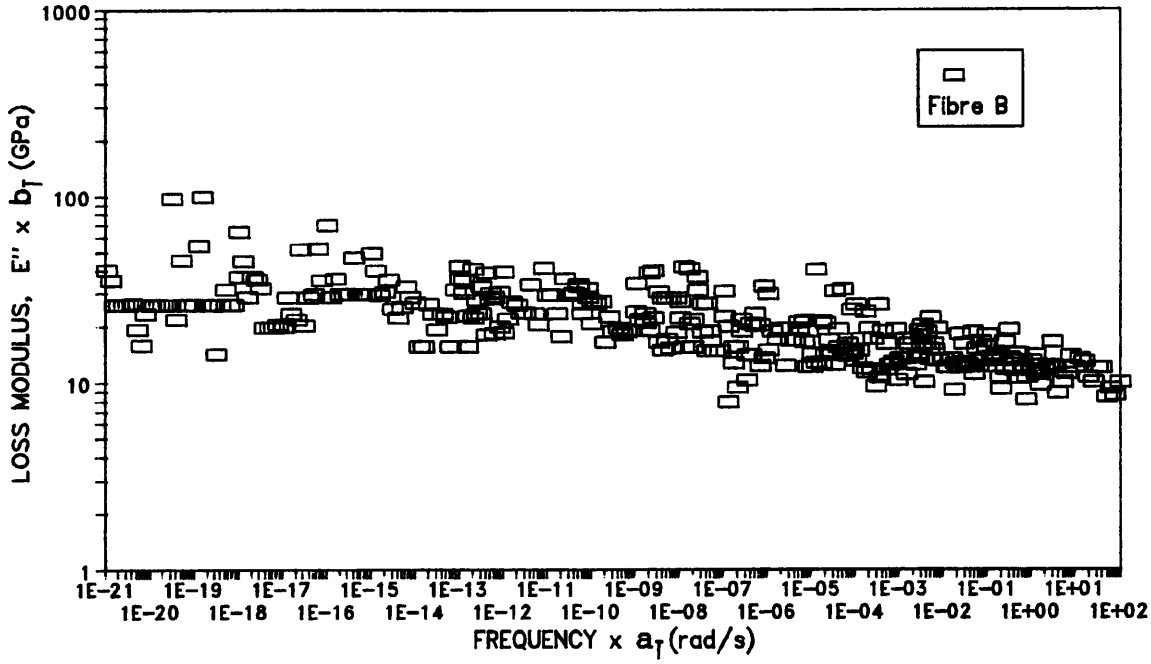

(b)

Fig.4.22 Master curves of E^* for the (a) gel-spun (Fibres A, C and E), and (b) melt-spun (Fibre B) PE monofilaments, at reference temperature of 30°C.

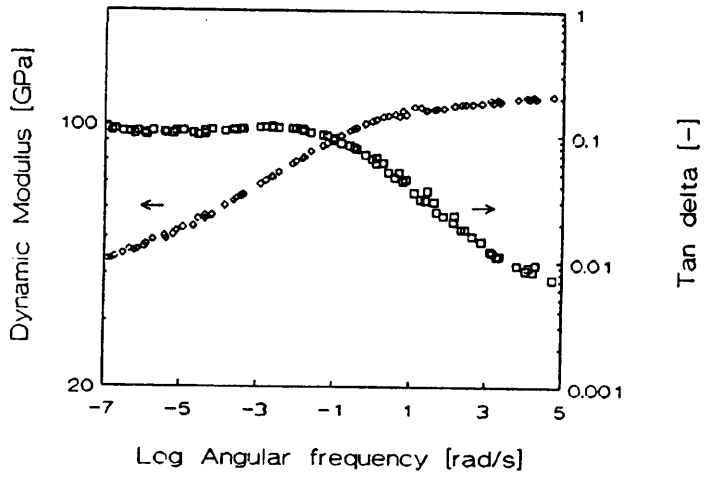

Fig.4.23 Master curves of the dynamic modulus and tan δ vs frequency for a reference temperature of 30°C for Dyneema SK66 by Govaert [94].

the higher modulus Fibres A and C, it is clear that Fibre C is superior in terms of dynamic mechanical properties at high frequency while Fibre A is superior at low frequency.

It is seen that the frequency dispersion of E'' (Fig.4.22) exhibits a quite broad dispersion peak and the profile is not symmetrical with respect to the logarithmic frequency axis. From this observation it can be inferred that although the broad dispersion curves may be expected to consist of two mechanisms (i.e. α and α') [88-92], the direct separation of the E'' into the respective contributions cannot be carried out owing to the lack of adequate data in the lower temperature range. However, the frequency ν can be related to the activation energy empirically by the Arrhenius equation [88]

$$\nu = \nu_o e^{-\Delta H/RT} \qquad (4.13)$$

where ν_0 is the pre-exponential factor and ΔH is the activation energy. Therefore, at the temperatures T_1 and T_2 the dynamic mechanical properties at frequencies ν_1 and ν_2 can be assumed to be related by the equation [88]

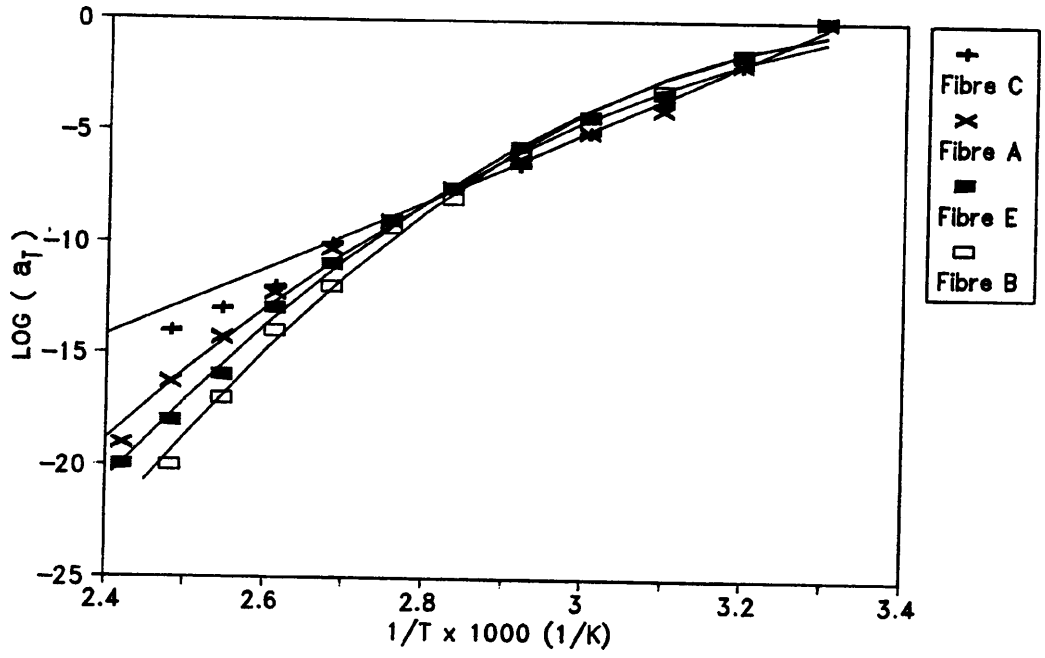

(a)

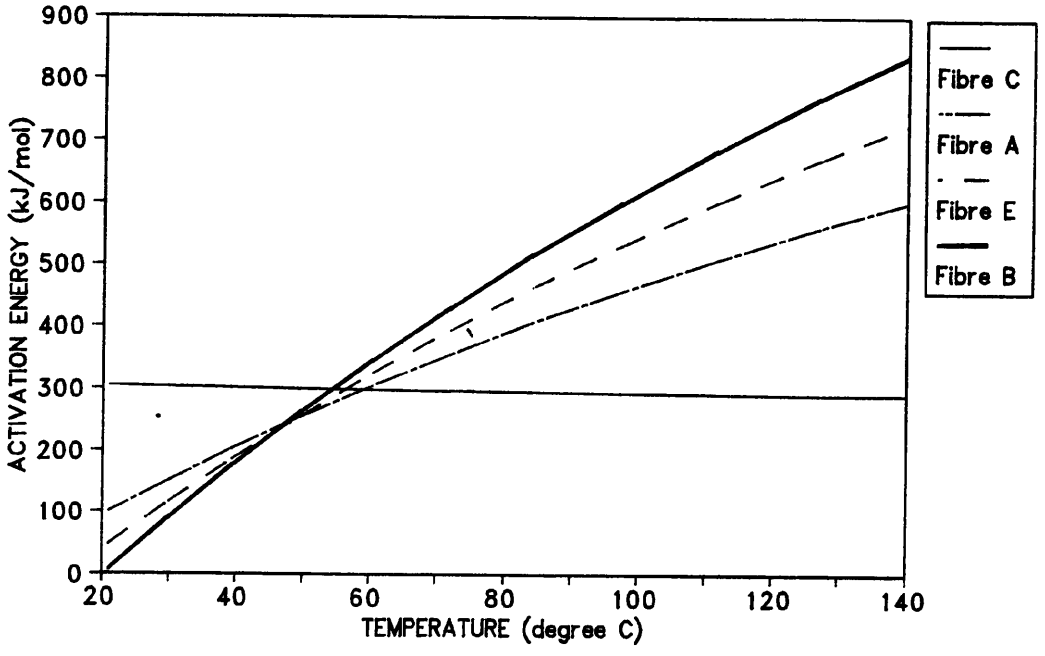

(b)

Fig.4.24 (a) Arrhenius plots of a_T vs reciprocal of temperature, and (b) the apparent activation energy at different temperatures, for various fibres.

$$\frac{\nu_1}{\nu_2} = \frac{e^{-\Delta H/RT_1}}{e^{-\Delta H/RT_2}} \qquad (4.14)$$

i.e.

$$\log \frac{\nu_1}{\nu_2} = \log a_T = \frac{\Delta H}{R}\left(\frac{1}{T_2} - \frac{1}{T_1}\right) \qquad (4.15)$$

The activation energy for the relaxation process can therefore be determined from the plot of log a_T against the reciprocal of the absolute temperature (Arrhenius plot). Fig.4.24a shows the Arrhenius plot of various monofilaments in order to classify the broad dispersion in the master curves (Fig.4.21 and Fig.4.22) into two components. The Arrhenius plot of Fibre C can be represented by a single straight line whereas others show a gradual increase of the apparent activation energy with

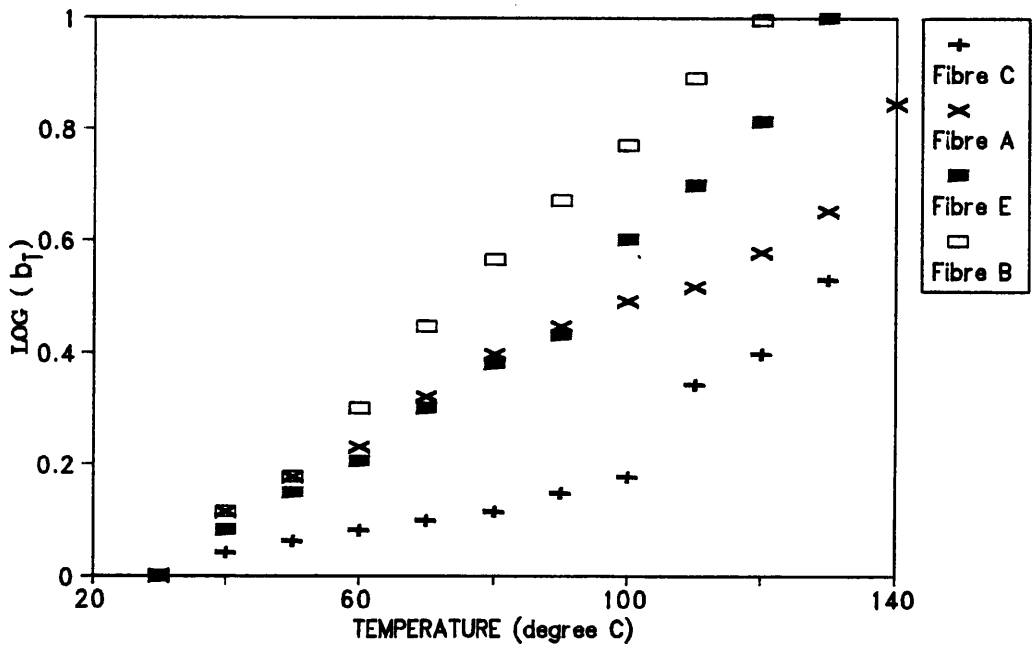

Fig.2.25 The plots of vertical shift factor b_T vs temperature for various fibres.

increasing temperature. For Fibres A, B and E, the apparent activation energy around 30°C is about 100 kJ/mol, but increases gradually with increasing temperature to physically unrealistic values of about 500-700 kJ/mol (Fig.4.24b). Similarly, Govaert [93] also obtained apparent energies of about 100 kJ/mol to 400 kJ/mol for gel-spun Dyneema SK66 at a reference temperature of 30°C with the specimen in the form of yarn. It is therefore impossible to identify exactly the α- and α'-relaxation temperatures. The apparent activation energy of Fibre C is found to be approximately 300 kJ/mol much higher than the literature values for gel-spun UHMW-PE films of about 100-200 kJ/mol [91]. However, it is clear that Fibre C shows a single thermally activated Arrhenius process, different from the other fibres. This is consistent with the result obtained by Matsuo *et al* [91] on gel-spun PE films with the highest draw-ratio. It should be noted that the vertical shift factor b_T used in constructing the master curve for Fibre C is very small and relatively insignificant (Fig.4.25). It appears that Fibre C shows a thermorheologically simple behaviour which deviates markedly from the behaviour of other samples.

4.6 CONCLUDING REMARKS

The measurement of mechanical properties along the fibre direction of the high-performance PE monofilaments presented a unique problem. Special care has to be taken for such a highly anisotropic material since the properties are very dependent on gauge length (Section 4.4.1) and strain rate (Section 4.4.2). They also show complex viscoelastic behaviour upon deformation

(Section 4.4.3) with significant stress relaxation and creep (Section 4.4.4). Consideration of the effect of time dependence adds additional complication in the mechanical behaviour of these monofilaments as demonstrated in the dynamic mechanical testing (Section 4.5.1). It has been demonstrated that reasonable dynamic mechanical data can be obtained from monofilaments of gel-spun PE fibres using the Rheometrics instrument. Reliable values of E^*, E' and E'' can be determined but the values of tan δ are more scattered. Apparently the high-performance PE monofilaments, particularly the gel-spun monofilaments, show no simple mechanical behaviour upon deformation, although they are highly oriented and nearly chain-extended. There are considerable differences in the stress-strain properties between the different gel-spun PE fibres, however, the similarity in the dynamic mechanical behaviour shows that the structure of the fibres differs mainly in degree. The detailed analysis of the viscoelastic relaxations in crystalline region (i.e. α- and α'-relaxations) shows that the higher modulus gel-spun PE monofilaments are apparently thermorheologically simpler in viscoelastic behaviour than lower modulus PE fibres and this is probably due to their higher degree of chain extension.

5

DEFORMATION MICROMECHANICS IN MONOFILAMENTS

5.1 INTRODUCTION

Earlier chapters have shown that gel-spun polyethylene (PE) fibres exhibit high strength and stiffness with highly oriented and highly extended polymer chains. Applying macroscopic strain along such fibres causes strain in the polymer molecules, inducing changes in bond angles and bond lengths. Raman microscopy, in fact, probes inter-chain vibrational motions which depend upon the conformations within each polymer chain. In general, strain results in a shift of Raman bands to lower wavenumbers [9-10] and it is this phenomenon that enables Raman microscopy to be used for the study of molecular deformation.

This chapter is concerned firstly with the molecular response of the PE monofilaments upon different deformations such as simple stretching, cyclic loading, and, stress relaxation and creep (Section 5.4). This is then followed by an attempt to characterize the molecular behaviour and to correlate the strain sensitivity of the Raman bands with the mechanical properties and microstructure of the monofilaments (Section 5.6).

5.2 RAMAN MICROSCOPY AND HIGH-PERFORMANCE POLYMERIC FIBRES

Raman microscopy has been demonstrated to be an important tool for studying the deformation characteristics of high-performance

polymeric fibres on the molecular level [10-23]. It can yield information concerning the relation between microscopic morphology and mechanical properties of the monofilaments. Therefore, it is valuable both for the understanding the properties of the fibres as well as to investigate ways improving them.

5.2.1 Principles of Raman Scattering

When electromagnetic radiation of wavelength λ_0 is passed through a gas, liquid or solid, it may be transmitted, absorbed or scattered. Raman spectroscopy is concerned with the scattering of radiation by vibrating molecules, which undergoes a change in wavelength (Raman scattering). It is named after the Indian scientist C.V. Raman who discovered it experimentally in 1928.

The essential features of Raman scattering can be obtained from consideration of classical electromagnetic theory which provides a useful conceptual model for Raman scattering. However, in the quantum mechanical approach the wave-particle duality of a light beam is incorporated by considering that the beam is composed of packets or quanta of light particles known as photons. Moreover, the quantization of molecular energy levels is taken into account in the approach with a model built around quantized vibrational and electronic energies [104].

5.2.1.1 Classical Electromagnetic Theory

In many respects the treatment of the scattering of light by a molecule is simplified by using classical wave picture for the light [105], expressed mathematically as a cosine function of

frequency and time.

When a molecule is introduced into an electric field of strength E, an electric dipole moment μ is induced in the molecule. If α is the polarizability of the molecule, the magnitude of the induced dipole is given by:

$$\mu = \alpha E \tag{5.1}$$

When electromagnetic radiation of frequency ν_0 falls on the molecule it introduces a varying electric field, which we express in terms of its amplitude E_0 and a time-dependent term:

$$\mu = \alpha E_0 \cos(2\pi\nu_0 t) \tag{5.2}$$

For a vibrating molecule, the molecular polarizability α will also vary with time. For very small vibrational amplitudes the polarizability of the molecule is related to the vibrational coordinates Q (which is a suitable internal coordinate chosen to represent the difference in displacements of the nuclei from their equilibrium positions) by the relation:

$$\alpha = \alpha_0 + \left(\frac{\partial\alpha}{\partial Q}\right)_0 Q \tag{5.3}$$

α_0 is the polarizability at the equilibrium configuration of the molecule, and $(\partial\alpha/\partial Q)_0$ refers to the rate of change of polarizability with bond length, evaluated at the equilibrium configuration.

Finally, since the molecule is vibrating with frequency ν_{vib}, the displacement Q is itself a function of time:

$$Q = Q_0 \cos(2\pi\nu_{vib} t) \tag{5.4}$$

where Q_0 is the coordinate of the initial position, taken as the maximum displacement from the equilibrium bond length.

By combining Equations (5.2), (5.3) and (5.4), and using a trigonometric identity, we obtain the expression

$$\mu = \alpha_0 E_0 \cos(2\pi\nu_0 t) + \left(\frac{\partial\alpha}{\partial Q}\right)_0 \frac{Q_0 E_0}{2}[\cos 2\pi(\nu_0 - \nu_{vib})t + \cos 2\pi(\nu_0 + \nu_{vib})t] \quad (5.5)$$

From Equation (5.5), the induced dipole moment μ varies with component frequencies ν_0, $(\nu_0 - \nu_{vib})$ and $(\nu_0 + \nu_{vib})$ which correspond to Rayleigh scattering, Stokes and anti-Stokes Raman scattering, respectively.

5.2.1.2 Quantum Mechanical Approach

The physical origin of Raman scattering lies in inelastic collisions between the photons and molecules. An inelastic collision means that there is an exchange of energy between the photon and the molecule with a consequent change in energy, and hence wavelength, of the photon.

Let ν_0 and ν'_0 be the frequencies of the incident and the scattered photons respectively, and E_a and E_b be the energies of the molecule before and after it scatters the photon. From the conservation of energy principle,

$$h\nu_0 + E_a = h\nu'_0 + E_b \quad (5.6)$$

where h is Planck's constant. The Equation (5.6) can be simplified to

$$\Delta E = E_b - E_a = -h(\nu'_0 - \nu_0) = -h\Delta\nu \quad (5.7)$$

The energy difference ΔE is the difference between two molecular energy levels and measurement of the Raman shift $\Delta\nu$ gives the

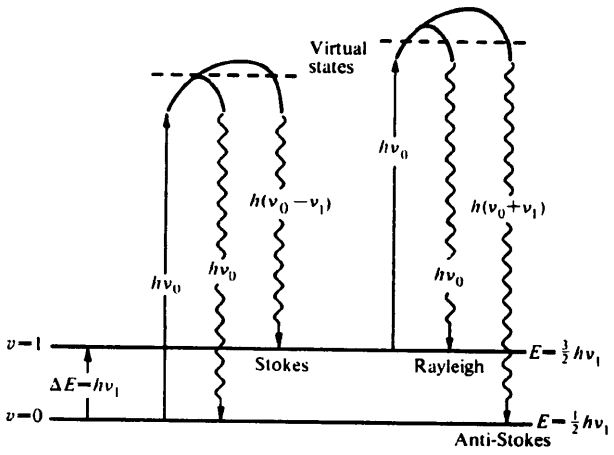

Fig.5.1 Vibrational Raman transitions [105].

molecular energy level spacings. In other words, by monitoring the inelastically scattered photons we can probe the molecular vibrations.

In the quantum mechanical model [104], light scattering is depicted as a two-photon process. The first step in this process is the combination of a photon and a molecule to raise the molecule to a higher virtual energy state (which is not a stationary energy state) of extremely short lifetime. This transition is depicted by the upward-pointing arrows in Fig.5.1 and this higher energy state may or may not correspond to the quantized energy state of the molecule. The second step, indicated by the downward-pointing arrows, involves the release of a photon after a very short time interval ($<10^{-11}$ s) and the energy of this second photon is given by the length of the downward-pointing arrows. In Rayleigh scattering, the energy of the photon $h\nu_0$ remains unchanged, whereas in Raman scattering it decreases or increases by an amount $h\nu_1$ producing Stokes and

anti-Stokes lines respectively. At ordinary temperatures most of the molecules are in the ground state and therefore Stokes lines have greater intensities than anti-Stokes lines which originate from an excited level with a lower population [105].

5.2.2 Experimental Raman Microscopy of Monofilaments

A major problem in the collection of good Raman spectra is the extreme weakness of the effect. The appearance of laser source in the 1960s, however, revitalized Raman spectroscopy into its present prominent position.

In a standard Raman spectrometer, intense monochromatic radiation provided by a laser is directed onto the sample. Some of the resulting scattered light is gathered by collecting optics and directed to a double monochromator which is designed to disperse and to separate spatially the scattered light on the basis of frequency. A double monochromator is essentially two monochromators connected in series and they are ideal for detecting the weak Raman scattering. The volume of sample illuminated by the laser and viewed by a standard spectrometer is about 100 x 50 μm which is not significant for micro-sampling. Coupling of a microscope attachment to the monochromator, however, enables the laser radiation to be focused on the sample through the microscope objective with a 2 μm diameter spot. It allows Raman microscopy to be used for micromechanical studies and also identifying the distribution of phases in a sample.

Fig.5.2 shows a schematic diagram of the Raman microscope system used for the micromechanical study of monofilaments. It is based on a SPEX 1403 double monochromator connected to a

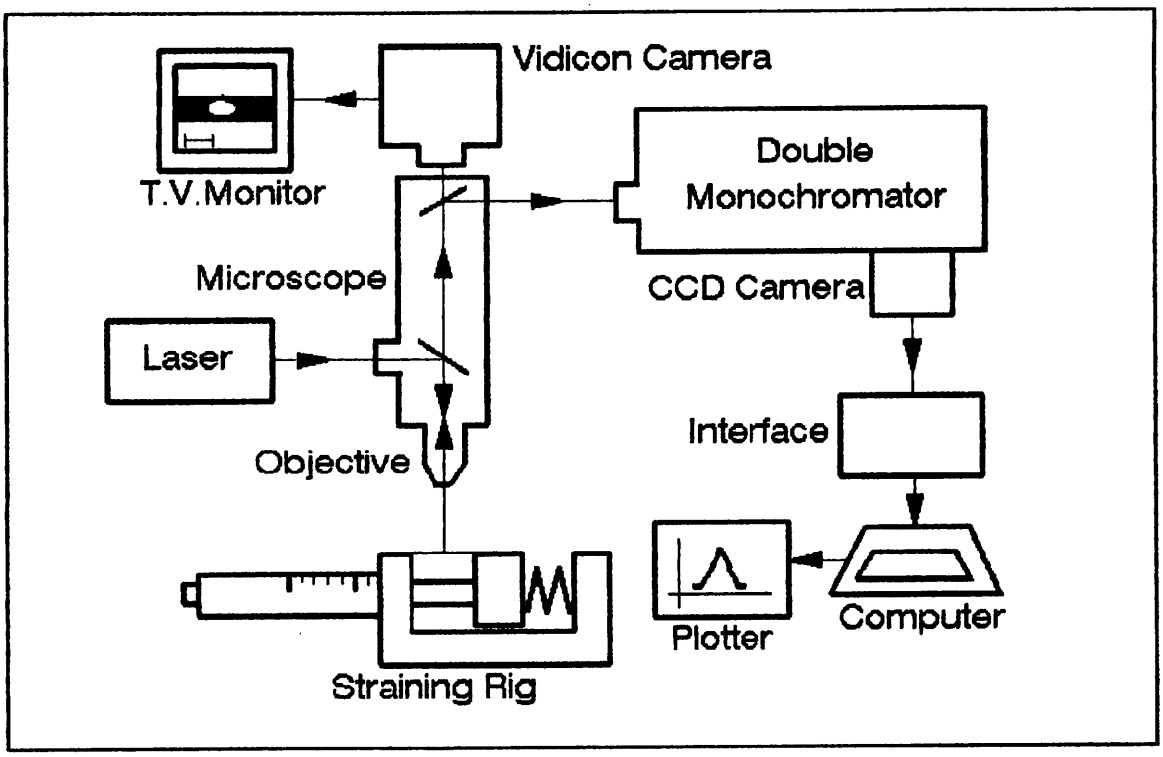

Fig.5.2 Schematic diagram of the Raman microscope system.

modified Nikon optical microscope with a x40 objective lens and a numerical aperture of 0.65. An image of the sample can be seen on a T.V. monitor by using a vidicon camera which makes focusing easier. A liquid-nitrogen cooled charge coupled device (CCD) camera is used for light detection and it is linked by an interface to AT1 computer system which enables camera readout operations, displays data in graphical and carries out data processing. The silicon based CCD detector has proven to be very effective for low-light level detection with low readout noise [106].

5.2.3 Raman Microscopy of High-Performance Polymeric Fibres

Raman microscopy has been used to follow the deformation of high-performance polymeric fibres, such as substituted polydiacetylene

[9-11], aramids [13-15] and poly(*p*-phenylene benzobisthiazole), PBT [16-17]. The relationship between the Raman active band frequency (Raman shift, $\Delta\nu$) and tensile strain (e) is obtained by loading a monofilament on a purpose-made straining rig placed on the stage of the Raman microscope system (Fig.5.2). The Raman spectra are taken along the fibre length at different levels of strain and it has been found that there are changes of band frequency which depends on the material, the modulus of the sample and the bond being studied [11,13-17].

Early work by Batchelder *et al* [10] was centred on substituted polydiacetylene single crystal whiskers such as polymerised single crystal of bis(*p*-toluene sulphonate) of 2,4-hexadiyne-1,6-diol (polyTSHD). This single crystal polymer shows large changes to lower frequency of the Raman band for the triple bond on the polymer backbone (at 2083 cm^{-1}) when stressed. There is linear dependence of the frequency on strain up to 2% (Fig.5.3) and the shift is thought to be related to the

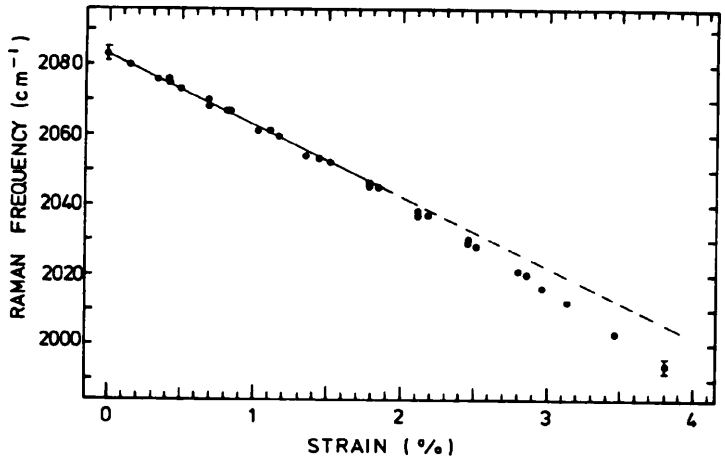

Fig.5.3 The dependence of Raman frequency 2083 cm^{-1} of polyTSHD on strain. The solid line is a least-square fit to the data below 2% strain [10].

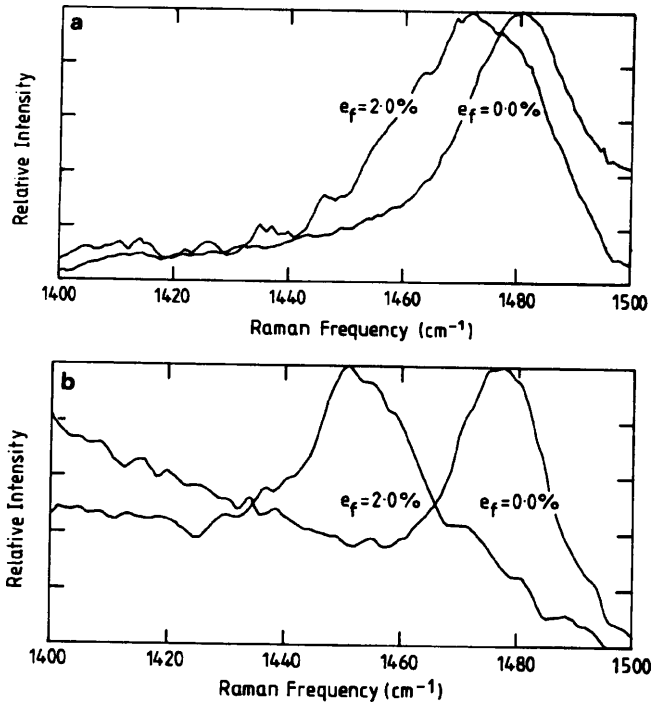

Fig.5.4 Raman spectra of the 1480 cm^{-1} band for the (a) as-spun and (b) heat-treated PBT fibres obtained at fibre strains of 0% and 2% [17].

distortion of the backbone covalent bonds produced by macroscopic deformation.

Detail studies by Young *et al* on other high-performance polymeric fibres such as aramids [13-15] and poly(*p*-phenylene benzobisthiazole), PBT [16-17] fibres has demonstrated similar changes in vibrational frequencies of the backbone polymer in Raman spectra upon deformation. However, the sensitivity of the Raman bands to strain is affected by the structure of fibres. Fig.5.4 shows that heat-treated PBT fibres with improved mechanical properties and structural order have a higher sensitivity than for as-spun fibres for the heterocyclic ring stretching band (1480 cm^{-1}) [17]. This is an indication that the molecular bonds in a better-oriented structure are subjected to higher stresses at a given level of strain. Similar behaviour has

Table 5.1

STRAIN DEPENDENCE OF THE MAIN RAMAN BANDS IN VARIOUS HIGH-PERFORMANCE POLYMERIC FIBRES

Fibre	Raman Band (cm^{-1})	$d\Delta\nu/d\varepsilon$ ($cm^{-1}/\%$)	Reference
PolyTSHD	2083	-20.3 ± 0.5	9
Kevlar 49	1613	-4.4 ± 0.2	12
As-spun PBT	1480	-8.3 ± 1.0	16
Heat-treated PBT	1480	-12.1 ± 0.6	16

in fact been found for aramid fibres with different levels of modulus [14]. Table 5.1 shows the sensitivity ($d\Delta\nu/d\varepsilon$) of the main strain-dependent Raman bands of various high-performance polymeric fibres.

Well-defined Raman spectra can also be obtained for the study of molecular deformation from high-performance fibres made from flexible molecules such as PE fibres [18-22]. Prasad *et al* [19] have shown that the peak positions of both the C-C symmetric (1127 cm^{-1}) and asymmetric (1059 cm^{-1}) stretching band of Spectra gel-spun ultra-high molecular-weight PE (UHMW-PE) fibres shifted linearly to lower frequency at low stresses. They also found significant band broadening with the appearance of a low frequency tail at higher stresses. They interpreted this as being due to non-crystalline overstressed tie molecules because they did not observe similar tail in their WAXS peaks for the (002) meridional reflection of monofilaments [107]. In contrast, Kip *et al* [20] studied the molecular deformation of gel-spun UHMW-PE by Raman microscopy and found that both asymmetric (1059 cm^{-1}) and symmetric (1127 cm^{-1}) C-C stretching modes demonstrated well-defined band splitting and a bi-modal load distribution (with low-load and high-load bearing C-C bonds) upon stretching. They

analyzed these two components by fitting the peaks in the Raman spectra to two Gaussian curves and this enabled them to study the different behaviour of each component upon deformation. Continuing the work on gel-spun UHMW-PE fibres, Kip *et al* [21] and Grubb *et al* [22] have demonstrated that an intense high-load bearing Raman peak could be obtained for both the asymmetric (1059 cm^{-1}) and symmetric (1127 cm^{-1}) C-C stretching modes at low temperature (<240K) which was intended to cause the stress relaxation to be suppressed. According to them, both components in the fibre structure are crystalline with one of them inefficiently coupled to the applied stress and carrying little load upon straining.

The Raman microscopic study of high-performance polymeric fibres is not restricted to the molecular deformation of [illegible] monofilaments. Using Raman microscopy, Young *et al* [12,108-111] have demonstrated stress transfer within the interface of the single-fibre model composite for various high-performance fibres. In fact Kip *et al* [112] have successfully carried out a similar study (pull-out tests) on gel-spun UHMW-PE fibre in composites which have a relatively weak Raman scattering compared with polydiacetylenes [12,108] or Kevlar [111].

5.3 EXPERIMENTAL

All the PE fibres in this work (Table 3.1) were used for the Raman microscopic work in order to obtain more detailed information on their structure/property relationships. However, only Fibre A was tested in cyclic loading and Fibres A, B and C were used for the stress relaxation and creep tests. Both Fibres

A and C are gel-spun UHMW-PE fibres while Fibre B is melt-spun conventional PE fibre.

5.3.1 Raman Experiments

Raman spectra were obtained from individual PE monofilaments using the Raman microscope system (Fig.5.2) at a resolution of the order of ± 5 cm^{-1} with the 488.0 nm line of a 15 mW Argon ion laser (Section 5.2.2). The laser beam was focused to a spot ~2 μm where the power was about 1.5 mW. It was then polarized parallel to the fibre axis with the exposure time of 50 seconds for all measurements.

Individual monofilaments were mounted across a hole on paper card using the Ciba-Geigy HY/LY two-part solvent-free cold-setting epoxy resin. The card was then mounted onto the aluminium

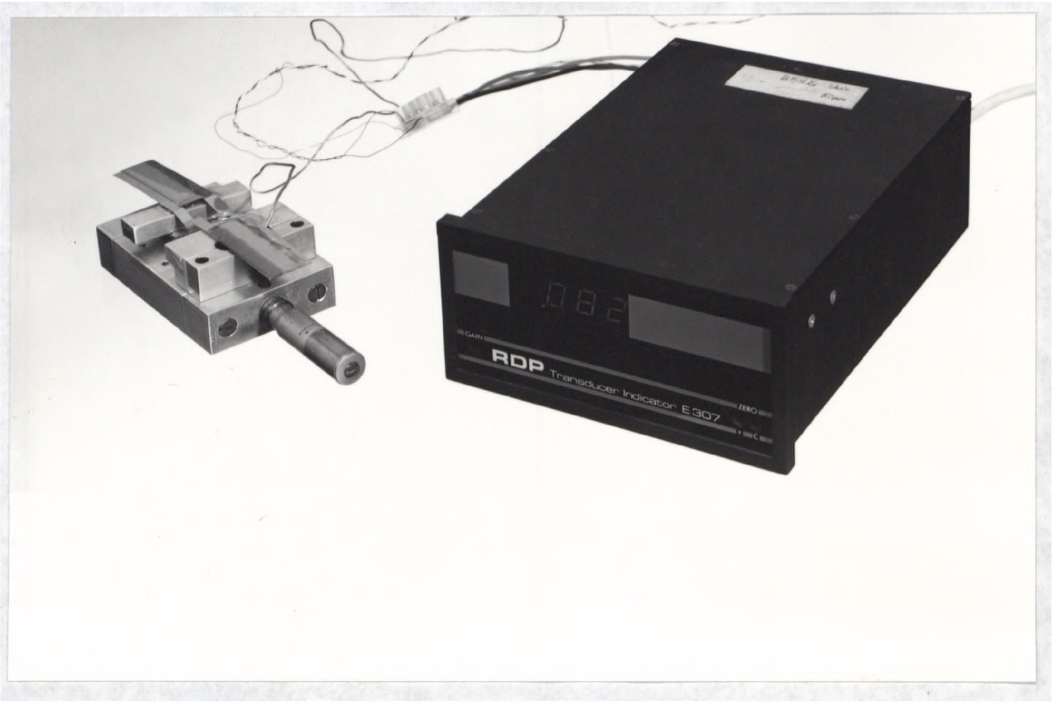

Fig.5.5 The straining rig with the PE monofilament attached onto the aluminium blocks and card edges cut.

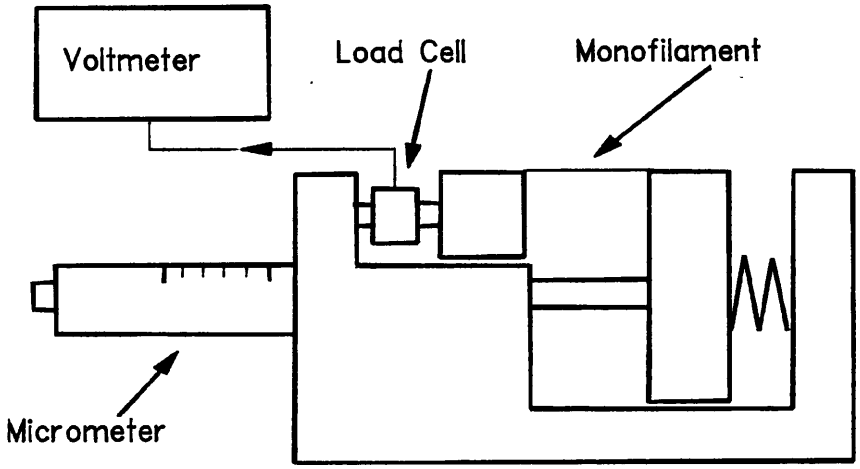

Fig.5.6 Schematic diagram of the straining rig with the attachment of 5N load cell.

blocks of the straining rig and the card edges were cut (Fig.5.5). The straining rig was equipped with a 5N load cell (Fig.5.6) and was fitted directly onto the microscope stage. The gauge length was measured accurately using the optical microscope and the stage micrometer.

The monofilament was stretched by displacing the blocks using the micrometer attachment. The displacement was applied in a stair-case fashion consisting of incremental steps as shown in Fig.5.7a. Each step required 60 s with 10 s for the focusing before the actual exposure. The Raman spectra were measured in the plateau region of the load response to minimize the inconsistency of load due to stress relaxation. By assuming the time required for applying each step is negligible, the effective strain rate could be defined as

$$\left(\frac{\delta l}{l}\right)\cdot\left(\frac{1}{\delta t}\right) \qquad (5.8)$$

where δl and δt are the applied displacement and the time of

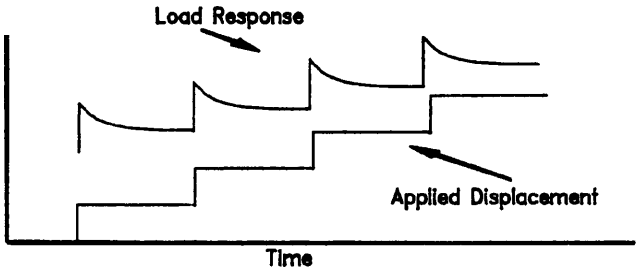

(a)

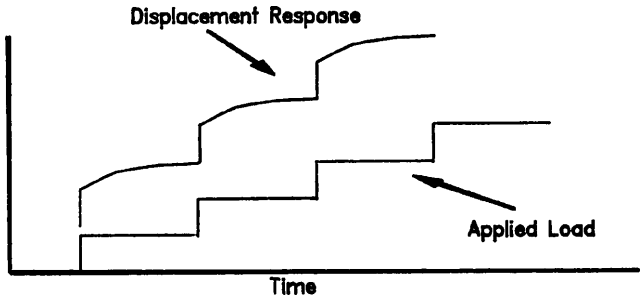

(b)

Fig.5.7 The applied (a) displacement, and (b) load during stretching of a monofilament with different load and displacement responses respectively.

individual step respectively, and l is the gauge length. Four different initial gauge lengths of 10.0, 15.0, 20.0 and 25.0 mm (at a constant strain rate of 1.33×10^{-4} s^{-1}) were employed and six different strain rates of 0.56×10^{-4}, 1.04×10^{-4}, 1.33×10^{-4}, 1.6×10^{-4}, 1.84×10^{-4} and 2.16×10^{-4} s^{-1} (at a constant gauge length of 25.0 mm) were applied. Additionally, cyclic loading to constant strain (at gauge length of 25.0 mm and constant strain rate of 1.33×10^{-4} s^{-1}) and stress relaxation at constant displacement were carried out

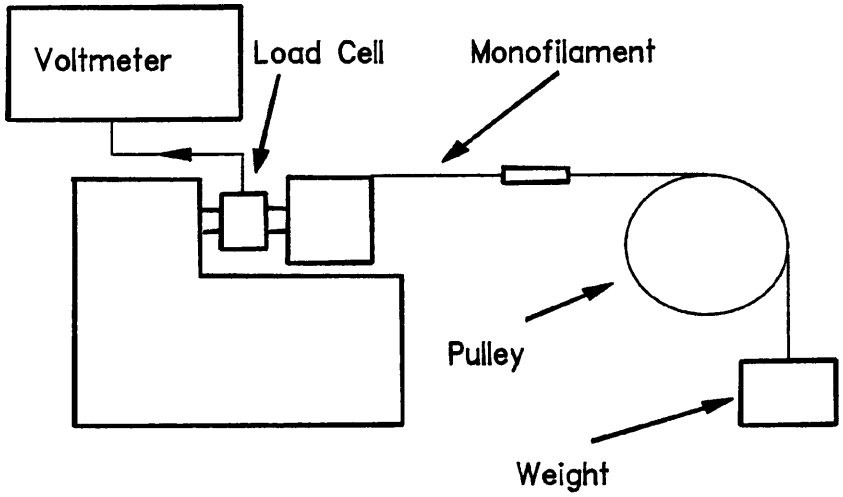

Fig.5.8 Schematic diagram of the rig arrangement in stressing a monofilament.

with the same straining rig. For stress relaxation, a series of scans were carried out to obtain Raman spectra over a period of time.

For stressing, the monofilament was attached to a rig with different arrangement as illustrated in Fig.5.8. A stair-case input (Fig.5.7b) was applied to the monofilament by adding weights of the same size after every scan. The weight size was 6-10 g depended on the diameter of the monofilaments in order to obtain a constant stress step. Similarly, different gauge lengths of 10.0, 15.0, 20.0 and 25.0 mm (at constant stress rate of 0.17 GPa/min) were employed and different stress rates i.e. 0.17, 0.36 and 0.53 GPa/min (at constant gauge length of 25.0 mm) were applied. The same rig arrangement was used for the creep test with the monofilaments subjected to constant load. Again, a series of scans were carried out during the creep test. In all the experiments, the Raman spectra were recorded at 25 ± 3°C.

5.3.2 Data Analysis and Curve Fitting

The experimental data were obtained from analyzing the behaviour of the symmetric C-C stretching bands (1128 cm^{-1}) which are found to be influenced directly by the tensile stress. A non-linear least squares fitting routine based on Levenberg-Marquardt algorithm was used to analyze the Raman data. A quadratic baseline was drawn on the spectra and the vibrational band of the subtracted data set was fitted to two Gaussian curves corresponding to both low-load and high-load bearing C-C bonds as shown by Kip *et al* [20]. In fact, fitting to two Gaussian curves gives the lowest Chi-squared value which is a measure of distances of the data points from the fitted curve. Equation (5.9) represents the Gaussian function $G(x)$:-

$$G(x) = i \exp\left[-\left(\frac{x-p}{w}\right)^2\right] \qquad (5.9)$$

where p is the peak position, i is the peak intensity and w is the full width at half maximum height. These three parameters were optimized for each band during analysis. Knowing these parameters, the area of both low-load and high-load bearing Raman peaks could be determined by integrating the corresponding Gaussian curves.

5.4 STRESS DISTRIBUTION AND MOLECULAR DEFORMATION

Raman spectra of the monofilaments of Fibre A at the range of 1000-1600 cm^{-1} and 2400-3000 cm^{-1} were recorded as shown in Fig.5.9. The interpretation of peak positions [113] is tabulated in Table 5.2. Both the asymmetric C-C stretching band (1060 cm^{-1}) and the symmetric C-C stretching band (1128 cm^{-1}) are usually

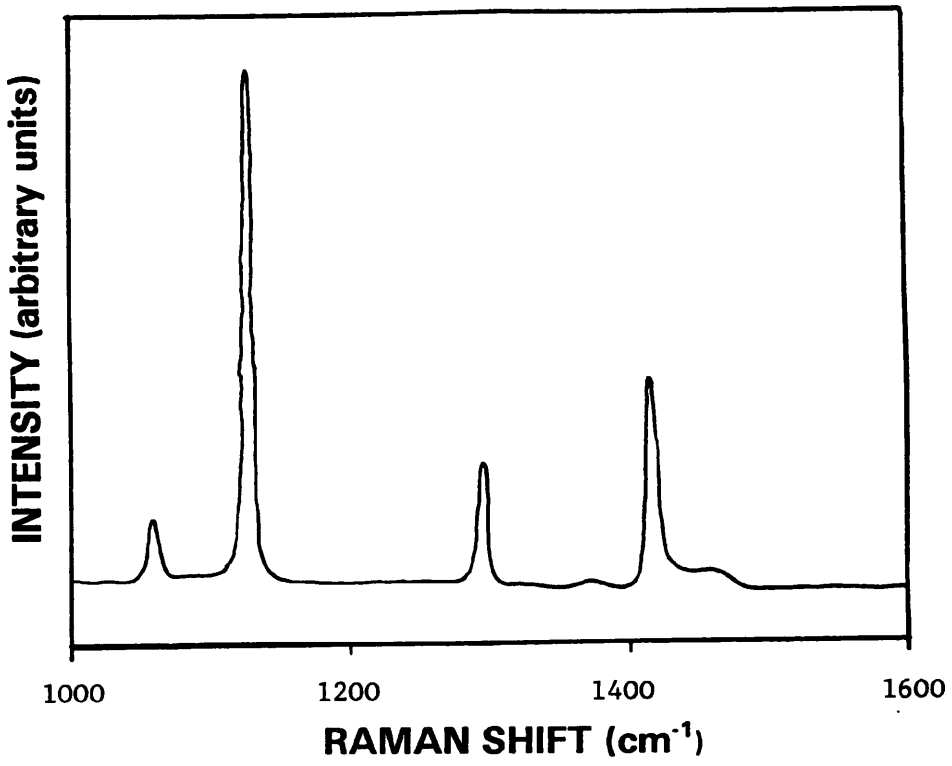

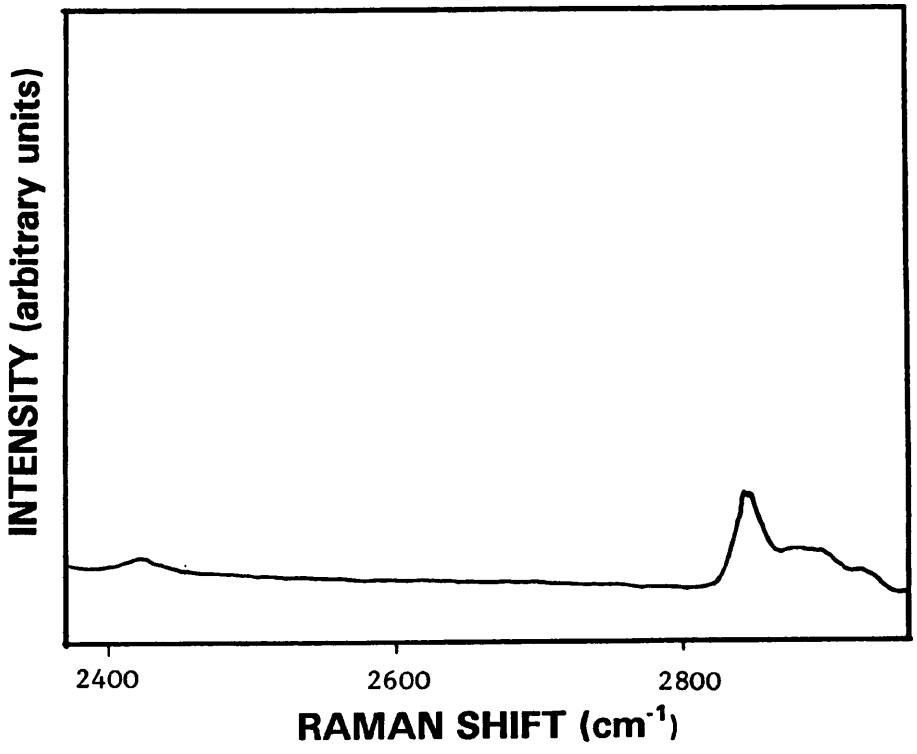

Fig.5.9 Raman spectra of the monofilaments of Fibre A at the range of 1000-1600 cm^{-1} and 2400-3000 cm^{-1}.

Table 5.2

INTERPRETATION OF PEAK POSITIONS IN RAMAN SPECTRA OF PE [113].

Wavenumber (cm^{-1})	Interpretation
1060	C-C asymmetric stretching
1127	C-C symmetric stretching
1295	CH_2 twisting
1418	CH_2 bend
2848	CH_2 symmetric stretch
2883	CH_2 asymmetric stretch

chosen for detailed study because, according to Prasad *et al* [19], they show the largest peak shifts per unit stress ($d\Delta\nu/d\sigma$). Peaks such as the 1295 cm^{-1} are sharp and well separated from all others but shift very little under stress. In this work, however, only the symmetric C-C stretching band (~1128 cm^{-1}) was used due to its high intensity compared with others.

The Raman spectra of the symmetric C-C stretching mode for the monofilaments of Fibres A, B and C are shown in Fig.5.10, Fig.5.11 and Fig.5.12, respectively, together with their spectra after deforming to various strains. The bi-modal stress distribution, resulting in band splitting, can be clearly seen which is consistent with the observation by Kip *et al* [20] for both asymmetric and symmetric C-C stretching bands. The spectra in the range from 1080 cm^{-1} to 1155 cm^{-1} can all be fitted with a linear background to one narrow and one broad Gaussian curves which correspond to both the low-load and high-load bearing C-C bonds as illustrated in Fig.5.13 for Fibre A. Fig.5.14 shows the typical Raman shift/strain curves for both the high-load and low-load bearing bands for Fibre A at a strain rate of 1.33×10^{-4} s^{-1}

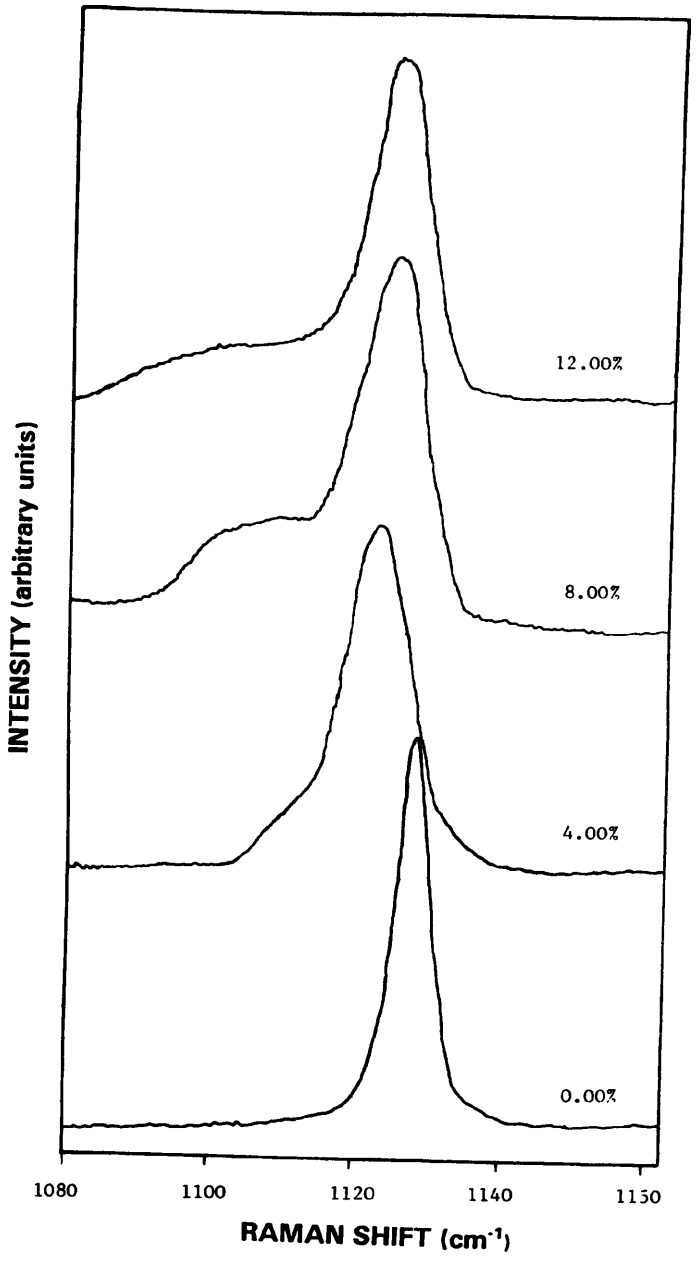

Fig.5.10 The Raman spectra of the symmetric C-C stretching mode of the monofilaments of Fibre A upon deformation at various strains.

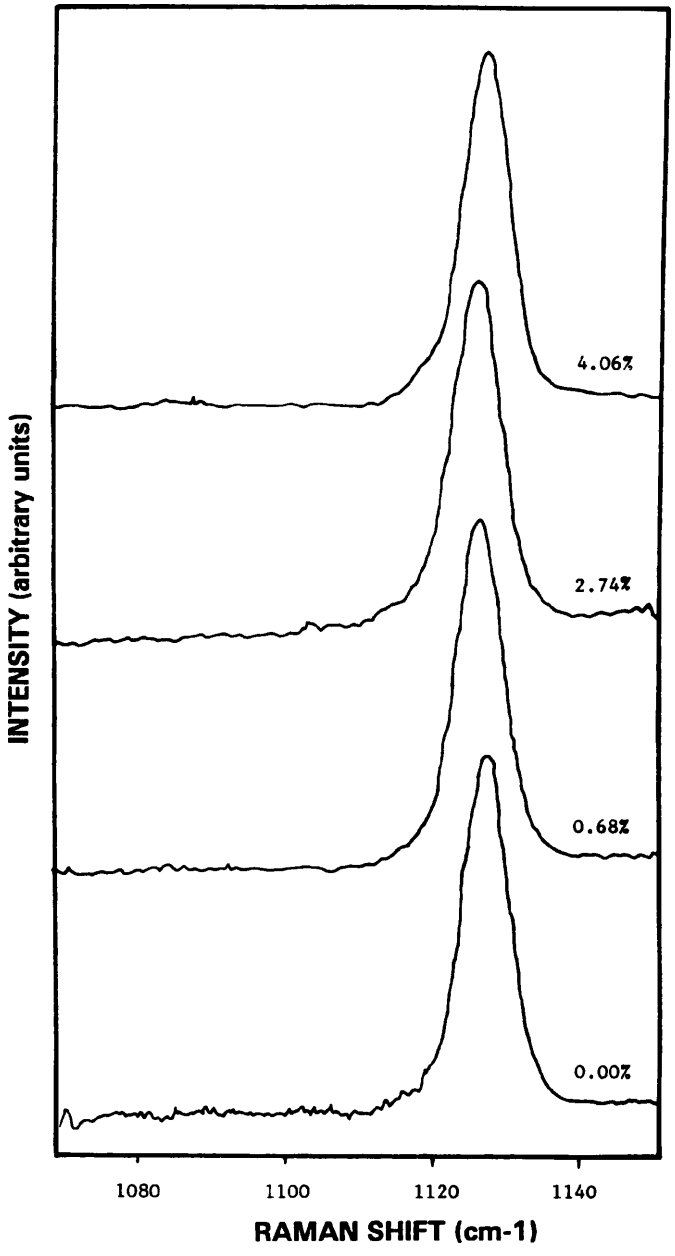

Fig.5.11 The Raman spectra of the symmetric C-C stretching mode of the monofilaments of Fibre B upon deformation at various strains.

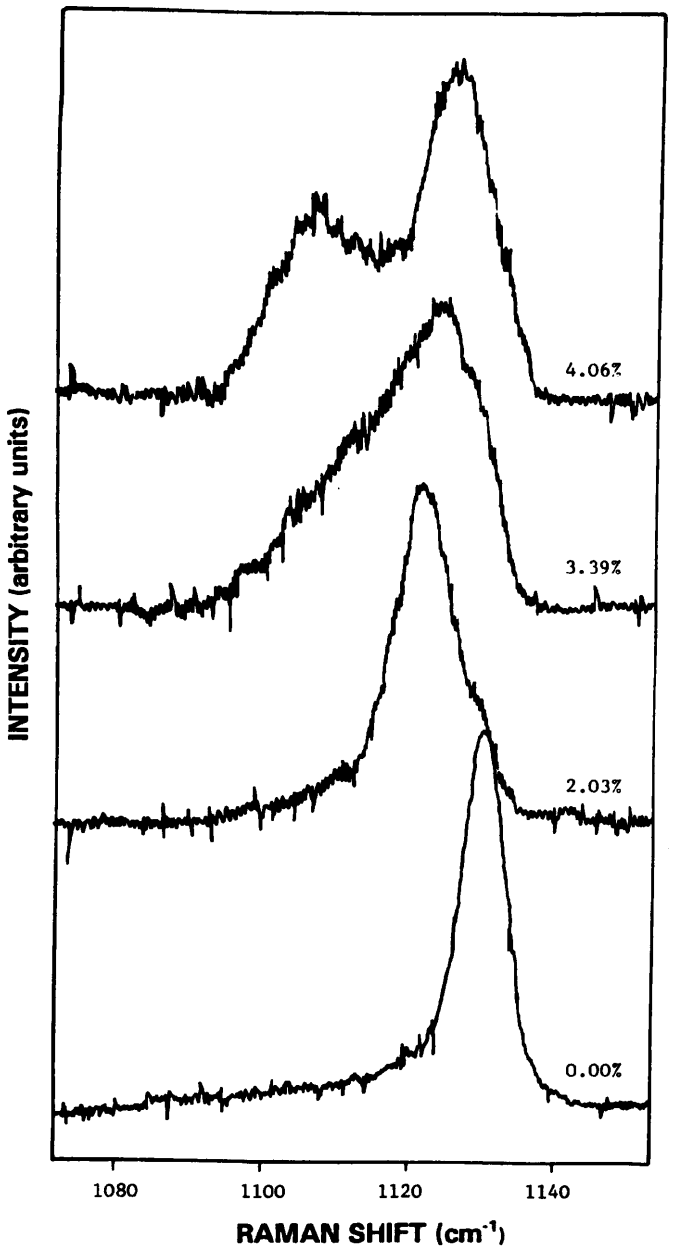

Fig.5.12 The Raman spectra of the symmetric C-C stretching mode for the monofilaments of Fibre C upon deformation at various strains.

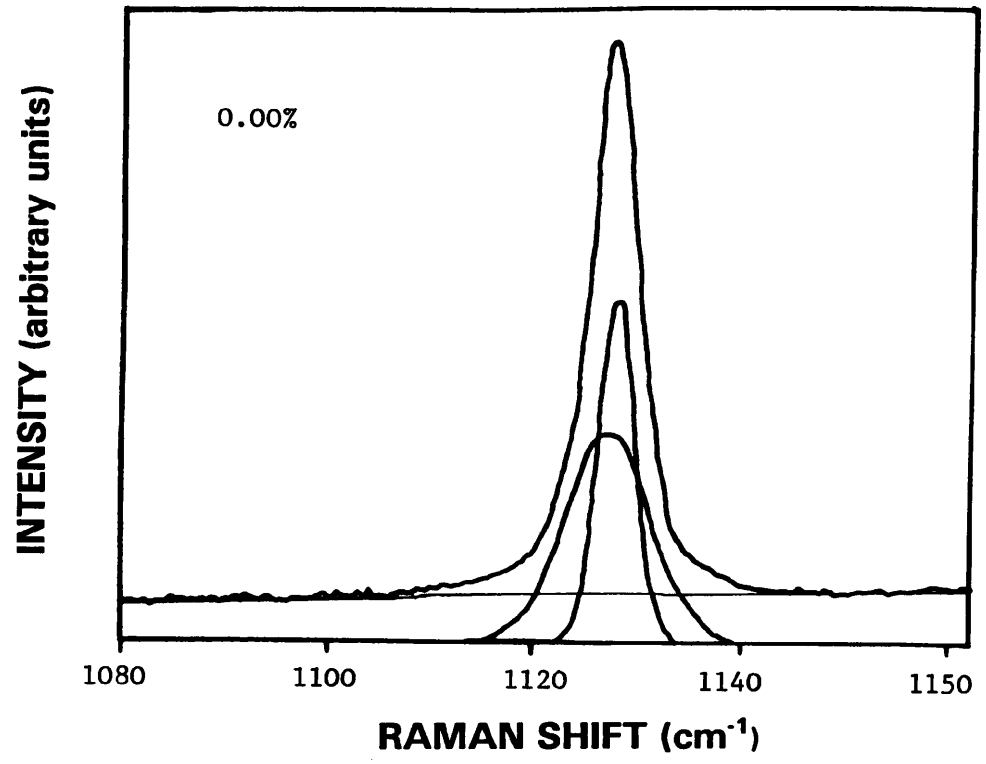

(a)

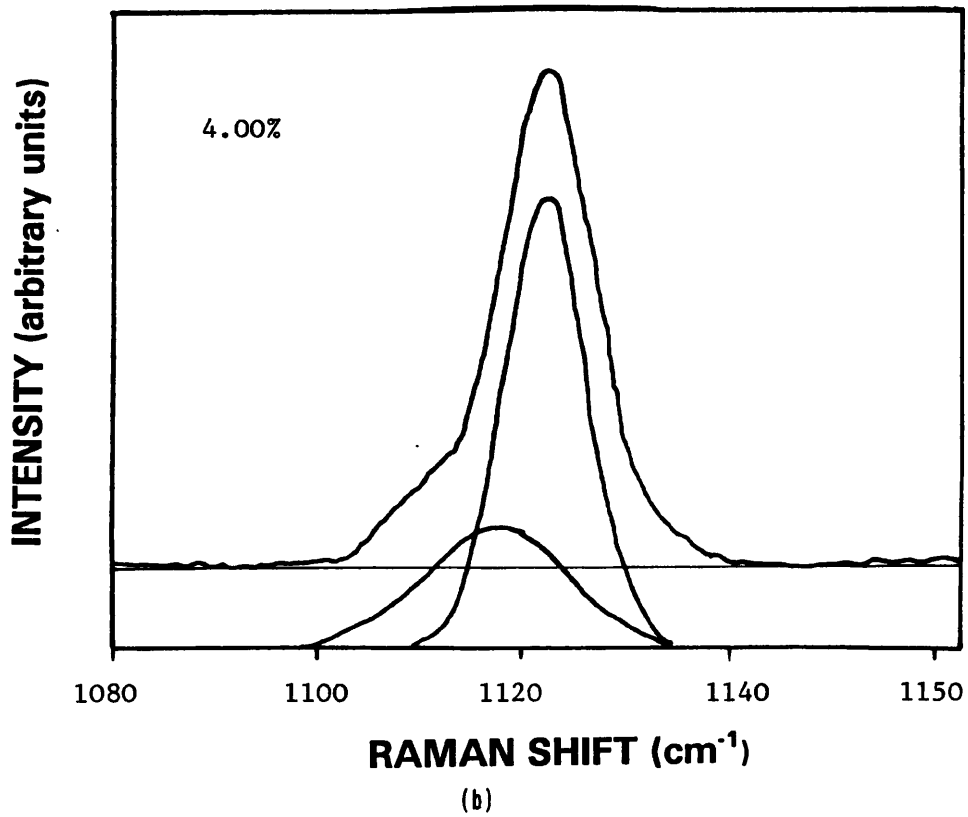

(b)

Fig.5.13 Raman spectra of the symmetric C-C stretching mode for the monofilaments of Fibre A at (a) 0.0%, and (b) 4.0% strains together with fitted Gaussian curves.

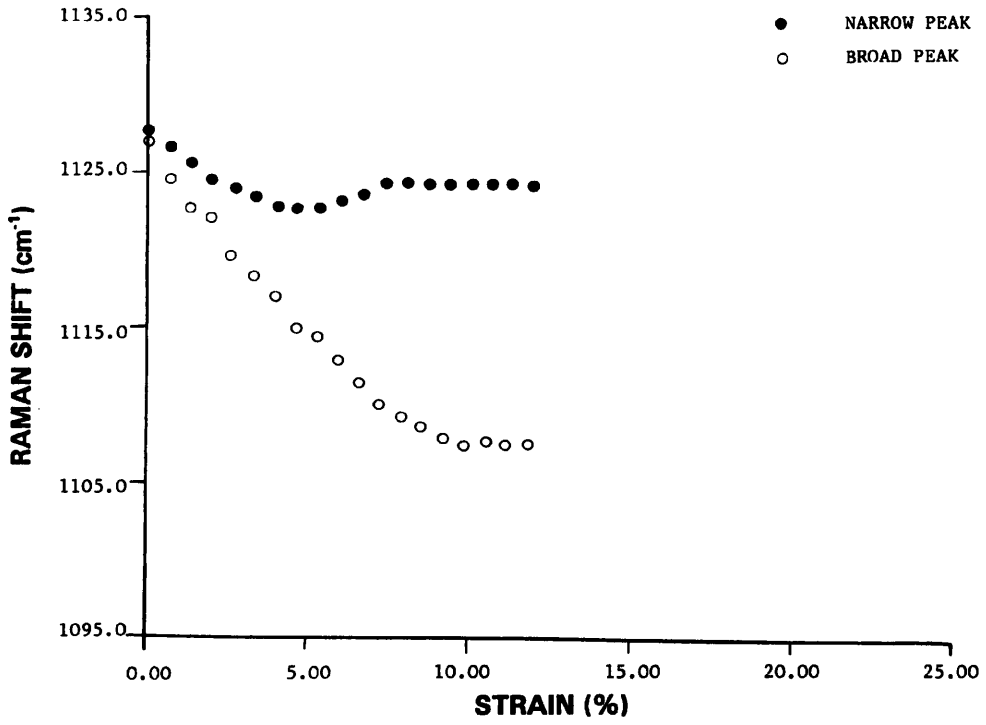

Fig.5.14 Raman shift vs strain curves of the monofilaments of Fibre A at strain rate of 1.33×10^{-4} s^{-1} and gauge length of 25.0 mm.

and a gauge length of 25.0 mm. Assuming a linear relation between shift and molecular strain, which is justified for a small strain (<2.0%), the observed change in peak position can be expressed in terms of a rate of shift ($d\Delta\nu/d\varepsilon$) in $cm^{-1}/\%$. The values of $d\Delta\nu/d\varepsilon$ of the low-load (narrow) and high-load (broad) bearing bands are 1.4 $cm^{-1}/\%$ and 2.3 $cm^{-1}/\%$ respectively and it can be seen that the high-load bearing band shifts to a greater extent than the low-load bearing band upon straining the monofilament.

5.4.1 Effect of Testing Parameters

It should be pointed out that end effects similar to those found

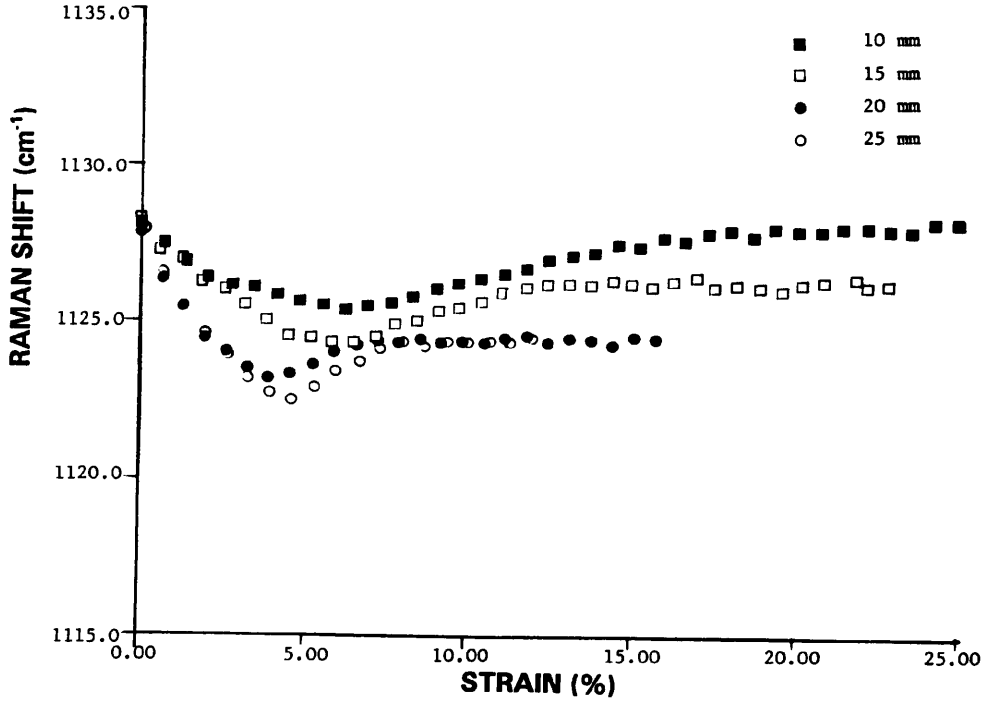

(a)

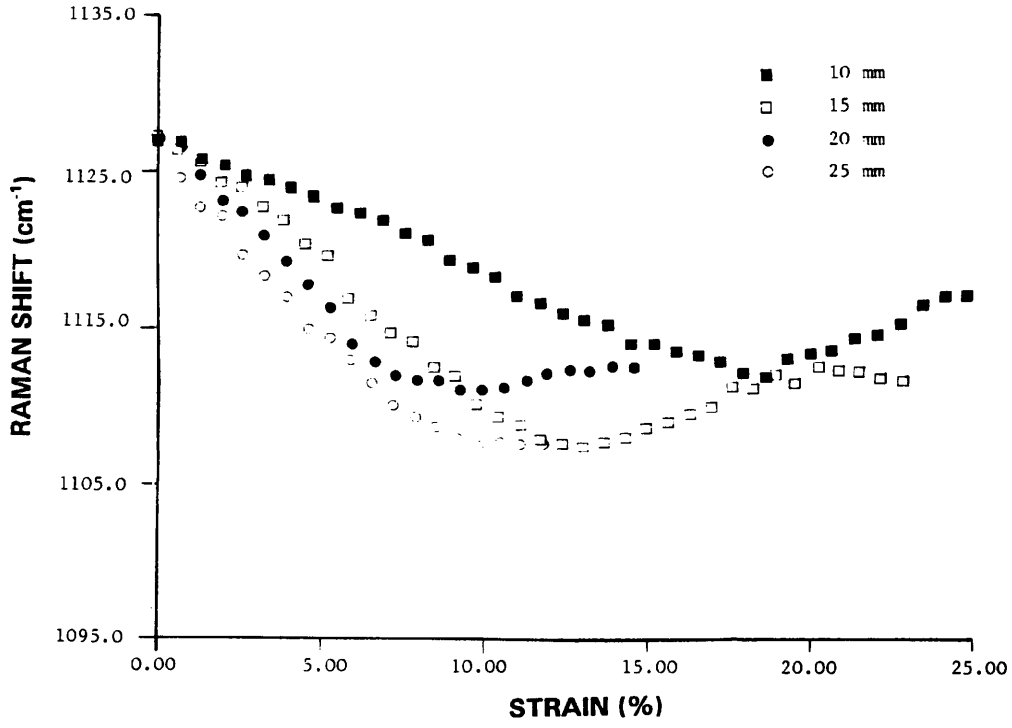

(b)

Fig.5.15 Raman shift vs strain curves of (a) narrow, and (b) broad peaks of the monofilaments of Fibre A at different gauge lengths and constant strain rate of 1.33×10^{-4} s^{-1}.

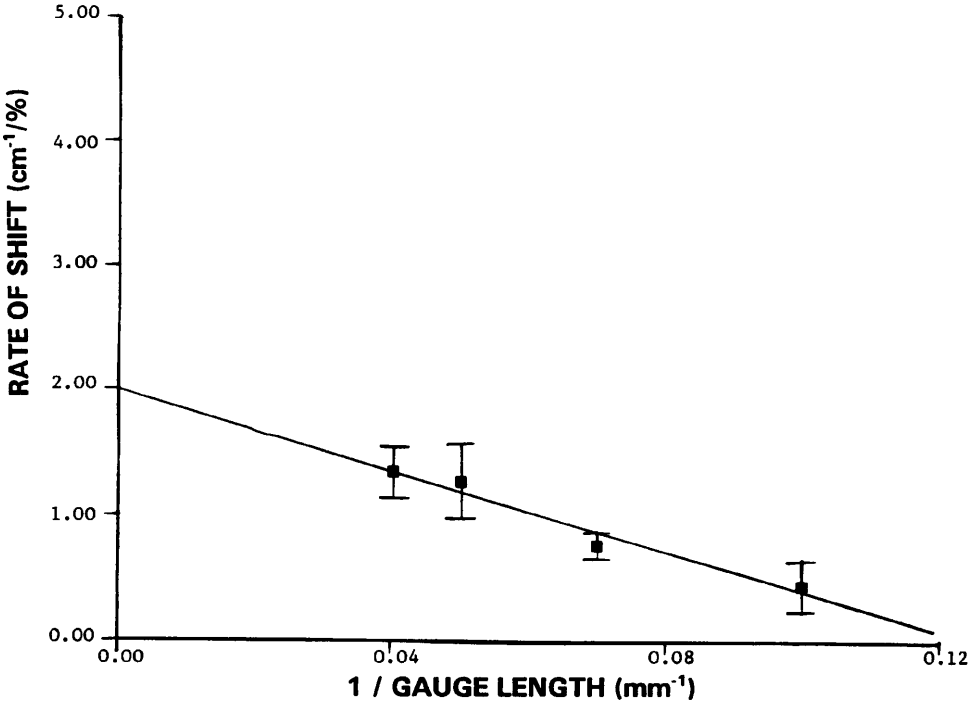

(a)

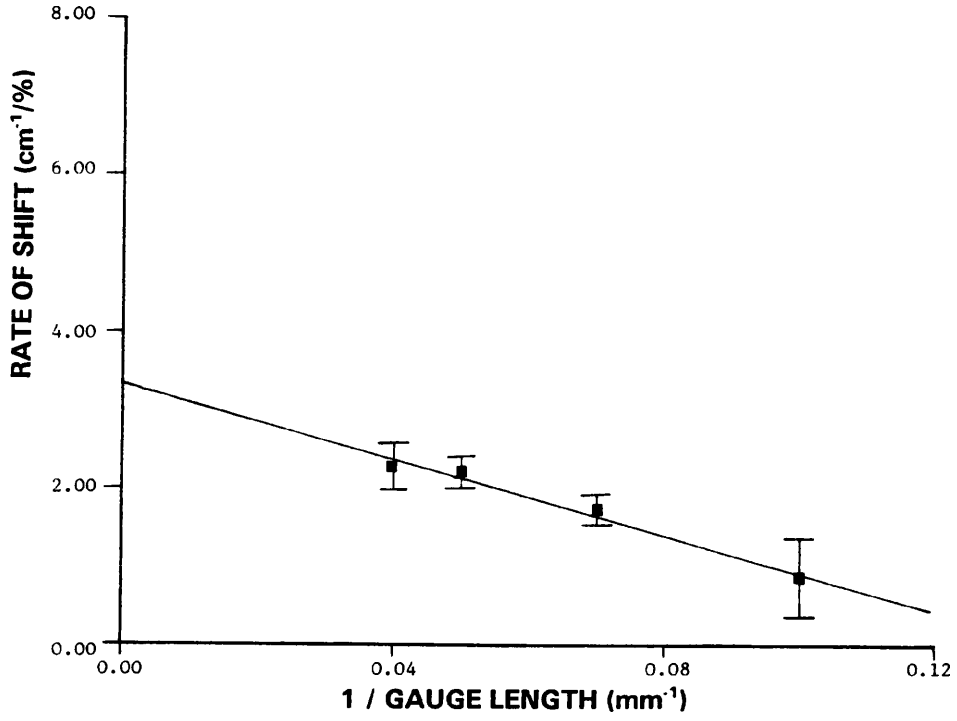

(b)

Fig.5.16 The values of dΔν/dε of (a) narrow, and (b) broad peaks plotted against the reciprocal of gauge length.

Table 5.3

CORRECTED VALUES OF $d\Delta\nu/d\varepsilon$ FOR ALL THE PE SAMPLES.

Fibre	Corrected $d\Delta\nu/d\varepsilon$ of Narrow Peak ($cm^{-1}/\%$)	Corrected $d\Delta\nu/d\varepsilon$ of Broad Peak ($cm^{-1}/\%$)
A	2.01	3.34
B	0.21	0.18
C	4.58	6.77
D	0.39	2.03
E	0.68	1.38
F	1.11	2.96
G	0.28	2.66
H	1.52	4.62
I	0.91	3.16

in tensile testing (Section 4.4.1) were observed from the Raman shift/strain curves for both the low-load (Fig.5.15a) and high-load (Fig.5.15b) bearing symmetric C-C stretching bands due to the insufficiently-long gauge lengths. By extrapolating to infinite gauge length, the corrected values of rates of shift ($d\Delta\nu/d\varepsilon$) for the monofilaments of Fibre A of the low-load (Fig.5.16a) and high-load (Fig.5.16b) bearing symmetric C-C stretching bands are 2.0 and 3.3 $cm^{-1}/\%$ respectively demonstrating that end effects are very significant. The corrected values of $d\Delta\nu/d\varepsilon$ for other samples are tabulated in Table 5.3.

The $d\Delta\nu/d\varepsilon$ values for both low-load and high-load bearing symmetric C-C stretching bands in the Raman spectra also show a strain-rate dependence as illustrated in Fig.5.17. The values of $d\Delta\nu/d\varepsilon$ of both the low-load and high-load bearing bands reach plateau values at strain rates of $\sim 1.5 \times 10^{-4}$ and $\sim 1.0 \times 10^{-4}$ s^{-1}

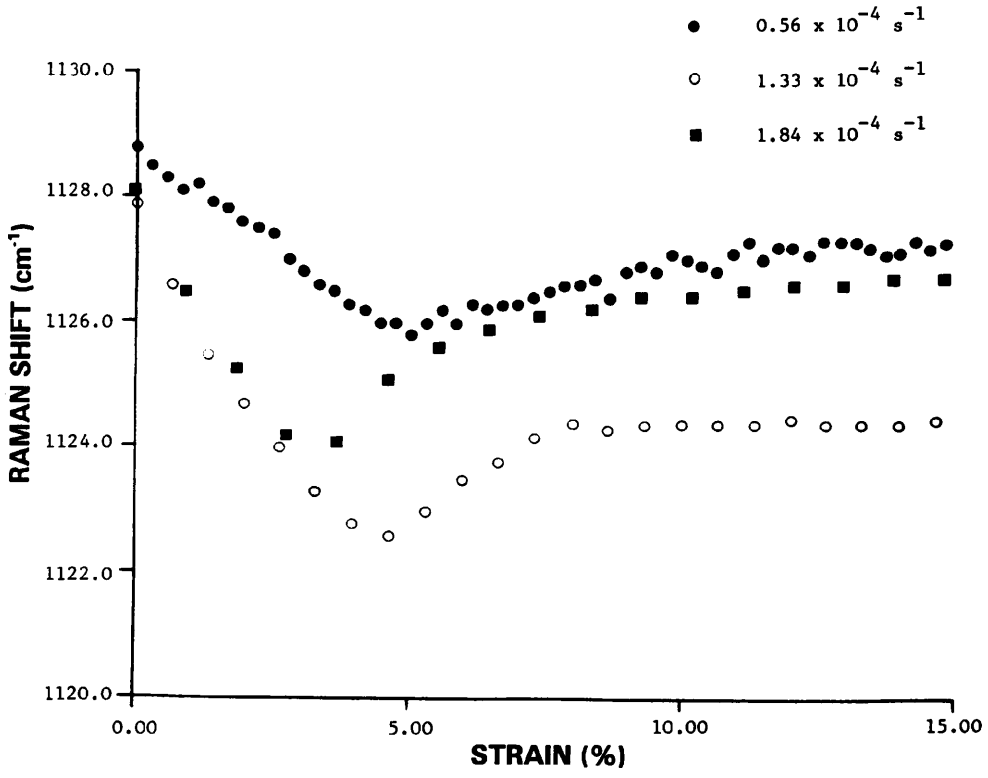

(a)

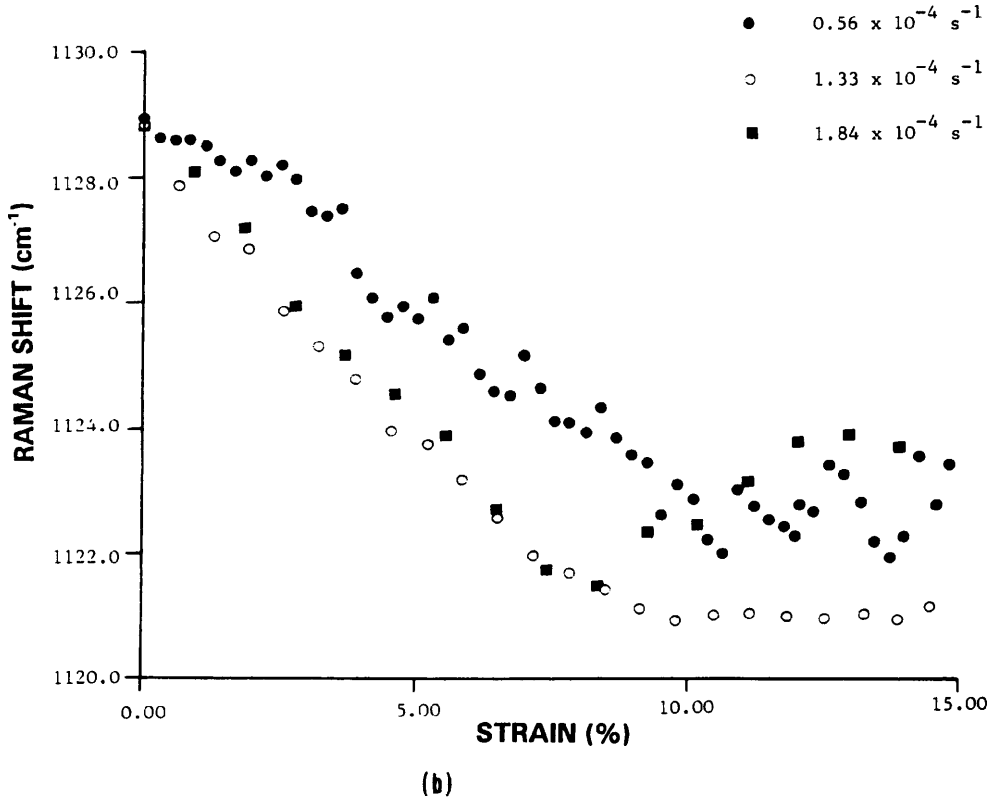

(b)

Fig.5.17 Raman shift vs strain curves of (a) narrow, and (b) broad peaks of the monofilaments of Fibre A at different strain rates and constant gauge length of 25.0 mm.

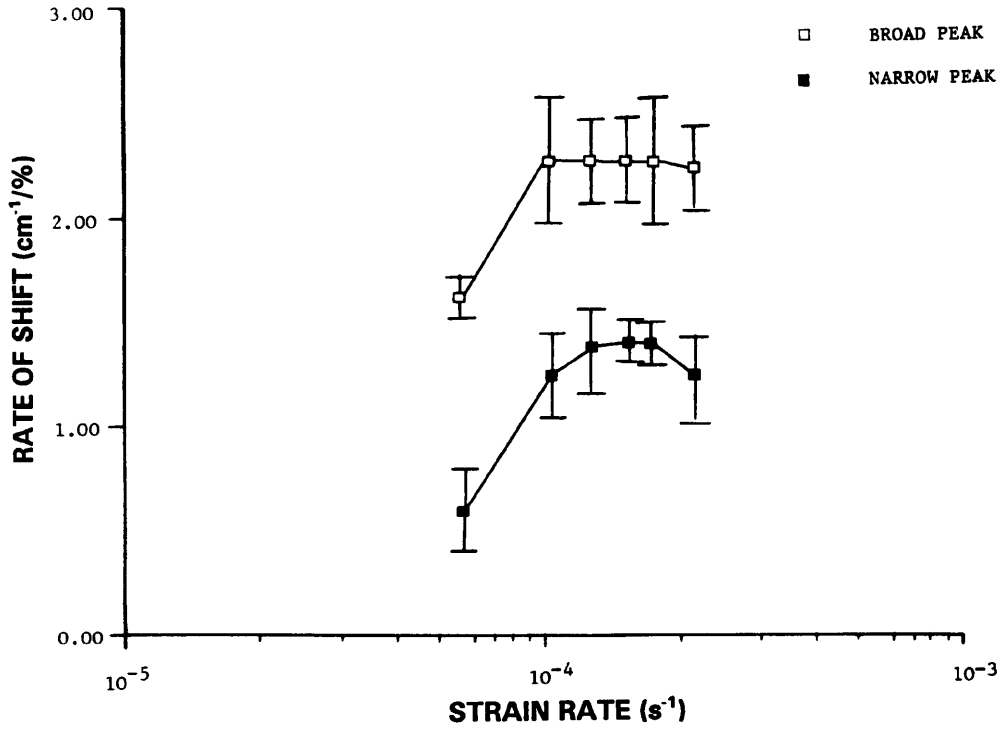

Fig.5.18 The values of dΔν/dε plotted against strain rate for the monofilaments of Fibre A at the gauge length of 25.0 mm.

respectively (Fig.5.18). Both low-load and high-load bearing C-C bands are apparently less rate sensitive at higher strain rates. It has been reported by Cansfield *et al* [114] that a similar plateau was observed in the mechanical behaviour for high-modulus PE fibres tested at different strain rates at a temperature of -10°C.

5.4.2 Molecular Deformation by Stressing

The monofilaments of Fibre A were deformed separately at both constant strain rate (straining at the rate of 1.33×10^{-4} s^{-1}) and constant stress rate (stressing at the rate of 0.17 GPa/min) as

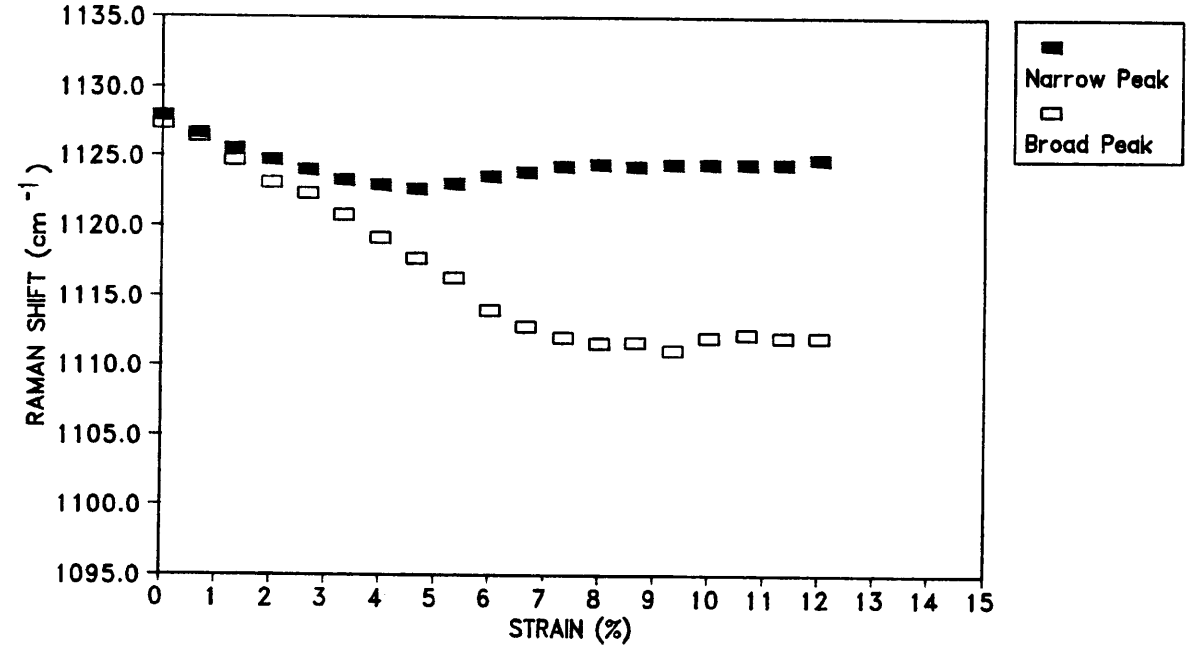

(a)

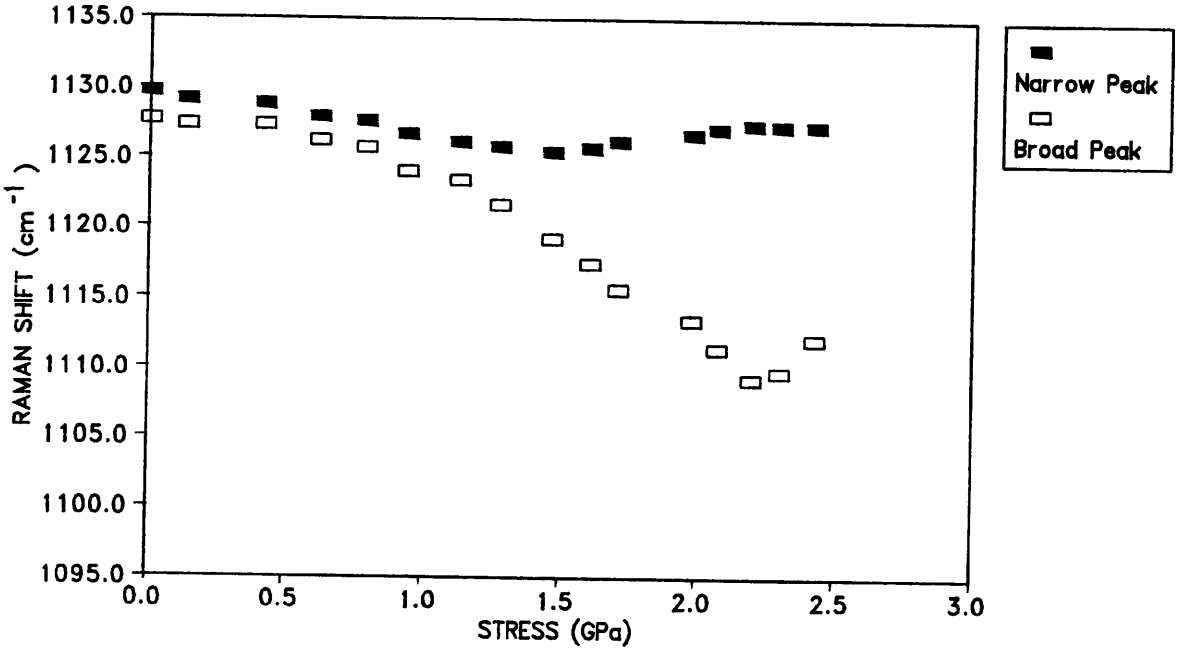

(b)

Fig.5.19 Both (a) the Raman shift/strain curve (at 1.33×10^{-4} s^{-1}, and (b) the Raman shift/stress curve (at 0.17 GPa/min) for the monofilaments of Fibre A.

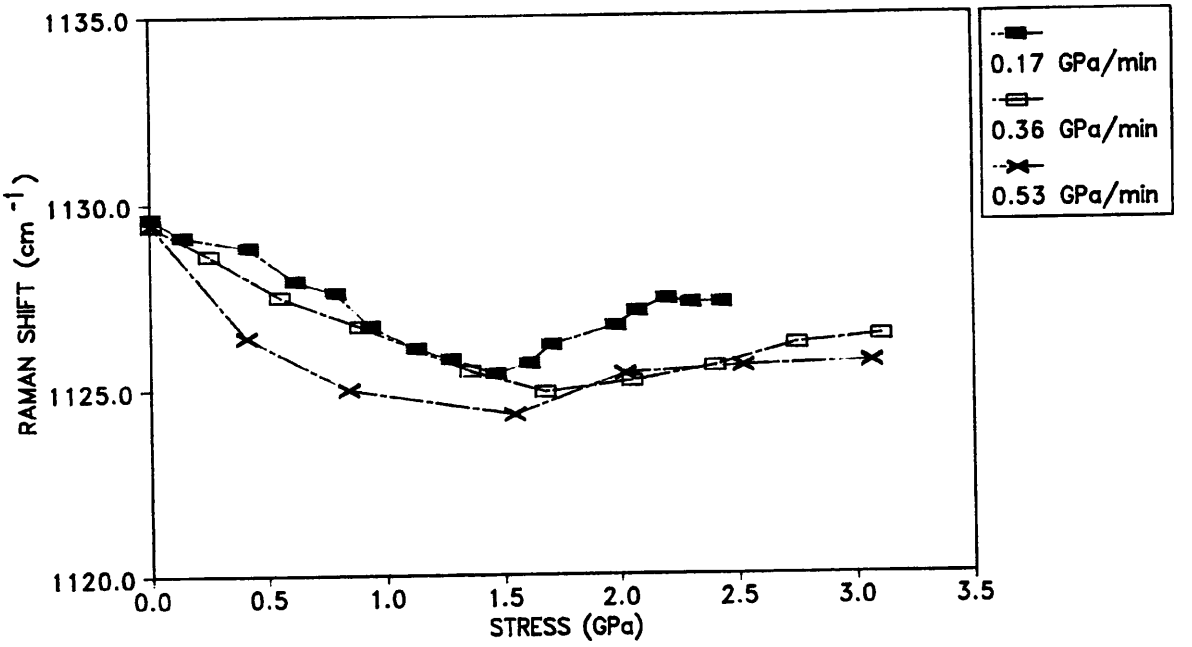

(a)

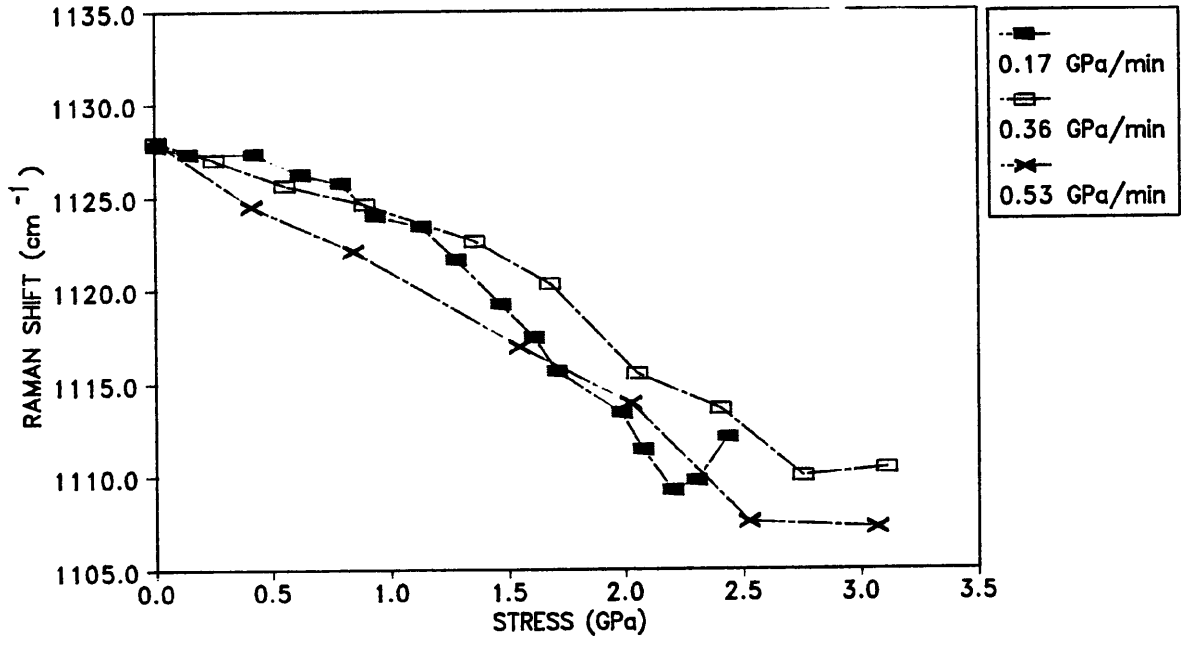

(b)

Fig.5.20 The Raman shift/stress curves of the (a) low-load, and (b) high-load bearing C-C symmetric stretching bands for the monofilaments of Fibre A at various stress rates.

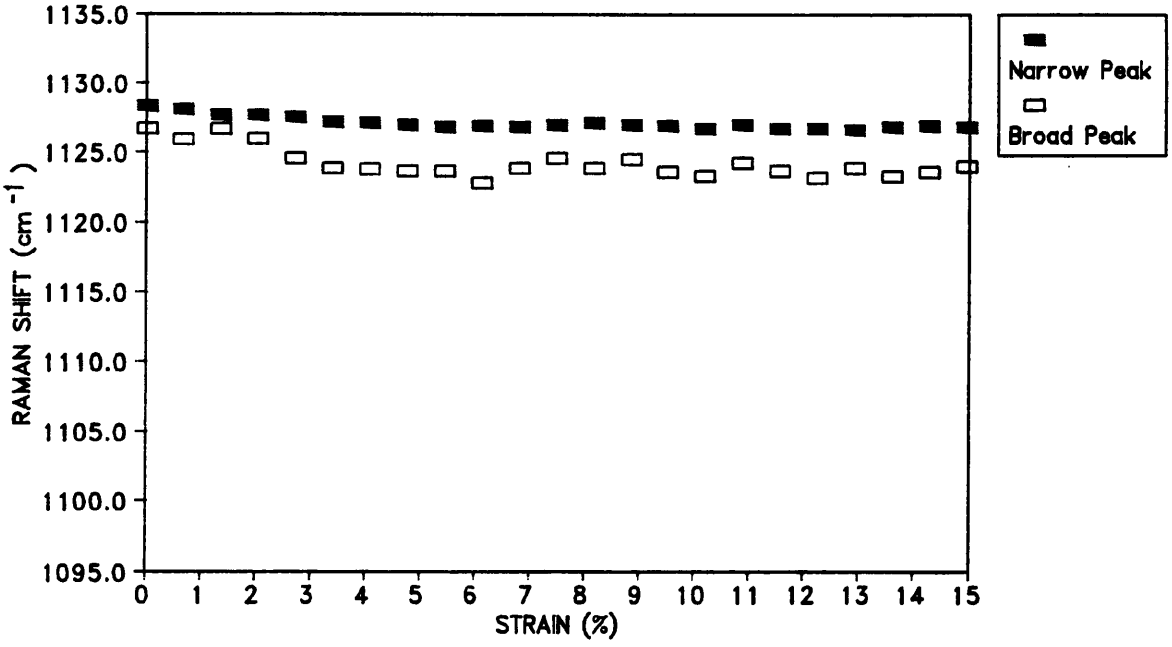

(a)

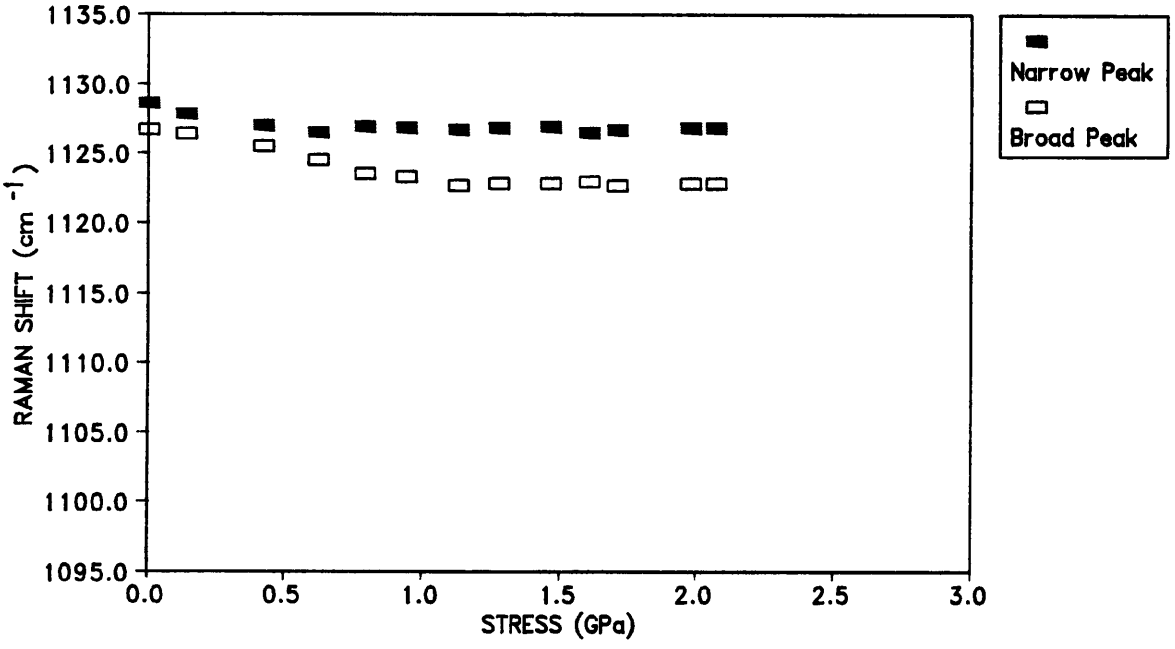

(b)

Fig.5.21 Both (a) the Raman shift/strain curve (at 1.33×10^{-4} s^{-1}, and (b) the Raman shift/stress curve (at 0.17 GPa/min) for the monofilaments of Fibre B.

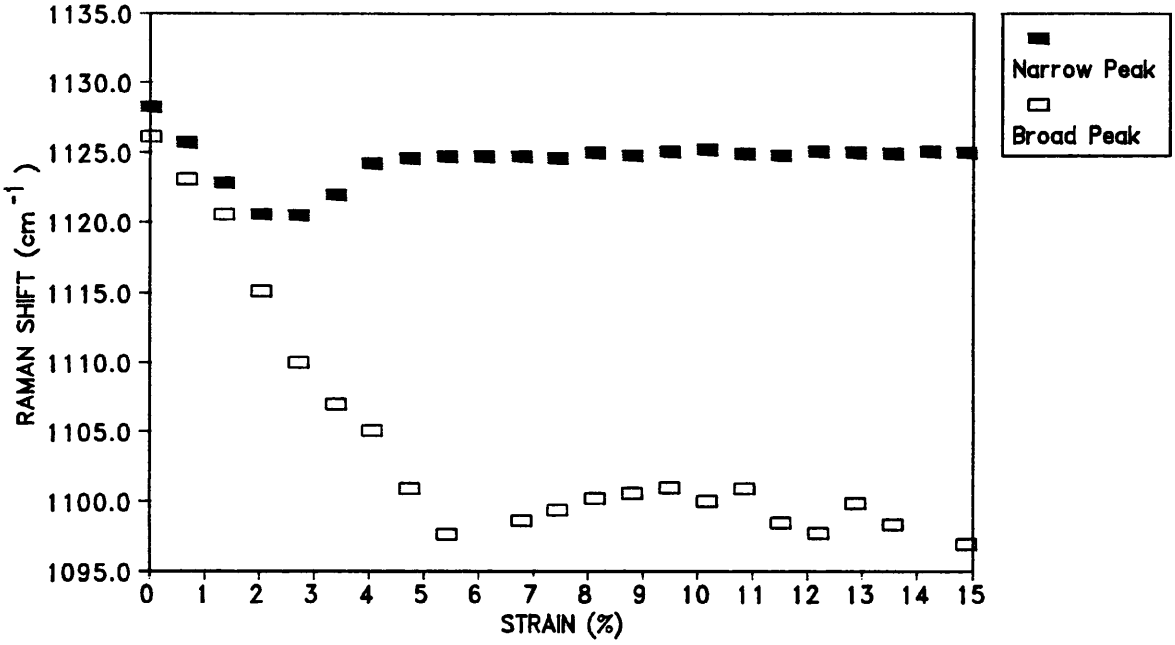

(a)

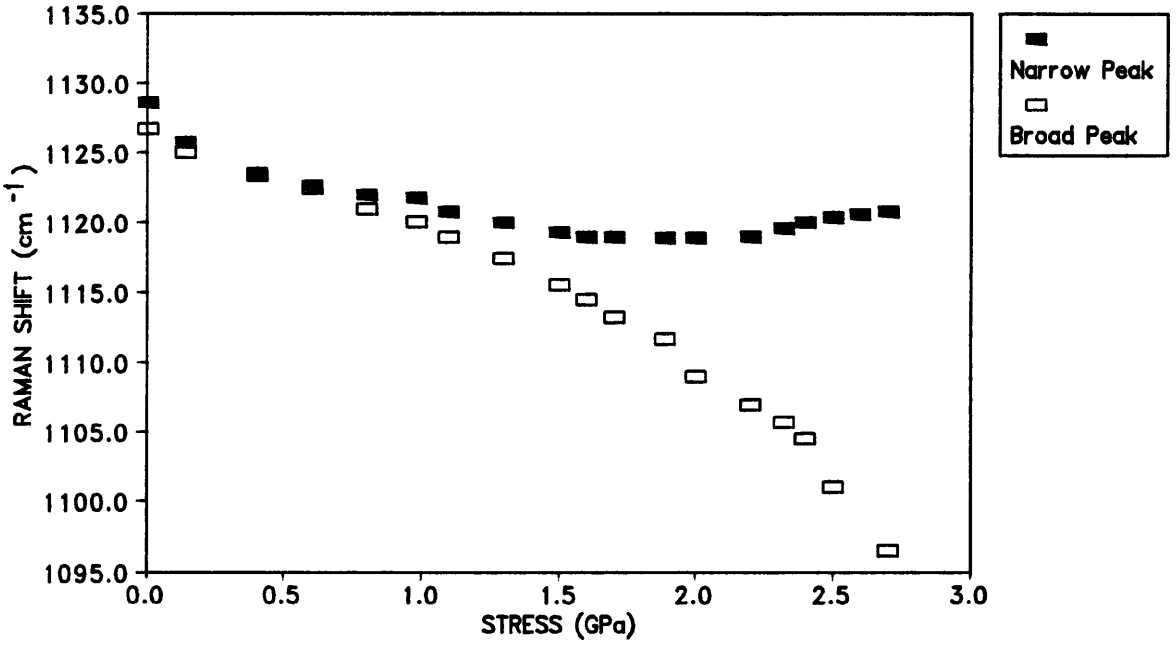

(b)

Fig.5.22 Both (a) the Raman shift/strain curve (at 1.33×10^{-4} s^{-1}, and (b) the Raman shift/stress curve (at 0.17 GPa/min) for the monofilaments of Fibre C.

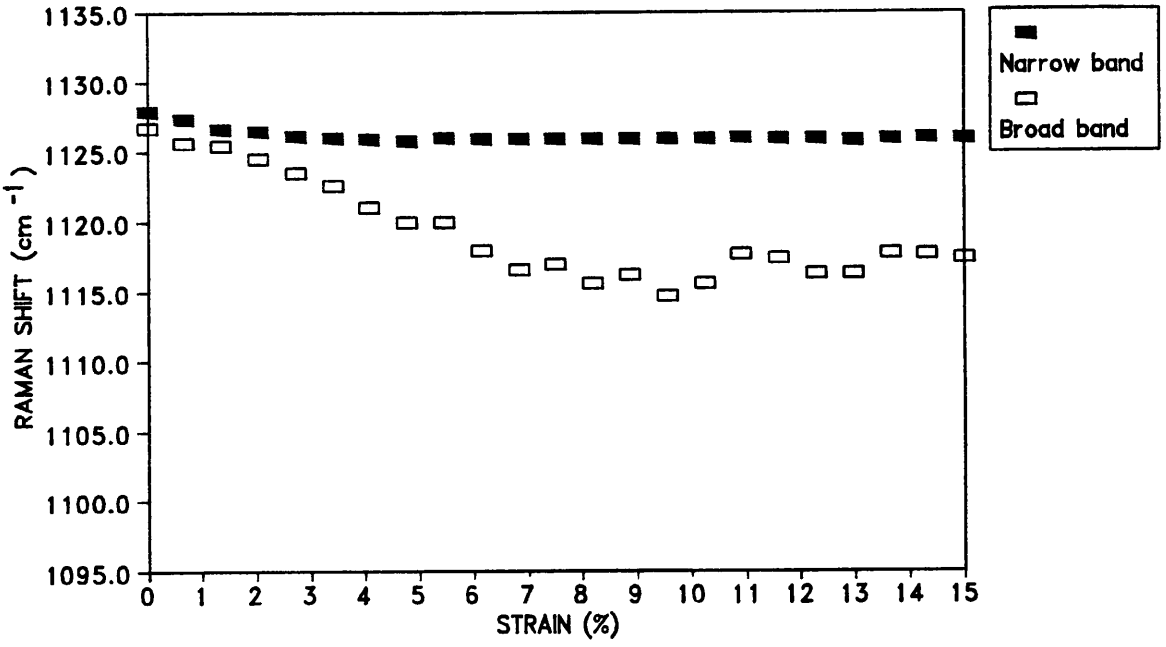

(a)

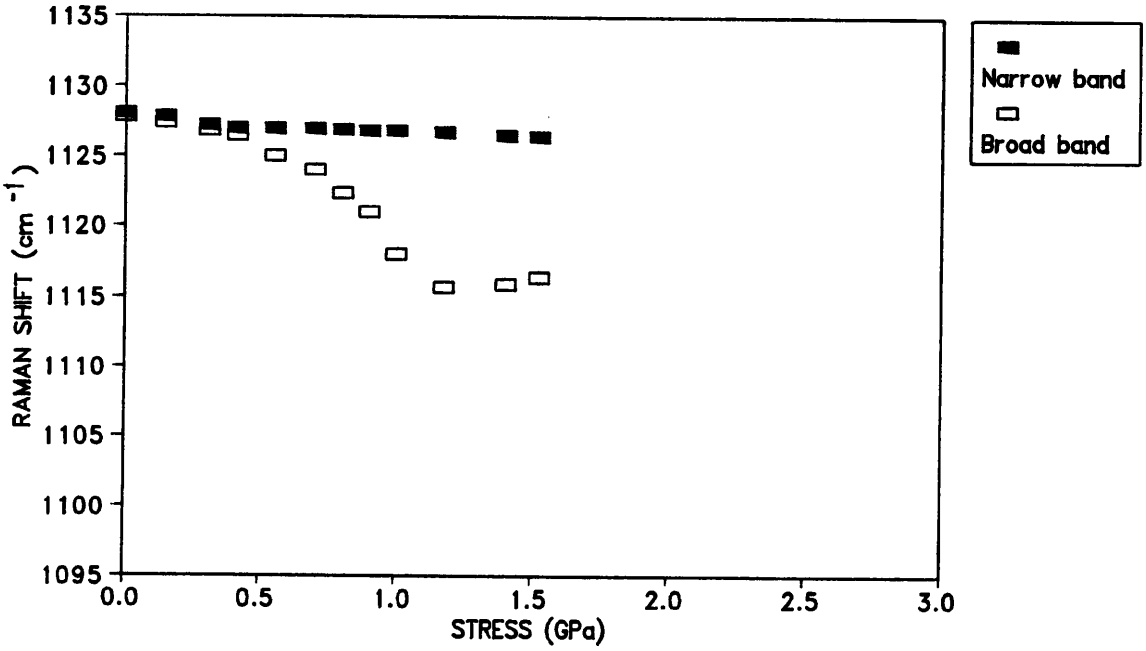

(b)

Fig.5.23 Both (a) the Raman shift/strain curve (at 1.33×10^{-4} s^{-1}, and (b) the Raman shift/stress curve (at 0.17 GPa/min) for the monofilaments of Fibre E.

shown in Fig.5.19. Likewise, the effect of testing parameters in stressing is as significant as those in straining. Although no gauge length effect was expected during stressing of the monofilament, the effect of rate of deformation (stress rate) remains significant as illustrated in Fig.5.20.

In the Raman shift/stress curve (Fig.5.19b), the initial rate of shift ($d\Delta\nu/d\sigma$) is defined in terms of cm^{-1}/GPa which is analogous to the initial ($d\Delta\nu/d\varepsilon$) in the Raman shift/strain curve. For Fibre A, the initial values of ($d\Delta\nu/d\sigma$) for the low-load and high-load bearing bands are 3.0 and 3.4 cm^{-1}/GPa respectively and it appears that both peaks shift at a similar rate upon stressing. In contrast, the high-load bearing band shifts at a relatively higher rate (2.3 cm^{-1}/%) than the low-load bearing band (1.4 cm^{-1}/%) upon straining (Fig.5.19a). The curvatures of both the Raman shift/strain curve (Fig.5.19a) and the Raman shift/stress curve (Fig.5.19b) for the low-load bearing band appear to be similar. However upon straining, the Raman shift/strain curve of the high-load bearing band shows a convex curvature with decreasing slope and apparently yields before fracture. On the other hand, the slope of the Raman shift/stress curve for the high-load bearing band becomes steeper upon further stressing. In fact, it appears that the non-linearity of the Raman shift/strain curves for the PE fibres (Fig.5.21-5.23) is very similar in curvature to those observed in the stress/strain curves of the monofilaments (Section 4.4). This indicating the measurement of the Raman shift can be taken as a direct measurement of the molecular stress within the fibre microstructure. Obviously this is an informative observation for

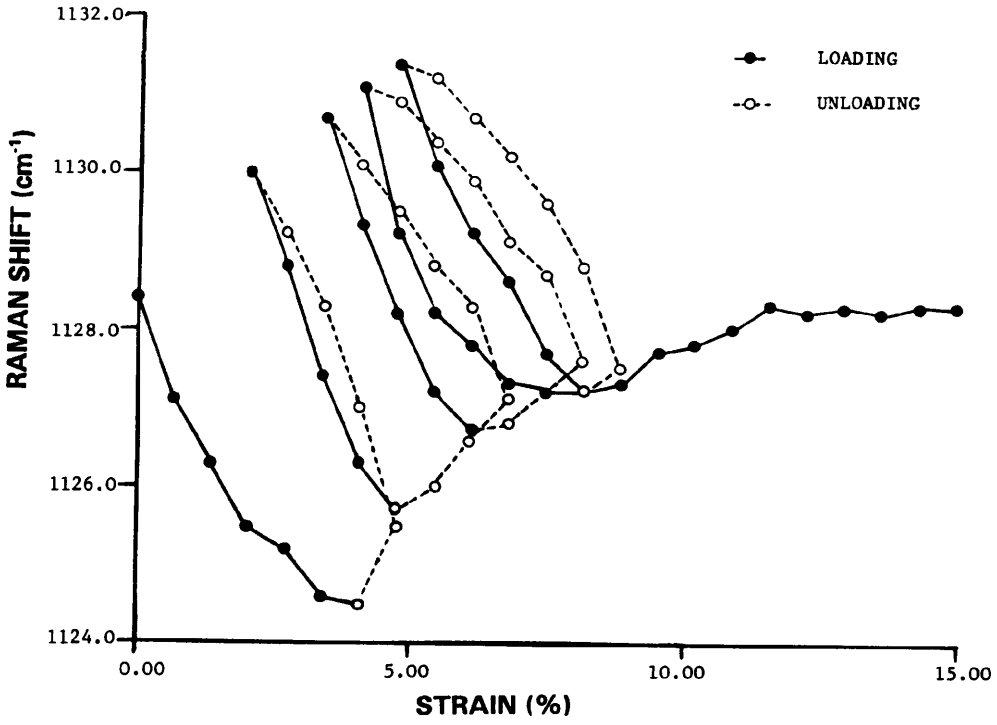

(a)

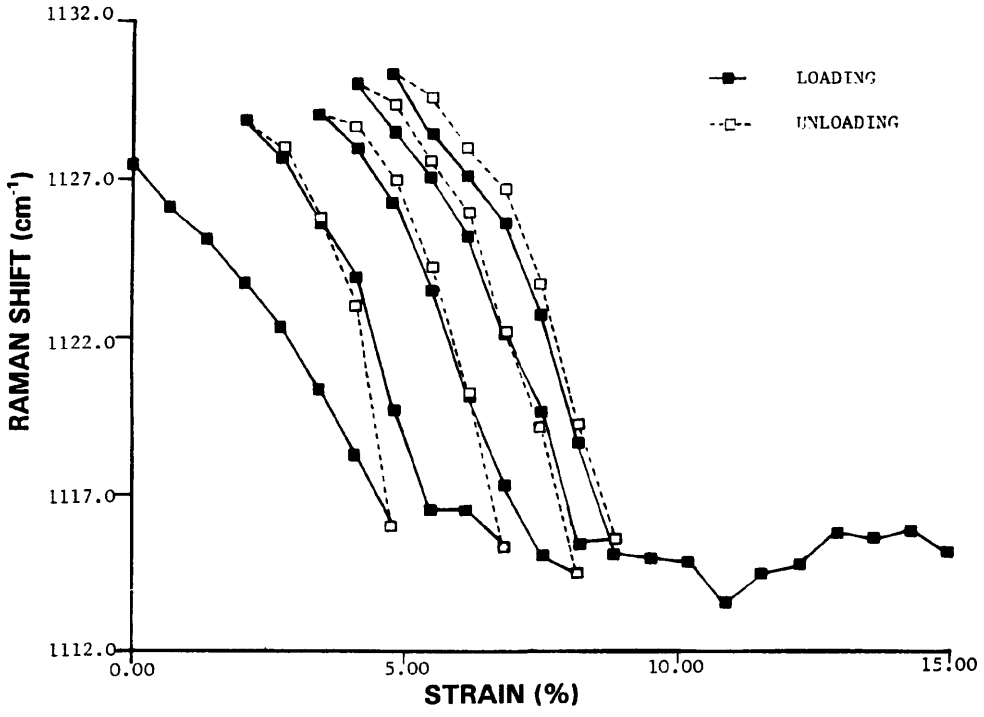

(b)

Fig.5.24 The Raman shift strain curves of (a) low-load, and (b) high-load bearing bands upon cyclic loadings of Fibre A.

the quantitative modelling (Section 6.4.2).

5.4.3 Cyclic Loading

In the Raman spectra for cyclic deformation, both the low-load (Fig.5.24a) and high-load (Fig.5.24b) bearing bands exhibit significant permanent deformation with loading and unloading following different paths. The Raman shift/strain curves for both the low-load (narrow) and high-load (broad) bands appear almost parabolic with convex and concave curvatures respectively. These two completely different curvatures indicates the different molecular response of the two differently-stressed C-C bonds upon

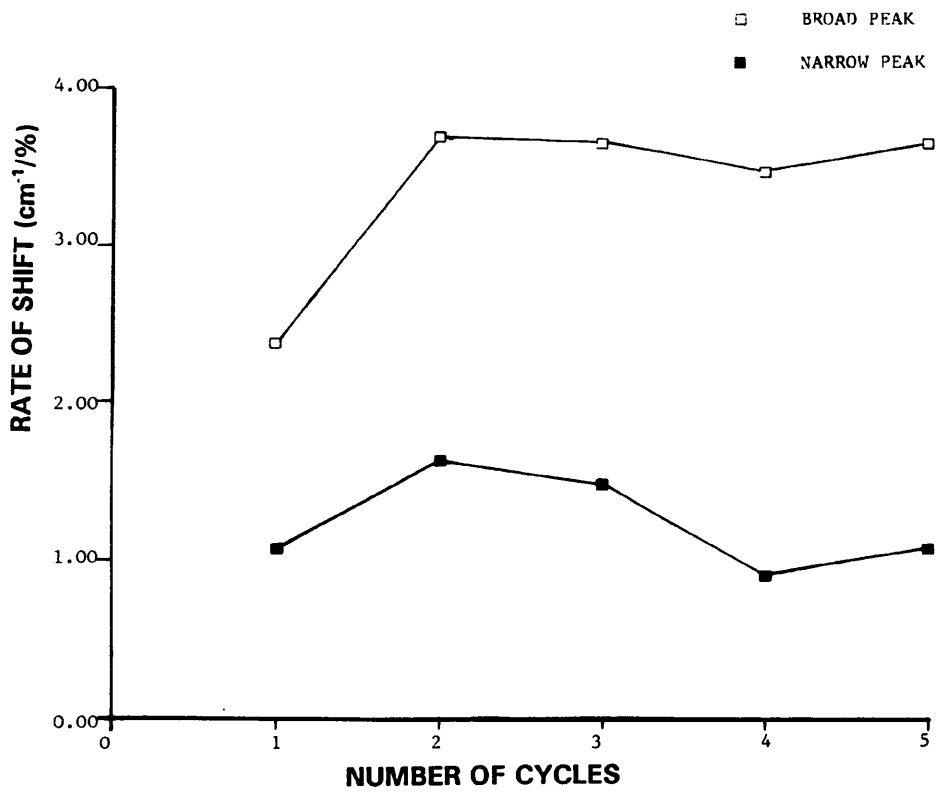

Fig.5.25 The effect of number of cycles on the rates of shifts of both low-load (narrow peak) and high-load (broad peak) bearing bands during cyclic loadings of Fibre A.

repeated loadings. The slopes of the reloading curves for the two bands are changing with the number of cycles as illustrated in Fig.5.25 where the rates of shift ($d\Delta\nu/d\varepsilon$) of the Raman band are measured from the initial slopes of the loading and reloading curves in Fig.5.24. The values of $d\Delta\nu/d\varepsilon$ of both the low-load and high-load bearing bands are higher for the second cycle and remain constant for subsequent cycles of reloading which is consistent with the strain hardening found during the cyclic loading in the mechanical testing (Section 4.4.3). Upon unloading, both low-load and high-load bearing bands shift to the higher wavenumber and it appears that the molecular chains were subjected to apparent compression in the microstructure.

5.4.4 Stress Relaxation and Creep

Both band shifts and changes in band intensity of the Raman bands for the symmetric C-C stretching Raman mode of the monofilaments were observed during the stress relaxation of the monofilaments of Fibres A (Fig.5.26), B (Fig.5.27) and C (Fig.5.28) at a constant displacement corresponding to 2.0% strain. A complex molecular behaviour is found in the Raman spectra where both the low-load (narrow) and high-load (broad) bearing bands shift toward the initial positions whilst the stress decays as shown in Fig.5.29 for Fibres A, B and C. The dashed line is the initial Raman peak position of the monofilaments. The stress relaxation curves are similar in curvature with the simultaneous changes of the Raman shift and again it is an indication that the Raman shift is a direct measurement of stress. It is noted that there is a significant positive shift of both low-load and high-load

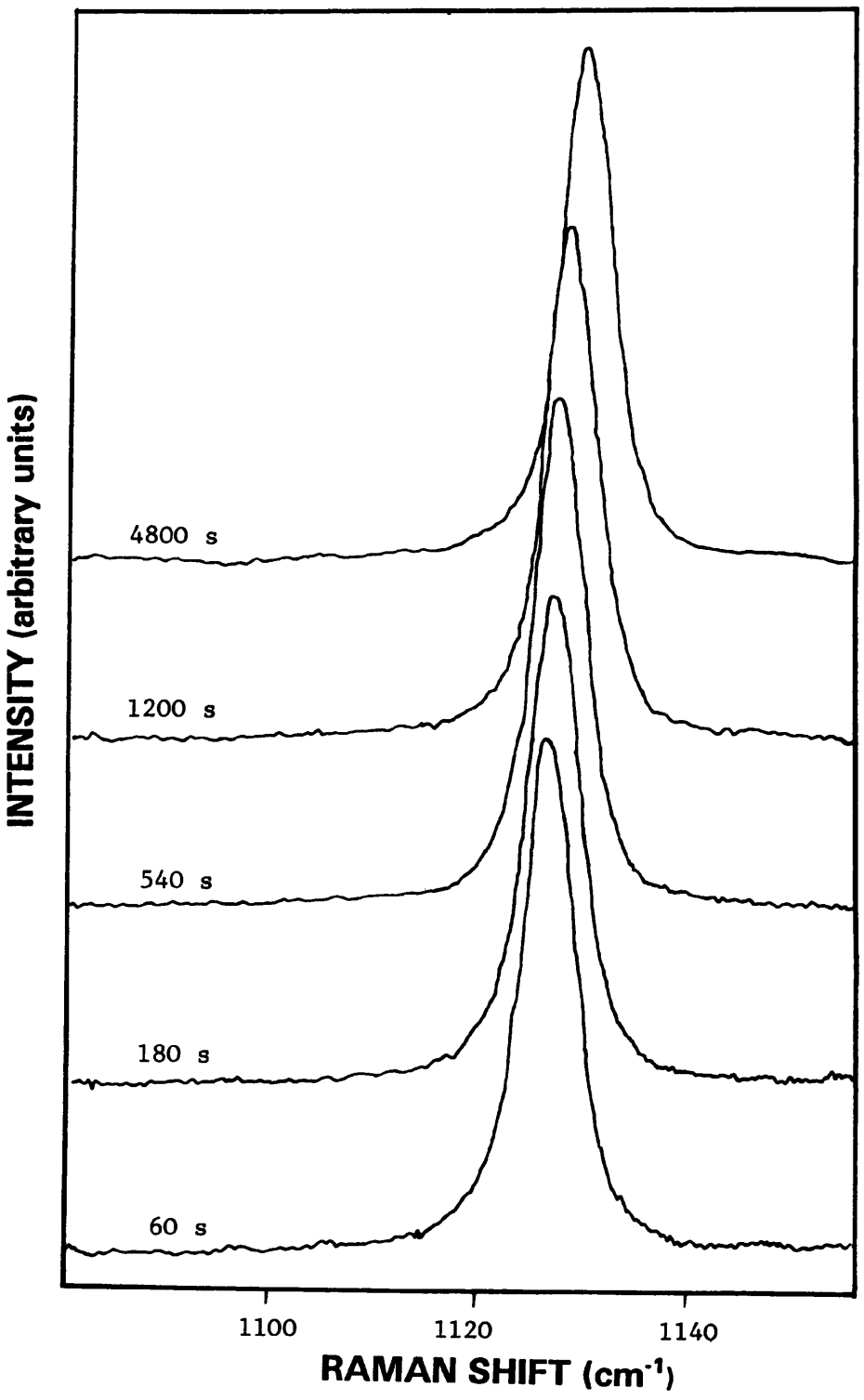

Fig.5.26 The Raman spectra of the C-C symmetric stretching mode of the monofilament of Fibre A upon stress relaxation at constant displacement of 2.0% strain.

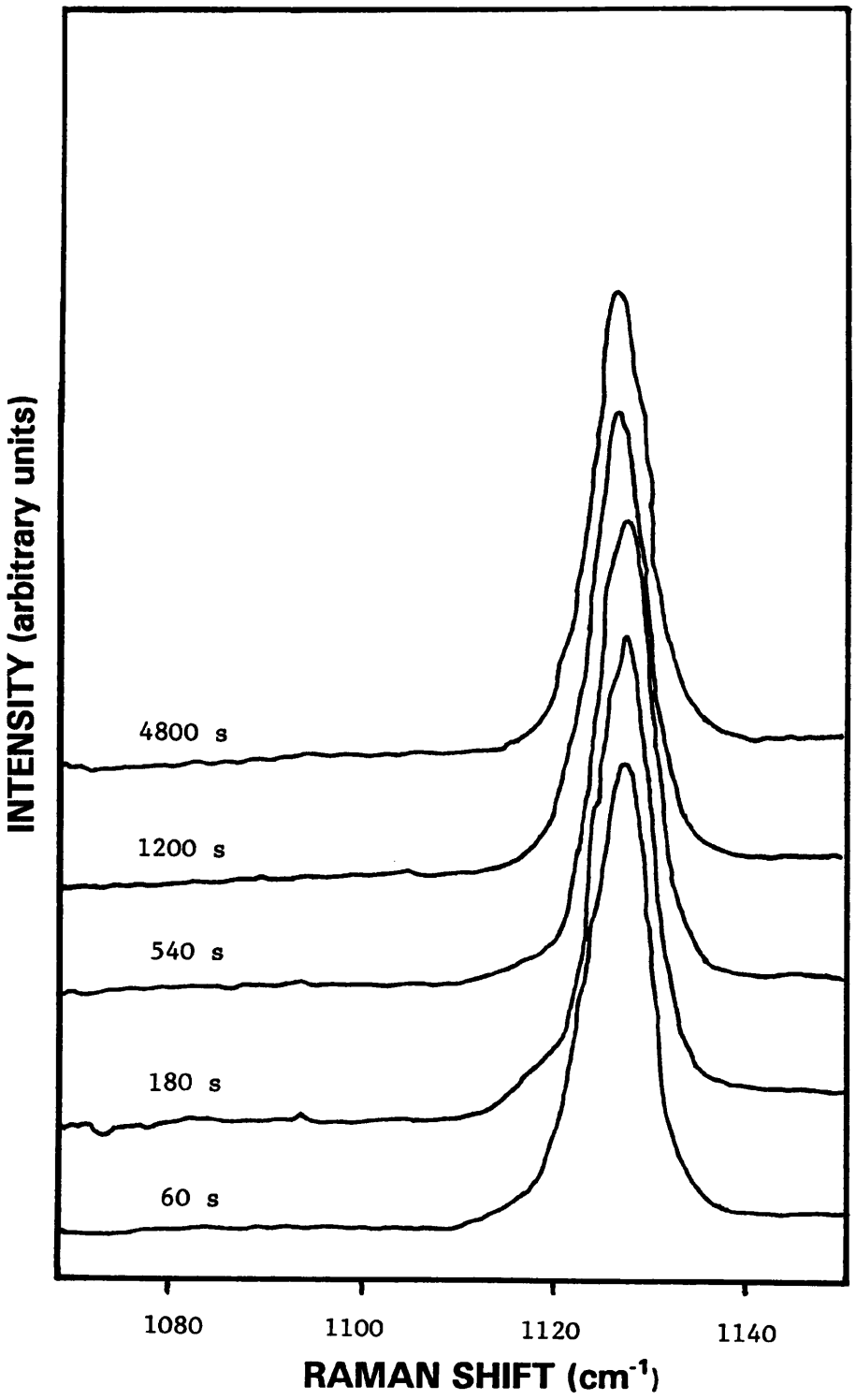

Fig.5.27 The Raman spectra of the C-C symmetric stretching mode of the monofilament of Fibre 8 upon stress relaxation at constant displacement of 2.0% strain.

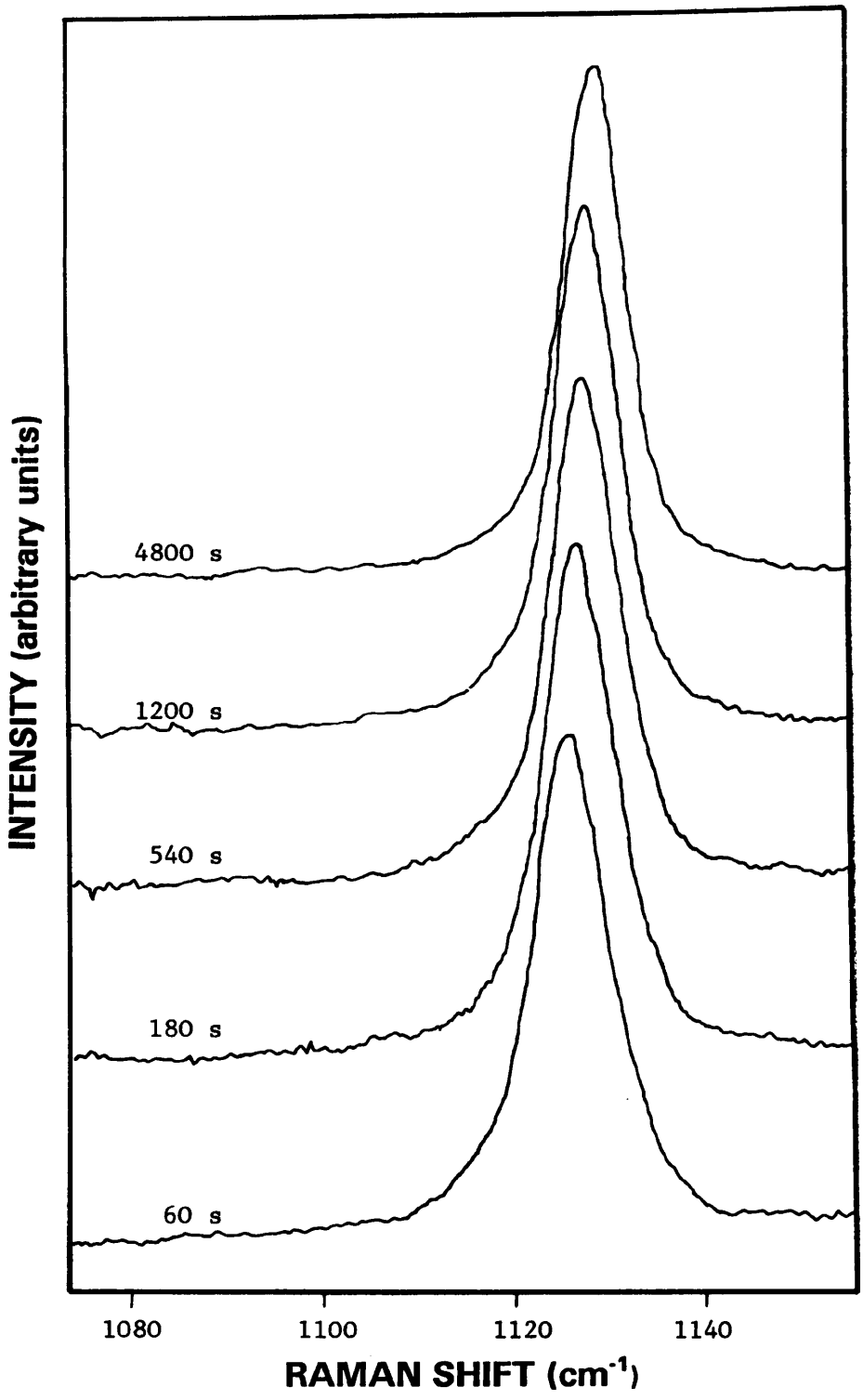

Fig.5.28 The Raman spectra of the C-C symmetric stretching mode of the monofilament of Fibre C upon stress relaxation at constant displacement of 2.0% strain.

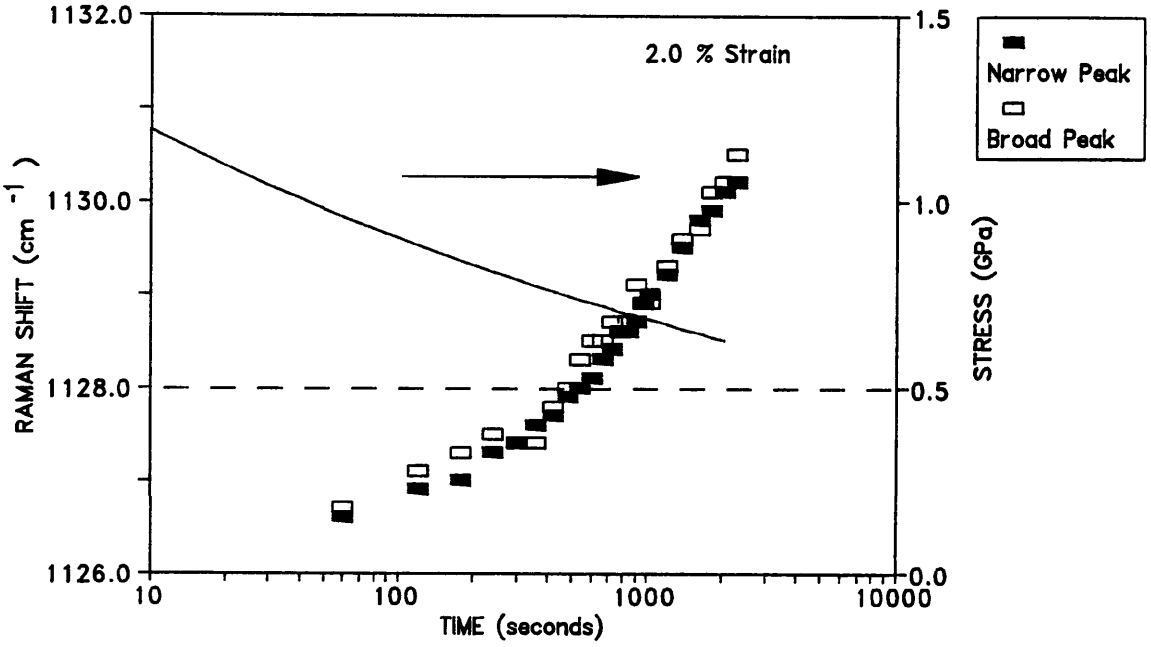

(a)

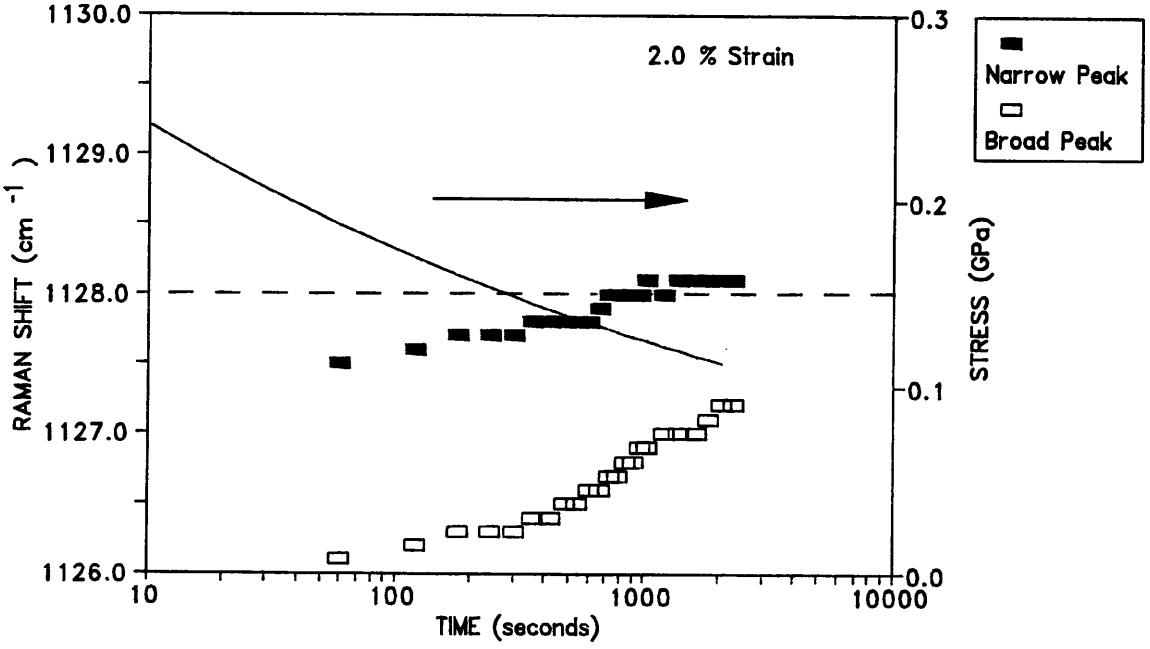

(b)

Fig.5.29 The Raman shift/time curve together with the decaying stress response during the stress relaxation at 2.0% strain for the monofilaments of (a) Fibre A, and (b) Fibre B.

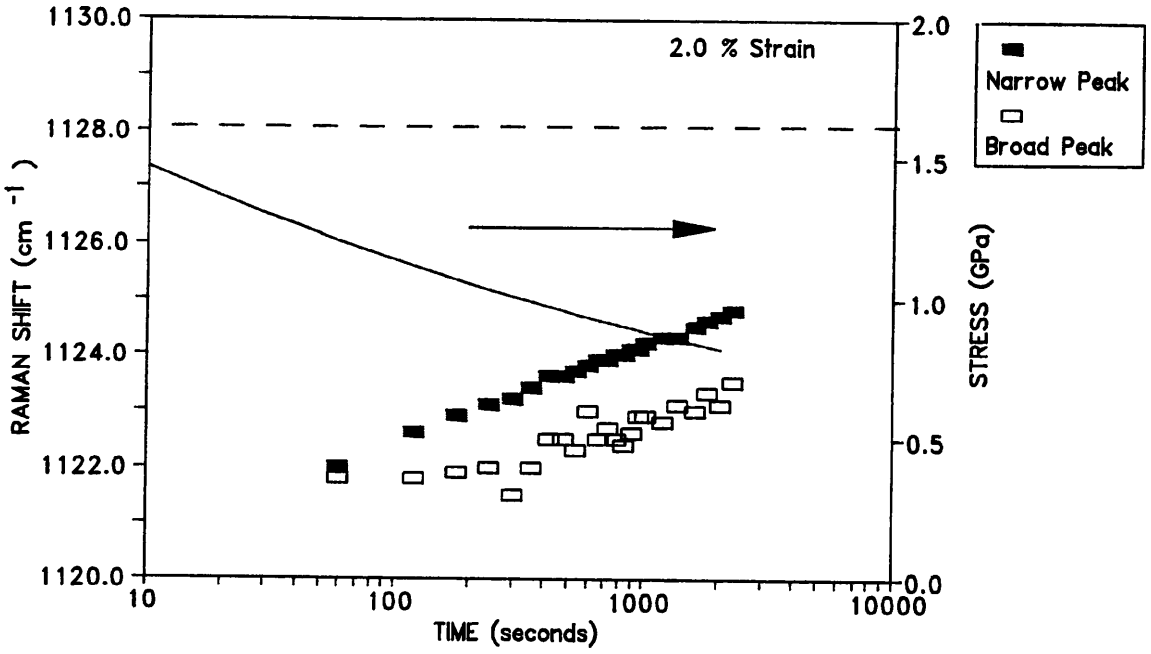

(c)

Fig.5.29c The Raman shift/time curve together with the decaying stress response during the stress relaxation at 2.0% strain for the monofilaments of Fibre C.

bearing Raman peaks for Fibre A relative to the original positions.

Fig.5.30 shows the time dependence of the peak positions of both the low-load and high-load bearing bands, respectively, for the monofilaments of Fibre A at constant strains of 2.0%, 4.0% and 6.0% over periods of time of up to 6000 seconds. At 2.0% strain, both the low-load and high-load bearing C-C bonds were subjected to apparent compression (a positive shift of the Raman peak relative to the original position) after ~600 seconds and ~200 seconds of relaxation respectively. At higher strain, however, the bands remained in tension. Again, a distinct yield phenomenon is observed for both bands which is similar to the behaviour in the extension-to-break experiments (Section 4.4). In fact, similar observations were also obtain for the

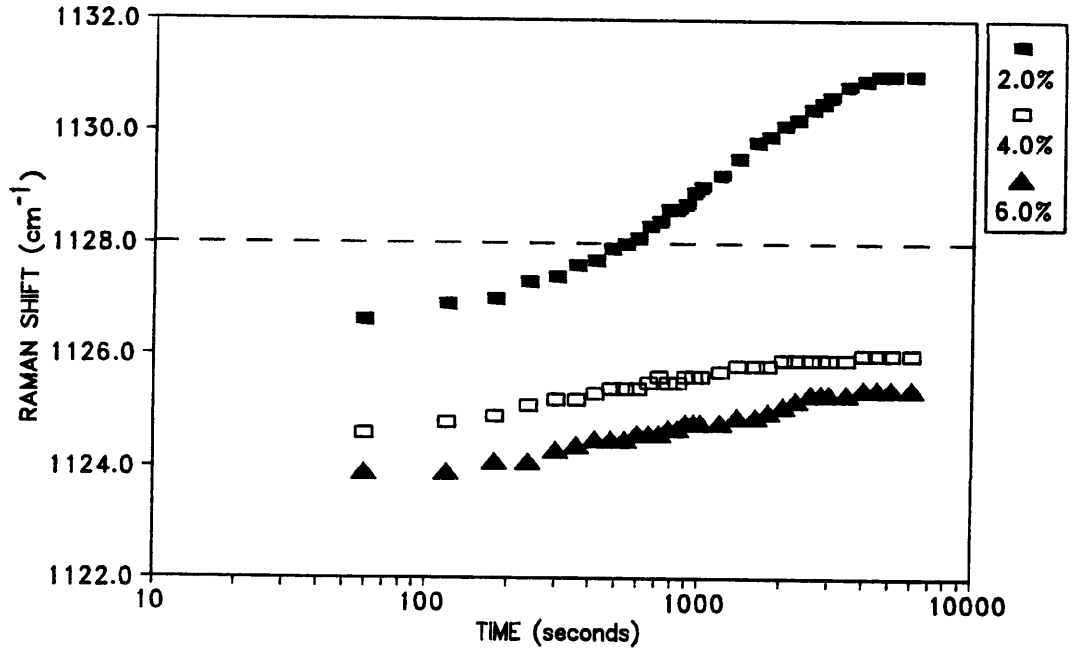

(a)

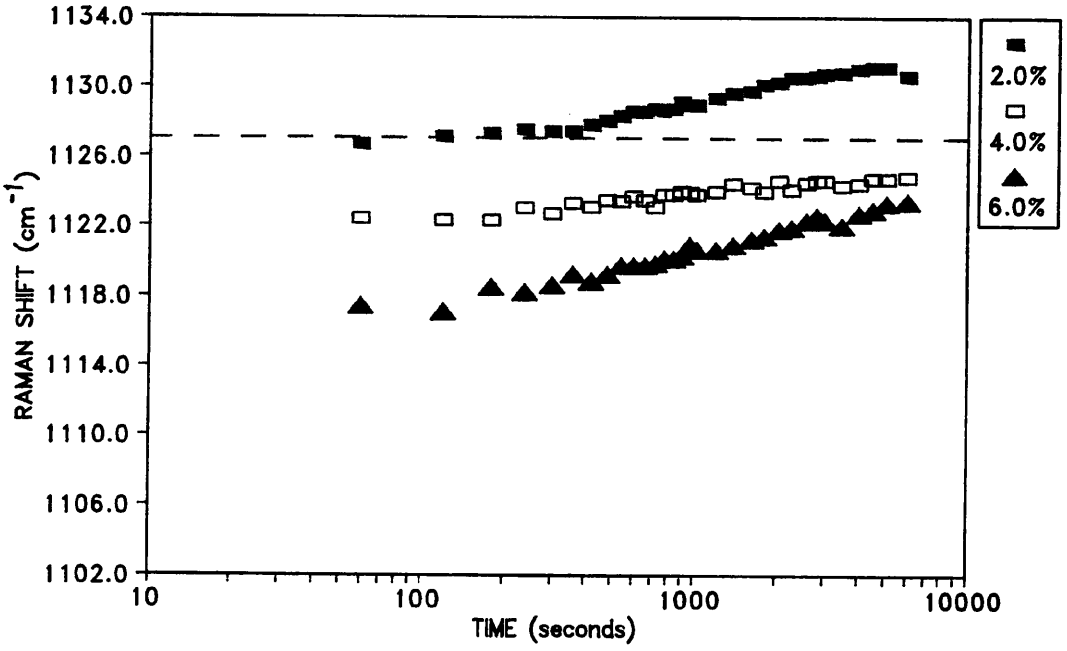

(b)

Fig.5.30 The Raman shift/time curves of both (a) low-load, and (b) high-load bearing bands for the monofilaments of Fibre A during stress relaxation at 2.0%, 4.0% and 6.0% strains.

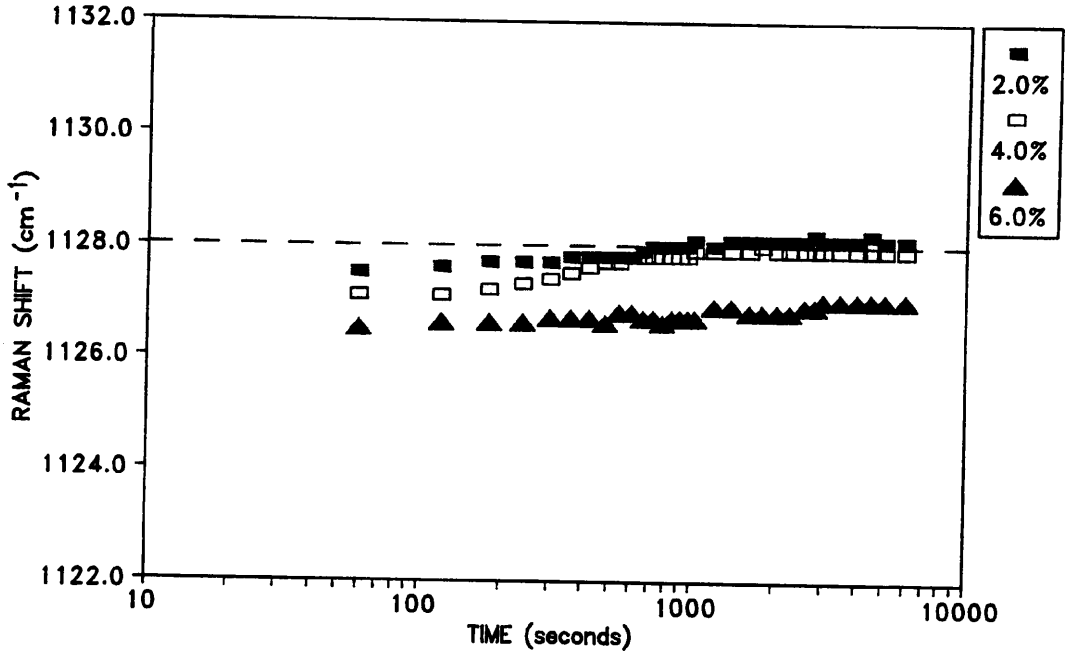

(a)

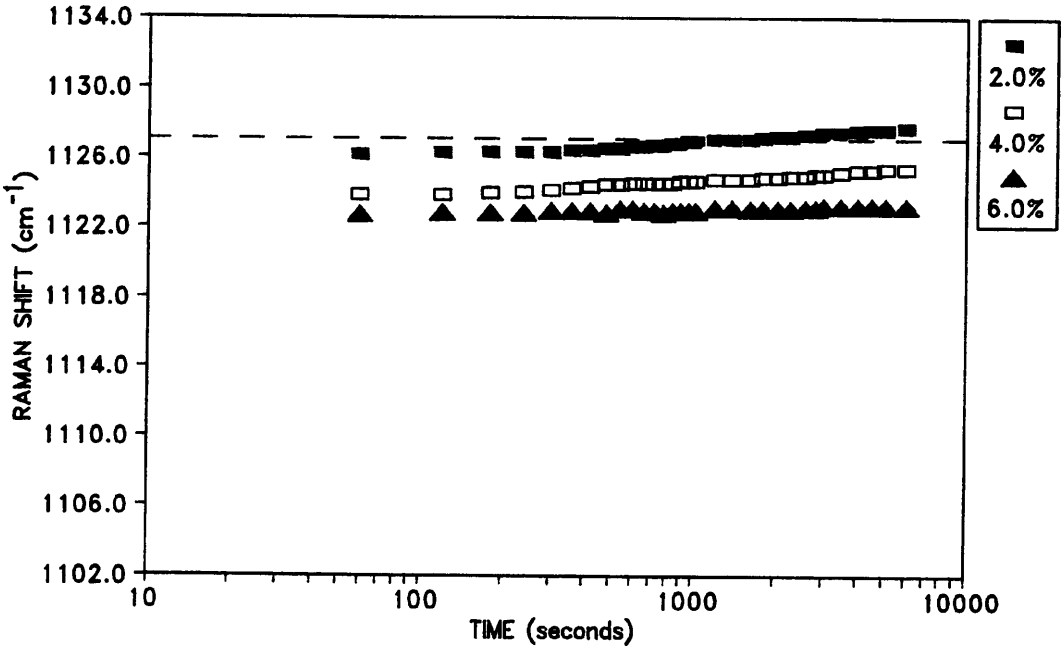

(b)

Fig.5.31 The Raman shift/time curves of both (a) low-load, and (b) high-load bearing bands for the monofilaments of Fibre B during stress relaxation at 2.0%, 4.0% and 6.0% strains.

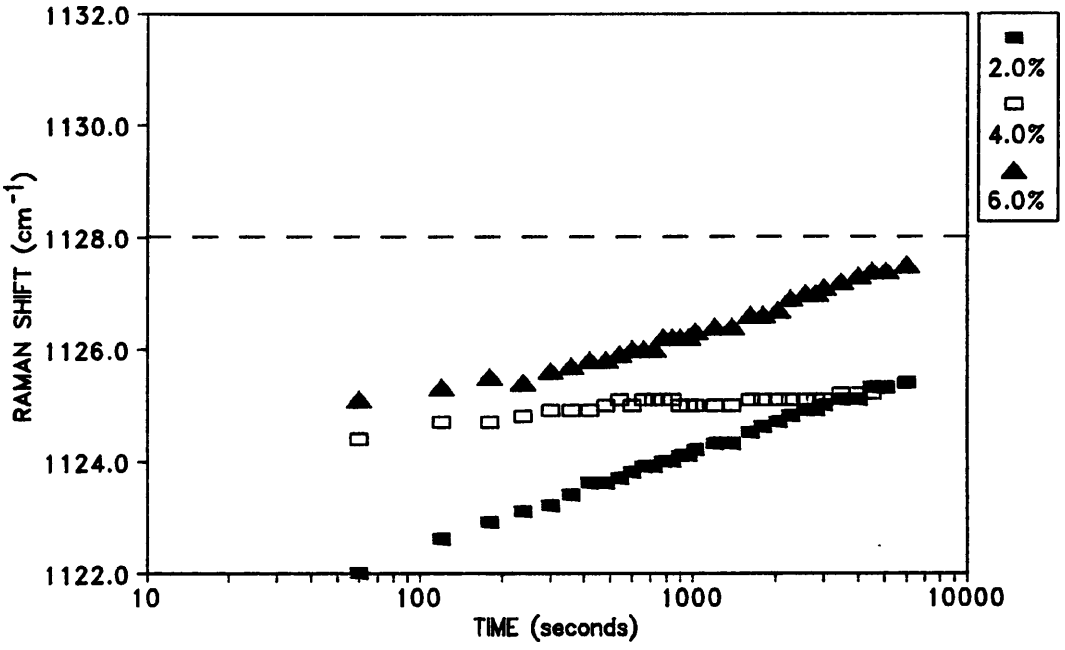

(a)

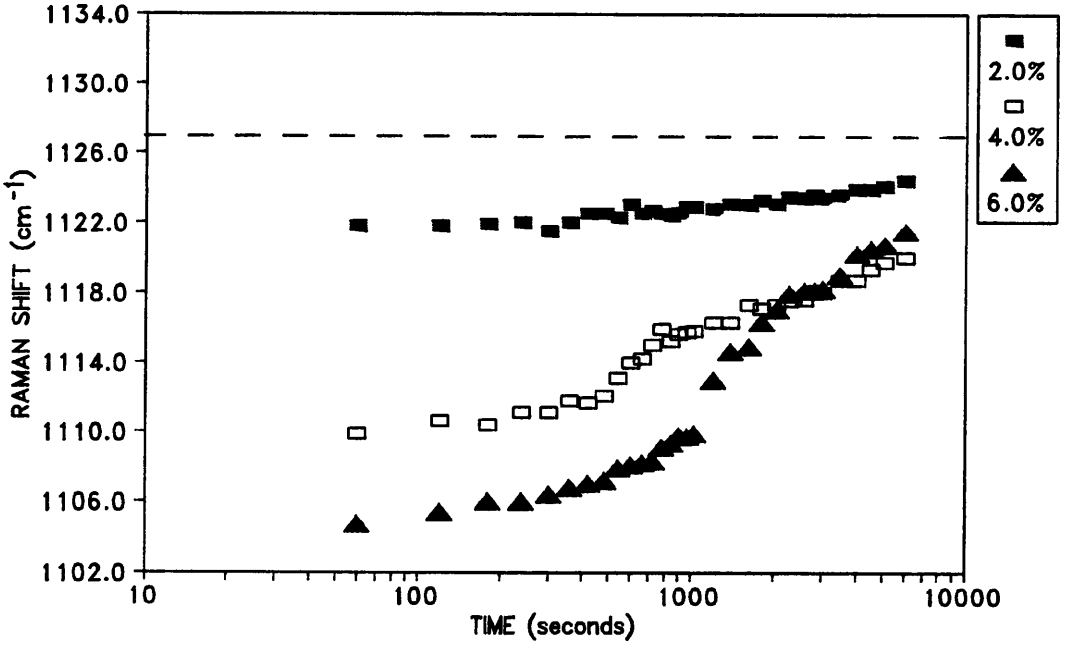

(b)

Fig.5.32 The Raman shift/time curves of both (a) low-load, and (b) high-load bearing bands for the monofilaments of Fibre C during stress relaxation at 2.0%, 4.0% and 6.0% strains.

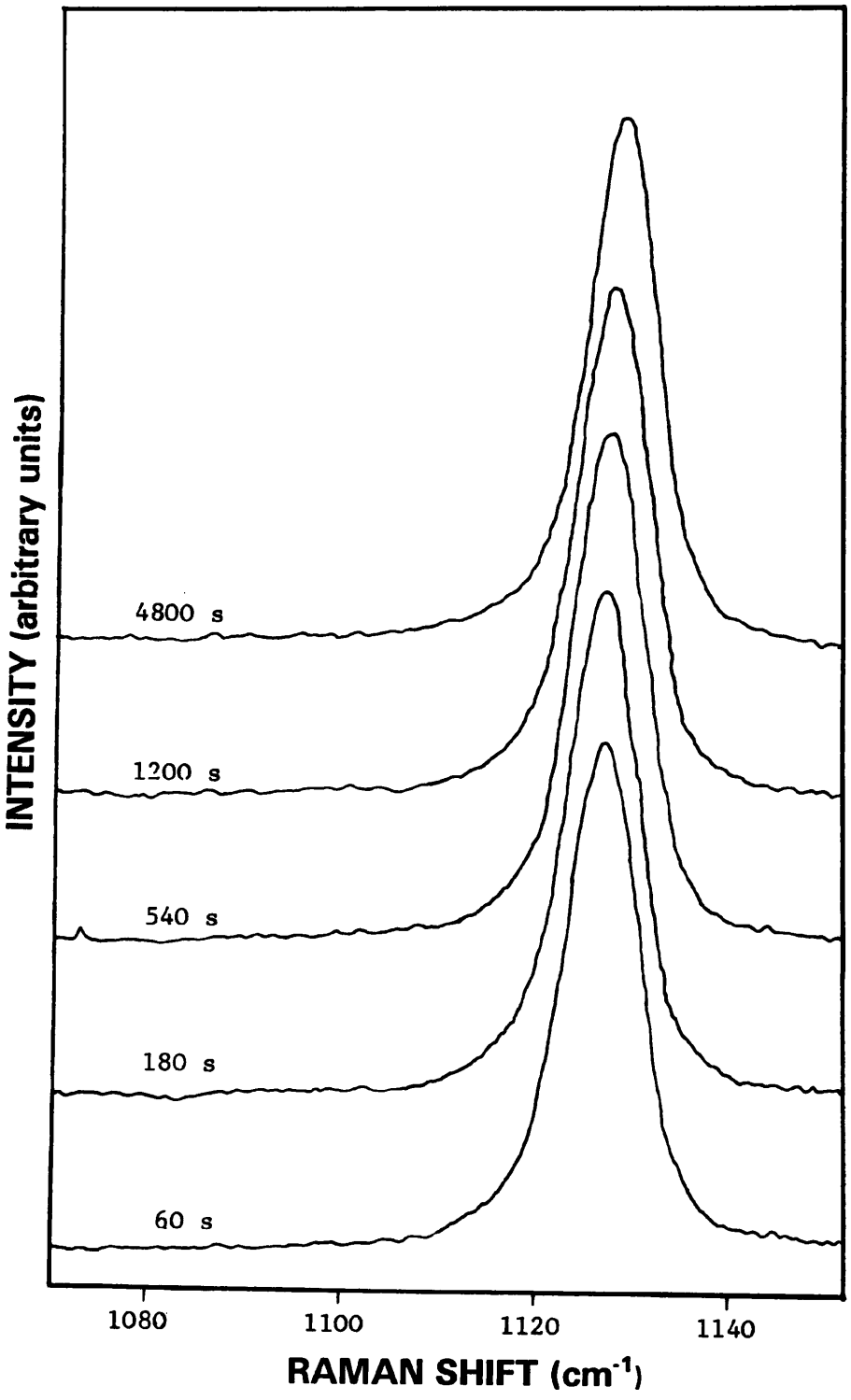

Fig.5.33 The Raman spectra of the C-C symmetric stretching mode of the monofilament of Fibre A upon creep experiment at constant stress of 0.5 GPa.

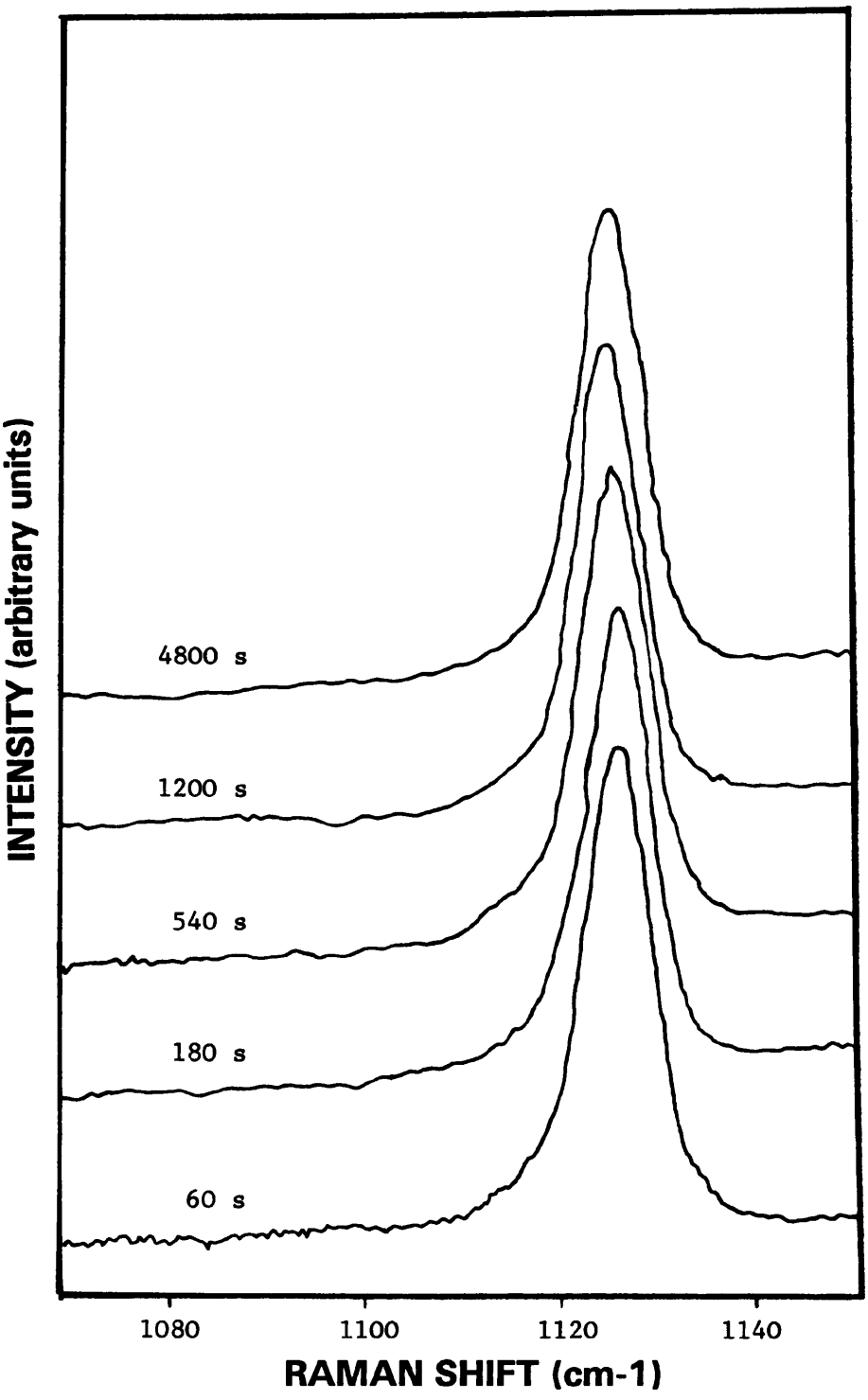

Fig.5.34 The Raman spectra of the C-C symmetric stretching mode of the monofilament of Fibre B upon creep experiment at constant stress of 0.5 GPa.

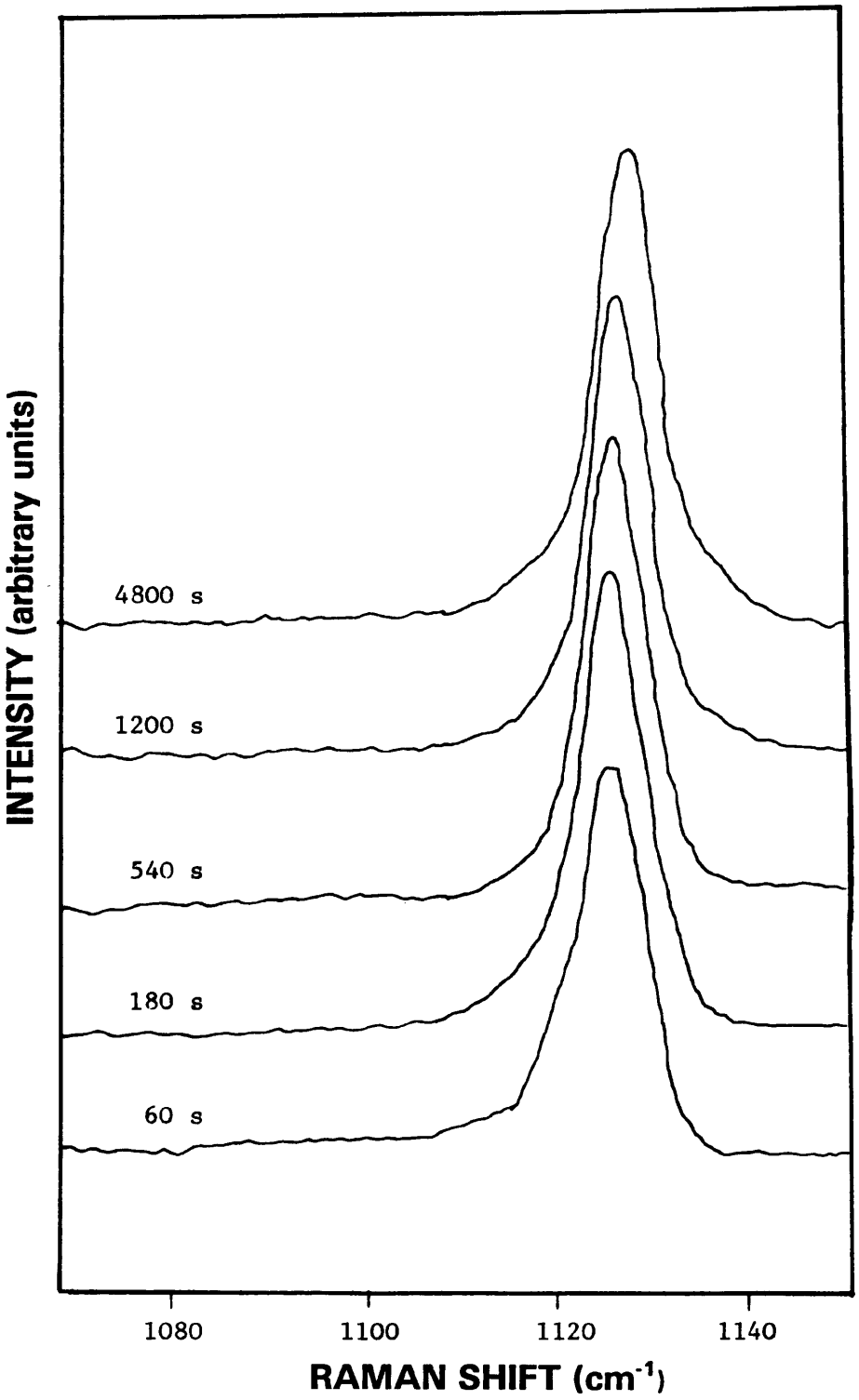

Fig.5.35 The Raman spectra of the C-C symmetric stretching mode of the monofilament of Fibre C upon creep experiment at constant stress of 0.5 GPa.

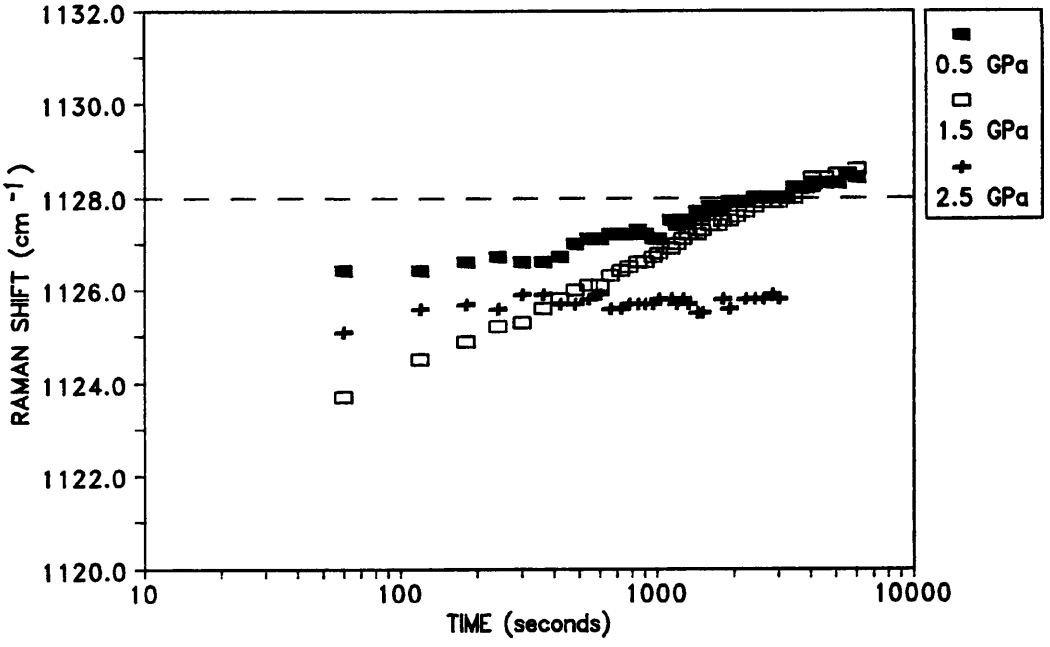

(a)

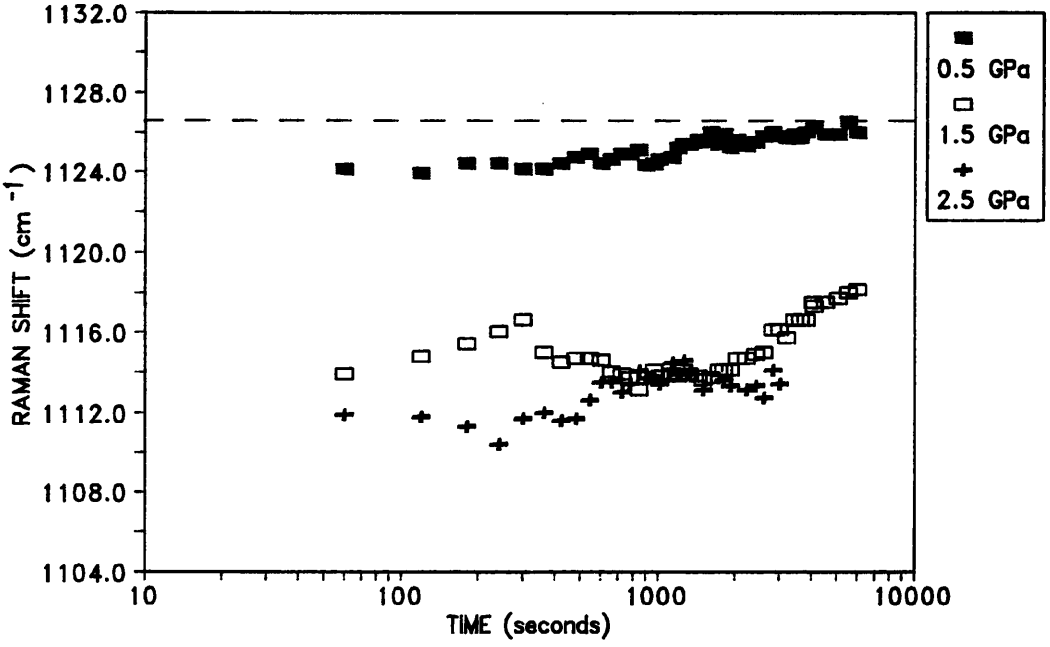

(b)

Fig.5.36 The Raman shift/time curves of (a) narrow, and (b) broad peaks for the monofilaments of Fibre A during creep experiment at constant stresses of 0.5, 1.5 and 2.5 GPa.

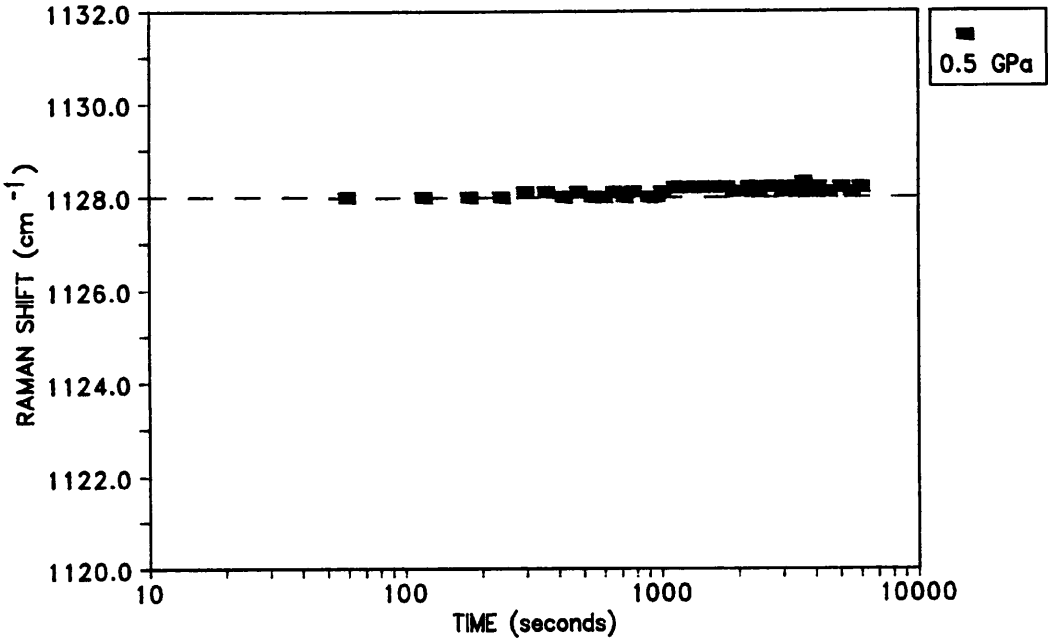

(a)

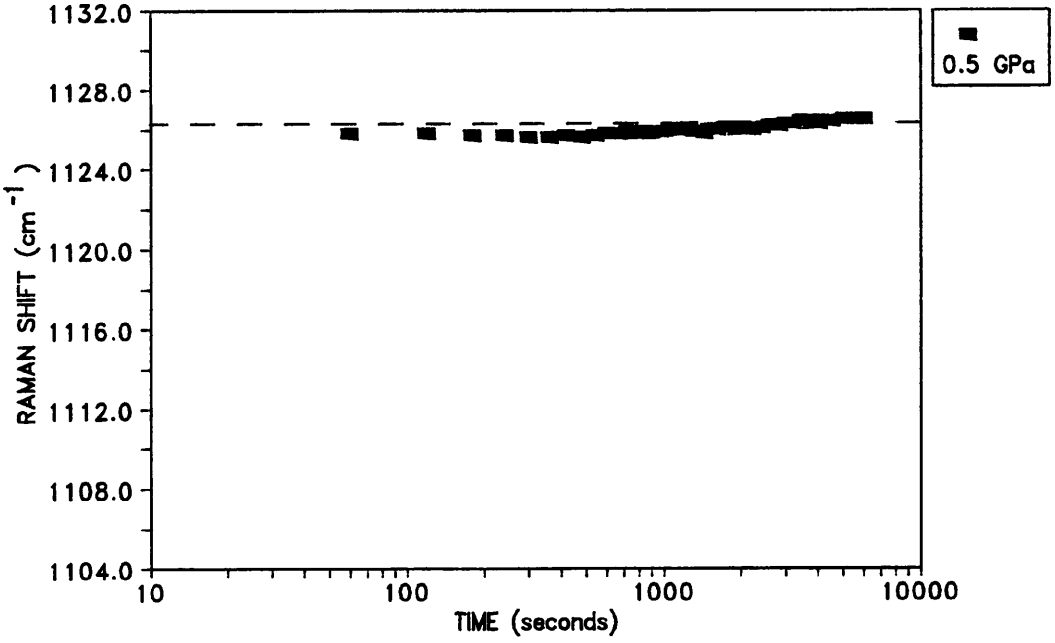

(b)

Fig.5.37 The Raman shift/time curves of (a) narrow, and (b) broad peaks for the monofilaments of Fibre B during creep experiment at constant stress of 0.5 GPa.

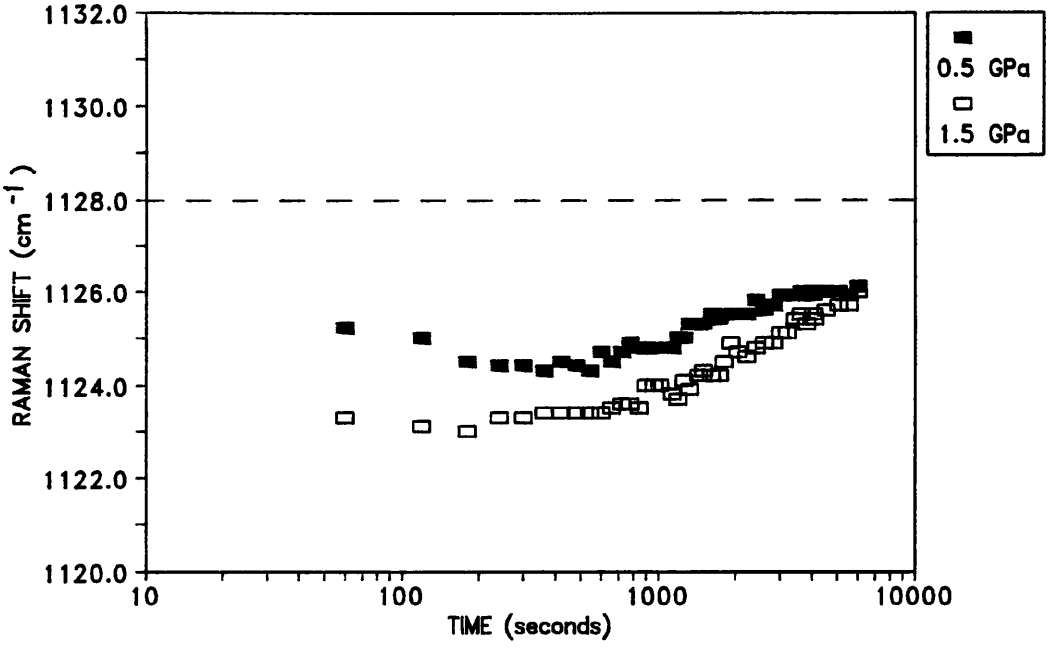

(a)

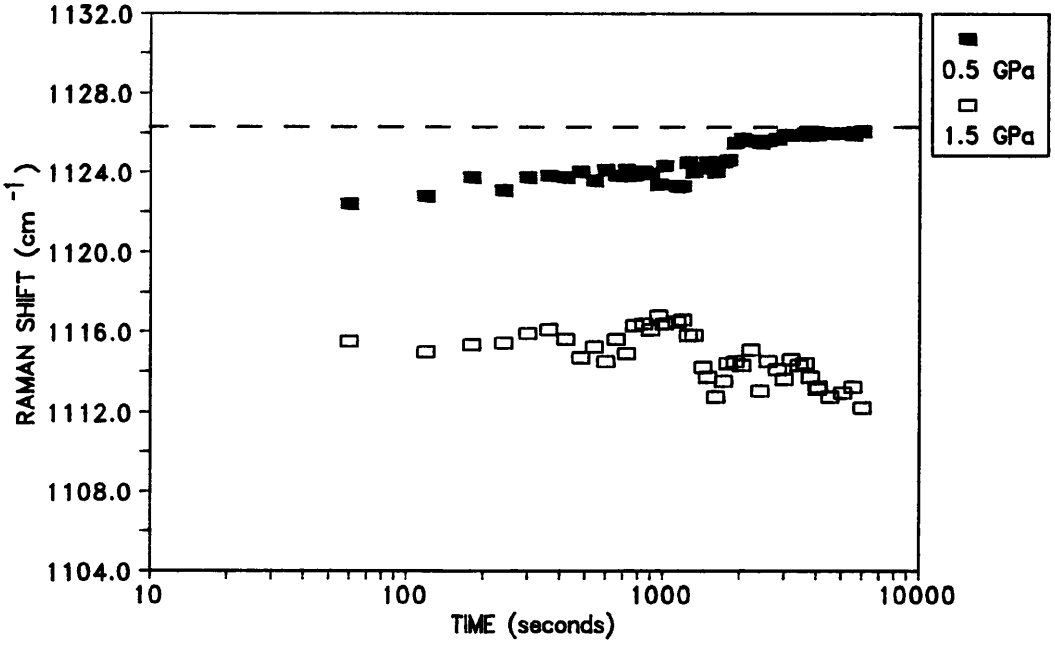

(b)

Fig.5.38 The Raman shift/time curves of (a) narrow, and (b) broad peaks for the monofilaments of Fibre C during creep experiment at constant stresses of 0.5 and 1.5 GPa.

monofilaments of Fibres B as shown in Fig.5.31. Although Fibre C shows a similar molecular behaviour of the Raman peaks shift toward the initial position, there is no sign of positive shift relative to the original position (Fig.5.32).

Fig.5.33-5.35 show the Raman spectra of Fibres A, B and C, respectively, during the creep experiments of the monofilaments. Again, the peak positions of the Raman bands shift toward the original position (i.e. higher frequency) even though the monofilament is under constant applied stress (Fig.5.36-5.38). However, the shifts are not as significant as those in stress relaxation and, apparently for Fibre A only the low-load bearing bands (narrow peak) show a positive shift relative to the original position at constant stresses of 0.5 GPa and 1.5 GPa after ~1500 seconds while Fibre B showsa relatively insignificant change of Raman shift during the creep experiment. Also, no positive shift was found in the creep experiment for Fibre C which is the highest modulus gel-spun PE fibres. However based on the microfibrillar model [23-24], the molecular deformation behaviour will be discussed in Chapter 6.

5.5 CHARACTERIZATION OF MOLECULAR BEHAVIOUR

Section 5.4 has demonstrated that Raman microscopy can be used to follow the molecular response of the PE monofilaments upon different modes of deformation. By using simultaneously Raman shift/stress/strain measurements, it has been possible to characterize the molecular behaviour of various PE monofilaments and to follow the effect of different processing parameters upon this molecular response. It is anticipated that this may enable

us to understand the factors which will allow enhancement of the mechanical properties of the fibres.

With the attachment of the 5N load cell onto the straining rig (Fig.5.6), it was possible to measure the values of Raman shift, stress and strain simultaneously. Fig.5.39a-5.47a show the Raman spectra of the monofilaments obtained at 0.0% and 4.0% strains for all the fibres used in this work (Table 3.1). In addition, the peak positions of both low-load (narrow peak) and high-load (broad peak) bearing C-C symmetric bands together with the stress response of the monofilaments are plotted against the strain (Fig.5.39b-Fig.5.47b). The values of stress were obtained at the end of each scan when the stress relaxation reached a plateau level (Fig.5.7a).

From the Raman shift/strain plots, it is possible to define three stages (i.e. 1, 2 and 3) of molecular behaviour of the monofilament upon straining. This is based on the effect of yielding upon both the low-load (narrow peak) and high-load (broad peak) bearing bands. The low-load bearing band shifts linearly with strain in Stage 1 before yielding whereas the high-load bearing band extends its linearity with strain to Stage 2 before it yields. Eventually the fibre fractures in Stage 3. Correspondingly, the values of modulus of the stress-strain curve (at the strain rate of 1.33×10^{-4} s^{-1}) for different stages of molecular behaviour are tabulated in Table 5.4. Obviously, the moduli obtained are much lower than those obtained by stress-strain measurements in Section 4.4 (at the strain rate of 1.67×10^{-3} s^{-1}) due to the effect of lower strain rates. However, the values of modulus are clearly decreasing from Stage 1 to 3

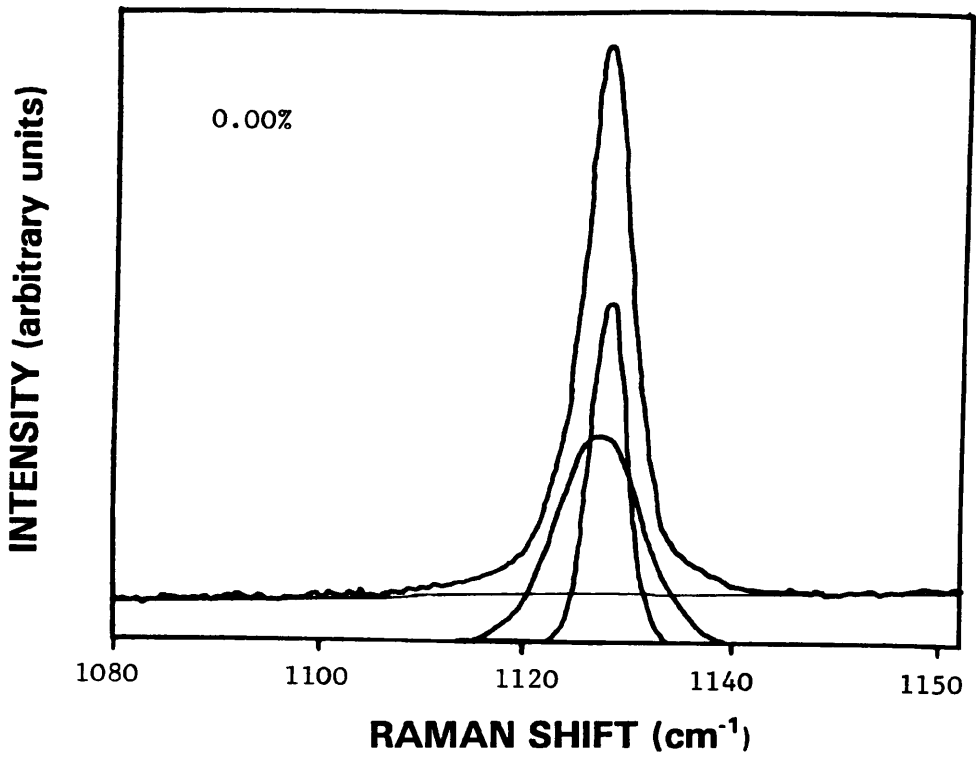

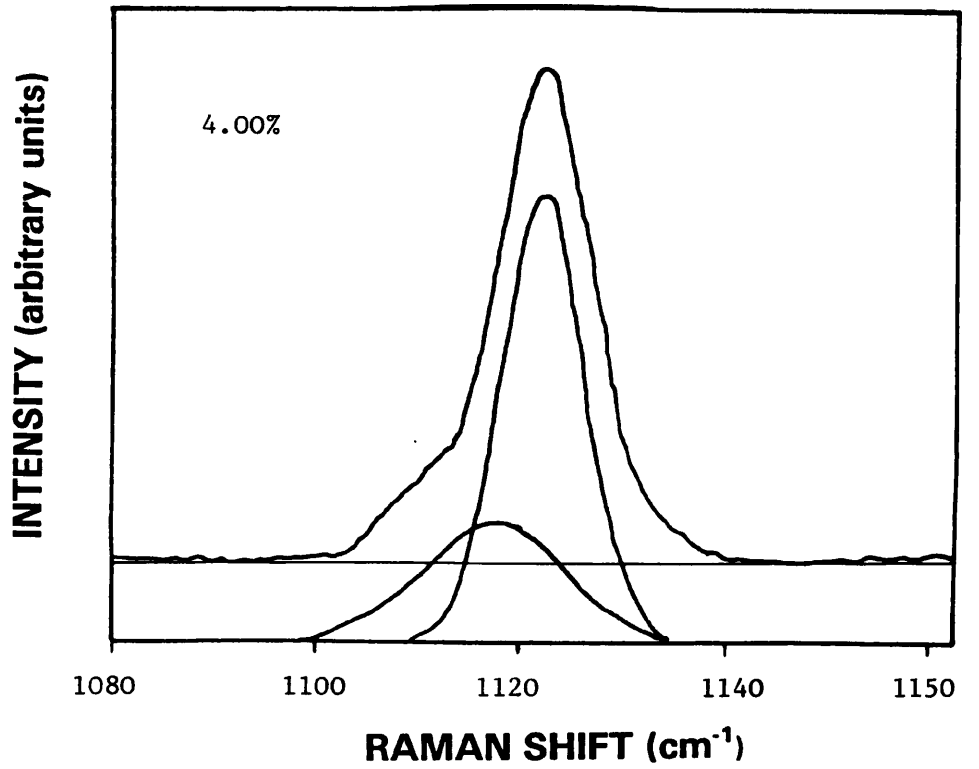

Fig.5.39a The Raman spectra of the C-C symmetric stretching mode of the monofilaments of Fibre A at 0.0% and 4.0% strains.

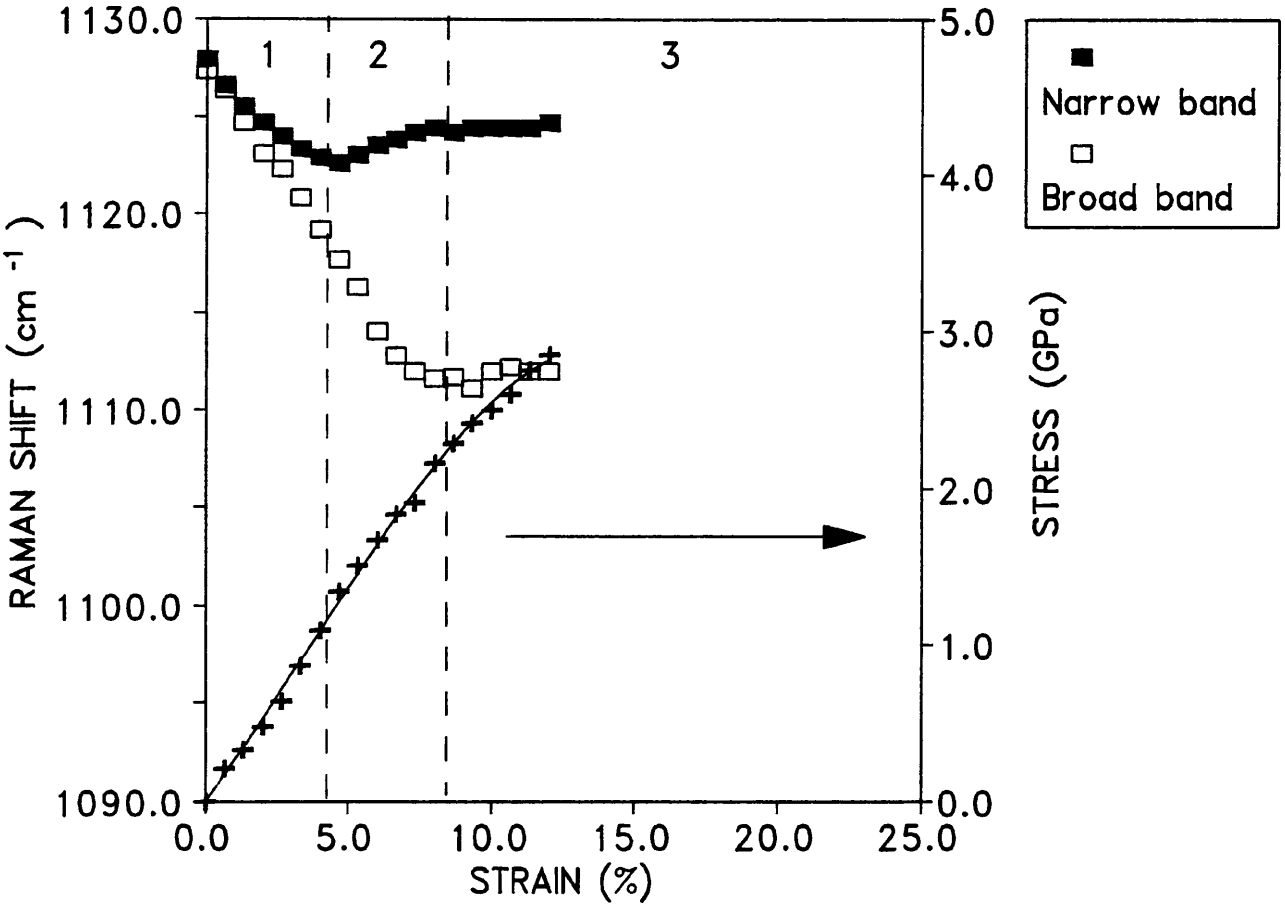

Fig.5.39b The values of Raman shift and stress plotted against the applied strain simultaneously for the monofilaments of Fibre A at constant strain rate of 1.33×10^{-4} s^{-1}.

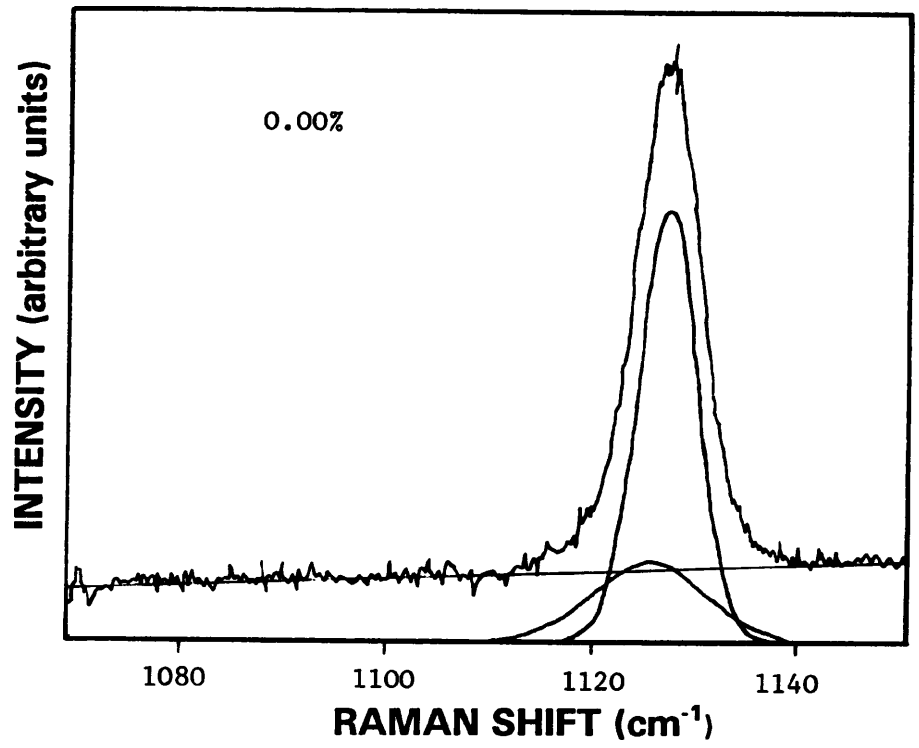

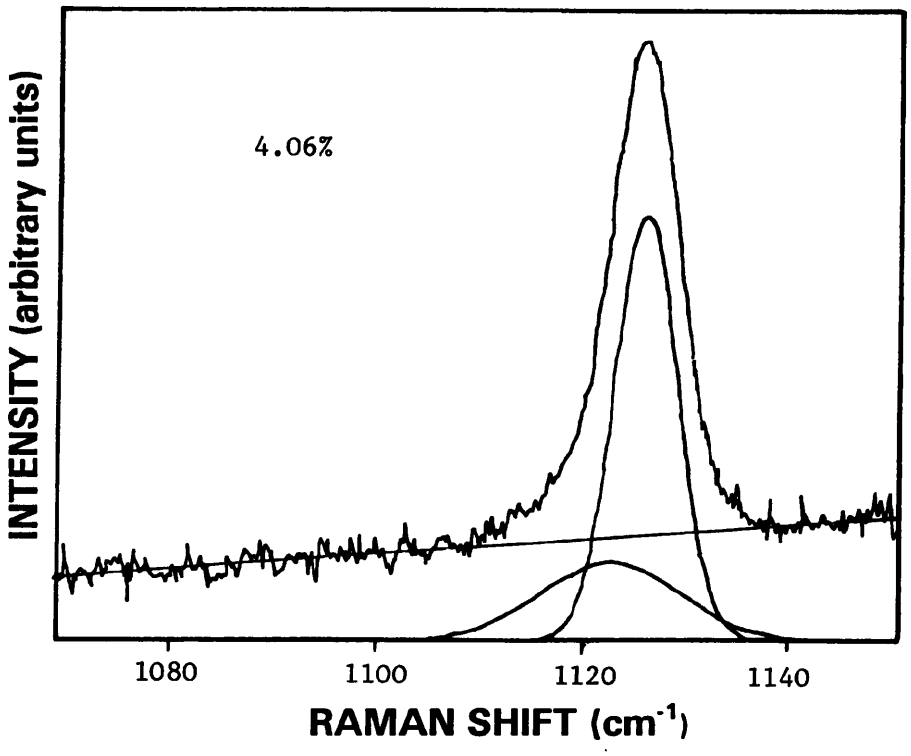

Fig.5.40a The Raman spectra of the C-C symmetric stretching mode of the monofilaments of Fibre B at 0.0% and 4.0% strains.

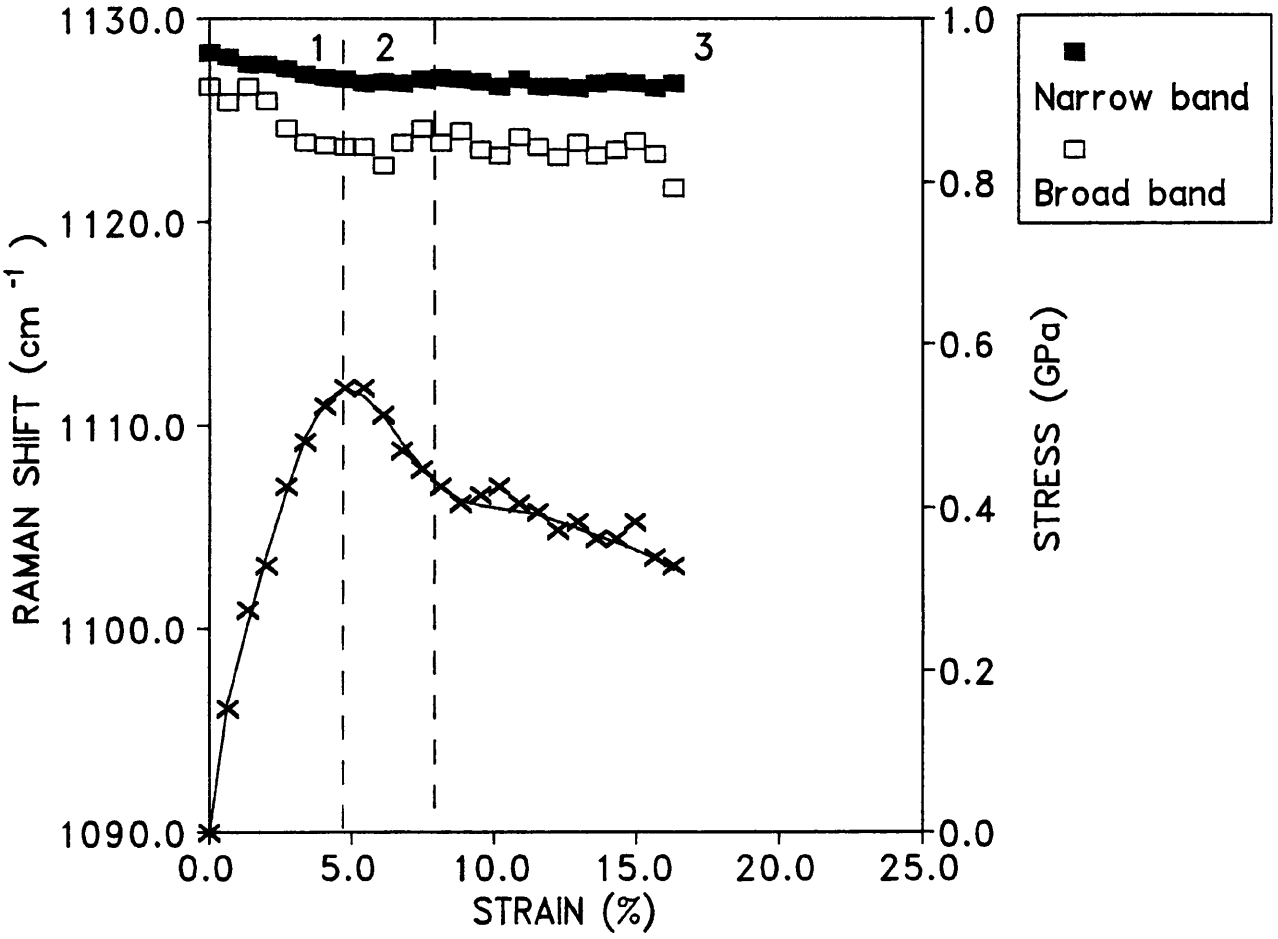

Fig.5.40b The values of Raman shift and stress plotted against the applied strain simultaneously for the monofilaments of Fibre B at constant strain rate of 1.33×10^{-4} s^{-1}.

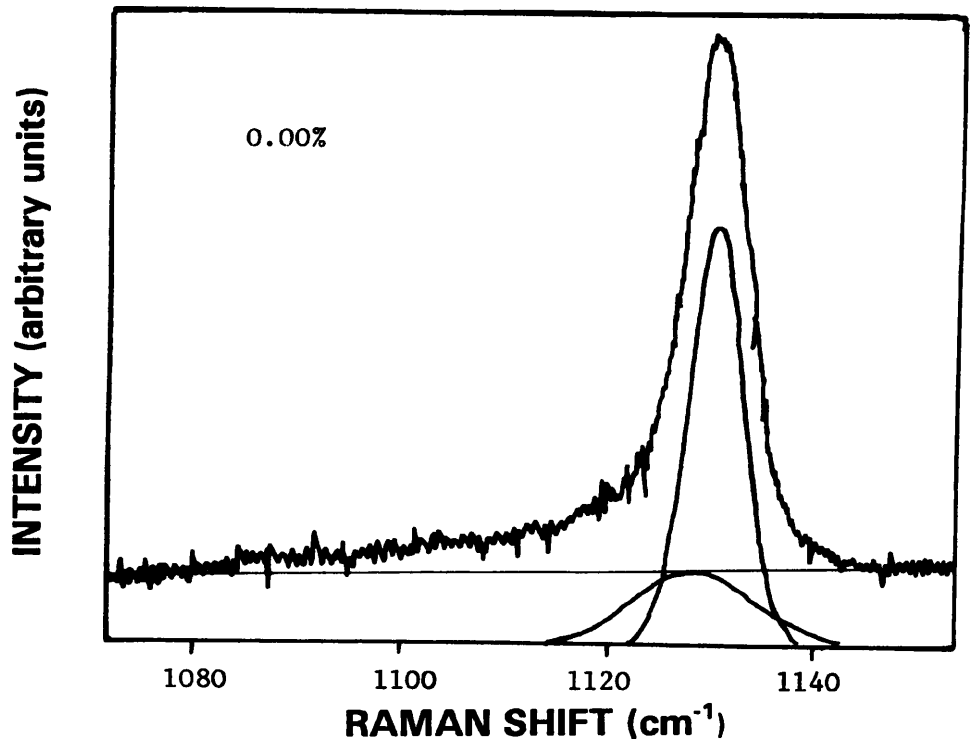

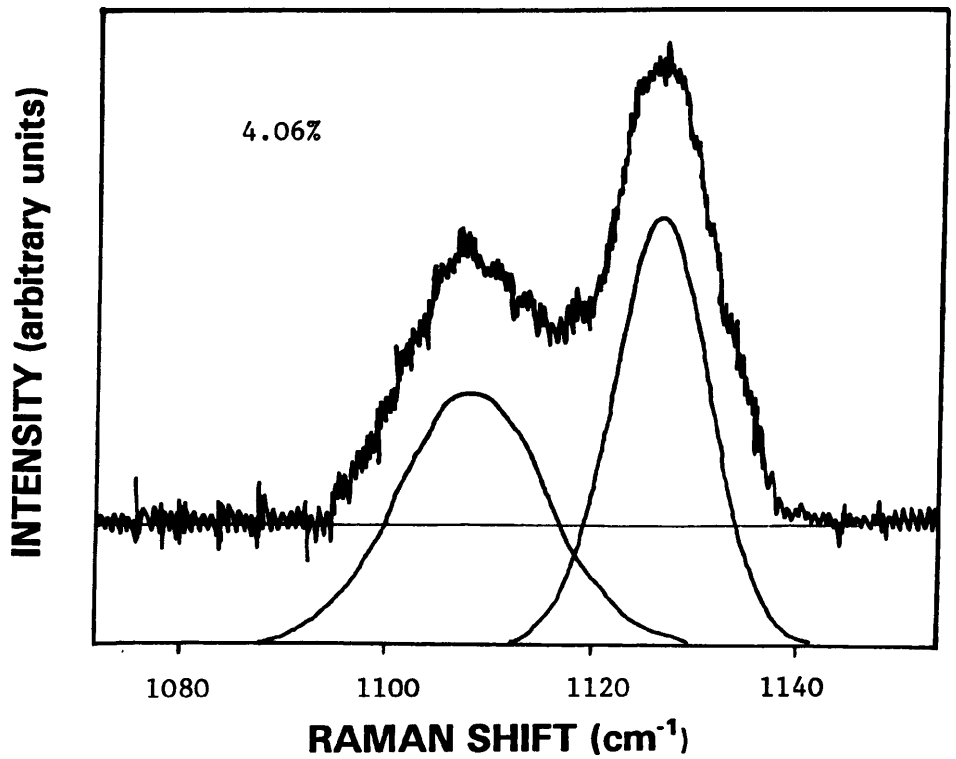

Fig.5.41a The Raman spectra of the C-C symmetric stretching mode of the monofilaments of Fibre C at 0.0% and 4.0% strains.

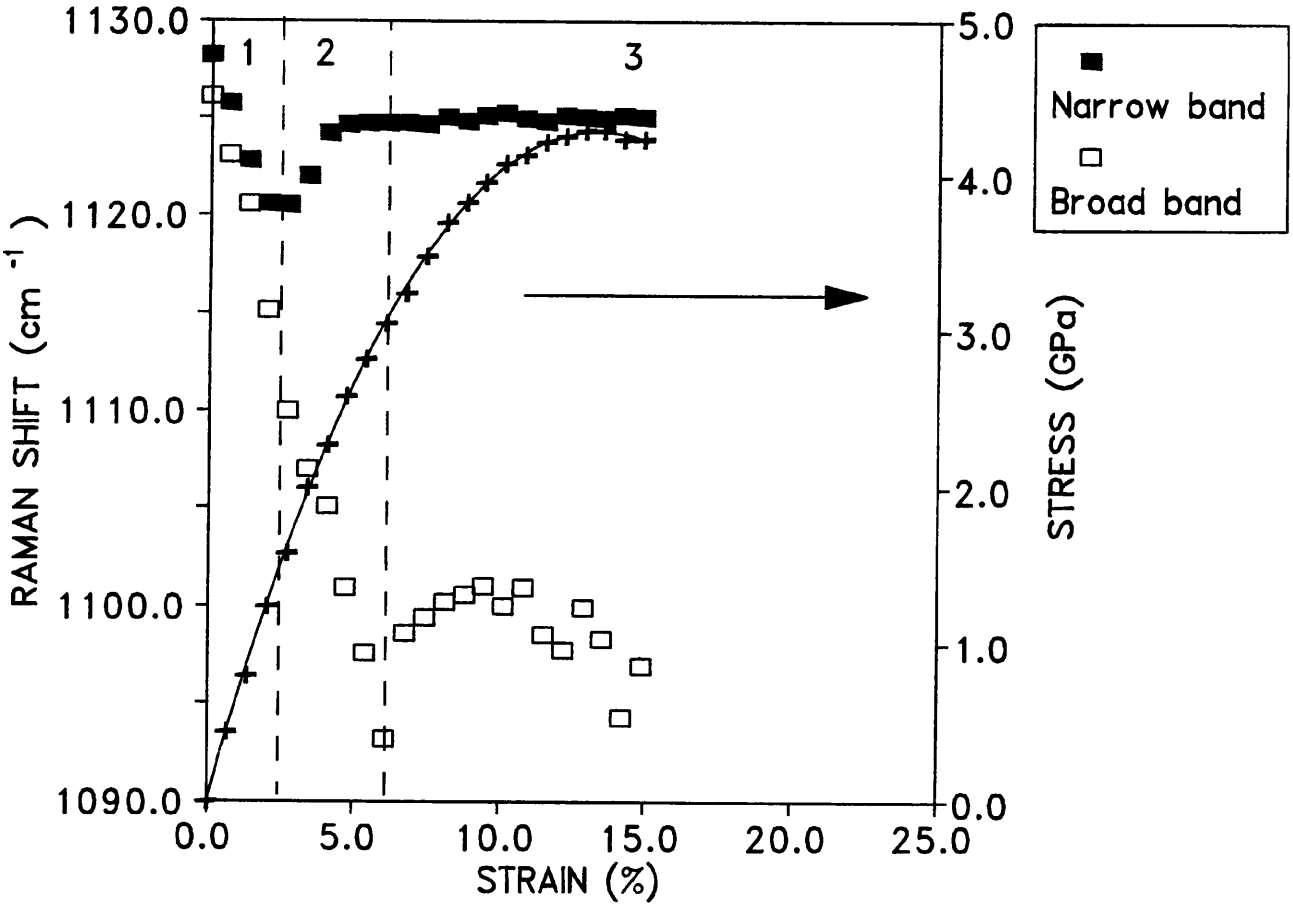

Fig.5.41b The values of Raman shift and stress plotted against the applied strain simultaneously for the monofilaments of Fibre C at constant strain rate of 1.33×10^{-4} s^{-1}.

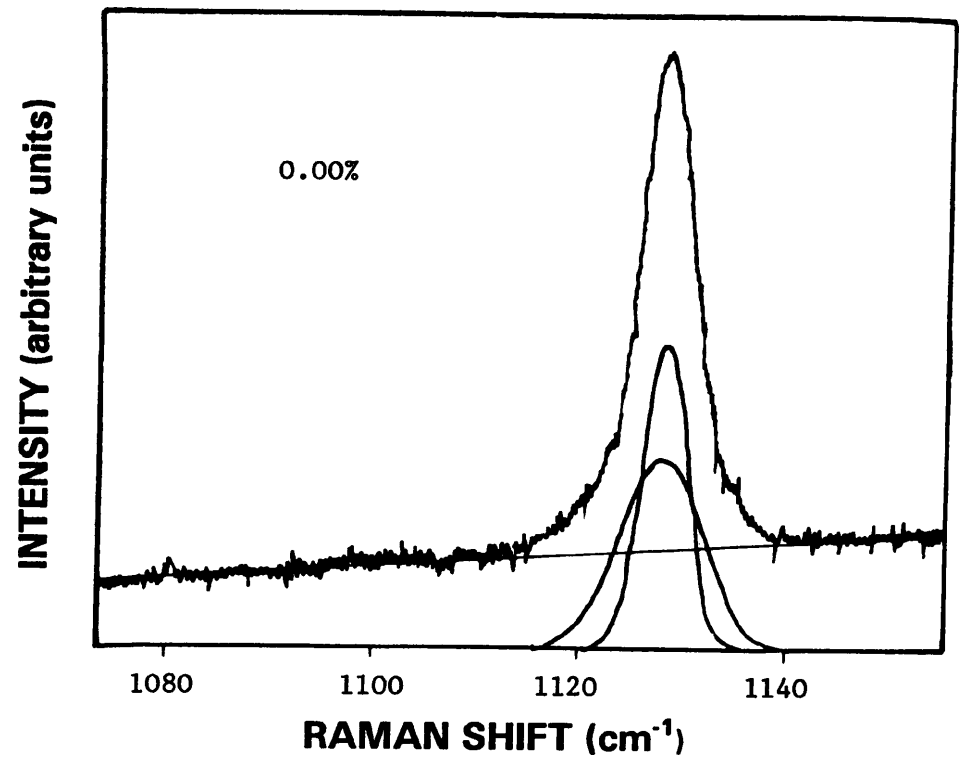

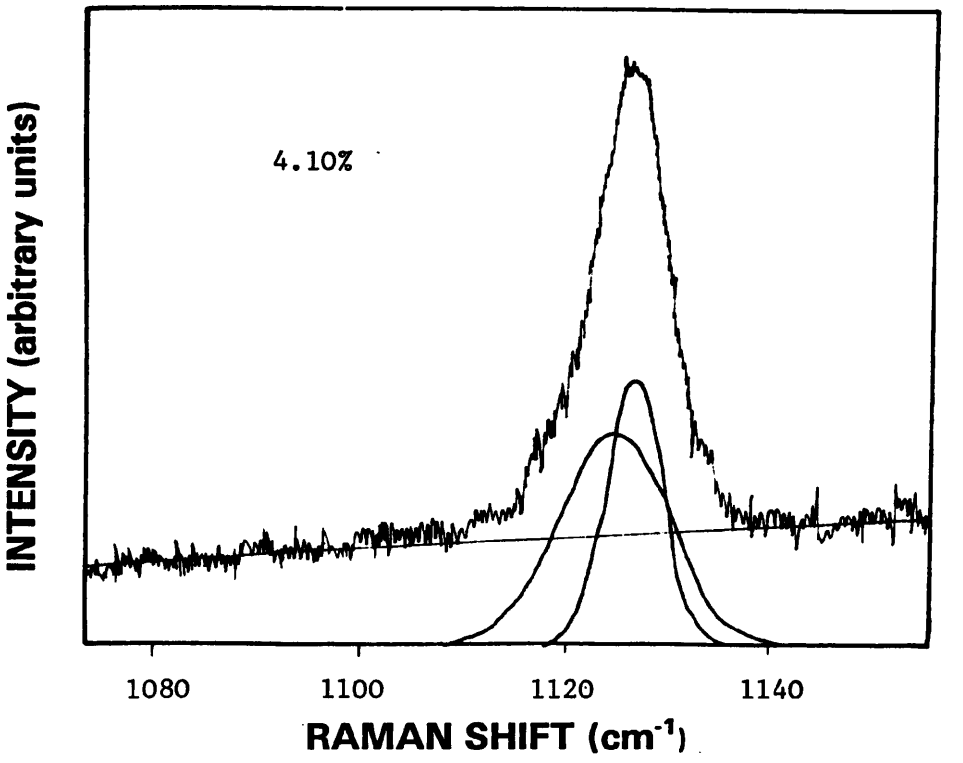

Fig.5.42a The Raman spectra of the C-C symmetric stretching mode of the monofilaments of Fibre D at 0.0% and 4.0% strains.

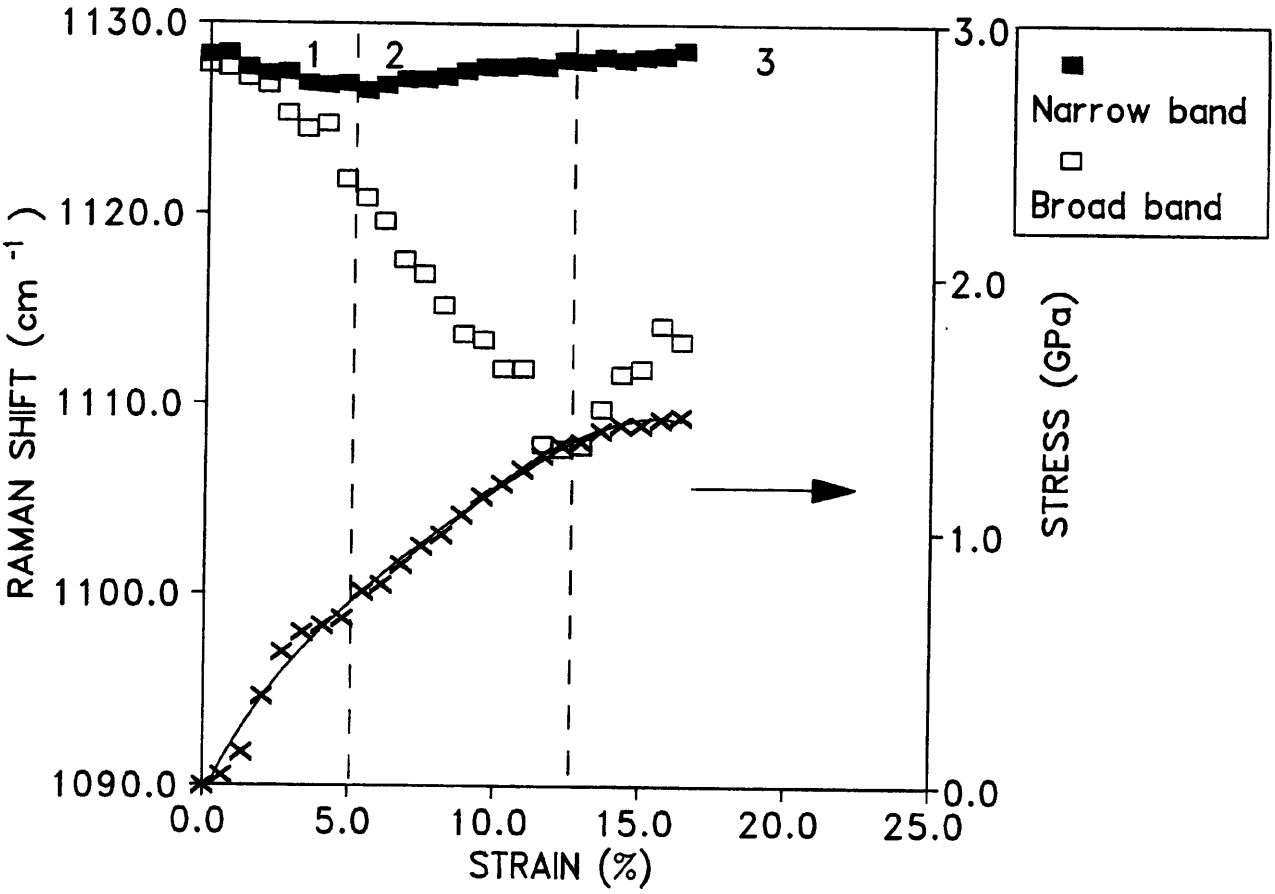

Fig.5.42b The values of Raman shift and stress plotted against the applied strain simultaneously for the monofilaments of Fibre D at constant strain rate of 1.33×10^{-4} s^{-1}.

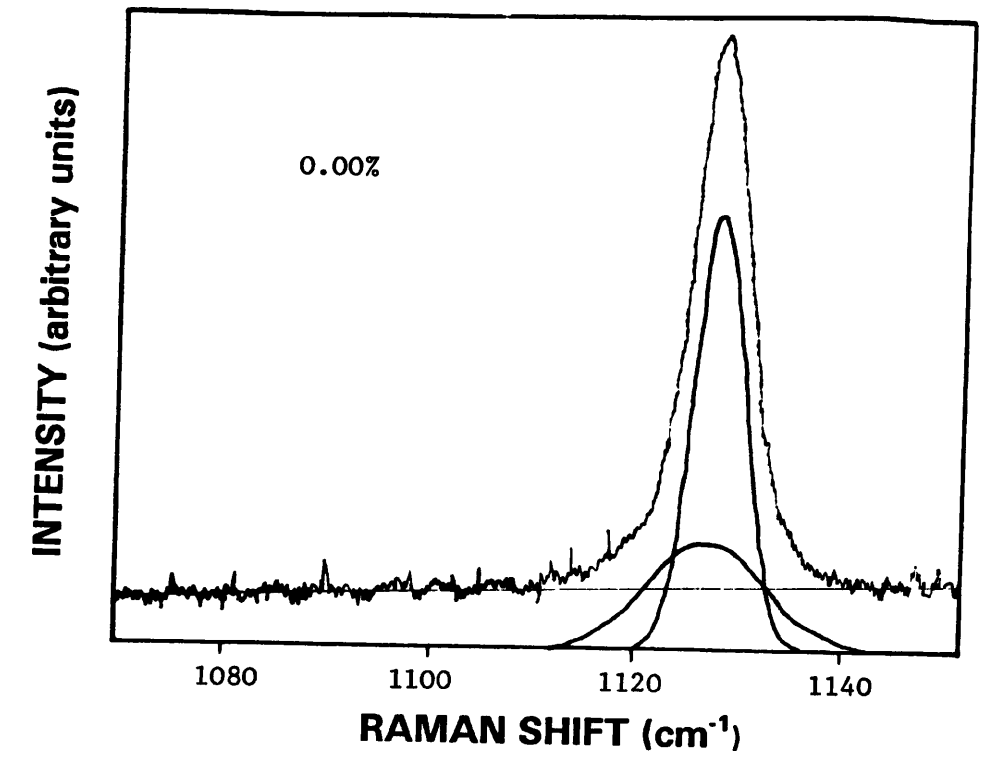

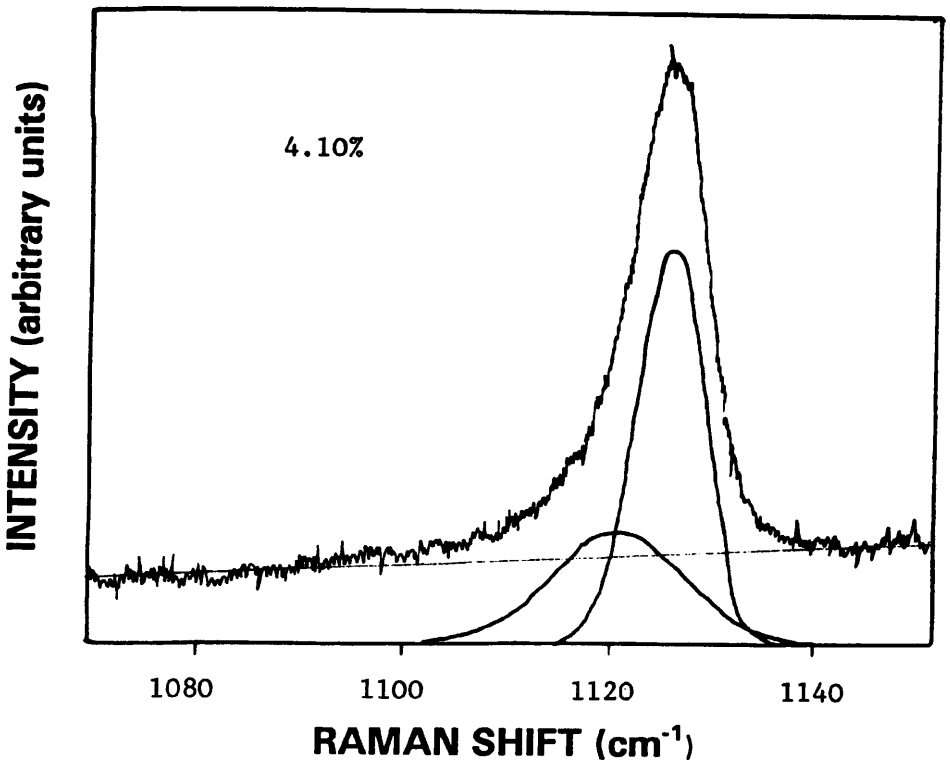

Fig.5.43a The Raman spectra of the C-C symmetric stretching mode of the monofilaments of Fibre E at 0.0% and 4.0% strains.

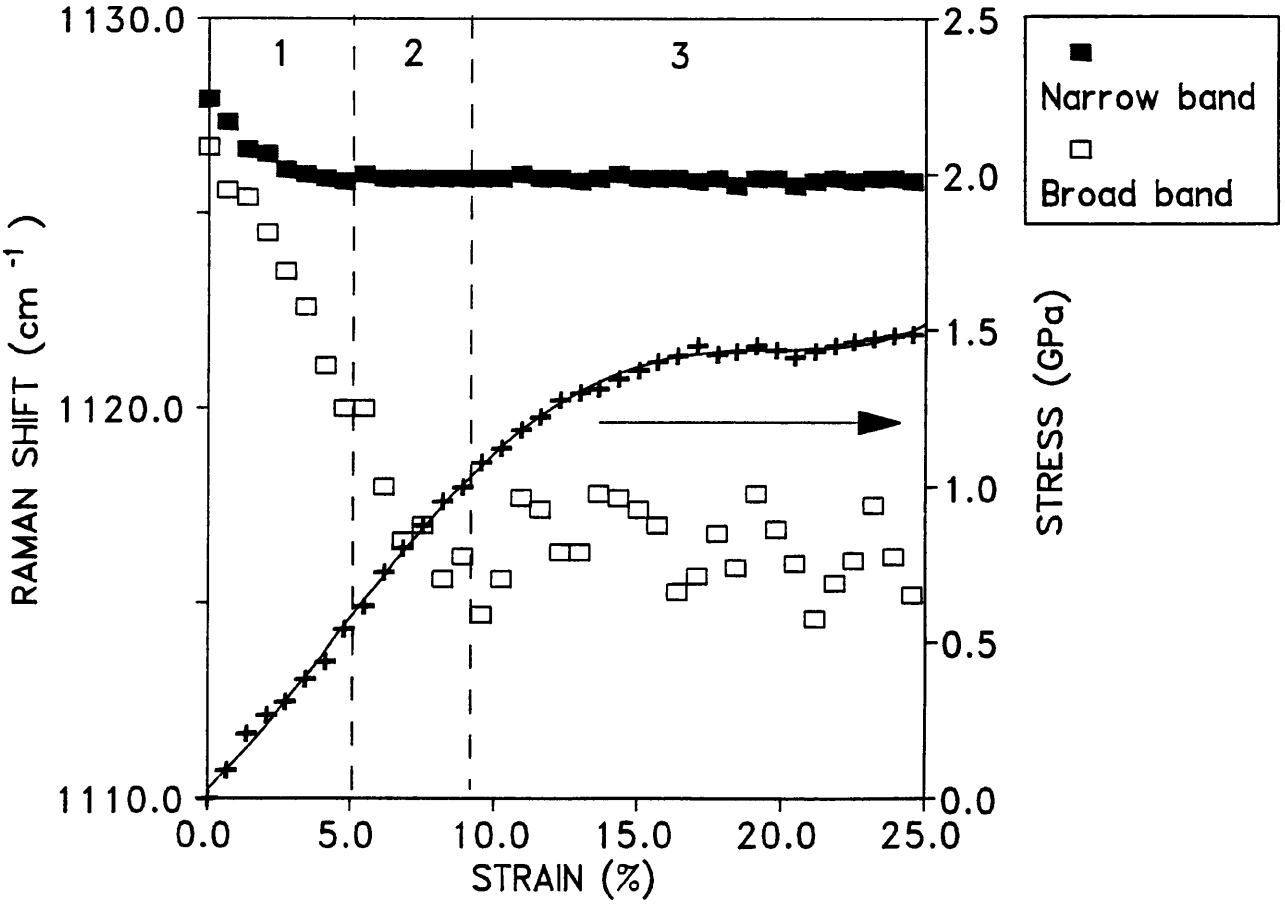

Fig.5.43b The values of Raman shift and stress plotted against the applied strain simultaneously for the monofilaments of Fibre E at constant strain rate of 1.33×10^{-4} s^{-1}.

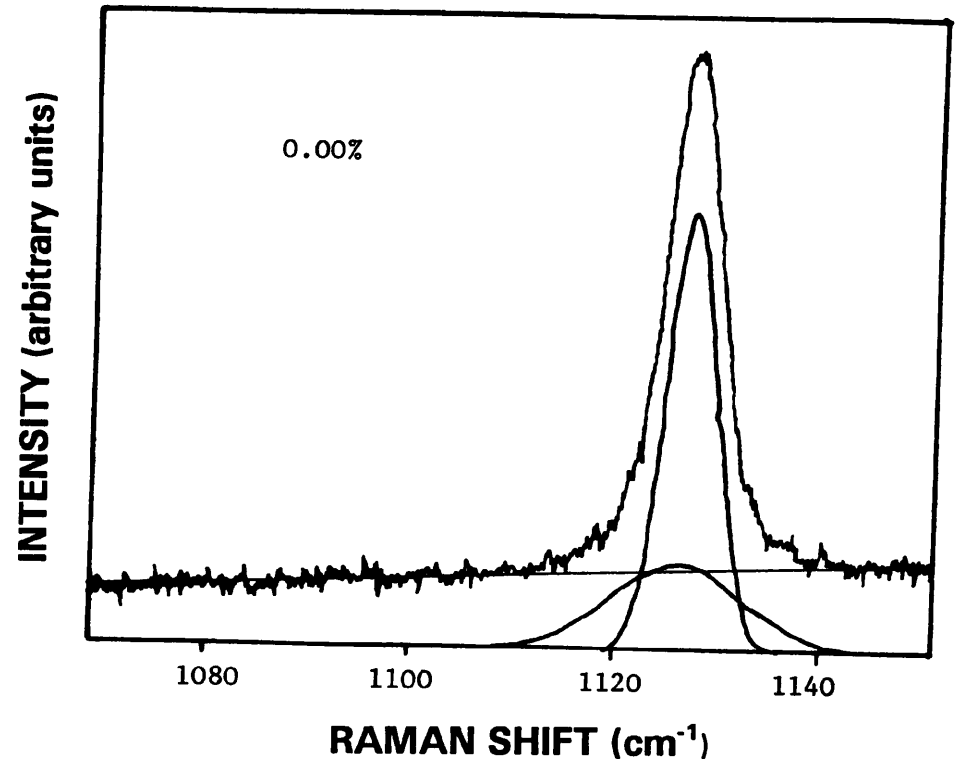

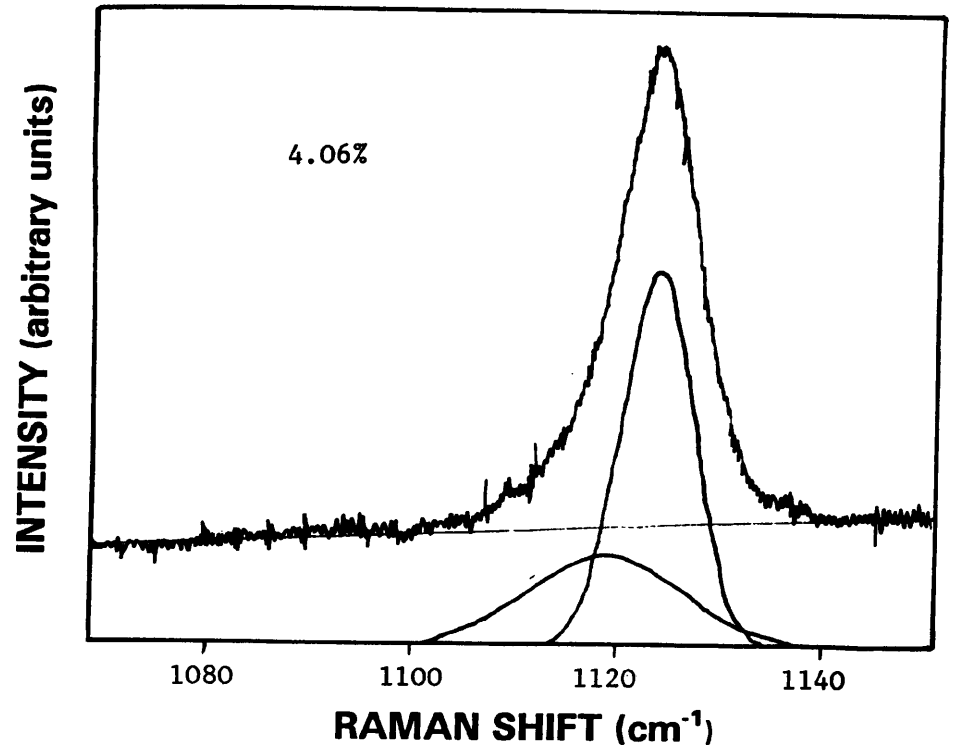

Fig.5.44a The Raman spectra of the C-C symmetric stretching mode of the monofilaments of Fibre F at 0.0% and 4.0% strains.

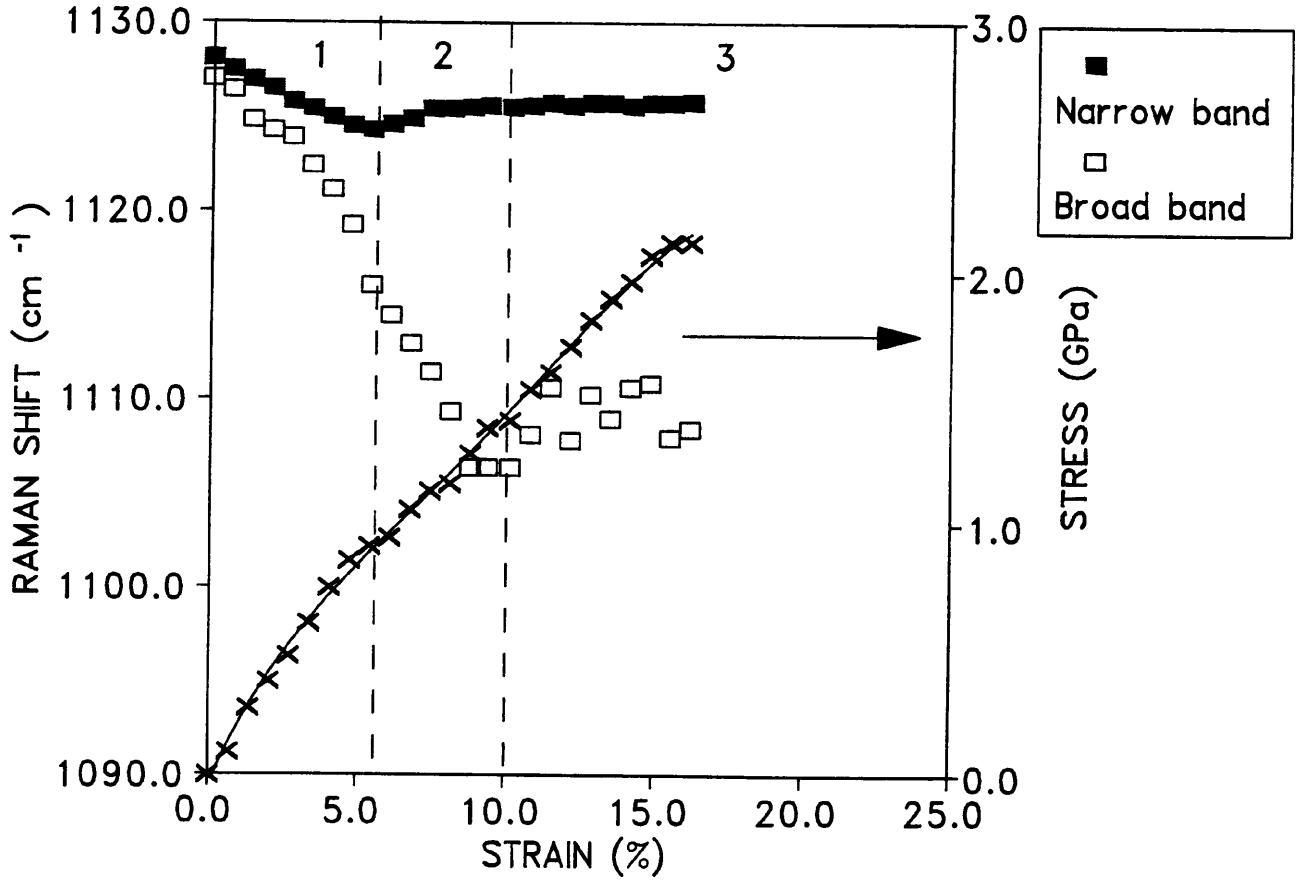

Fig.5.44b The values of Raman shift and stress plotted against the applied strain simultaneously for the monofilaments of Fibre F at constant strain rate of 1.33×10^{-4} s^{-1}.

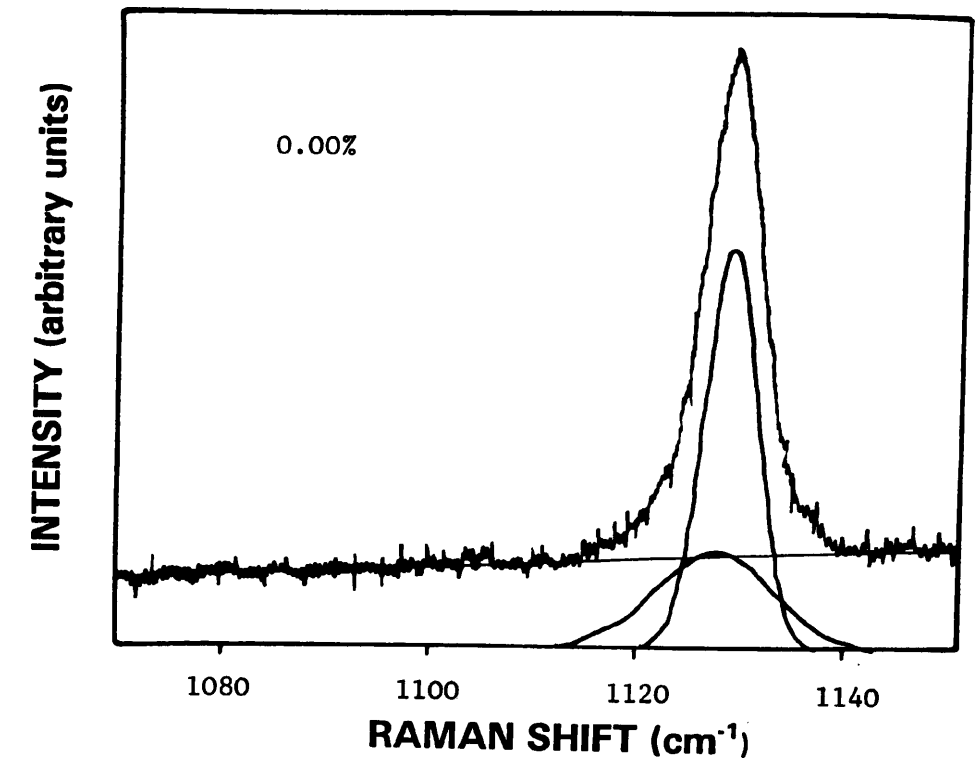

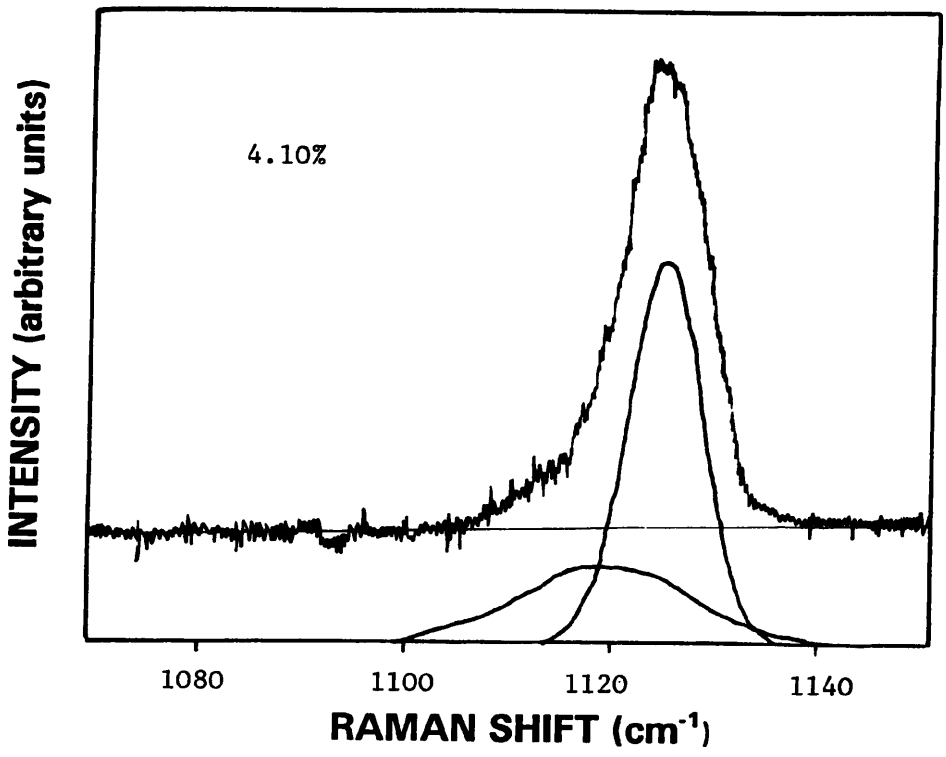

Fig.5.45a The Raman spectra of the C-C symmetric stretching mode of the monofilaments of Fibre G at 0.0% and 4.0% strains.

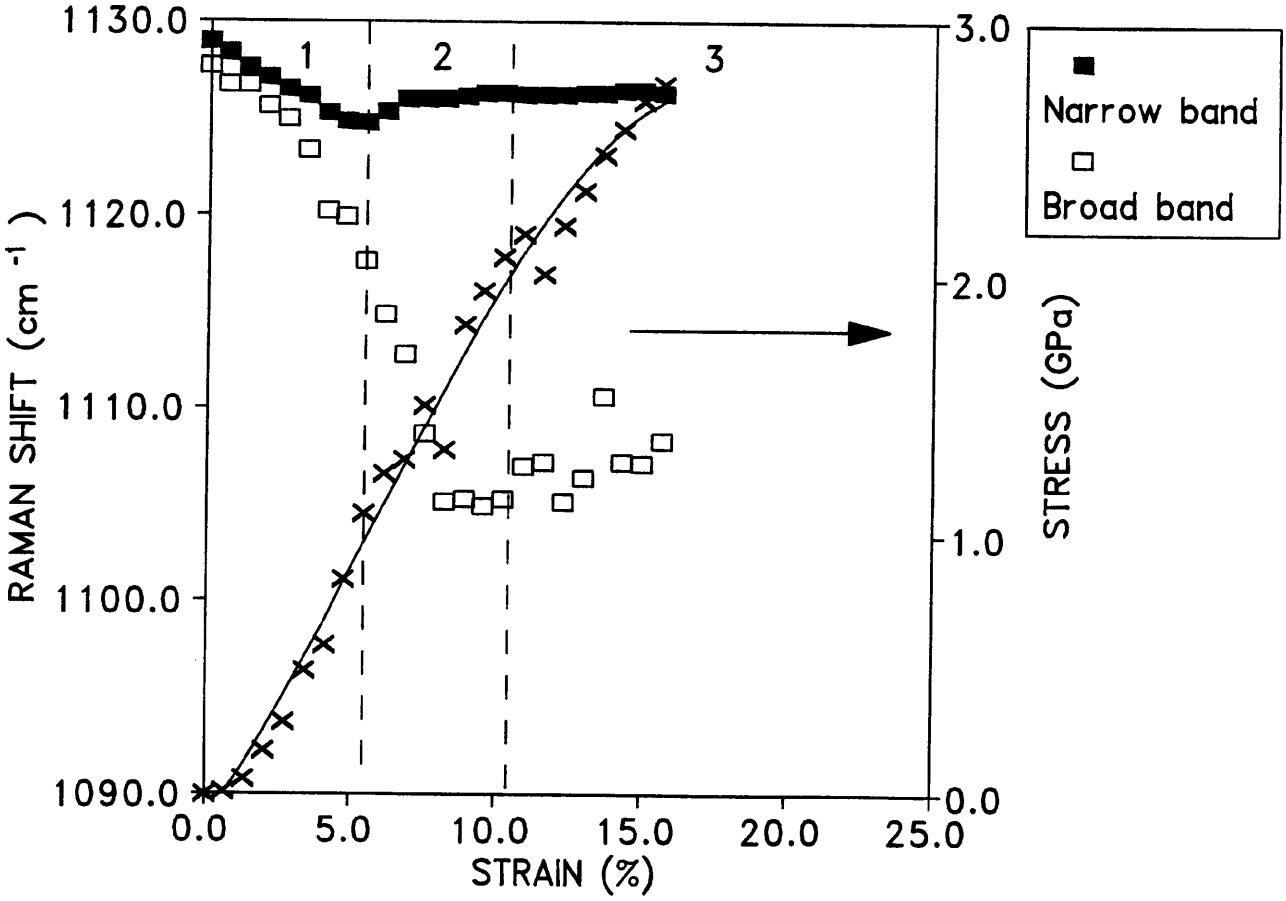

Fig.5.45b The values of Raman shift and stress plotted against the applied strain simultaneously for the monofilaments of Fibre G at constant strain rate of 1.33×10^{-4} s^{-1}.

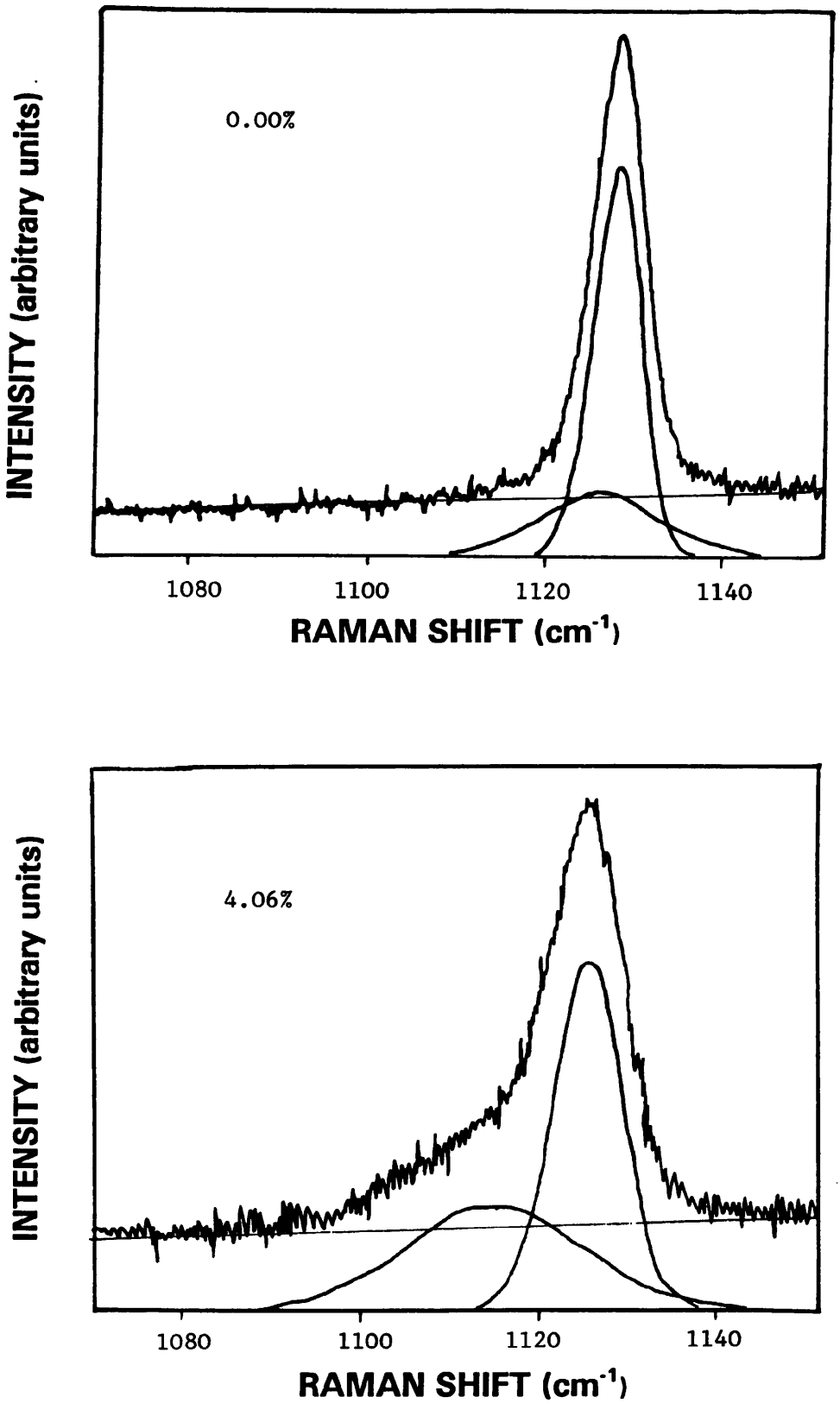

Fig.5.46a The Raman spectra of the C-C symmetric stretching mode of the monofilaments of Fibre H at 0.0% and 4.0% strains.

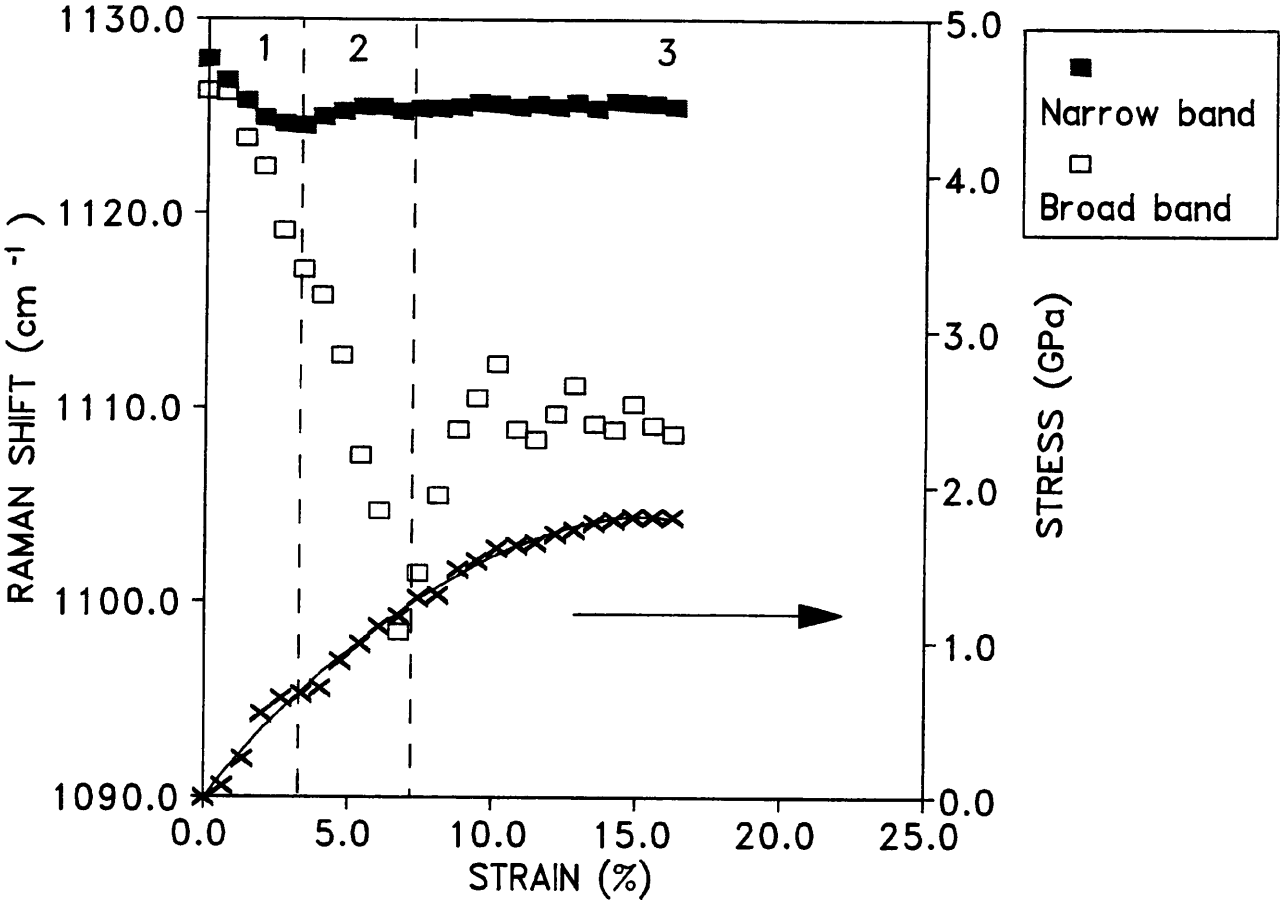

Fig.5.46b The values of Raman shift and stress plotted against the applied strain simultaneously for the monofilaments of Fibre H at constant strain rate of 1.33×10^{-4} s^{-1}.

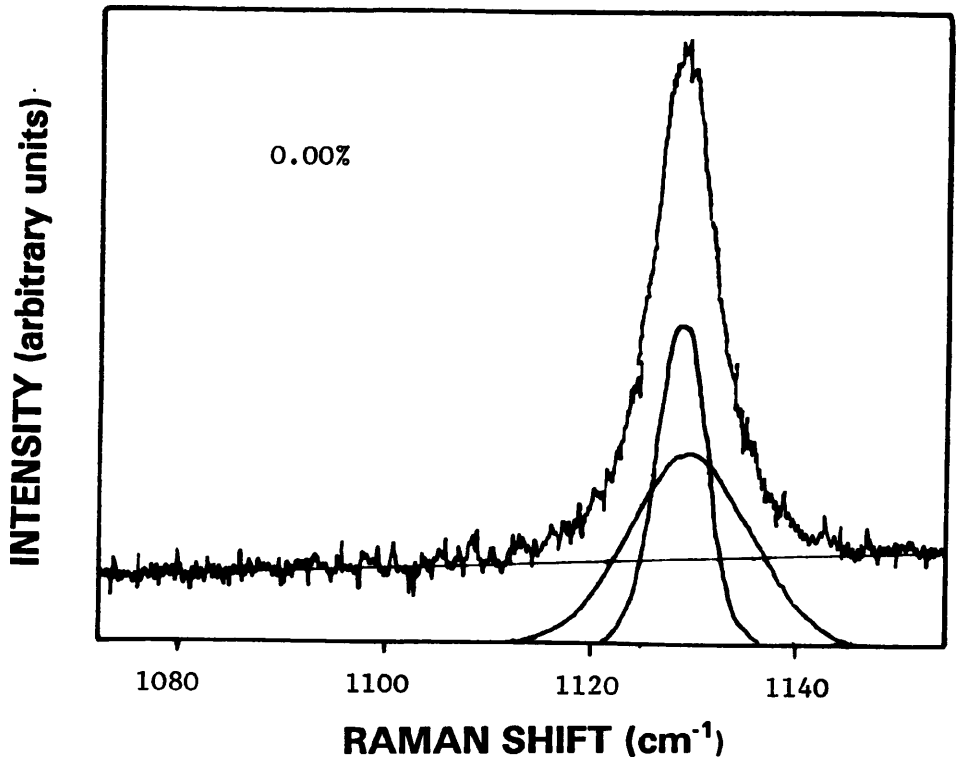

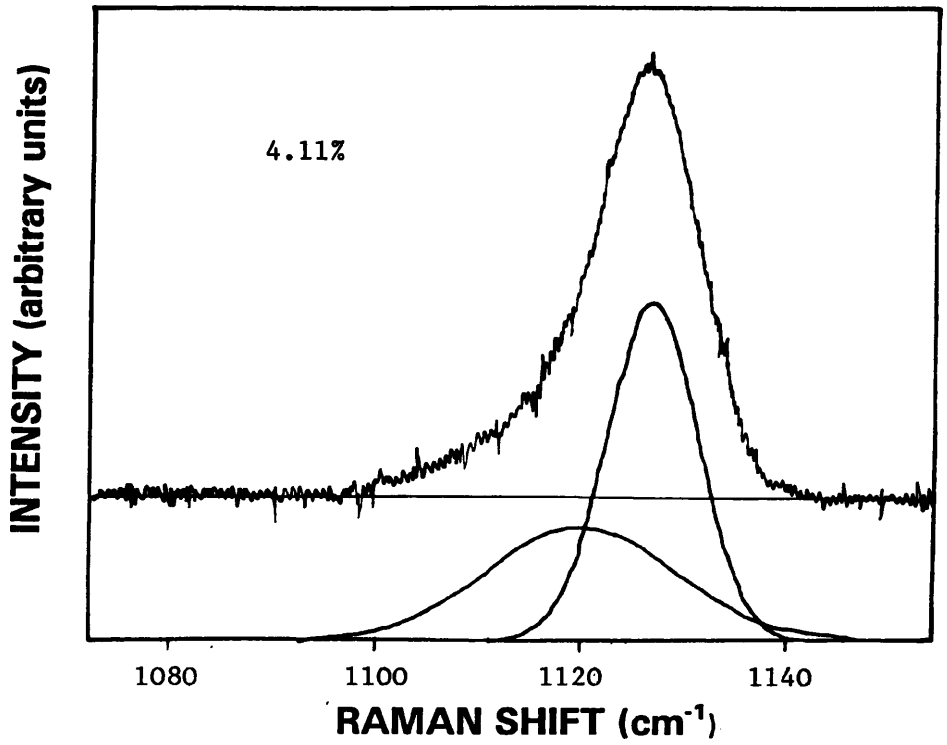

Fig.5.47a The Raman spectra of the C-C symmetric stretching mode of the monofilaments of Fibre I at 0.0% and 4.0% strains.

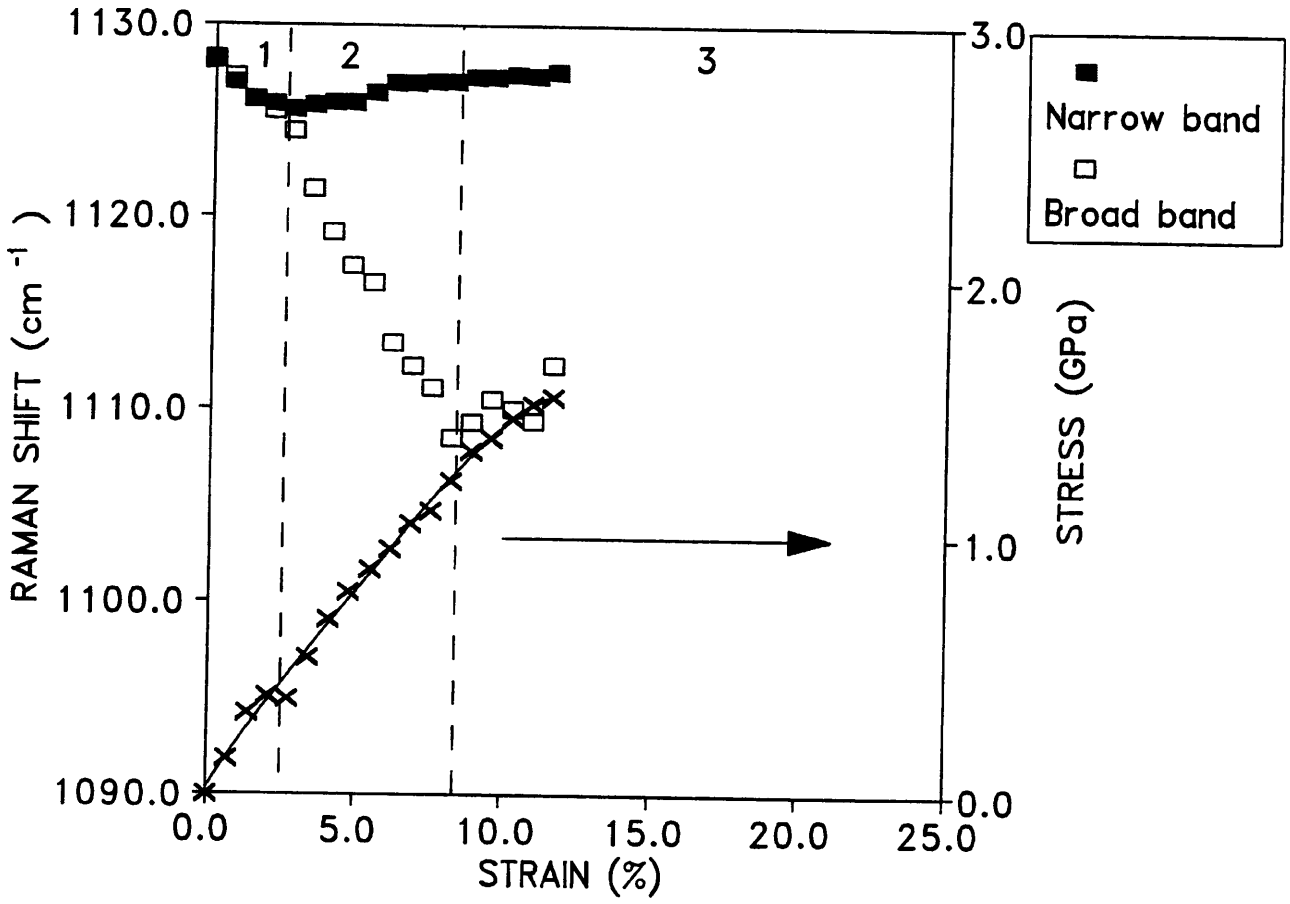

Fig.5.47b The values of Raman shift and stress plotted against the applied strain simultaneously for the monofilaments of Fibre I at constant strain rate of 1.33×10^{-4} s^{-1}.

Table 5.4

THE VALUES OF MODULI AT STAGES 1, 2 AND 3 OF THE MOLECULAR BEHAVIOUR FOR THE STRESS-STRAIN CURVES AT THE STRAIN RATE OF $1.33 \times 10^{-4} s^{-1}$ FOR ALL THE SAMPLES.

Fibre	Modulus at Stage 1 (GPa)	Modulus at Stage 2 (GPa)	Modulus at Stage 3 (GPa)
A	27.3	26.8	17.3
B	16.0	5.9	4.9
C	58.6	43.6	28.4
D	16.9	8.8	3.7
E	11.2	11.0	7.1
F	16.6	12.6	12.3
G	21.2	20.1	11.4
H	19.7	14.5	11.3
I	18.6	14.4	12.7

for all the monofilaments. In fact, both the low-load and high-load bearing C-C symmetric bonds appear to be equally important in determining the highest value of modulus in Stage 1 (which is equivalent to tensile modulus, *E*). In Stage 2, however, the low-load bearing C-C bonds were subjected to decreasing stress while the high-load bearing C-C bonds remained contributing to the mechanical performance of the monofilament. Interestingly, Fibre B which is the melt-spun conventional PE fibre shows a significant drop in stress before fracture (Fig.5.40). Such a phenomenon was not found in the gel-spun UHMW-PE fibres even though the straining was carried out at a very slow strain rate.

Although all the PE monofilaments behave in a similar way at the molecular level upon straining, the nature of the changes varies between different individual monofilaments (Table 5.3). Apparently at 4.0% strain, Fibre C shows the highest degree of

shift of the Raman bands and there are significant changes in band intensity corresponding to the possible appearance of more high-load bearing C-C bonds in the structure upon straining (Fig.5.41a). In fact, Fibre C shows the highest rate of shift ($d\Delta\nu/d\varepsilon$) for both the low-load and high-load bearing bands (Fig.5.41b) which correlates well with its corrected value of higher strain rate tensile modulus of 163.6 GPa (Table 4.2). Similarly, Fibre E which has the lowest tensile modulus (Table 4.2) also shows the lowest rate of shift (Fig.5.43b). However, there is an unique structure present in Fibre I as illustrated in Fig.5.47a. At 0.0% strain, the high-load bearing band is at a higher Raman frequency than the low-load bearing band. This is an indication that for this fibre the high-load bearing C-C bonds were in a state of compression compared to the low-load bearing C-C bonds. Such a behaviour could be due to the processing history and molecular structure of the fibre.

It is interesting to consider the relative area of the broad peak (high-load bearing band) compared to the total area of the 1128 cm^{-1} Raman band for individual monofilaments. Earlier discussion has mentioned that in the process of straining, it appears the high-load bearing C-C bonds are responsible for the high-performance properties of the monofilaments. However, this would not be possible if only a small fraction of the high-load bearing C-C bonds are present in the molecular structure. Table 5.5 shows the relative areas of the high-load bearing band with respect to the total area of the Raman band at different applied strains. The area of the individual peak was determined by integrating the area under the fitted Gaussian curve. Again,

Table 5.5

THE RELATIVE AREA OF THE BROAD PEAK TO THE TOTAL AREA OF THE 1128 cm^{-1} RAMAN BAND FOR PE MONOFILAMENTS AT DIFFERENT STRAINS.

Fibre	Relative Area of Broad Peak, $A_1/(A_1+A_2)^*$					
	0.0%	2.0%	4.0%	6.0%	8.0%	10.0%
A	0.42	0.38	0.28	0.43	0.49	0.53
B	0.33	0.30	0.34	0.33	0.32	0.33
C	0.29	0.34	0.45	0.70	0.75	0.48
D	0.53	0.34	0.57	0.29	0.30	0.37
E	0.35	0.41	0.37	0.42	0.32	0.37
F	0.35	0.35	0.38	0.38	0.46	0.58
G	0.36	0.37	0.32	0.44	0.41	0.49
H	0.26	0.41	0.42	0.40	0.47	0.44
I	0.59	0.50	0.43	0.49	0.55	0.54

* A_1 and A_2 are the areas of broad peak and narrow peak respectively.

Fibre C demonstrates a distinct increase in area of the high-load bearing band upon straining. This indicates an apparent increase of the number of high-load bearing C-C bonds due to structural rearrangement or possibly aligning of highly-oriented molecules towards the fibre axis direction increasing the load-bearing capacity of the monofilament.

Fibre H (Fig.5.46b) shows a similar high rate of Raman band shift as Fibre C (Fig.5.41b) for the high-load bearing band with strain, but it has a lower fraction of high-load bearing C-C bonds and therefore an inferior performance to Fibre C. Fibre E has a relatively low area of the high-load bearing band which does not change at different applied strains. Also, it has very low rate of Raman band shift with strain (Table 5.3) and it is

consistent with general inferiority of the mechanical properties of this fibre. It appears that fibre with superior mechanical properties shows both higher rate of Raman band shift with strain and higher maximum area of the high-load bearing Raman bands during straining. Obviously, these two parameters are equally significant for the high-performance mechanical properties of the gel-spun fibres.

5.6 CONCLUDING REMARKS

Using the technique of Raman microscopy, it is possible to obtain an unique view of the molecular deformation of the PE monofilaments. The appearance of band splitting in the Raman spectra upon straining can be interpreted as an inhomogeneous distribution of the applied stress for two differently-stressed C-C bonds in the PE molecules of the monofilaments. As with mechanical testing, the effect of testing parameters are apparently significant for molecular deformation (Section 5.4.1). In addition, different molecular behaviour was found for different modes of deformation such as straining or stressing (Section 5.4.2), cyclic loading (Section 5.4.3), and stress relaxation and creep (Section 5.4.4). It appears that the molecular behaviour upon straining could be defined into three different stages with the high-load bearing bonds being responsible for the good mechanical properties of the fibres (Section 5.5). Generally, gel-spun PE fibres with high-performance mechanical properties show both high rate of Raman band shift with strain and high maximum relative area of the high-load bearing Raman band during straining which are important

parameters for the molecular interpretation of fibre deformation in next chapter.

6

MOLECULAR STRUCTURE AND MECHANICAL BEHAVIOUR

6.1 INTRODUCTION

The information obtained from the structural and morphological studies of the gel-spun PE fibres (Chapter 3) is of practical importance especially in relation to the mechanical properties of the fibres (Chapter 4). This provides a fundamental basic understanding of the molecular deformation behaviour observed by Raman microscopy (Chapter 5) which was proven earlier to be a powerful technique to follow the molecular response of the polyethylene (PE) monofilaments upon deformation [18-22]. In this chapter, an attempt is made to correlate the structural parameters with the mechanical properties and the results from Raman microscopy (Section 6.3). This enables the molecular behaviour of the gel-spun PE fibres during deformation to be modelled (Section 6.4). This modelling involves a structural approach to the morphology of the fibres and a quantitative analysis of the low-strain mechanical properties.

6.2 INTERPRETATION OF MECHANICAL BEHAVIOUR

Even for most highly-oriented polymers including gel-spun PE fibres, the very high theoretical modulus along the chain axis direction is not achieved in practice. Crystalline polymers are essentially composite materials with alternating crystalline and non-crystalline regions. Although the crystalline regions can

become very highly aligned during processing, the non-crystalline regions are less oriented. Even if the overall orientation of the chain segments is apparently quite high, there will still be very few chains where the whole lengths of the molecules are aligned parallel to a single direction. Apparently, it is these molecules that responsible for the increase of the stiffness of the highly oriented polymers [115-116].

6.2.1 Structural Approaches for Highly Oriented Polyethylene

There are several approaches based on different effects observed in the fibrous structure of the highly-oriented linear PE. Two very different approaches have been used to give insight into the effect of microstructure upon mechanical properties of the material [88].

6.2.1.1 Composite Model Approach

This approach, as proposed by Barham and Arridge [117-118], considers that the oriented polymer consists of a needle-like crystal phase embedded in partially oriented amorphous phase

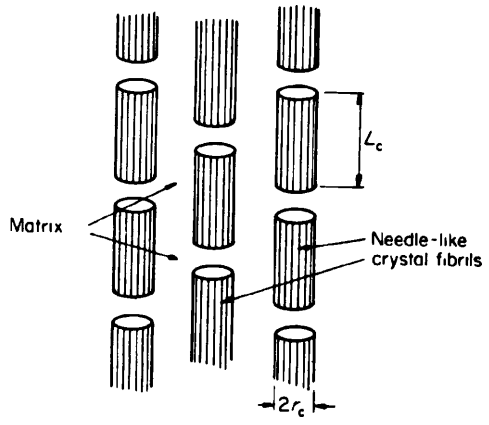

Fig.6.1 Schematic diagram of Barham and Arridge model for the ultrahigh modulus polyethylene [88].

(Fig.6.1). The fibrillar needle-like crystal phase was observed by staining the oriented PE with chlorosulphonic acid and uranyl acetate and microtoming thin sectionsperpendicular to the draw direction.

The validity of this model is mainly based on the good description of elastic modulus of PE as function of draw ratio. In fact, the increase in modulus on drawing is postulated as being due to the increase in the aspect ratio of the fibrils, and hence their increased efficiency as reinforcing elements. However, it is difficult to envisage a means by which the aspect ratio of the fibrils could increase through the amorphous matrix during the deformation.

6.2.1.2 Taut-tie Molecules and Intercrystalline Bridges

Peterlin [23-24] has proposed a hypothesis that the tensile modulus of oriented fibres such as PE, polyoxymethylene (POM) and polypropylene (PP), is essentially determined by the proportion of taut-tie molecules (i.e. extended chains) which produce links between the crystalline blocks in the fibre direction. This microfibrillar model assumes that drawing of the lamellar materials destroys the lamellae and transforms them into long, narrow microfibrils of finite length. These microfibrils are the structural elements of filaments and consist of crystalline material arranged in series with amorphous material through which taut-tie molecules connecting adjacent crystalline blocks run. The stiffness and strength of the whole filament is primarily determined by the microfibrils with the taut-tie molecules playing the crucial role.

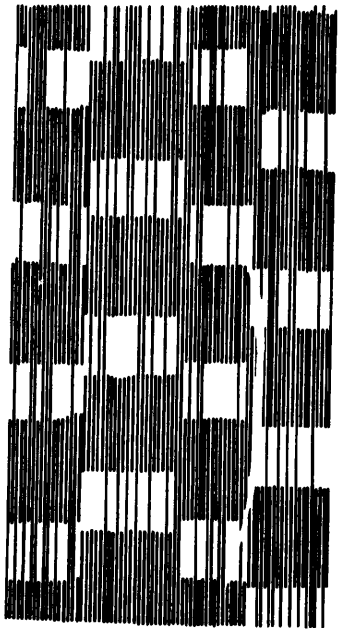

Fig.6.2 Schematic diagram of intercrystalline bridges connecting the crystalline blocks in a highly oriented polyethylene structure [88].

An alternative proposal of intercrystalline bridges by Ward *et al* [32,88,115-116] suggests they play a similar role to the taut-tie molecules. In fact, the intercrystalline bridges are thought to be narrow clumps of crystalline chains linking the crystalline blocks as illustrated in Fig.6.2. The lines joining the adjacent crystalline stacks indicate intercrystalline bridges. The main essence of these two models is that the increase in modulus with increasing draw ratio arises primarily from an increase in the proportion of the fibre-phase material (i.e. taut-tie molecules or intercrystalline bridges) and not from the changing aspect ratio of a constant proportion of fibre phase material (needle-like crystals) [88].

6.2.2 Quantitative Modelling

Interpretation of mechanical behaviour requires quantitative models which are based on either variation in molecular orientation or the composite nature of a crystalline polymer. In

fact, there are two distinct types of quantitative models, namely the *aggregate model* [88,119-120] and the *Takayanagi model* [26], for the low-strain mechanical behaviour of oriented polymers.

6.2.2.1 The Aggregate Model

The aggregate model [88,119-120] predicts the changes in elastic constants with the development of orientation. It assumes that the polymer consists of an aggregate of anisotropic units as illustrated in Fig.6.3. The calculation of the elastic constants can be made by assuming either uniform stress throughout the aggregate (Fig.6.3a), which involves a summation of compliance constants, or uniform strain (Fig.6.3b), which implies a summation of stiffness constants. The mechanical properties of the units are taken from those of a highly-oriented polymer obtained from experimental results.

This model was proposed in the knowledge that it was likely to provide only a first approximation to actual behaviour, because the assumptions of perfectly elastic behaviour and no changes in morphology during orientation process are known to be

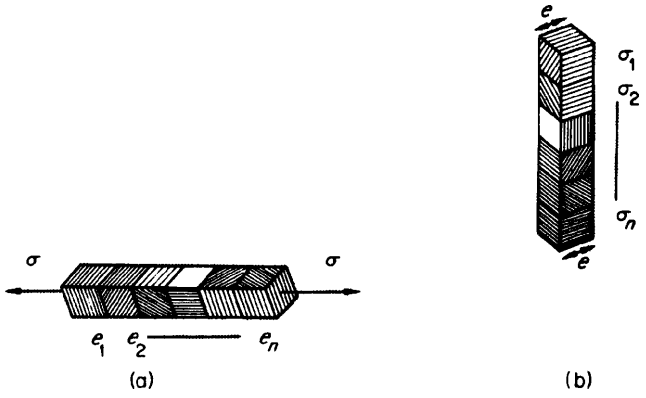

Fig.6.3 The aggregate model (a) for uniform stress, and (b) for uniform strain [88].

untrue for crystalline polymers [120]. Besides, it originated as a single-phase model, and it is clearly unsuitable for the two-phase structure of the highly-oriented linear PE.

6.2.2.2 The Takayanagi Model

The Takayanagi model [26,119-120] recognises the two-phase nature of crystalline polymers and the mechanical behaviour is explained in terms of two separate components representing crystalline and amorphous fractions. In its original form, the resultant response will depend on whether the two components are in parallel or series (Fig.6.4). For the parallel model the modulus E is given by

$$E = \lambda E_A + (1-\lambda) E_B \qquad (6.1)$$

where subscripts refer to the two components, and λ is the volume fraction of phase A in parallel with phase B. This situation gives a Voigt average modulus. In contrast the series model yields a Reuss average modulus:

$$\frac{1}{E} = \frac{\phi}{E_A} + \frac{(1-\phi)}{E_B} \qquad (6.2)$$

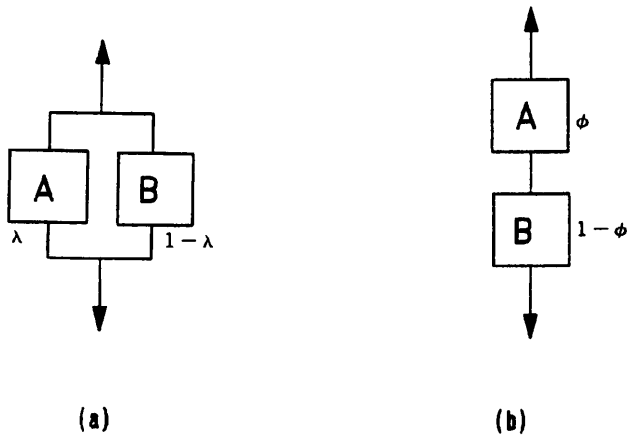

Fig.6.4 The parallel (a) and series (b) models [120].

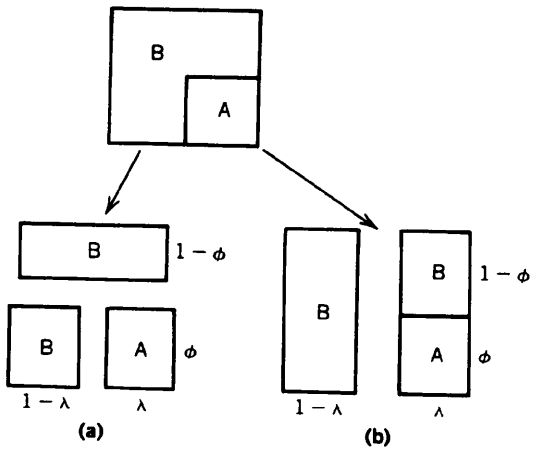

Fig.6.5 The series-parallel (a) and parallel-series (b) Takayanagi models [88].

where ϕ now represents the volume fraction of phase A in series with phase B. If, however the components are dispersed, two alternative Takayanagi models arise as illustrated in Fig.6.5. The modulus E of the series-parallel model could then be expressed as

$$\frac{1}{E} = \frac{\phi}{\lambda E_A + (1-\lambda) E_B} + \frac{1-\phi}{E_B} \qquad (6.3)$$

where λ and ϕ are the volume fractions of phase A in parallel and in series with phase B respectively. While for the parallel-series model

$$E = \lambda\left(\frac{\phi}{E_A} + \frac{1-\phi}{E_B}\right)^{-1} + (1-\lambda) E_B \qquad (6.4)$$

In fact with these arrangements (Fig.6.5), the effect of taut-tie molecules or intercrystalline bridges can be taken into account by allowing some proportion of crystalline material to be in parallel with the non-crystalline component. This has been successfully used by Ward *et al* [115-116] for the interpretation of the dynamic mechanical properties of the high-modulus PE fibres.

6.3 MECHANICAL PROPERTIES IN RELATION TO MOLECULAR STRUCTURE

It is of great interest to correlate the mechanical properties of the fibres with the structural parameters irrespective of whether the fibres were spun from different conditions, different precursors or were drawn to different draw-ratios.

The morphological observation presented in Sections 3.5.1 and 3.5.2 shows that the microstructure of the fibres is fibrillar and this structure could be responsible to the high-performance properties of the fibres. The microfibrils in the structure displays an apparently long-range crystal coherence with occasional discontinuities which are probably attributed to actual crystal defects. In fact according to Schaper *et al* [59-60], this supermolecular structure is thought to contain gross topological defects such as distortion and termination of the

Table 6.1

TENSILE PROPERTIES AND STRUCTURAL PARAMETERS FOR ALL THE PE FIBRES.

Fibre	T_m (°C)	Corrected Modulus (GPa)	Corrected Ultimate Stress (GPa)	Crystallinity ϕ_c (%)	*d*-spacing (Å)	
					(200)	(020)
A	147.5	91.7	3.9	92.5	3.69	2.46
B	141.5	50.7	0.9	90.5	3.70	2.46
C	145.6	163.6	5.4	96.3	3.70	2.46
D	145.0	61.7	2.3	90.2	3.69	2.47
E	142.4	37.8	1.9	89.6	3.70	2.46
F	144.5	51.5	2.7	88.9	3.70	2.46
G	144.7	88.5	3.1	88.7	3.70	2.46
H	144.2	60.7	1.5	90.8	3.69	2.46
I	132.7	61.2	1.9	87.6	3.74	2.47

microfibrils. This shows that the mechanical properties of the fibres depend on many structural parameters including the whole range of possible molecular and morphological defects.

Possible correlations between the degree of crystallinity ϕ_c and the tensile properties were examined as shown in Table 6.1. The degree of crystallinity is apparently high for all the fibres and neither the ultimate stress nor the tensile modulus exhibits a simple dependence on the degree of crystallinity. The *d*-spacings of (200) and (020) reflections in the wide-angle X-ray diffraction (WAXD) are the measure of the lateral spacings in the PE crystal lattice. However, the tensile properties and the corresponding *d*-spacings of the observed (200) and (020) reflections show no useful relation. Interestingly, Fibre I which has the lowest melting point (T_m) shows the highest *d*-spacings of (200) and (020) reflections. However, it has an equally-high value of intrinsic viscosity (Table 3.2) as other ultra-high molecular-weight PE (UHMW-PE) fibres. This is an indication that Fibre I was gel-spun from very high molecular-weight precursor but due to its low T_m it is probably a branched high molecular-weight PE.

High-performance properties require many of the molecules to become extended and aligned in order to take full advantage of the long-chain nature of the ultra-high molecular-weight PE (UHMW-PE) but such molecular arrangements were not quantified in the project. However, it has been reported by Allied-Signal that the degree of molecular orientation is similar for all the gel-spun fibres [74]. The structural characterization of the fibres (Chapter 3) has shown considerable structural similarities

between the fibres and no obvious differences by transmission electron microscopy (TEM) and WAXD. Clearly, the difference in mechanical properties of the fibres is not due to the difference in fibrillar microstructure or molecular orientation as in the case of Kevlar [122]. In fact, a similar fibrillar microstructure was found by Schaper *et al* [59-60] for other high-performance PE fibres and it appears that the degree of chain extension is the most significant structural parameter for the high-performance properties of gel-spun PE fibres. That could result from changes in the phase topology e.g. continuity of the crystalline phase or in the orientation of the non-crystalline materials.

6.4 STRUCTURAL MODEL FOR POLYETHYLENE FIBRES

Several models exist for the structure of high-performance PE fibres as discussed in Section 6.2.1. However based on the observation of replicas of etched surfaces using transmission electron microscopy (TEM), the morphology of the gel-spun PE fibres is fibrillar in nature and therefore the proposed structural model will be primarily based on the microfibrillar model [23-24].

6.4.1 Morphological Basis of the Model

Fig.6.6 shows the schematic diagram of the proposed structural model to explain the observed structure/property relationship of the gel-spun PE fibres. For convenience the polymer backbone chains are represented by lines and the crystalline phase is effectively continuous in the direction of *c*-axis. Within the microfibrils, there are randomly-distributed non-crystalline

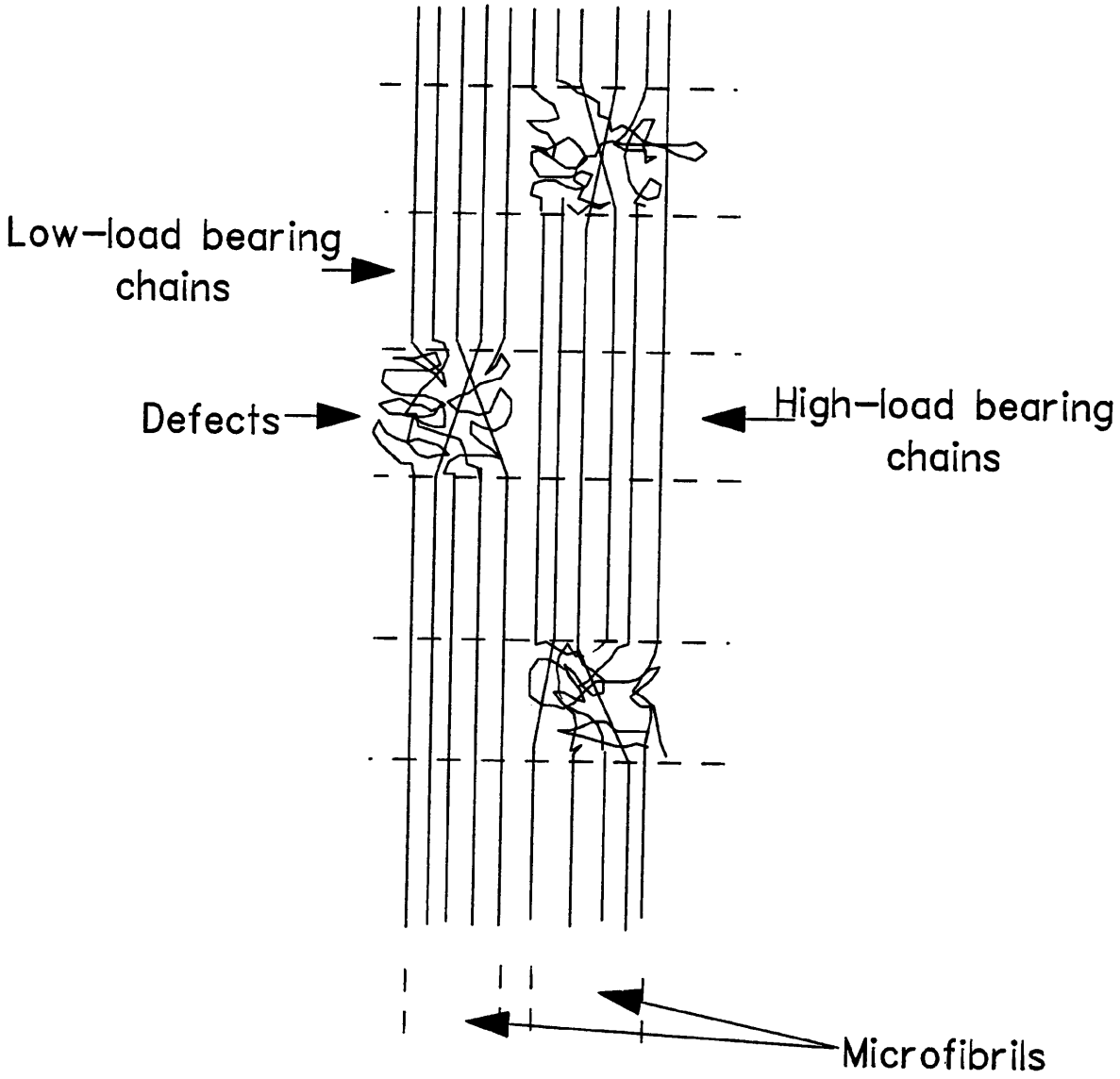

Fig.6.6 Schematic diagram of the proposed structural model for gel-spun PE fibres.

layers between consecutive, almost fully-oriented crystalline blocks. Although little is known at present about the way in which the linking molecules are arranged in the non-crystalline interface, it is assumed that a fraction of these molecules could be highly chain-extended. This is similar to the taut-tie molecules or intercrystalline bridges as proposed by Peterlin [23-24] and Ward *et al* [32,88,115-116] respectively.

At the molecular level, the Raman microscopic data show that there is a bimodal stress distribution upon deformation. In fact, this phenomenon has been confirmed by Kip *et al* [21] and Grubb *et al* [22] for their Raman microscopic work at low temperature. According to these two reports, there are two differently stressed molecular chains within the crystalline phase which was also confirmed by WAXD work [21]. Apparently part of the crystalline phase is inefficiently coupled to the applied stress which carries little load upon straining. However at low temperature, more than 80% of the total crystalline material in the structure has high-load bearing chains [22]. Therefore the inhomogeneous stress distribution could not be solely due to the presence of a fraction of taut-tie molecules or intercrystalline bridges in the non-crystalline layers as they are thought to be the minority in the whole structure [22]. However according to Prevorsek [121], this could be explained as upon straining the fibre, the stress is concentrated on the high-load bearing chains in the crystalline block by the adjacent non-crystalline layer between the two microfibrils as illustrated in Fig.6.6.

6.4.2 Quantitative Analysis: The Takayanagi Model

The Takayanagi model is the simplest way of relating tensile behaviour, particularly the low-strain mechanical properties to the topology of the phases. There are two possible versions of the general model i.e. parallel-series and series-parallel models (Fig.6.5) and these give different expressions for the tensile modulus E, depending upon the assumptions made about stress transfer between the components.

6.4.2.1 Parallel-series Model

In this model, the high-load bearing crystalline component (C_1) which is induced by the defect region of the adjacent microfibril, is arranged in parallel with the low-load bearing region which consists of components A and C_2 (Fig.6.7). The non-crystalline component A is arranged in series with the crystalline component C_2 by assuming there is perfect stress transmission between the two components. However, it is also

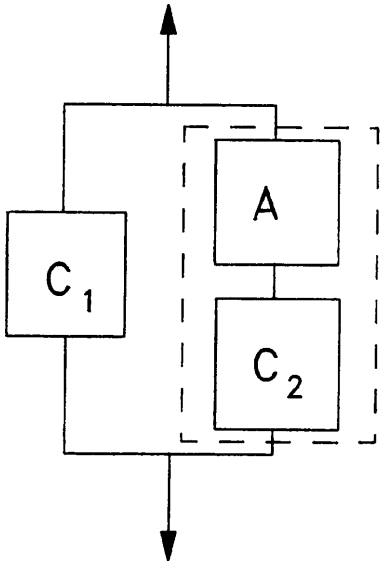

Fig.6.7 The schematic diagram of the parallel-series model used for gel-spun PE fibres.

assumed that there is no stress transmission between the high-load and low-load bearing regions. In the real case, stress transmission will take place by shear displacement between the components. Unfortunately, this is a fundamental limitation of the Takayanagi model which fails to take account of this factor.

Previous Raman microscopic work on high-performance fibres such as poly(*p*-phenylene benzobisthiazole) (PBT) [110] and Kevlar [111,122] have shown that the rate of shift of the Raman peak ($d\Delta\nu/de$) is directly proportional to the tensile modulus E,

$$\frac{d\Delta\nu}{de} \propto E = kE \qquad (6.5)$$

where k is a constant. Therefore, the value of modulus can be determined from the rate of shift of the Raman peak.

The quantitative modelling was carried out on the assumptions that:-

1. The volume fractions of each component is proportional to the area of the fitted Raman peaks. Fig.6.8 shows the variation of the relative area of the high-load bearing peak i.e.

$$A_1 = \frac{A_1}{A_1 + A_2} \qquad (6.6)$$

at low levels of strain. A_1 and A_2 are the area of the high-load and low-load bearing peaks respectively. Apparently there is no significant variation within this range of strain and therefore the initial value of the relative area for the high-load bearing peak A_1 may be

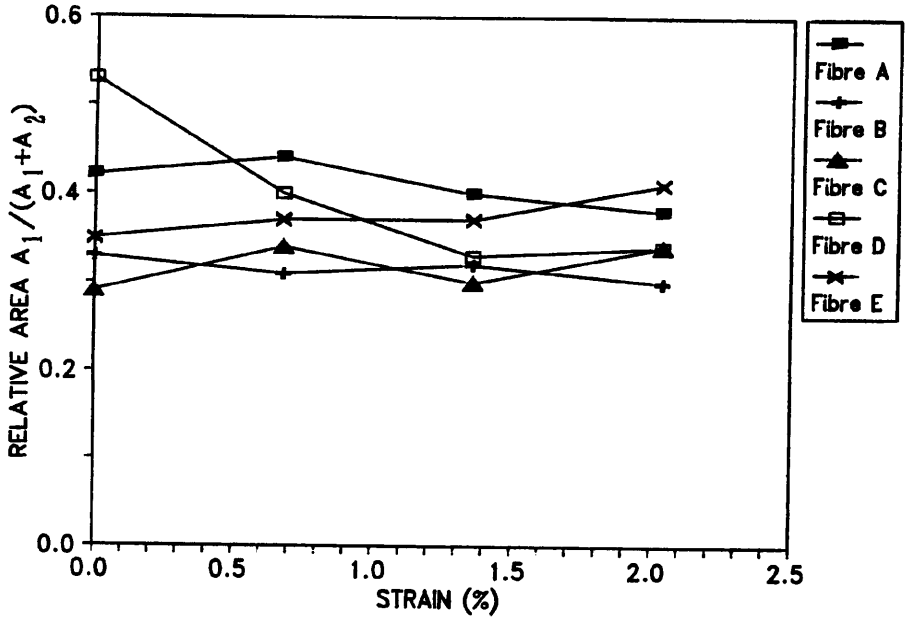

(a)

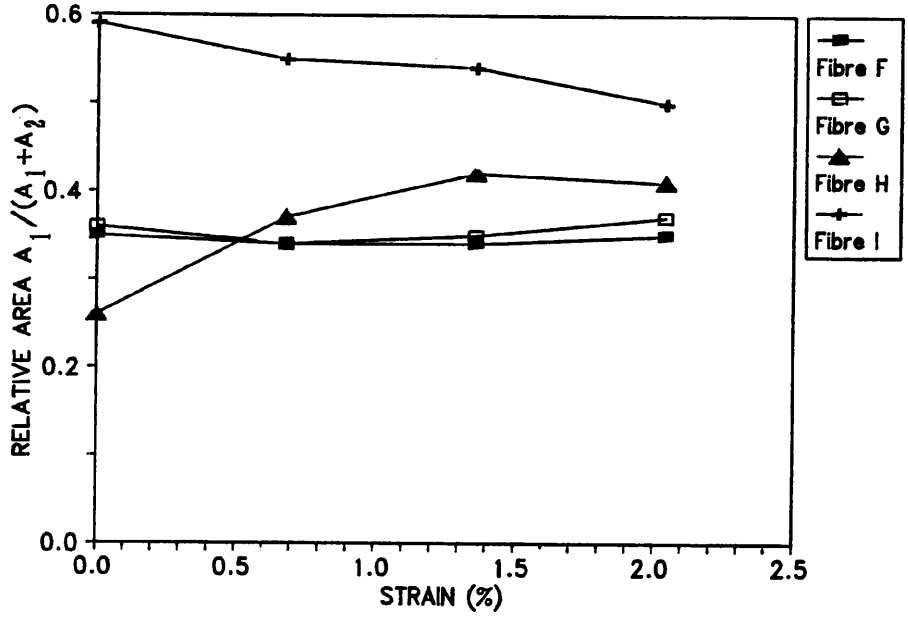

(b)

Fig.6.8 The dependence of the relative area of the high-load bearing Raman peak up to 2.0% strain.

Table 6.2

CRYSTALLINITY AND RAMAN MICROSCOPIC DATA OF ALL THE PE SAMPLES.

Fibre	ϕ_c	$(d\Delta\nu/d\varepsilon)_1$	A_1	$(d\Delta\nu/d\varepsilon)_2$	A_2
A	0.925	3.34	0.41	2.01	0.59
B	0.905	1.18	0.32	0.21	0.68
C	0.963	6.77	0.32	4.58	0.68
D	0.902	2.03	0.40	0.39	0.60
E	0.896	1.38	0.38	0.68	0.62
F	0.889	2.96	0.35	1.11	0.65
G	0.887	2.66	0.36	0.28	0.64
H	0.908	4.62	0.37	1.52	0.63
I	0.876	3.16	0.55	0.91	0.45

determined by averaging the values of relative area up to 2.0% strain as tabulated in Table 6.2 together with thefractional degree of crystallinity ϕ_c. The values of the rate of shift ($d\Delta\nu/d\varepsilon$) are corrected values obtained from Table 5.3 and $A_2 = (1-A_1)$ is the relative area of the low-load bearing peak.

2. If V_1, V_2 and V_3 are the volume fractions of the regions C_1, C_2 and A respectively, then it can be assumed that the relative areas of the two Raman peaks are equal to the volume fraction of each crystalline component. Therefore,

$$A_1 = \frac{V_1}{V_1 + V_2} \quad \textit{and} \quad A_2 = \frac{V_2}{V_1 + V_2} \tag{6.7}$$

3. Applying tensile stress parallel to the fibre axis will cause both stretching of the crystallites and a rotation towards the fibres axis due to shear deformation [122]. Therefore, usually the total strain in the fibre upon

straining is contributed by both effects. However for the flexible-chain PE molecules under consideration, it is assumed that the molecular deformation is dominated by the stretching of the crystallites rather than rotation and consequently, the C-C symmetric stretching Raman band (1128 cm^{-1}) is a direct measure of the molecular response upon straining.

4. It is also assumed that there is no Raman scattering from the non-crystalline (amorphous) region.

The fractional degree of crystallinity ϕ_c determined from differential scanning calorimetry (DSC) is related to the volume fractions of each component by

$$\phi_c = \frac{V_1 + V_2}{V_1 + V_2 + V_3} \qquad (6.8)$$

Therefore the volume fraction of the high-load bearing region is

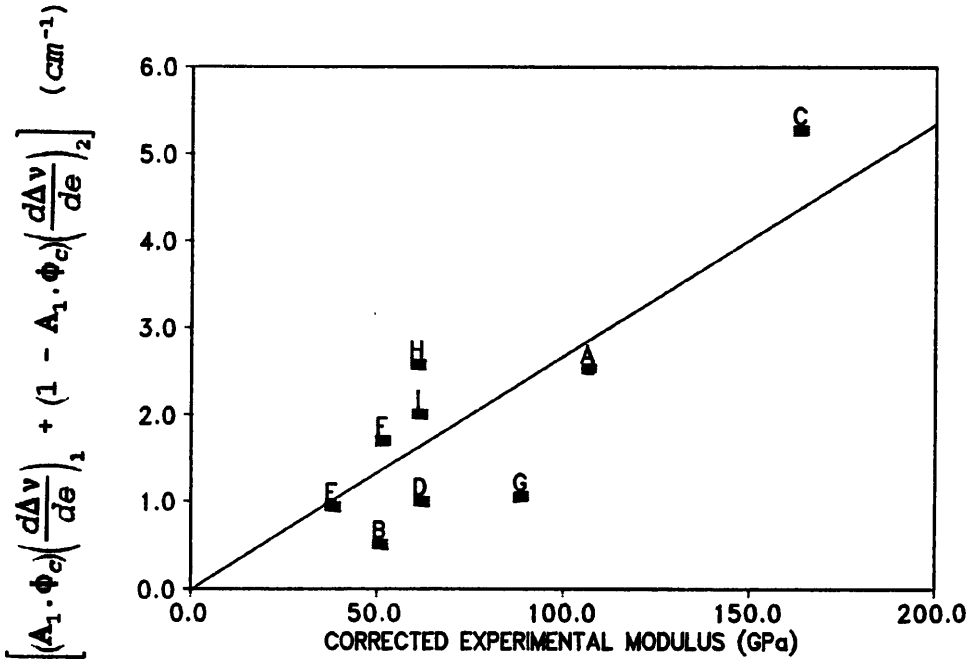

Fig.6.9 The value of the composite rate of shift of the Raman peaks plotted against the experimental modulus of the fibres for the parallel-series model.

$$\frac{V_1}{V_1 + V_2 + V_3} = A_1 . \phi_c \qquad (6.9)$$

and for the low-load bearing region is

$$\frac{V_2 + V_3}{V_1 + V_2 + V_3} = 1 - A_1 . \phi_c \qquad (6.10)$$

Since the high-load bearing region is in parallel with the low-load bearing region, the tensile modulus is given by combining Equations (6.1), (6.5), (6.9) and (6.10) as

$$E = \frac{1}{k}\left[(A_1 . \phi_c)\left(\frac{d\Delta\nu}{d\varepsilon}\right)_1 + (1 - A_1 . \phi_c)\left(\frac{d\Delta\nu}{d\varepsilon}\right)_2\right] \qquad (6.11)$$

where k is the constant in Equation (6.5) and $(d\Delta\nu/d\varepsilon)_1$ and $(d\Delta\nu/d\varepsilon)_2$ are the rate of shift of both the high-load and low-load bearing Raman peaks respectively. In Fig.6.9, the right-hand side of Equation (6.11) is plotted against the corrected

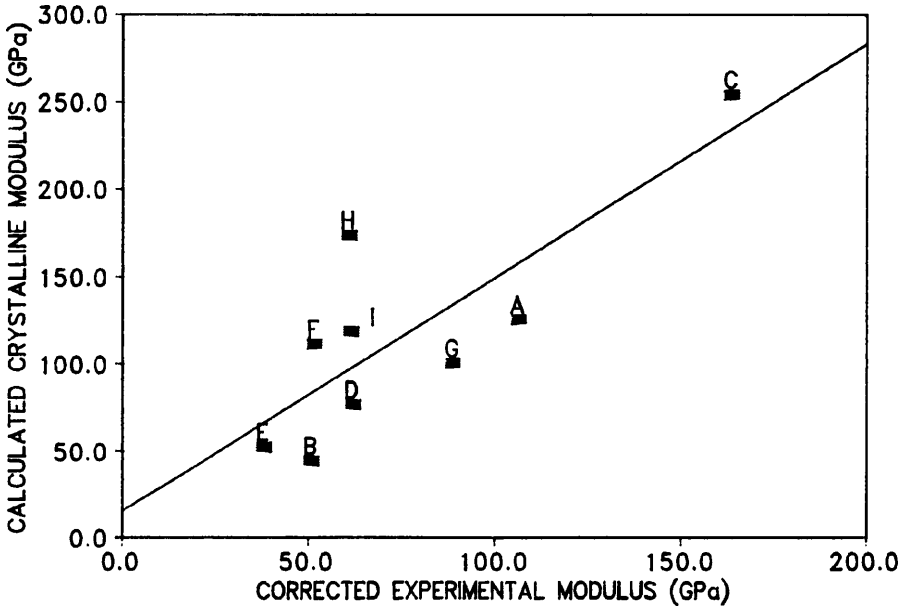

Fig.6.10 The dependence of the crystalline modulus E_c upon the experimental modulus of the fibres for the parallel-series model.

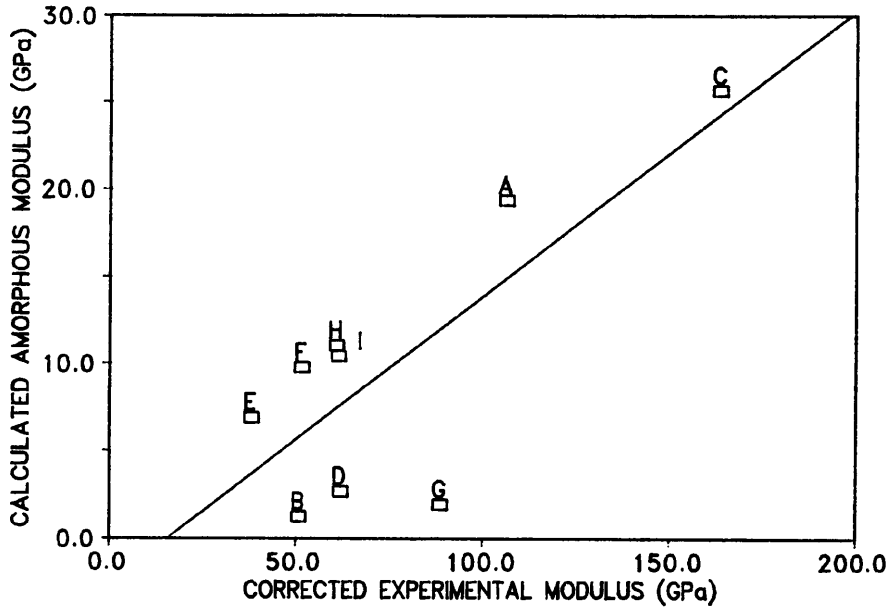

Fig.6.11 The dependence of the non-crystalline modulus E_a with the experimental modulus of the fibres for the parallel-series model.

experimental modulus E and it can be seen that the data fall near a straight line with a slope k=0.027 (cm.GPa)$^{-1}$ or $(1/k)$=37.037 cm.GPa. Assuming that the crystalline phase in both high-load and low-load bearing regions has the same value of modulus, the modulus of the crystalline phase E_c for the parallel-series model (Fig.6.7) can be determined simply by

$$E_c = 37.037\left(\frac{d\Delta\nu}{de}\right)_1 \qquad (6.12)$$

From Equation (6.12), the theoretical rate of shift $(d\Delta\nu/de)_{theo}$ for the 1128 cm^{-1} Raman band is found to be 8.0 cm^{-1}/% based on the theoretical modulus of 300 GPa [7]. This value in fact similar to the value of 14.0 cm^{-1}/% calculated by Wool *et al* [113] based on the anharmonic (Morse) potential energy function for the C-C stretching mode in the PE crystal unit.

In the low-load bearing region, the non-crystalline

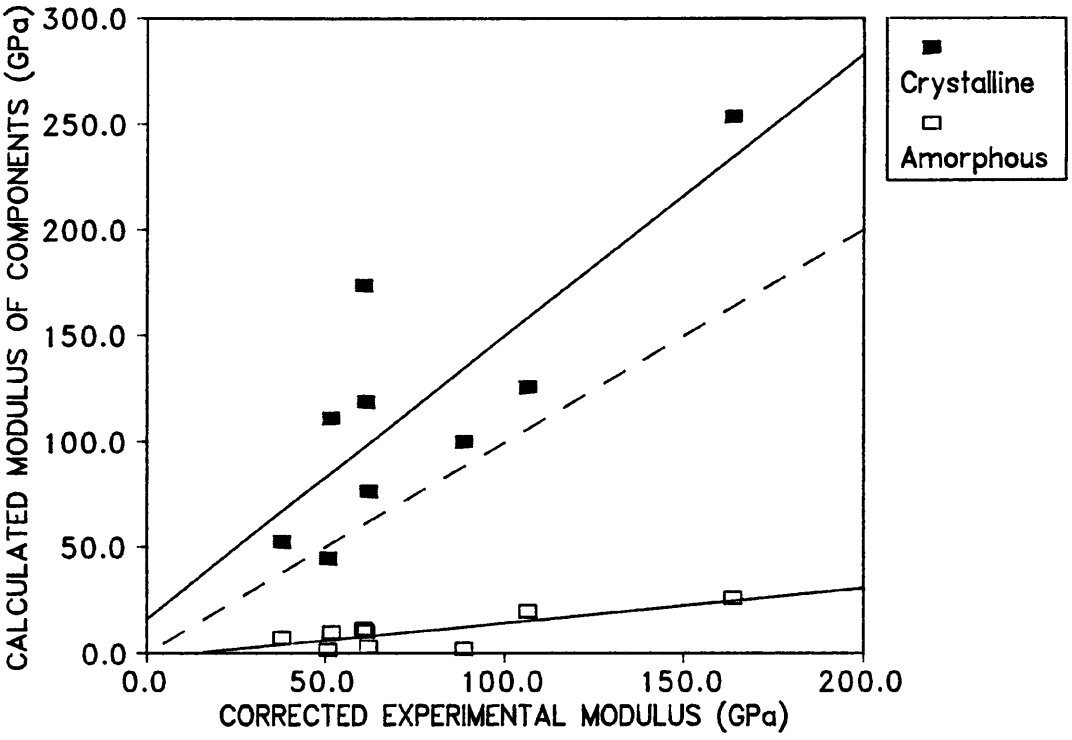

Fig.6.12 The dependence of both the crystalline and non-crystalline moduli with the experimental modulus of the fibres for the parallel-series model.

component (A) is arranged in series with the crystalline component (C_1) and therefore the effective modulus of the low-load bearing region is

$$\frac{1}{E_{eff}} = \frac{1}{E_a}\left(1 - \frac{A_2\phi_c}{1 - A_1\phi_c}\right) + \frac{1}{E_c}\left(\frac{A_2\phi_c}{1 - A_1\phi_c}\right) \qquad (6.13)$$

where E_a is the non-crystalline (or amorphous) modulus in the low-load bearing region. Therefore

$$E_a = \frac{\left(1 - \frac{A_2\phi_c}{1 - A_1\phi_c}\right)}{\frac{1}{E_{eff}} - \frac{1}{E_c}\left(\frac{A_2\phi_c}{1 - A_1\phi_c}\right)} \qquad (6.14)$$

Fig.6.10 and Fig.6.11 show dependence of the calculated crystalline E_c and non-crystalline E_a moduli respectively upon experimental fibre modulus. It appears that the highest modulus Fibre C has the value of E_c of ~250 GPa (Fig.6.10) which is

approaching the theoretical modulus of PE. Interestingly, E_a (Fig.6.11) also increases with the fibre modulus indicating the presence of an increasing number of the taut-tie molecules or intercrystalline bridges in the non-crystalline phase. Also, the lower mass melt-spun Fibre B has a lower E_a (about 2 GPa) which is probably due to fewer taut-tie molecules present in the non-crystalline phase. Fig.6.12 shows the dependence of the calculated moduli of both crystalline and non-crystalline phases upon the experimental modulus of the fibres. Apparently E_c increases at a higher rate than E_a and it appears that if E_c achieves the theoretical value of 300 GPa, the highest possible experimental modulus that the gel-spun PE fibres can be obtained is ~200 GPa. In fact, such a relation between the molecular behaviour (from the C-C symmetric stretching bonds) and the mechanical properties shows that the tensile deformation takes place mainly by chain stretching. This is quite different from Kevlar fibres in which both chain stretching and crystal rotation are thought to be involved during the tensile deformation [122].

6.4.2.2 Series-parallel Model

It is also important to consider if the behaviour of the fibres could be determined using the series-parallel model. The arrangement of this model is illustrated in Fig.6.13 with the high-load bearing component (C_1) in series with the low-load bearing region. The low-load bearing region consists of the crystalline (C_2) and the non-crystalline (A) components arranged in parallel. Based on the same nomenclature used in parallel-series model, the tensile modulus E is then related to $(d\Delta v/de)_1$

and $(d\Delta\nu/d\varepsilon)_2$ through

$$E = \frac{1}{k}\left[\frac{A_1\phi_c}{\left(\frac{d\Delta\nu}{d\varepsilon}\right)_1} + \frac{1 - A_1\phi_c}{\left(\frac{d\Delta\nu}{d\varepsilon}\right)_2}\right]^{-1} \qquad (6.15)$$

Likewise, reasonable agreement can be obtained with this relation as shown in Fig.6.14 with $(1/k)$=43.333 cm.GPa but not as good as for the parallel-series model (Fig.6.9). However,

$$E_c = 43.333\left(\frac{d\Delta\nu}{d\varepsilon}\right)_1 \qquad (6.16)$$

and the theoretical value of rate of shift $(d\Delta\nu/d\varepsilon)_{theo}$=6.9 $cm^{-1}/\%$ which is lower than the $(d\Delta\nu/d\varepsilon)_{theo}$ for the parallel-series model. The calculated crystalline modulus E_c shows a similar relation with the experimental modulus (Fig.6.15) as the one obtained by parallel-series model. For this series-parallel model, the effective modulus of the low-load bearing chain is defined as

$$E_{eff} = \left(1 - \frac{A_2\phi_c}{1 - A_1\phi_c}\right).E_a + \frac{A_2\phi_c}{1 - A_1\phi_c}.E_c \qquad (6.17)$$

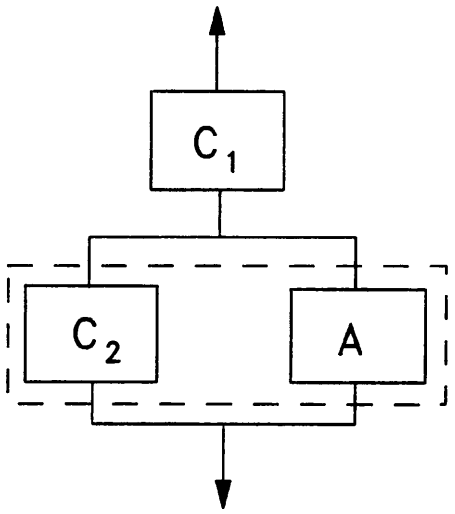

Fig.6.13 The schematic diagram of the series-parallel model used for the gel-spun PE fibres.

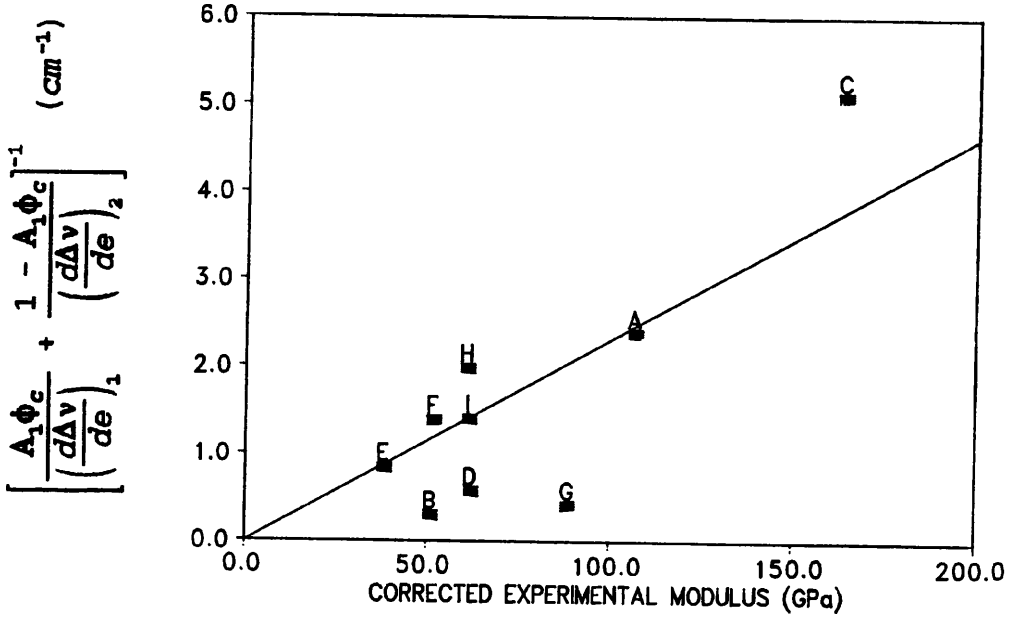

Fig.6.14 The value of the composite rate of shift of the Raman peaks plotted against the experimental modulus of the fibres for the series-parallel model.

As a result,

$$E_a = \frac{E_{eff} - \left(\frac{A_2\phi_c}{1 - A_1\phi_c}\right).E_c}{1 - \frac{A_2\phi_c}{1 - A_1\phi_c}} \qquad (6.18)$$

In this case, all the calculated E_a are negative values as shown in Fig.6.16 which shows very clearly that the series-parallel model is not valid. Clearly, the assumption that there is no stress transmission between the crystalline (C_1) and non-crystalline (A) components in the low-load bearing region is untrue. On closer examination, this is also not consistent with the structural model proposed earlier.

The findings outlined above are consistent with the result obtained by Ward *et al* [115-116] on the interpretation of the dynamic mechanical behaviour in high-modulus PE fibres. According to their result, the parallel-series model (Fig.6.17b) gives a

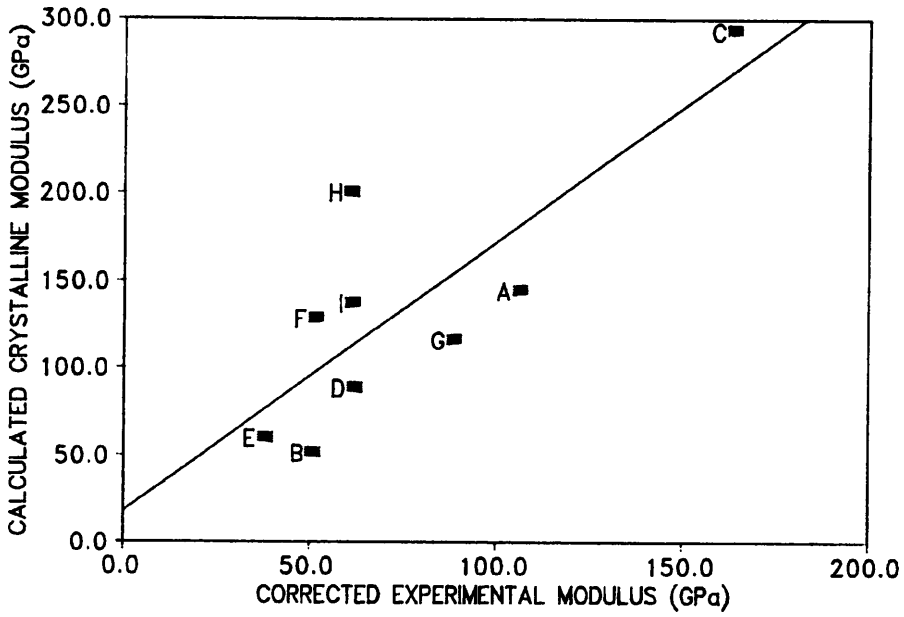

Fig.6.15 The dependence of the crystalline modulus E_c upon the experimental modulus of the fibres for the series-parallel model.

much better experimental agreement than the series-parallel model (Fig.6.17a) which over-estimates the modulus of the fibres.

6.4.3 Qualitative Analysis

6.4.3.1 Molecular Behaviour upon Deformation

Upon straining the fibre, the high-load bearing region (C_1) is subjected to a high concentration of stress on the molecular chains in the crystalline block adjacent to the non-crystalline layer between the two microfibrils (Fig.6.6). Upon further straining, this will result in shear displacement between the microfibrils and consequently an increase in the area C_1 of the high-load bearing region as shown in Fig.6.18. This could be used to explain the linear relationship between the maximum relative area of the broad Raman peak (high-load bearing peak) and the corrected ultimate stress (Fig.6.19). The area of the broad Raman

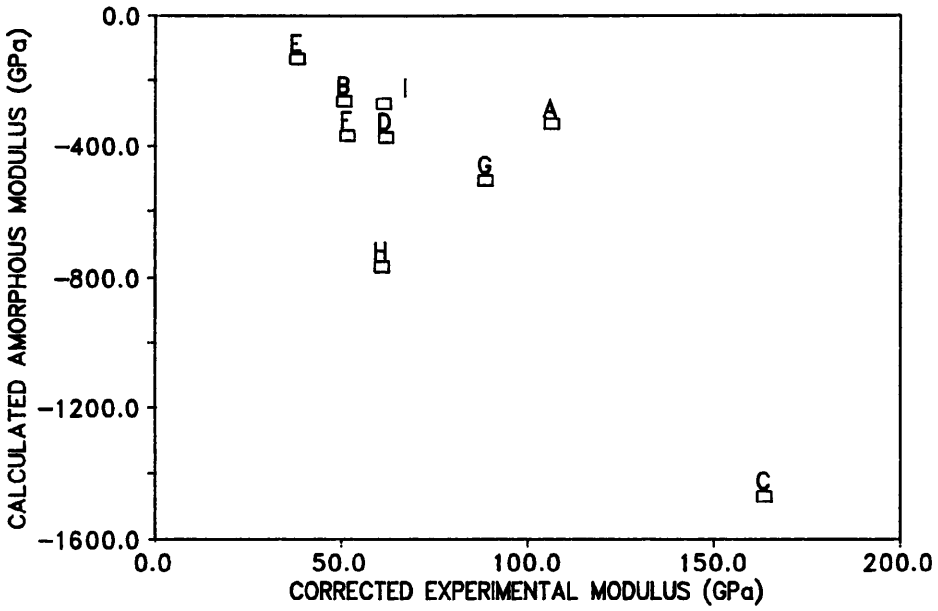

Fig.6.16 The dependence of the non-crystalline modulus E_a upon the experimental modulus of the fibres for the series-parallel model.

peak is a measure of the number of high-load bearing chains and it could be assumed to be indicative of the volume of region C_1. However, the maximum in area C_1 was generally attained at a level of strain (Table 5.5) below the fibre fracture strain. This shows that at the point of failure the molecular chains are no longer predominantly bearing the applied load, due probably to molecular processes such as molecular slippage and disentanglement within the non-crystalline or defect regions.

Based on the effect of yield in the Raman shift/strain plots (Fig.5.39-5.47), it is possible to define three stages (i.e. 1, 2 and 3) of molecular behaviour of the monofilament upon straining. Both the low-load and high-load bearing chains couple efficiently to the applied stress in Stage 1 and carrying almost equally high-load upon straining. However in Stage 2, there is sign of yielding in the low-load bearing region (C_2) which is

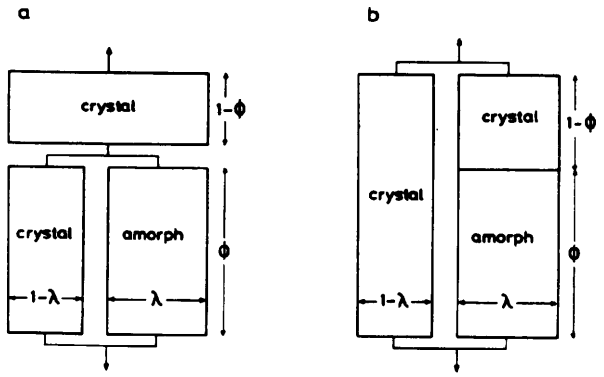

Fig.6.17 The Takayanagi models used by Ward *et al* [116] for the interpretation of the dynamic mechanical properties of high-modulus PE fibres.

probably due to shear displacement between the molecular chains within the microfibrils. Obviously, the stress remains concentrated on the high-load bearing region (C_1) until the fibre fractures in Stage 3.

6.4.1.2 Stress Relaxation and Creep

During stress relaxation, the wavenumber of both the low-load and high-load bearing peaks shift toward the higher wavenumber (Fig.5.29) indicating the crystalline blocks are in compression. This is probably because on the application of constant displacement, there are molecular processes such as molecular slippage and molecular disentanglement within the non-crystalline region (Fig.6.18). This results in the crystalline region being subjected to higher rate of stress relaxation than the non-crystalline region and consequently it appears to be subjected to compressive stress after a period of time. In Section 5.4.4, it was noted that there is a significantly higher positive (compression) shift of both low-load and high-load bearing Raman

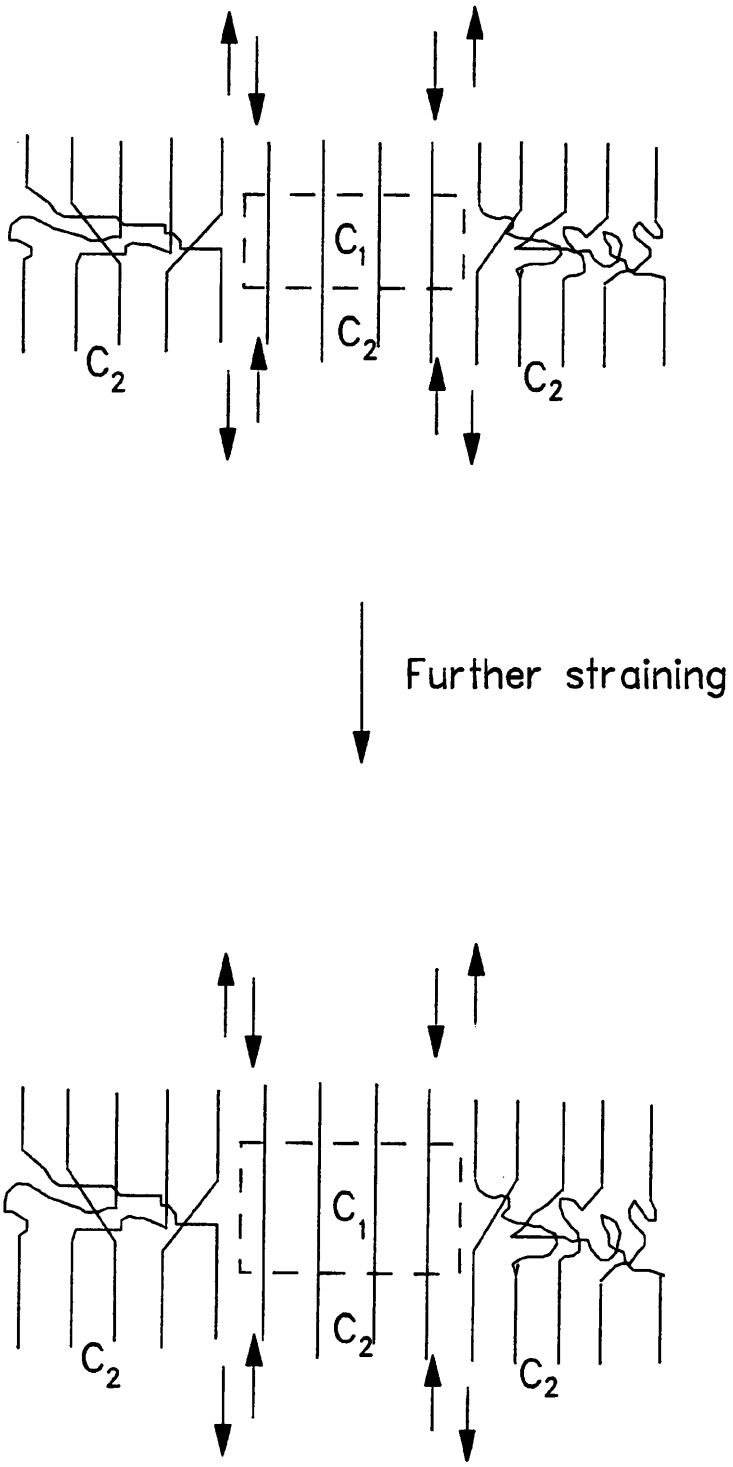

Fig.6.18 Schematic diagram showing the shear displacement of the microfibrils and an increase of the area C_1 of the high-load bearing chains upon further straining.

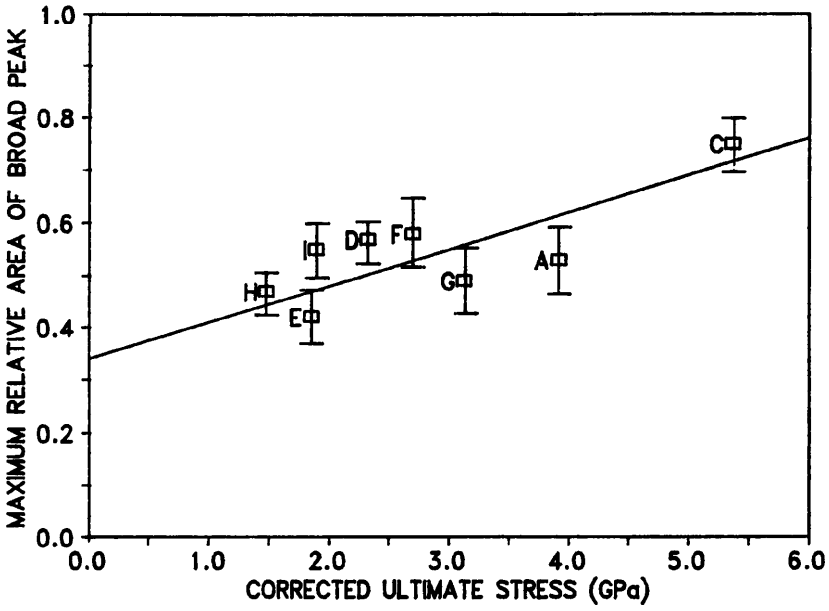

Fig.6.19 The variation of the maximum relative area of the high-load bearing Raman peak (from Table 5.5) with corrected ultimate stress.

bands for Fibre A than for Fibre C (by comparing Fig.5.29a and Fig.5.29c). Fibre C is the highest modulus gel-spun PE fibre and such observation could be due to Fibre C having a lower number of defects in the microstructure (e.g. non-crystalline regions) than Fibre A. As a result, molecular slippage and molecular disentanglement are more significant in Fibre A than C with the crystalline region of Fibre A under greater compression during stress relaxation. For the melt-spun Fibre B, the positive shift of the Raman bands is not as significant as for Fibre A (Fig.5.29b) and the molecular chains are not highly-extended as the gel-spun fibre (Section 3.5.2). This could be because during the application of constant displacement, the molecular chains within Fibre B are subjected to molecular rearrangement such as unfolding which results in minimum stress relaxation of the

molecules within the microstructure.

During the creep experiment (Fig.5.36-5.38), a similar positive shift of the Raman bands is observed but it is not as significant as in stress relaxation. Apparently, not all the molecular chains within the crystalline region couple efficiently with the applied stress. Therefore, molecular stress relaxation in the crystalline region is possible even though the fibre is under constant applied stress. Again, Fibre A show a more significant positive shift of Raman bands (Fig.5.36) than Fibre C. Obviously, the higher number of defects in the microstructure of Fibre A has an effect on reducing the efficiency of molecular coupling with the applied stress. Whereas in Fibre C, the molecular chains efficiently couple to the applied stress and show no significant positive shift of Raman bands in the constant stress creep experiment (Fig.5.38). The melt-spun Fibre B also shows very little positive shift of the Raman band (Fig.5.37) which is probably due to the undergoing of chain unfolding during the creep experiment with the molecular chains being subjected to constant stress.

6.5 CONCLUDING REMARKS

The structure/property relationships in gel-spun PE fibres (Section 6.3) show that fibres of similar orientation but processed under different conditions were found to show a different molecular response upon deformation. It appears that the difference in mechanical properties of the fibres is not due to a major difference in microstructure. Instead, it is very likely due to the extent of chain extension within the highly

oriented structure of the gel-spun PE fibres. A structural approach based on the original microfibrillar model of Peterlin [58-59] was used (Section 6.4.1) and it was able to explain successfully the molecular deformation of the PE fibres as observed in Raman microscopy (Section 6.4.3). Using the Takayanagi models (both parallel-series and series-parallel models), the moduli of both the crystalline and non-crystalline (amorphous) phases in the microstructure of the PE fibres were calculated (Section 6.4.2). However, sensible results could only be obtained from the parallel-series model which appears to be consistent with the structural model. Based on this model, it has been shown that both values of crystalline and amorphous modulus increase with the increasing values of experimental modulus of the fibres. Apparently, the increase of crystalline modulus is due to the increasingly higher degree of chain extension in the high-modulus fibres, while the increase of amorphous modulus can be due to the increase of volume fraction of the taut-tie molecules or intercrystalline bridges. It is noted that in both quantitative and qualitative modelling, the data of the melt-spun Fibre B also fits in well with that for the gel-spun PE fibres. This again shows that both gel-spun and melt-spun PE fibres have an fundamentally similar fibrillar microstructure but different degrees of chain extension.

7

CONCLUSIONS AND SUGGESTIONS FOR FURTHER WORK

7.1 CONCLUSIONS

Using structural characterization techniques, it has been demonstrated that the high-performance gel-spun polyethylene (PE) fibres show a great number of similarities in structure and morphology. Comparing with the high-performance melt-spun PE fibre, both are equally highly crystalline. Except for the experimental gel-spun Fibre I, melting points of the other gel-spun and melt-spun fibres are very close, although the melting behaviour of the two is different. In contrast, there are considerable differences in the mechanical properties between different gel-spun and melt-spun PE fibres. In general, the mechanical behaviour of these high-performance PE fibres is complex because it is highly dependent on gauge length and strain rate. Furthermore, stress relaxation and creep experiments show a significant effect of time dependence of the fibres. This adds additional complication in the mechanical behaviour as demonstrated in the dynamic mechanical testing. In fact, it has been proven that reasonable dynamic mechanical data can be obtained from the gel-spun PE fibres in the monofilament form using the Rheometrics instrument.

An unique view of molecular deformation in the PE monofilaments can be obtained by Raman microscopy. The appearance of band splitting in the Raman spectra upon straining can be

interpreted as an inhomogeneous distribution of the applied stress for two differently-stressed (low-load bearing and high-load bearing) C-C bonds in the crystalline phase of the microstructure. This molecular deformation of the fibres is highly complicated as demonstrated in different modes of deformation such as stressing, cyclic loading, stress relaxation and creep. It appears that this behaviour could be divided into different stages with the high-load bearing C-C bonds being responsible for the good mechanical properties of the fibres. Generally, PE fibres with superior mechanical properties show both a high rate of Raman band shift with strain and high maximum relative area of the high-load bearing Raman band during straining. Both, in fact, are important parameters for the molecular interpretation of the gel-spun PE fibres.

From the structure/property relationships in gel-spun PE fibres, it appears that the differences in the mechanical properties of the fibres is not due to a difference in microstructure. Instead, it is due to different degree of chain extension within the highly oriented structure of the gel-spun PE fibres. Therefore, it is possible to explain the molecular deformation behaviour observed by Raman microscopy in the high-performance PE monofilaments in terms of the microfibrillar model. Additionally, the low-strain mechanical properties of the fibres can be analyzed by The Takayanagi model to calculate the moduli of both crystalline and non-crystalline phases in the microstructure. Apparently, they are well correlated to the experimental values of modulus for the PE fibres. This relationship shows the variation of chain extension in the

crystalline phase and the role of taut-tie molecules (or intercrystalline bridges) in the non-crystalline phase. Both are, in fact, significant in contributing the high-performance mechanical properties of the gel-spun PE fibres.

7.2 SUGGESTIONS FOR FURTHER WORK

7.2.1 Structural Characterization

Further work on the high-performance gel-spun PE fibres should include extended work on the structural characterization. This is particularly important in order to determine a more in-depth insight of the microstructure of fibres.

Transmission electron microscopy (TEM) provides detailed structural information not only in the image mode but also for electron diffraction patterns which provide an important complementary information. To obtain this information, it is necessary to prepare samples that are truly representative of the fibre by ultramicrotoming. However, this is always difficult particularly for PE with difference in stiffness between the crystalline and non-crystalline phases. Therefore, a staining technique such as chlorosulphonation [68] is required before sectioning in order to improve the mechanical properties required for satisfactory ultramicrotoming as well as improving contrast.

Other techniques such as small-angle X-ray diffraction (SAXD) can be used for the structural characterization of the PE fibres. The general shape (arcing) of the SAXD pattern gives an indication of the extent of crystal orientation. Usually the broadening of SAXD peaks can be a consequence of disorder of the crystal and/or if there is a range of long period present.

Although it is difficult to separate these two effects, the complementary information obtained from SAXD can be significant.

7.2.2 Molecular Study of Deformation

Even though Raman microscopy has been proven to be a successful technique to study deformation of gel-spun PE fibre on a molecular level, it would be very informative if it is possible to investigate the similar deformation of crystals in the fibres. A fairly recent development is the use of a synchrotron source which provides a very intense X-ray beam [123]. The source is sufficiently intense to permit measurement in a matter of minutes. Besides, it has a very small spot size (0.8 mm^2) which might enable the use of wide-angle X-ray diffraction (WAXD) to study the structural changes during deformation of fibres in the monofilament form. Obviously, this together with Raman microscopy, might be able to reveal a full picture of the complex mechanical behaviour of the gel-spun PE fibres.

7.2.3 Interfacial Studies in Composites

Raman microscopy can also be used for the interfacial study in a single-fibre model composite. Due to weak Raman scattering of the PE fibres, it is usually difficult to obtain a decent spectrum from a single-PE fibre model composite. This is due to the fluorescence from the matrix resin which overshadows the Raman scattering of the fibre [124]. More work will be required to reduce the fluorescence in the Raman spectrum before any detailed interfacial studies can be carried out. This involves selecting a better grade of resin which does not fluoresce so

badly. Interfacial studies such as determining the fibre-strain distribution in tension and the effect of high stress concentration at fibre ends for different geometries could be carried out. The load transfer profiles at different levels of matrix strain can be obtained and be compared with analytical models [12].

7.2.4 Fibre Compression

Using Raman microscopy, it is possible to obtain an insight into the kinking mechanisms which are responsible for poor compressive properties of the fibres. It involves the redistribution of strain along the fibre in compression. This is particularly useful because the dependence of kinking strain upon fibre structure and mechanical properties can be used to determine the structural factors which control the kinking mechanism [122].

7.2.5 Other Fibres

There are other gel-spun flexible polymer fibres such as polypropylene (PP), poly(acrylonitrile) (PAN) and poly(vinyl alcohol) (PVA) [1]. It is of great interest to investigate the structure/property relationships in these fibres and compare to them with gel-spun PE fibres. Also, it will be useful to study the effect of different molecular structures upon the deformation behaviour of different gel-spun polymeric fibres using Raman microscopy.

REFERENCES

1. P.J. Lemstra and R. Kirschbaum, in *Developments in Oriented Polymers 2*, Ed. I.M. Ward, Elsevier Applied Science, London, 1987.
2. Allied Corp., US Patent 4,413,110.
3. Dyneema VoF Information Brochure on *Dyneema SK60: High Strength/High Modulus Fiber, Properties & Applications,* DSM, 1987.
4. Dyneema VoF Information Brochure on *Dyneema SK60: High Performance Fibers in Composites,* DSM, 1988.
5. E.H.M. van Gorp and J.L.J. van Dingenen, in *Innovative Technologies in Industrial Textiles: Textile Institute Industrial, Technical and Engineering*, Textile Conferences, 5-6 February 1990.
6. K.F. Mulder, in *High Performance Plastics August 1991*, Ed. A. Duckett and I. Guy, Elsevier Applied Science, Oxford, p.1.
7. R.J. Young, in *Comprehensive Polymer Science: The Synthesis, Characterization, Reactions & Applications of Polymers, Vol.2: Polymer Properties*, Ed. C. Booth and C. Price, Pergamon Press, Oxford, 1989, p.515.
8. L. Holliday, in *Structure and Properties of Oriented Polymers*, Ed. I.M. Ward, Applied Science, London, 1975, p.242.
9. V.K. Mitra, *J. Chem. Phys.*, 66, 2731 (1977).
10. D.N. Batchelder and D. Bloor, *J. Polym. Sci., Polym.*

Phys. Edn., 17, 569 (1979).

11. C. Galiotis, R.J. Young and D.N. Batchelder, *J. Polym. Sci., Polym. Phys.*, 21, 2483 (1983).

12. R.J. Young, in *Developments in Oriented Polymers 2*, Ed. I.M. Ward, Elsevier Applied Science, London, 1987, p.1.

13. C. Galiotis, I.M. Robinson, R.J. Young, B.J.E. Smith and D.N. Batchelder, *Polym. Comm.*, 26, 354 (1985).

14. S. van der Zwagg, M.G. Northolt, R.J. Young, I.M. Robinson, C. Galiotis and D.N. Batchelder, *Polym. Comm.*, 28, 276 (1987).

15. R.J. Young, D. Lu and R.J. Day, *Polym. International*, 24, 71 (1991).

16. R.J. Young, R.J. Day and M. Zakikhani, *J. Mater. Sci.*, 25, 127 (1990).

17. R.J. Day, I.M. Robinson, M. Zakikhani and R.J. Young, *Polymer*, 28, 1833 (1987).

18. K. Tashiro, G. Wu and M. Kobayashi, *Polymer*, 29, 1768 (1988).

19. K. Prasad and D.T. Grubb, *J. Polym. Sci., Polym. Phys. Edn.*, 27, 381 (1989).

20. B.J. Kip, M.C.P. van Eijk and R.J. Meier, *J. Polym. Sci., Polym. Phys. Edn.*, 29, 99 (1991).

21. J.A.H.M. Moonen, W.A.C. Roovers, R.J. Meier and B.J. Kip, *J. Polym. Sci., Polym. Phys.*, 30, 361 (1992).

22. D.T. Grubb and Z. Li, *Polym.*, 30, 2587 (1992).

23. A. Peterlin, in *Ultra-high Modulus Polymers*, Ed. A. Ciferri and I.M. Ward, Applied Science, London, 1979,

p.279.

24. A. Peterlin, in *The Strength and Stiffness of Polymers*, Ed. A.E. Zachariades and R.S. Porter, Marcel Dekker, N.Y., 1983, p.97.

25. M. Takayanagi, K. Imada and T. Kajiyama, *J. Polym. Sci. Part C*, 15, 263 (1966).

26. Allied Fibres Division, in *Advanced Composites Bulletin, September 1991*, Ed. P.J. Hogg, Elsevier Applied Science, Oxford, p.4.

27. Allied Fibres Division, in *Advanced Composites Bulletin, November 1991*, Ed. P.J. Hogg, Elsevier Applied Science, Oxford, p.3.

28. Allied Fibres Division, in *High Performance Textiles, December 1991*, Ed. P. Lennox-Kerr, Elsevier Applied Science, Oxford, p.3.

29. M. Jaffe, in *Encyclopedia of Polymer Science and Engineering, Vol. 7*, John Wiley & Sons, N.Y., 1987, p.700.

30. R. Schellekens and H. Ketels, *Polym. Comm.*, 31, 212 (1990).

31. G. Capaccio and I.M. Ward, *Polymer*, 15, 233 (1974).

32. G. Capaccio, A.G. Gibson and I.M. Ward, in *Ultra-high Modulus Polymers*, Ed. A. Ciferri and I.M. Ward, Applied Science, London, 1979.

33. A.E. Zachariades, W.T. Mead and R.S. Porter, in *Ultra-high Modulus Polymers*, Ed. A. Ciferri and I.M. Ward, Applied Science, London, 1979.

34. A.J. Pennings and K.E. Meihuizen, in *Ultra-high*

Modulus Polymers, Ed. A. Ciferri and I.M. Ward, Applied Science, London, 1979.

35. J.R. Schaefgen, in *The Strength and Stiffness of Polymers*, Ed. A.E. Zachariades and R.S. Porter, Marcel Dekker, N.Y., 1983.

36. M. Jaffe and R.S. Jones, in *Handbook of Fiber Science and Technology: Vol.3 High Technology Fibers Part A*, Ed. M. Lewin and J. Preston, Marcel Dekker, N.Y., 1985.

37. S.R. Allen, A.G. Filippov, R.J. Farris and E.L. Thomas, in *The Strength and Stiffness of Polymers*, Ed. A.E. Zachariades and R.S. Porter, Marcel Dekker, N.Y., 1983.

38. J.F. Wolfe, in *Encyclopedia of Polymer Science and Engineering, Vol. 11*, John Wiley & Sons, N.Y., 1988, p.628.

39. J. Economy and W.L. Volksen, in *The Strength and Stiffness of Polymers*, Ed. A. Zachariades and R.S. Porter, Marcel Dekker, N.Y., 1983. p.293.

40. T. Hongu and G.O. Phillips, *New Fibers*, Ellis Horwood, N.Y., 1990.

41. J. Preston, in *Encyclopedia of Polymer Science and Engineering, Vol. 11*, John Wiley & Sons, N.Y., 1988, p.381.

42. S. Kumar, *Indian J. Fibre & Text. Res.*, 16, 52 (1991).

43. M.G. Dobb, D.J. Johnson and B.P. Saville, *J. Polym. Sci., Polym. Phys. Edn.*, 15, 2201 (1977).

44. S.J. Krause and D.L. Vezie, *Polym. Comm.*, 30, 10 (1989).

45. L.R.G. Treloar, *Polymer*, 1, 95 (1960).

46. R.J. Young and P.A. Lowell, *Introduction to Polymers, 2nd Edn.*, Chapman and Hall, London, 1992.

47. J.M. Andrews and I.M. Ward, *J. Mater. Sci.*, 5, 411 (1970).

48. A. Zwijnenburg and A.J. Pennings, *Colloid & Polym. Sci.*, 253, 452 (1975).

49. P. Smith, P.J. Lemstra, B. Kalb and A.J. Pennings, *Polym. Bull.*, 1, 733 (1979).

50. P. Smith and P.J. Lemstra, *J. Mater. Sci.*, 15, 505 (1980).

51. A. Keller, in *Future Trends in Polymer Science and Technology*, Ed. E. Martuscelli, C. Marchetta and L. Nicolais, Technomic Publishing, Pennysylvania, 1987.

52. P.J. Lemstra and R. Kirschbaum, *Polymer*, 26, 1372 (1985).

53. P. Smith, P.J. Lemstra and H.C. Booij, *J. Polym. Sci., Polym. Phys. Edn.*, 19, 877 (1981).

54. W. Hoogsteen, R.J. van der Hooft, A.R. Postema, G. ten Brinke and A.J. Pennings, *J. Mater. Sci.*, 23, 3459 (1988).

55. W. Hoogsteen, H. Kormelink, G. Eshuis, G. ten Brinke and A.J. Pennings, *J. Mater. Sci.*, 23, 3467 (1988).

56. DSM, in *High Performance Textiles, January 1992*, Ed. P. Lennox-Kerr, Elsevier Applied Science, Oxford, p.3.

57. Z. Bashir, J.A. Odell and A. Keller, *J. Mater. Sci.*, 19, 3713 (1984).

58. Z. Bashir, M.J. Hill and A. Keller, *J. Mater. Sci.*

Letter, 5, 876 (1986).

59. A. Schaper, E. Walenta and E. Schulz, *Progr. Colloid Polym. Sci.*, 78, 183 (1988).

60. A. Schaper, D. Zenke, E. Schulz, R. Hirte and M. Taege, *Phys. Stat. Sol.*, 116, 179 (1989).

61. P.F. van Hutten, C.E. Koning, J. Smook and A.J. Pennings, *Polym. Comm.*, 24, 237 (1983).

62. D. Hoffmann and E. Schulz, *Polymer*, 30, 1964 (1989).

63. D. Hoffmann, E. Schulz and E. Walenta, *Acta Polymerica*, 41, 371 (1990).

64. H.D. Chanzy and P. Smith, *Polym. Comm.*, 28, 133 (1987).

65. B.K. Vainshtein and L.I. Tatarinova, in *Applied Fibre Science Vol. 1*, Ed. F. Happey, Academic Press, London, 1978, p.239.

66. L.C. Sawyer and D.T. Grubb, *Polymer Microscopy*, Chapman and Hall, London, 1987.

67. P.R. Blakey and B. Micklethwaite, in *Applied Fibre Science, Vol.1*, Ed. F. Happey, Academic Press, London, 1978, p.349.

68. D. Campbell and J.R. White, *Polymer Characterization: Physical Techniques*, Chapman and Hall, London, 1989.

69. D.C. Bassett, in *Developments in Crystalline Polymers - 2*, Ed. D.C. Bassett, Elsevier Applied Science, London, 1988, p.67.

70. R.H. Olley and D.C. Bassett, *Polym. Comm.*, 23, 1707 (1982).

71. J.M.G. Cowie, *Polymers: Chemistry and Physics of*

Modern Materials, 2nd Edition, Blackie, London, 1991.

72. F.W. Billmeyer Jr., *Textbook of Polymer Science, 3rd Edition*, John Wiley and Sons, N.Y., 1984.

73. M.J. Richardson, in *Comprehensive Polymer Science: The Synthesis, Characterization, Reactions and Applications of Polymers Vol. 1, Polymer Characterization*, Ed. C. Booth and C. Price, Pergamon, Oxford, 1989, p.867.

74. Allied-Signal Inc., *Private Communication.*

75. J. Brandrup and G.H. Immergut, *Polymer Handbook, 3rd Edn.*, Wiley Chichester.

76. F.A. Quinn, Jr. and L. Mandelkern, *J. Am. Chem. Soc.*, 80, 3178 (1958).

77. B. Wunderlich and C.M. Cormier, *J. Polym. Sci., Part A-2*, 5, 987 (1967).

78. M.J. Richardson, *J. Polym. Sci., Part C*, 38, 251 (1972).

79. M.G. Broadhurst, *J. Res. Natl. Bur. Stand., Sect. A*, 67, 233 (1963).

80. K. Tanaka, T. Seto, *J. Phys. Soc. Japan*, 17, 873 (1962).

81. C.W. Bunn, *Trans. Faraday Soc.*, 35, 482 (1939).

82. C.W.M. Bastiaansen and P.J. Lemstra, *Makromol. Chem. Macromol. Symp.*, 28, 73 (1989).

83. A.J. Pennings and A. Zwijnenburg, *J. Polym. Sci., Polym. Phys. Edn.*, 17, 1011 (1979).

84. N.A.J.M. van Aerie, P.J. Lemstra and A.W.M. Braam, *Polym. Comm.*, 30, 7 (1989).

85. N.S. Murthy, S.T. Correale and S. Kavesh, *Polym. Comm.*, 31, 50 (1990).

86. R.G.C. Arridge, P.J. Barham, C.J. Farrell and A. Keller, *J. Mater. Sci. Letter*, 11, 788 (1976).

87. J.J. Aklonis and W.J. MacKnight, *Introduction to Polymer Viscoelasticity, 2nd Edn.*, Wiley Intersience, 1983.

88. I.M. Ward, in *Mechanical Properties of Solid Polymers, 2nd Edn.*, John Wiley & Sons, Chichester, 1983.

89. T. Murayama, in *Dynamic Mechanical Analysis of Polymeric Material*, Elsevier Scientific, Amsterdam, 1978.

90. M. Takayanagi, *J. Macro. Sci., Phys.*, B9(3), 391 (1974).

91. M. Matsuo, C. Sawatari and T. Ohhata, *Macromolecules*, 21, 1317 (1988).

92. S.K. Roy, T. Kyu and R.J. Manley, *Macromolecules*, 21, 1741 (1988).

93. L. Govaert, *PhD. Thesis*, University of Eindhoven, The Netherlands, 1990.

94. Rheometrics®, *RMS-800/RDS-II Owner's Manual*, 1990.

95. R.G.C. Arridge and M.J. Folkes, *Polymer*, 17, 495 (1976).

96. A. Keller and J.A. Odell, *J. Polym. Sci., Polym. Symp.*, 63, 155 (1978).

97. P. Schwartz, A. Netravali and S. Sembach, *Textile Res. J.*, 56, 502 (1986).

98. C.H. Anderson, *Textile Res. J.*, 59, 555 (1989).

99. D.J. Dijkstra and A.J. Pennings, *Polym. Bulletin*, 19, 73 (1988).

100. H. van der Werff and A.J. Pennings, *Colloid and Polym. Sci.*, 269, 747 (1991).

101. M.A. Wilding and I.M. Ward, *Polymer*, 22, 870 (1981).

102. M.A. Wilding and I.M. Ward, *J. Mater. Sci.*, 19, 629 (1984).

103. J. Sweeney and I.M. Ward, *J. Mater. Sci.*, 25, 697 (1990).

104. P.R. Carey, in *Biochemical Applications of Raman and Resonance Raman Spectroscopies*, Academic Press, N.Y., 1982.

105. G.P. Matthews, in *Experimental Physical Chemistry*, Clarendon Press, Oxford, 1985.

106. D.N. Batchelder, *European Spectroscopy News*, 80, 28 (1988).

107. K. Prasad and D.T. Grubb, *J. Polym. Sci., Polym. Phys.*, 28, 2199 (1990).

108. I.M. Robinson, R.J. Young, C. Galiotis and D.N. Batchelder, *J. Mater. Sci.*, 22, 3642 (1987).

109. R.J. Young, R.J. Day, J.L. Stanford, P.P. Ang and X. Hu, in *8th Int. Conf. Def. Yield and Frac. Polym.*, Churchill College, Cambridge, 8-11 April 1991.

110. P.P. Ang, *PhD. Thesis*, UMIST, 1990.

111. D. Lu, *PhD. Thesis*, UMIST, 1991.

112. L.C.N. Boogh, R.J. Meier, H. Kausch and B.J. Kip, *J. Polym. Sci., Polym. Phys.*, 30, 325 (1992).

113. R.P. Wool and R.S. Bretzlaff, *J. Polym. Sci.*, B24,

1039 (1986).

114. D.L.M. Cansfield, I.M. Ward, D.W. Woods, A. Buckley, I.M. Pierce and J.L. Wesley, *Polym. Comm.*, 24, 130 (1983).

115. A.G. Gibson, G.R. Davies and I.M. Ward, *Polymer*, 19, 683 (1978). 86.

116. A.G. Gibson, G.R. Davies and I.M. Ward, *Polym. Eng. Sci.*, 20, 941 (1980).

117. P.J. Barham and R.G.C. Arridge, *J. Polym. Sci. Polym. Phys.*, 15, 1177 (1977).

118. R.G.C. Arridge and P.J. Barham, *Polymer*, 19, 654 (1978).

119. D.W. Hadley and I.M. Ward, in *Encyclopedia of Polymer Science and Engineering, Vol. 9*, John Wiley and Sons, N.Y., p.379.

120. D.W. Hadley and I.M. Ward, in *Structure and Properties of Oriented Polymers*, Ed. I.M. Ward, Applied Science, London, 1975, p.264.

121. D.C. Prevorsek, *Private Communication*, Allied-Signal Inc.

122. R.J. Young, D. Lu, R.J. Day, W.F. Knoff and H.A. Davis, *J. Mater. Sci.*, 27, 5431 (1992).

123. R.G. Brown, *Spectroscopy Europe*, 4, 10 (1192).

124. W-F, Wong, *MSc Dissertation*, UMIST, 1990.